Identification of Driver Steering and Speed Control

Andrew Murray Charles Odhams

Queens' College

A dissertation submitted to the University of Cambridge

for the Degree of Doctor of Philosophy

Cambridge University Engineering Department

September 2006

To Nina

Summary

This thesis addresses the modelling of driver steering control and speed choice during road vehicle driving. Speed choice is an important factor in road accidents, and also in driver learning. Driver steering control is an important factor in speed choice. Improved understanding of speed choice could assist in the design of roads and vehicles to aid more appropriate, and therefore safer, speed choice. Research into the steering and speed choice behaviour of drivers was carried out to address this need.

Chapter one reviews previous literature relevant to driver speed choice. Literature relating to driver steering control and system identification was also reviewed.

Chapter two addresses the modelling of speed choice by testing existing models against simulator data, and assesses a path error based speed choice hypothesis by examining a subject's path error and speed choice during a simulator experiment. A need to quantify driver steering strategy is identified, leading to the work of chapters three, four and five.

Chapter three describes and compares driver steering models developed from Sharp's LQR steering model. These include simplified internal models for novice drivers, and a model of the neuromuscular system.

Chapter four describes the design and validation of identification algorithms and simulator experiments for the identification of driver preview models from closed loop driver data.

Chapter five describes the results of this driver preview model identification from measured simulator data comparing different driver preview models, test subjects, speeds and road widths. Conclusions and recommendations for future work are given in chapter six.

Preface

A PhD research project was carried out between October 2002 and September 2006 aimed at identifying the speed choice and steering control of drivers. This work on driver speed choice was funded by a research studentship from the Engineering and Physical Sciences Research Council (EPSRC). Financial assistance was also given by Queens' College Cambridge. I would like to thank these organisations for their support.

My thanks go to Dr David Cole, who originally proposed the project, and supervised throughout. His help, advice and encouragement have been invaluable in the completion of this work.

I would like to thank all of the test subjects, some of whom did not enjoy the tests at all, and many of whom were not included in the final results. I would also like to thank all the members of the MRO, DVRO, and other members of the DVRG past and present who have made the duration of the project both more productive, and more enjoyable. My thanks also go to the mechanics group technicians, who helped to build the simulator hardware and gave much practical advice.

I would also like to thank my family and friends for their encouragement and support throughout. My particular thanks go to Nina Pickett for her help and emotional support.

This dissertation is my own work and contains nothing that is the outcome of work done in collaboration with others, except as specified in the text and acknowledgements. No part of the work has already been, or is currently being, submitted for any degree, diploma or other qualification. This dissertation contains 46,024 words and 139 figures.

<div align="right">Andrew Odhams, September 2006</div>

List of Notation

[0/0]	Noise model order [numerator order/denominator order]
$\mathbf{A}$	2 DOF bicyle model state space matrix
$\mathbf{A_d}$	Discretised $\mathbf{A}$ matrix
$\arg\min_x f(x)$	Value of x which minimises $f(x)$
a	Front axle to CG distance
$B(\omega)$	Identification bias term in Ljung's derivation.
b	Rear axle to CG distance
a_1, b_1	Constants for Felip & Navin's model of speed choice
a_2, b_2	Constants for De Fazio's model of speed choice
a_3, b_3	Constants for Bottoms' model of speed choice
a_4, b_4, c_4, d_4	Constants for surface model of speed choice
a_5, b_5, c_5, d_5	Constants for lateral error vs. speed vs. curvature surface
a_7	Velocity offset for TLC model
$\mathbf{B}$	2 DOF bicycle model state space matrix
$\mathbf{B_d}$	Discretised $\mathbf{B}$ matrix
B_{nms}	Neuromuscular system damping from Pick's model of limb dynamics
C_f	Front axle tyre cornering stiffness
C_r	Rear axle tyre cornering stiffness
C	Road curvature
$\mathbf{C_1}$	Transformation matrix for Sharp's LQR model
ΔC_{max}	Driver's curvature margin in Reymond's model
$\mathbf{D}$	Track shift register matrix in Sharp's LQR model
$\mathbf{E}$	Input matrix for new point on track in Sharp's LQR model
$e(t)$	Driver steer angle white noise
$F(q)$	Vehicle system as a linear transfer function

$G_I, G_{II}, G_{III}, G_{IV}, G_V,$ $G_{VI}, G_{VII}, G_{VIII}$	Set of LQR driver models proposed in chapter 3
$G(q)$	Driver LQR controller
$G'(q)$	Estimate of driver LQR controller
$H(q)$	Driver noise filter
$H'(q)$	Estimate of driver noise filter (noise model)
$H'\{q_y', q_\theta', \tau'\}$	Estimate of noise model based on identified parameters $\{q_y', q_\theta', \tau'\}$
I	Vehicle yaw moment of intertia
J_{nms}	Neuromuscular system inertia in Pick's model
J	Cost function value
K_{sw}	Steering wheel to front wheel angle gain
K_{nms}	Neuromuscular system stiffness from Pick's model
K_1, K_2	Parameters of Odhams' speed adaptation model
k	Ratio of steer angle error to steer angle from Reymond's T_{LC} model
k_1	Constant in linearisation of Prokop's steer model.
$k_{pi}\{G_I\}$	Preview gains for model G_I
$(k_{\delta_{N_d}} \ldots k_\delta)$	Steer angle delay state gains for model G_{IV}
k_ω	Yaw rate state gain in $\mathbf{k_{LQR}}$
k_υ	Sideslip state gain in $\mathbf{k_{LQR}}$
M	Vehicle body mass
N_d	Number of delay states in model G_{IV}
$n(t)$	Vehicle position signal
$n'(t)$	Estimated vehicle position signal
$\mathbf{Q}$	Matrix of lateral and heading error weights in Sharp's LQR model

q_y	Lateral error weight in LQR cost function for models G_I to G_{VIII}
q_θ	Heading angle error weight in LQR cost function for models G_I to G_{VIII}
$q_y{'}, q_\theta{'}$	Estimates of q_y and q_θ used in estimated driver model G'
$q_y{}^G, q_\theta{}^G$	True values of q_y and q_θ used to generate dummy data for identification validation in chapter 4.
$q_y{'}_{[1]\{U=30\}}$	Three $q_y{'}$ values for subject 1 at $U = 30$ m/s.
R	Road curve radius
∂R	Curve radius error of driver in Reymond's T_{LC} model
$r(t)$	Road path input signal
S_{p0}	Value of S_t for track point perpendicular to the vehicle
(S, ψ)	Vehicle path defined in intrinsic co-ordinates
(S_t, ψ_t)	Track defined in intrinsic co-ordinates
T	Time step of discrete LQR model formulation
T_{LC}	Time to lane crossing parameter.
T_d	Tracking difficulty in Bottoms' model
$T_{dem}(s)$	Torque applied to neuromuscular system through the steering wheel
U	Forward speed of vehicle
$\mu(U)$	Mean forward speed of vehicle
$\mu(U_{cc})$	Mean of U_{cc}
U_0	Maximum comfortable speed on straights
U_{cc}	U in constant radius part of $180°$ curve
$u(t)$	Input signal to the driver
$u'(t)$	Estimate of inputs $u(t)$ in indirect method where vehicle $F(q)$ operates in closed loop with the estimated driver $G'(q)$
W	Width of left hand lane of road, beyond which buzzers sound
W_v	Vehicle width

W_1, W_2, W_3	Weights for path error based speed choice hypothesis
$\mathbf{x_v} = \begin{bmatrix} v & \omega & y_v & \theta \end{bmatrix}$	Vector of vehicle velocity and position states used in derivation of Sharp's LQR controller.
(x, y)	Position in global Cartesian co-ordinates
$(\tilde{x}, \tilde{y})$	Position in local driver Cartesian co-ordinates (centered on Vehicle, and yawing with vehicle)
$(\mathbf{x_t}, \mathbf{y_t})$	Vector of discrete track points in global co-ordinates
$(\mathbf{\tilde{x}_t}, \mathbf{\tilde{y}_t})$	Vector of discrete track points in local driver co-ordinates
$(\mathbf{y_r}) = (y_{r1}, y_{r2} \ldots y_{ri})$	Vector of previewed lateral offsets in global co-ordinates
$(\mathbf{y_p}) = (y_{p1}, y_{p2} \ldots y_{pi})$	Vector of previewed lateral offsets in local driver co-ordinates
y_v	Vehicle position state in $\mathbf{x_v}$
y_{p0}	Vehicle lateral error from path.
$\mathbf{z}$	Vector of vehicle and track states joined
α	Angle subtended to lane exit with radius error in Reymond's T_{LC} model.
β	Expedience parameter in Herrin and Neuhardt's model.
Γ	Lateral acceleration
$\Delta\Gamma$	Lateral acceleration safety margin
Γ_{cc}	Lateral acceleration in constant radius part of 180° curve
Γ_{max}	Driver prediction of maximum available lateral acceleration
γ	Track angle PSD frequency roll-off parameter
δ_f	Front wheel angle of vehicle
$\delta(t)$	Driver steering wheel angle
$\delta'(t)$	Estimate of driver steering wheel angle
$\delta_{out}(t)$	Driver steer angle output post NMS system
$(\delta_{Nd-1}, \ldots, \delta)$	Delay states of steer angle for model G_{IV}
ε	Weighted steer angle prediction error
ς	Constant in Emmerson's model of speed choice
$\eta(t)$	Driver steer angle filtered noise $= He(t)$

θ	Vehicle yaw angle
Θ	Generalised effort parameter encompassing driver steering strategy.
κ	Track angle PSD amplitude parameter
λ	Percentile of lateral error (0 to 100)
λ^{W_1}	Percentile of lateral error recorded for width W_1
λ_1	Damping in Odhams' adaptation model
$\mu_{[1:5]}(q_\theta{'}), \mu_{[1:5]}(q_y{'}),$ $\mu_{[1:5]}(\omega_n{'}), \mu_{[1:5]}(\xi{'})$	Mean of the estimates of q_y, q_θ ,ξ' and ω_n' across 5 subjects and 3 repetitions for each subject for a given speed
$\mu_{[1:5]}(\Xi(\upsilon))$	Mean of $\Xi(\upsilon)$ across 5 subjects and 3 repetitions for each subject for a given speed.
$\mu_{err}(q_y{'},q_\theta{'})$	Percentage error of mean of parameter estimates $(q_y{'},q_\theta{'})$ from their true values $(q_y{}^G,q_\theta{}^G)$
ν	Lateral speed of vehicle (sideslip)
$\Xi(e)$	RMS of driver noise e(t)
$\Xi(\eta)$	RMS of filtered driver noise η(t)
$\Xi(\varepsilon)$	RMS of weighted steer angle prediction error ε
$\Xi(\delta_{e=0})$	RMS of steer angle of model G_I driving road with no added noise e .
$\Xi(\upsilon)$	RMS of unweighted steer angle prediction error υ
ξ	Neuromuscular system damping factor
Π_y	Ratio of 95th percentile steer angle to 95th percentile lateral error
Π_θ	Ratio of 95th percentile steer angle to 95th percentile yaw error
$\rho_{95}(y_{p0})$	95th percentile lateral error
$\sigma_{err}(q_y{'},q_\theta{'})$	Standard deviation of parameter estimates $(q_y{'},q_\theta{'})$ as a percentage of their true values $(q_y{}^G,q_\theta{}^G)$
τ	Driver delay
$\tau{'}$	Estimate of driver delay τ used in estimated driver model G'

τ^G	True value of driver delay used to generate dummy data for identification validation in chapter 4
υ	Unweighted steer angle prediction error
$\Phi_r(\omega)$	Spectrum of road input $r(t)$
$\Phi_u(\omega)$	Spectrum of driver input $u(t)$
$\Phi_u^e(\omega)$	Spectrum of input $u(t)$ resulting from driver noise $e(t)$ fed back through vehicle.
χ	Wavenumber for definition of track angle PSD
ψ_t	Track angle defined in intrinsic coordinates
ψ_{pi}	i^{th} increment of track angle ψ_t in the vehicle reference frame
ω	Yaw rate of vehicle
ω_n	Natural frequency of 2nd order neuromuscular system model

Contents

Chapter 1: Review of driver speed choice and steering models

1.1   Introduction: Motivation for understanding speed choice

Vehicles are generally operated in the linear region of their handling, where drivers are familiar with the control of the vehicle. However, outside this region the vehicle can become non-linear due to tyre saturation effects. This non-linearity can be difficult for the driver to control due to its unfamiliarity, and the resulting loss of control can lead to accidents involving departure from the road, or rollover. Speed choice on approach to curves (preview speed control) is therefore important for drivers of many vehicle types since it influences the degree of non-linearity of the vehicle, and its familiarity to the driver. On approach to a curve, the driver must choose a speed based on their ability to negotiate the curve, so their speed choice interacts with their steering ability.

About 20% of rural accidents involve vehicles going too fast for the situation with a further 25% likely to be associated with speed [1]. In an urban area about 4% were directly related to excessive speed and another 21% due to speed related factors [2]. Results from studies of the responses of 5000 drivers to a questionnaire about accident involvement and speed choice indicate that for an individual who drives at a speed more than about 10-15% above the average speed of the traffic around them, the likelihood of their being involved in an accident increases significantly [3-5]. Figure 1.1 reproduced from [6] shows the relative accident involvement of a driver compared to that of a driver travelling at the average speed (i.e. one with a relative speed of 1.0). It shows that drivers who habitually travel faster than average are involved in more accidents in a year's driving.
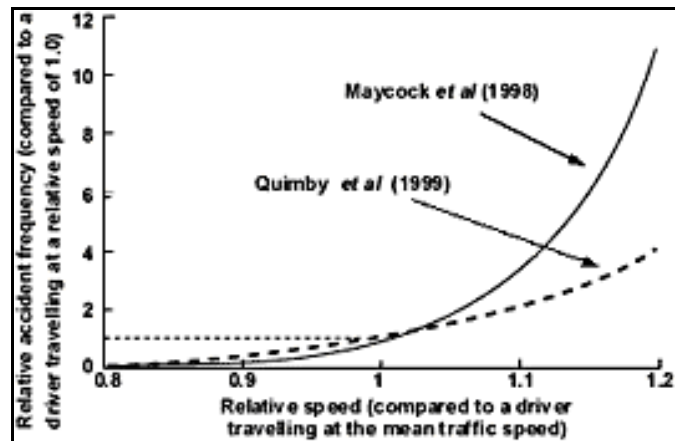
Figure 1.1: Relative accident involvement of a driver compared to a driver travelling at the average speed reproduced from [6]. Quimby et al (1999) refers to [4, 5] Maycock et al (1998) refers to [3]

An understanding of how to design roads and vehicles to encourage more appropriate speed choice could therefore be useful in reducing the number of speed related accidents on roads.

Reducing the number of rollover accidents for heavy vehicles is also one of the motivations of the research. Winkler et al. reported that, in the US between 1992 and 1996, rollover was the cause of approximately 12% of fatal truck and bus accidents and 58% of accidents in which truck drivers were killed [7, 8]. A study by Kusters on rollover accidents in The Netherlands attributed these accidents to three main causes: sudden course deviation, load shift, and speed choice [9].

Speed choice is also an important part of the safety assessment of the road network. Levison [10] cites a speed choice model as an important part of the framework for the Interactive Highway Safety Design Model (IHSDM). The IHSDM is to be developed by the Federal Highway Administration in order to be used in the safety assessment of new highway designs.

Speed choice is also important when modelling driver learning of the steering task. To clarify the role of speed control in the driving task, a generic learning model [11] is shown in Figure 1.2 with driving specific terms substituted. The driver controls the vehicle in order to follow an intended path using feedforward and feedback control. The model importantly incorporates a critic of task performance by comparing measured performance to that intended. The output of this critic is shown in the diagram as path error, which represents both lateral error and heading error.

The learning element represents the driver's ability to update their feedforward and feedback control based on information from the critic. Speed choice is the 'problem generator' for the driver, because it determines the difficulty of the steering task presented to the driver. A more adventurous driver can improve their learning of the feedforward and feedback control by exploring more of the vehicle's performance envelope. This may be sub-optimal in the short term, but lead to better control in the long run.
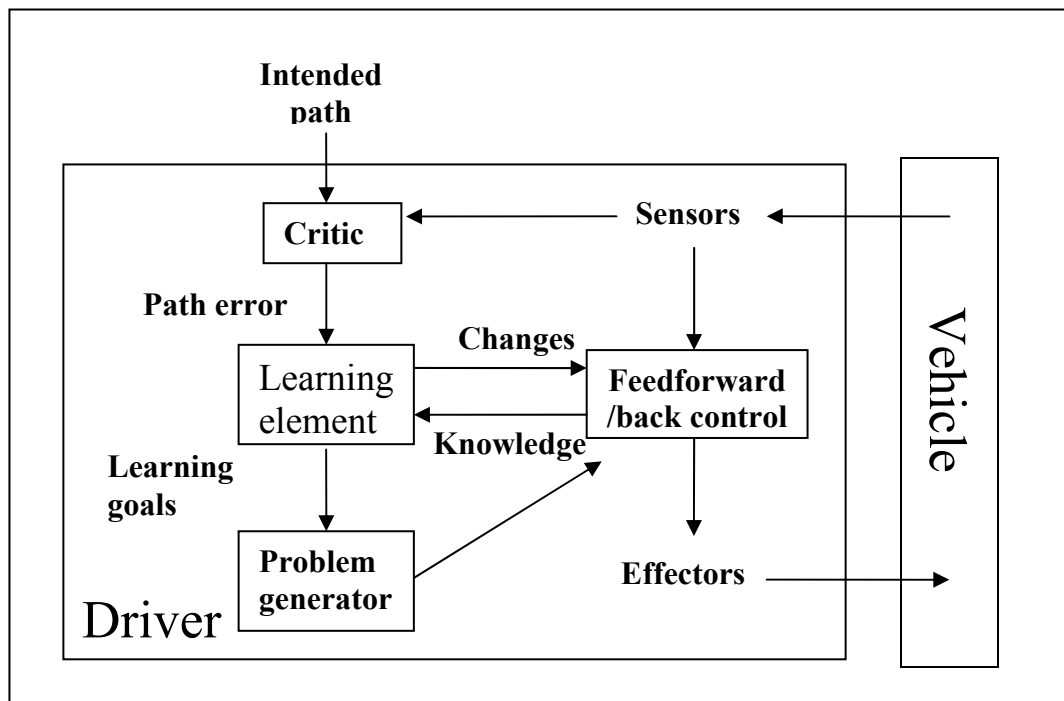
Figure 1.2: Generic learning model adapted from Russell [11]

The study of speed control is therefore linked to that of steering control through the learning aims of the driver. The literature to date on both speed choice and driver steering control was studied to establish the state of the art, and is reviewed in the following sections, 1.2 and 1.3.

1.2   Models of speed choice

The models of speed choice have been categorised into three types. First, the early models based on lateral acceleration as the primary cue are described in section 1.2.1. The models based on speed choice as a function of 'available tolerance', and hence road width, are described in section 1.2.2. Models of speed choice based on a prediction of driver path following error are described in section 1.2.3, and in section 1.2.4 coupled models of steering and speed choice are described. Finally, the speed adaptation effect is described in section 1.2.5.

1.2.1   Lateral acceleration

Attempts to characterise speed choice in curves first concentrated on lateral acceleration as the major cue, with speed a simple function of curvature [12-14]. Ritchie [12] recorded lateral acceleration (Γ) and speed (U) for fifty subjects during normal road driving. He found that lateral acceleration was constant below 9 m/s (32 km/h), so that speed U was related to curve radius R by:

$$\Gamma = \frac{U^2}{R} \qquad (1.1)$$

At speeds above 9m/s, drivers were found to choose a lower speed than that which would yield constant lateral acceleration, such that there was a linear relationship between lateral acceleration and speed. The relationship observed by Ritchie is shown schematically in Figure 1.3.
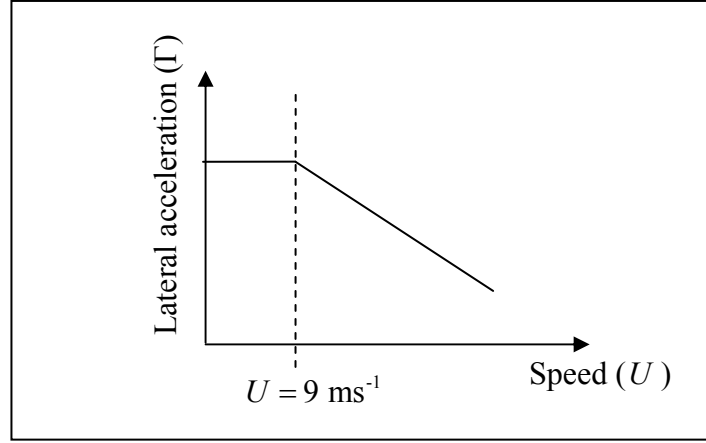
Figure 1.3: Schematic of Lateral Acceleration vs. speed observed by Ritchie [12]

Herrin & Neuhardt [15] recorded similar results to Ritchie's, and fitted an empirical model to the reduction of lateral acceleration with speed of the form:

$$\frac{\Gamma}{\Gamma_{max}} = 1 - e^{[\beta(U_0 - U)]}$$ (1.2)

Γ/Γ_{max} is the fraction of the driver's maximum tolerable lateral acceleration used, and $(U_0 - U)$ is the speed reduction from the driver's maximum comfortable straight-line speed U_0. β is an expedience parameter, reflecting the driver's trade-off between lateral acceleration and speed. High β implies that the driver travels at his or her maximum comfortable speed unless the maximum tolerable lateral acceleration is reached. Lower β implies a more gradual trade-off. Figure 1.4 shows the effect of β on lateral acceleration predicted by Herrin's model. Drivers were found to display higher β when more familiar with the road. Drivers who were told to drive as if they were 'late for a meeting' displayed higher maximum comfortable speed, and higher lateral acceleration tolerance.
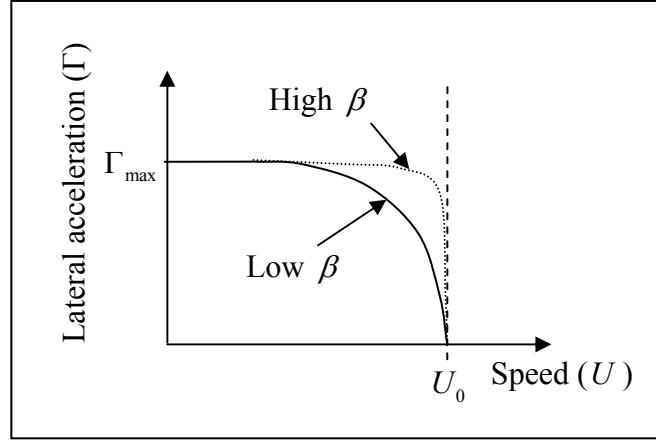
Figure 1.4: Schematic of Herrin and Neuhardt's [15] expedience parameter model

McLean [16] fitted several models to speed vs. road curvature data from previous studies. The most successful fits were a linear variation of speed with curvature (from Taragin [17]):

$$\mu(U) = 20.9 - 0.578C + 0.681(W_p - 7.3) \tag{1.3}$$

where:

$$\begin{aligned}
\mu(U) &= \text{Mean speed (m/s)} \\
C &= \text{Curvature (rad/m)} \\
W_p &= \text{'Pavement' width (m)}
\end{aligned} \tag{1.4}$$

and an exponential model proposed by Emmerson [18]:

$$U = U_0\left(1 - e^{-\varsigma R}\right) \tag{1.5}$$

Where ς is a constant. Both models predict zero speed for small radii, and asymptotically approach the 'free speed' (U_0) on straights for large radii, as shown in Figure 1.5. McLean noted that 'data for large radius curves could be distorted by free approach speeds being less than the curve design speed'. This is significant to the design of speed choice experiments, as it must be ensured that the speed attainable on straights between test curves is high enough not to distort the curve speeds.
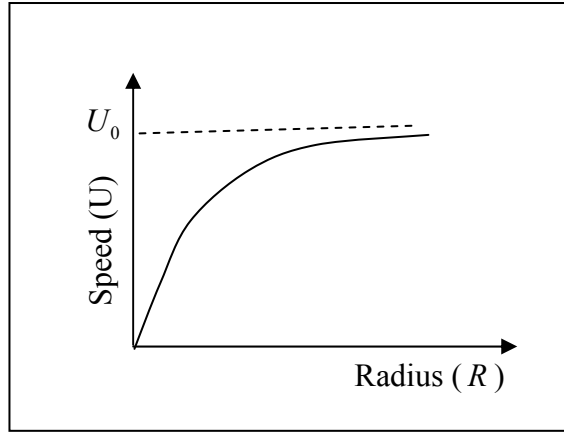
Figure 1.5: Schematic of variation of speed with Radius for Taragin's [17], and Emmerson's [18] models

Felipe & Navin [19] fitted several of these previous models to data from test track and road driving. Speed and lateral acceleration were measured, and the models of Herrin & Neuhardt [15], Taragin [17], and Emmerson [18] were fitted with some success. A logarithmic model (equation (1.6)) for predicting lateral acceleration reduction with increased speed fitted best to the data collected, however, no mechanism was suggested. The relationship in equation (1.6) is similar to Figure 1.5.

$$U = a_1 + b_1 \ln(R) \tag{1.6}$$

Where a_1 and b_1 are constants.

1.2.2 Available tolerance

Available tolerance is the allowable lateral error before the road edge is reached as defined in equation (1.7).

$$\text{Available tolerance} = (W - W_v)/2 \tag{1.7}$$

$$\begin{aligned} W_V &= \text{Vehicle width} \\ W &= \text{Road width} \end{aligned} \tag{1.8}$$

Research on the speed of self-paced tracking tasks as a function of available tolerance has considered the influence of path width [14, 16, 20].

Drury [13] timed subjects tracing lines and circles by hand, with various available tolerances with the intention of providing an analogy to the task of self-paced track following in car driving. A linear relationship between speed and tolerance was found. For driving tests on a circular track, De Fazio et al [21] found speed to be proportional to road width as shown in equation (1.9). Figure 1.6 shows equation (1.9) schematically.

$$U = a_2 + b_2 W \qquad (1.9)$$

Where a_2 and b_2 are constants.
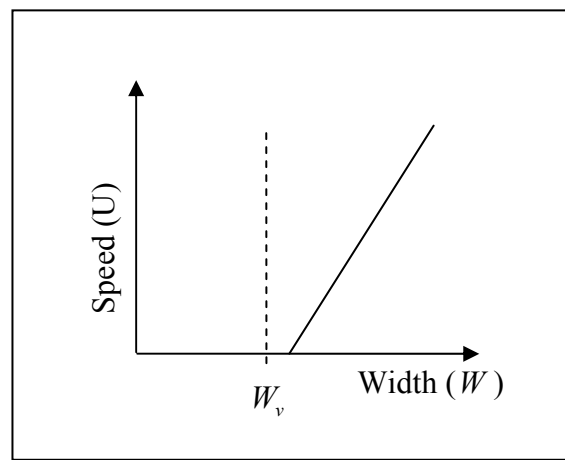
Figure 1.6: Dependence of speed on path width W, with a vehicle of width W_v for DeFazio's [21] linear model

The negotiation of competition 'gates' with tractors was studied by Bottoms [20]. A linear relationship between mean speed ($\mu(U)$) and tolerance gave good agreement but a logarithmic model, shown in equations (1.10) and (1.11) and in Figure 1.7, performed better:

$$\frac{1}{\mu(U)} = a_3 + b_3.T_d \qquad (1.10)$$

$$T_d = \ln\left[\frac{2W_V}{W - W_V}\right] = \text{Tracking difficulty} \qquad (1.11)$$

Where a_3 and b_3 are constants.
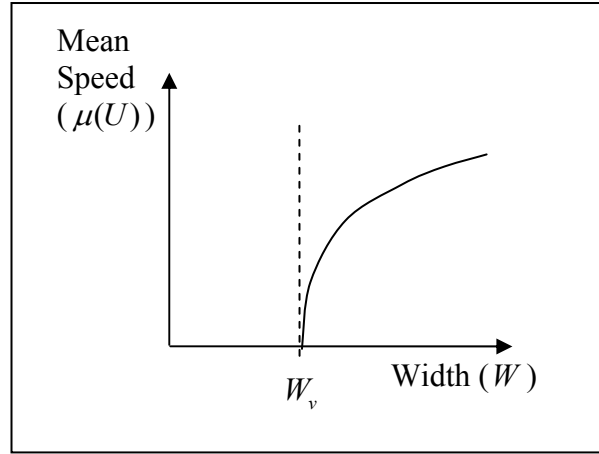
**Figure 1.7: Dependence of speed on path width $\mathbf{W}$ with a vehicle of width $\mathbf{W_v}$ for Bottoms'
[20] logarithmic model**

However, as for Drury [13] and De Fazio et al [21], the effect of path curvature is not included in the model. Bottoms [20] proposed an extension to the model to make it more suitable for continuous tracking tasks such as road driving. This model included heading angle tracking difficulty as well as lateral position tracking difficulty, but was more relevant to very long vehicles such as tractors with trailers, than to cars.

1.2.3 Path error models

Several studies have attempted to characterise speed choice as a function of the driver's anticipated path following error [13, 20, 22, 23].

Van Winsum and Gothelp [24] defined a measure of safety margin using the 'time to lane crossing' (T_{LC}) which is the predicted time for the vehicle to cross a lane boundary based on the vehicle's present trajectory. The driver is assumed to assess the T_{LC}, and take action to change speed or trajectory to keep T_{LC} above a minimum acceptable value.

In simulator tests using 40, 80, 120 and 160 m radius curves [24], T_{LC} was found to be kept above a constant minimum level by drivers. Also, steer angle error was found to be proportional to steer angle (and hence bend radius). It was claimed that a driver model with these two features could explain the speed vs. radius behaviour of drivers, and in turn the reduction of lateral acceleration with speed.

However, Reymond [23] later found that T_{LC} was not an invariant parameter in driver speed choice. Reymond evaluated the T_{LC} model by assuming that as the driver attempted to follow the centre line of the road, the minimum T_{LC} would occur when the vehicle crossed the centre line of the road, as shown in Figure 1.8. Reymond assumed negotiation of a curve with steering angle (and hence curvature) error proportional to curvature (as found by Van Winsum [24]), as shown in Figure 1.8, and equation (1.12). The vehicle is assumed to be travelling at speed U crossing the centreline of a curve of radius R, with radius error ∂R. α is the angle traversed before the road edge is reached if this steering error is not corrected. This gave T_{LC} as shown in equation (1.13).

$$\partial R = \frac{k.R}{(1+k)}$$
$$k = 0.1$$

(1.12)

$$T_{LC} = \frac{\alpha.(R-\partial R)}{U}$$
$$\alpha = \cos^{-1}\left\{1 - \frac{W\left(2.R - \frac{W}{2}\right)}{4.\partial R.(R-\partial R)}\right\}$$

(1.13)
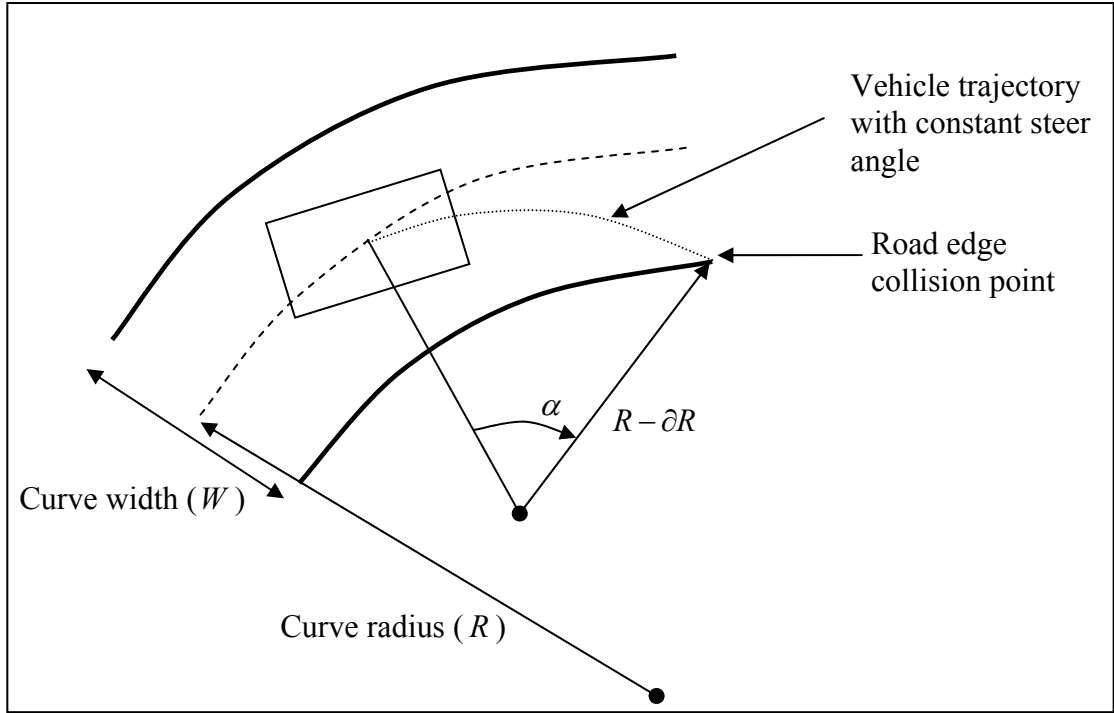
Figure 1.8: Reymond's model [23] of Van Winsum's [24] T_{LC} model, showing the driver steering with radius error ∂R

Reymond evaluated this model for a variety of curve radii, but found that assuming a constant T_{LC} gave incorrect speed choice behaviour, with little reduction of lateral acceleration at high speed. This disagreed with the results in the literature [12, 15, 19], and with Reymond's own experiments [23].

Reymond [23] instead proposed a lateral acceleration safety margin to explain reduction of lateral acceleration with speed. This safety margin is predicted by the driver based on his or her expectation of steering errors, obstacles, or a sudden road curvature increase. It can therefore be reduced for an expert driver with good knowledge of the road ahead, but would be increased in the case of an inexperienced driver following a hazardous road. The safety margin model is shown in equations (1.14) and (1.15), and illustrated in Figure 1.9.

$$\Gamma \le \Gamma_{\max} - \Delta\Gamma \qquad (1.14)$$

$$\Delta\Gamma = \Delta C_{\max} U^2 \qquad (1.15)$$

11
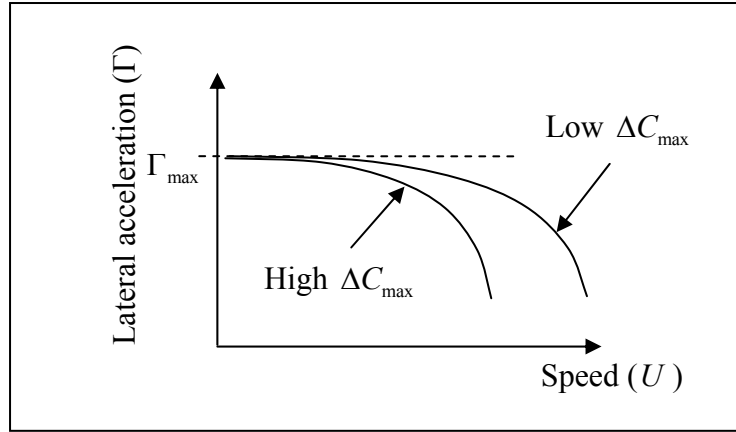
Figure 1.9: Reymond's [23] lateral acceleration margin model of speed choice

The driver chooses a lateral acceleration Γ that is less than his or her prediction of the maximum available Γ_{max} by an amount that is the lateral acceleration safety margin $\Delta\Gamma$. The margin is proportional to the driver's uncertainty of the future curvature deviation ΔC_{max}, which is independent of speed. In on-road tests it was found that the curvature margin ΔC_{max} decreased and Γ_{max} increased as drivers tried to drive more urgently. Curvature margin ΔC_{max} was found to be lower when the same road was driven on a moving base simulator, and lower still when a fixed-base simulator was used. Γ_{max} did not change from road to simulator tests (tyre saturations were included in the simulator vehicle model).

Reymond's 'risk estimation' bears similarities to an earlier model based on the driver choosing a speed with acceptable path error proposed by Levison [10]. Levison proposed the speed choice model as part of the framework for the Interactive Highway Safety Design Model (IHSDM) which was to be used in the safety assessment of new highway designs. He did not provide any data to support the model but proposed it as a starting point for the speed choice module of the IHSDM. Reymond's model refers to a curvature deviation, which is directly related to a path deviation for a given speed. For both models, the safety margin which the driver allows for this error is assumed to reduce for well known curves, and for confident drivers. Also, both models were proposed to be based on an assessment of the driver's path following error. More recently Cole [22] proposed a more detailed model for speed choice based on path error. A development of this model is described in chapter 2 section 2.3.

1.2.4 *Coupled models of steering and speed control*

Many models of driver steering control also include speed control models in which a target speed is maintained by closed loop control of the vehicle's longitudinal dynamics. The target speed is usually based on the assumption of a maximum lateral acceleration or a speed limit [25, 26], or a measured speed profile [27].

Prokop [28] provides a more sophisticated speed choice model using a coupled model of speed control and steering. Prokop's model plans its path and speed by minimising a cost function of vehicle state variables: travel time, horizontal accelerations (longitudinal and lateral), brake use, lane keeping, deviation from desired vehicle speed and engine speed. Prokop names this strategy 'Model Predictive Online Optimisation' (MPOO). The weightings of the cost function are dependent on the preferences of the driver, e.g. a driver in a hurry will place high weight on travel time, and less weight on lateral and longitudinal acceleration. The model then uses a feedback (compensatory) controller to ensure that the path and speed trajectories planned by the optimisation process are followed.

The choice of speed is made by the predictive part of the model based on an assumption that the chosen path will be followed perfectly. No account is taken of path errors arising from internal or external disturbances, or by imperfect knowledge of the vehicle dynamics. This would imply that drivers do not assess the accuracy of their path following control and do not adjust their speed accordingly, which seems to be an important omission.

1.2.5 *Speed adaptation*

Speed adaptation is the tendency of drivers to misinterpret their speed after prolonged exposure to another speed, in the absence of absolute speed information e.g. speedometer. Since the speedometer is not necessarily used by the driver in speed judgement for oncoming curves, adaptation could be significant in the speed choice problem in two ways. Firstly if speed is misperceived this may lead to an improper selection of an appropriate speed for a particular corner. Secondly if the speed at

which a corner was taken was misperceived, this could lead to the incorrect updating of the driver's understanding of their own competence e.g. believing that they managed to go faster or slower than they actually did for a given path error.

Research into the effects of adaptation has been carried out by several researchers [29-33]. Denton's experiments [29, 30] aimed to relate the driver's perceived speed ($\hat{U}$) to the real vehicle speed (U). Experiments were carried out in a car [29], and later in a specially constructed test rig where only visual speed cues were available to the driver, and where they controlled their speed using a lever [30].

The speed perception errors displayed during Denton's experiments can be summarised by Figure 1.10 which shows axes of perceived speed ($\hat{U}$) against actual speed (U). It is assumed that the perceived and actual speeds are equal in the fully adapted (long term) state, because the driver can 'recalibrate' their perceived speed using the speedometer in this long-term case. This fully adapted state is shown as a dashed line with unity gradient.
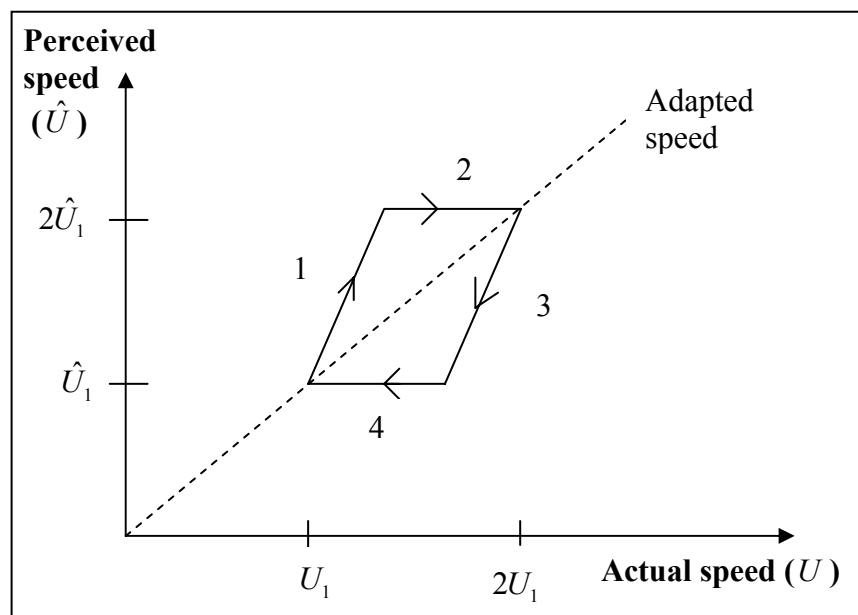
Figure 1.10: Adaptation effect on Actual vs. Perceived speed

Two types of test were carried out by Denton, the first in a real car with the speedometer and engine noise obscured, and the second in a specially constructed test machine. During the first set of tests subjects asked to double their (perceived) speed (from $\hat{U}_1$ to $2\hat{U}_1$), changed their actual speed by less than a factor of two. This is

shown as line (1) in Figure 1.10 which has gradient greater than unity. Drivers asked to halve their speed reduced their speed by less than a factor of two, shown by line (3).

The second set of tests were carried out in a test machine where the driver was given only visual cues of speed by a moving roadway, and had control of the speed of the roadway using a hand lever. The results of the test are illustrated by Figure 1.10 as follows:

1. Subjects were adapted to a constant speed (U_1) by prolonged exposure to that speed. The subjects were then suddenly exposed to a higher speed (following line (1)) causing their perceived speed to be $2\hat{U}_1$.

2. The subjects were then asked to keep their perceived speed ($2\hat{U}_1$) constant by altering their actual speed (U) using the hand lever. Subjects increased their actual speed U in order to keep their perceived speed constant (following (2)). Their speed asymptotically approached the fully adapted speed $2U_1$.

3. The second half of the test was a reversal of the first half. Subjects were adapted to a higher speed ($2U_1$) by prolonged exposure to that speed. The subjects were then suddenly exposed to a lower speed (following (3)) causing their perceived speed to become $\hat{U}_1$.

4. Subjects were then asked to keep their perceived speed $\hat{U}$ constant by altering their actual speed (U) using the hand lever. Subjects decreased their actual speed U in order to keep their perceived speed ($\hat{U}_1$) constant (following (4)). Their speed U asymptotically approached the fully adapted speed U_1.

The resulting hysteretic behaviour was modelled using a mechanical linear system analogy as shown in Figure 1.11. Such a model was not suggested by Denton, but fits to the important aspects of his experimental data. Force (F) represents perceived speed ($\hat{U}$), while position (x) represents actual speed (U). Parameters were fitted to data from Denton's experiments [29, 30].
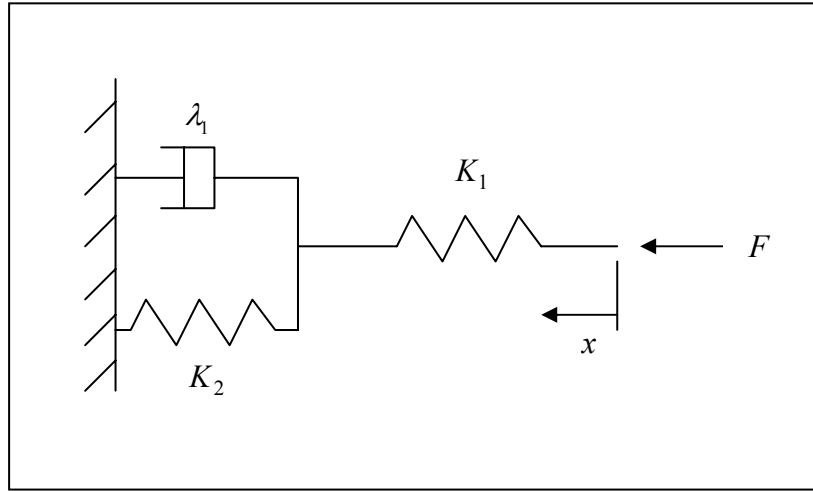
Figure 1.11: Mechanical speed adaptation model

First, the unity gradient of the adapted speed line gives:

$$\frac{K_1 K_2}{K_1 + K_2} = 1 \tag{1.16}$$

The gradient K_1 of the instantaneous speed change lines (1) and (3) was fitted to Denton's data [29] giving:

$$K_1 = 1.14 \tag{1.17}$$

The time constant of the speed change in (2) and (4) is given by:

$$T_{adaptation} = \frac{\lambda_1}{K_1 + K_2} \tag{1.18}$$

Denton found the time constant to vary with speed from 10 to 25 seconds [30], but is approximated as 20 seconds for this simulation.

Figure 1.12 shows actual speed recorded during a simulator test, and the resulting estimated perceived speed from the adaptation model. Having adapted to zero speed at the start of the test, perceived speed is higher than actual speed. However, after prolonged exposure to higher speeds, a drop in speed for the last ten seconds causes perceived speed to be lower than the actual speed.
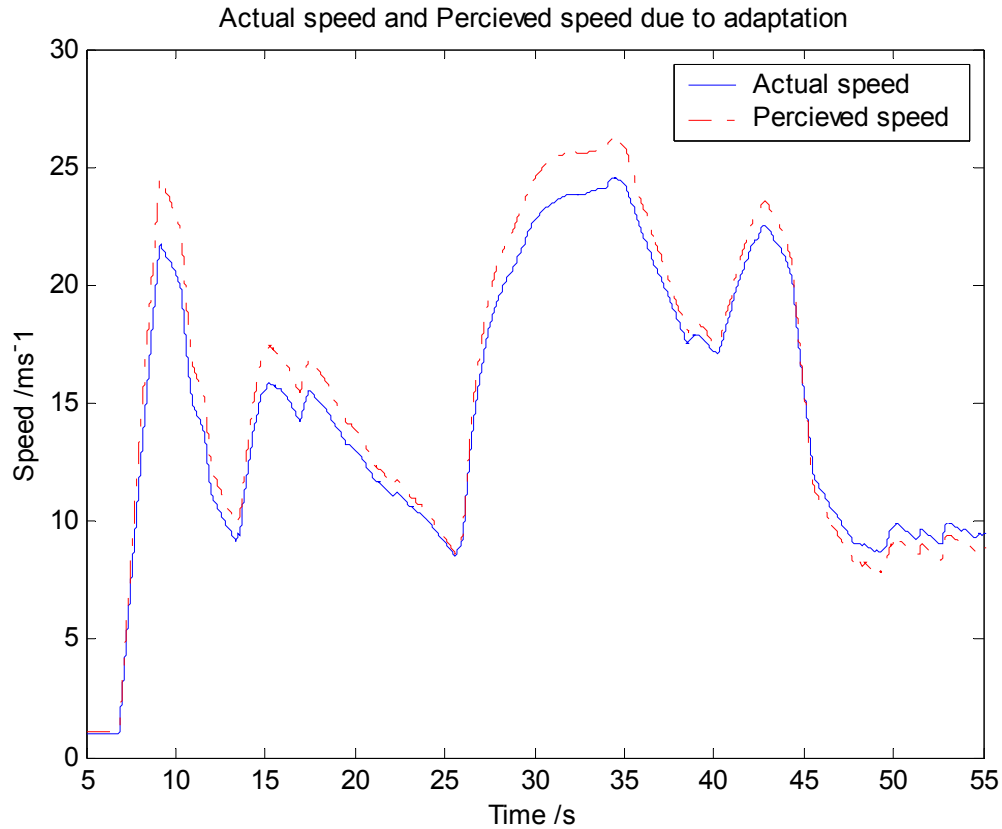
Figure 1.12: Perceived speed and actual speed for a driver adapted to zero speed at the start of the test

The error in perceived speed is small with the parameter values derived from Denton's experiments. The results of Figure 1.12 suggest a maximum 14% misperception of speed, which only occurs when speed is changed significantly faster than the 20 second time constant. Denton found the degree of adaptation to be subject dependent, with some people showing no measurable adaptation tendency.

The effect of including this model of speed adaptation in a path error based speed choice model was assessed using the speed choice model explained later, in chapter 2 section 2.3. Speed adaptation was found to have little effect on speed choice using the parameters derived from Denton's experiments, so the effect of adaptation will not be included in the discussion of the path error based speed choice model in chapter 2.

1.2.6   Summary of speed choice

Table 1.1 shows a summary of the literature on speed choice. Listed are the types of test performed, models proposed, and the variables measured during experiments.

			Ritchie, McCoy & Welde [12] 1968	Drury [13] 1971	Herrin & Neuhardt [15] 1974	McLean [16] 1974	Bottoms [20] 1983	Gawron & Ranney [34] 1990	DeFazio, Wittman& Drury [21] 1992	Van Winsum & Gothelp [24] 1996	Levison [10] 1998	Prokop [28] 1998	Felipe & Navin [19] 1998	Reymond at al. [23] 2001	Cole [22] 2002
Tests	non-driving	Curve tracing		X					X						
	driving	Road	X		X	X								X	
		Track				X			X			X	X	X	
	simulator driving	Moving base												X	
		Fixed-base						X		X				X	
Controlled variables/ measurements		Tolerance		X			X	X	X						
		Radius				X		X		X			X	X	
		Lateral Accel.	X										X	X	
Models	speed	Lateral Accel.	X		X							X	X	X	
		Path error		X			X				X	X		X	X
		T_{LC}								X				X	
	steering	MPOO										X			

Table 1.1: Summary of literature on speed choice, where grey indicates inclusion of that test, model or variable

Attempts to characterise speed choice as a function of curvature first concentrated on lateral acceleration as the major cue. Drivers were observed to reduce their lateral acceleration as speed increased [12, 14, 15, 19, 23]. Research on the speed of self-paced tracking tasks as a function of available tolerance successfully fitted models to the relationship between road width and vehicle speed [13, 20, 21].

Research modelling speed choice as a function of anticipated error, found that a constant T_{LC} was maintained by the driver, and that steering error increased

proportionally with steer angle. However later analysis of this result by Reymond [23] found that it could not explain drivers' reduction of lateral acceleration at high speed.

Reymond's combined model incorporating both lateral acceleration and path error (in the form of a lateral acceleration margin) was more successful [23]. Drivers' curvature error margin ΔC_{max} (equivalent to a path error) was found to change with driving style, and to decrease in a simulator.

1.3 Driver steering control

The development of driver steering control models is well documented, and several authors have reviewed the field. Guo and Guan [35] provided a comprehensive review of both compensatory and preview driver models, and Pick [36] and Rutherford [37] have more recently reviewed the topic. Compensatory and preview controllers are summarised in the following sections.

1.3.1 Compensatory control

McRuer [38, 39] modelled the performance of a driver in the road path tracking task using the 'crossover' model. In the crossover model, the driver was presumed to use only visual information of their lateral error to perform feedback lateral position control. McRuer found that drivers changed their control gains and lead/lag compensation to ensure good phase margin, and a roll-off of 20dB per decade at the crossover frequency of the driver-vehicle open loop transfer function. Weir & McRuer [40] later refined this model to include nested feedback loops for heading error as well as lateral error. It was found that by using heading angle feedback, no lead/lag terms were required to stabilise the vehicle, only gain terms. In experiments McRuer [39] found drivers' cognitive delay to be approximately 0.2 seconds, and their actuation delay 0.1 seconds.

Compensatory control models are suitable for modelling the driver's reaction to random disturbances such as side-winds. However, drivers also use information previewed from the road ahead, so preview control models of the driver were developed to take account of this.

1.3.2 Preview control

McRuer [40] used a single point preview model which eliminated the need for lead compensation by the driver if the correct look-ahead distance was chosen.

MacAdam modelled the driving process using a model predictive preview controller [41]. This controller compared a target path with a prediction of the vehicle trajectory assuming present states, and a constant steer angle input. Steer angle input was then chosen to minimise the error between target and predicted trajectory over the prediction horizon. Peng [42] noted that this controller is a special case of model predictive control (MPC). The model was used for the Carsim driver model (www.carsim.com), and much of the research at the University of Michigan Transportation Research Institute (UMTRI). Peng [42] extended MacAdam's use of predictive control theory to include heading and curvature errors in the cost function and to allow for non-constant steer angle control.

As mentioned in section 1.2.4, Prokop [28] used a cost function approach, optimising a more sophisticated cost function than MacAdam [41]. However, this was not model predictive control (MPC) in its strictest sense, as the planned steering control was corrected using a compensatory controller, and the optimisation was only used offline for trajectory planning. Prokop [28] also included a simplified vehicle model for novice drivers who viewed the vehicle's transfer function as that of a point mass. This could be a useful approach when modelling subjects with a range of driving abilities.

Sharp & Valtetsiotis [43] used a linear quadratic regulator (LQR) controller, and included the previewed road path in the model. This allowed the derivation of a controller with invariant gains for vehicle states and previewed lateral errors. The gains were chosen to minimise a cost function of lateral error, heading angle error, and steer angle input. Choosing the weights of this cost function allows different control strategies to be chosen. This controller is used extensively in chapters 3, 4 and 5, and its derivation is discussed in detail in chapter 3.

LQR control can be shown to be equivalent to model predictive control (MPC) with no constraints on controller output or input [44]. The LQR model was shown by Sharp to give good path following performance while following three different road paths. Also, Pick [36] developed LQR controllers using a more complex cost function including lateral acceleration. Pick also incorporated delay into the model by the addition of delay states.

1.3.3 Neuromuscular systems

It may be important when modelling the driver to include the effects of the driver's neuromuscular system (NMS). Primarily, the neuromuscular system acts to limit the bandwidth of the driver's control because of the limb dynamics and delays inherent in the system. The neuromuscular system is a limb mass under influence of driver controlled muscle force, with 'local' reflex feedback control to achieve demanded force or position [36]. The bandwidth limiting properties of the NMS make it an important element in a driver model.

Magdaleno & McRuer [45] used a 3rd order system to represent the driver's neuromuscular system. A simple NMS model was used by MacAdam [46], featuring pure delay, and a first order low-pass filter. Pick [36] carried out identification of a limb system transfer function by using a steering wheel shaker test. During this test a random torque was applied to the steering wheel using an electric motor while the driver held the steering wheel with both arms. This yielded a second order transfer function model for the intrinsic (without reflex feedback) limb dynamics as follows:

$$\frac{\delta(s)}{T_{dem}(s)} = \frac{1}{J_{nms}s^2 + B_{nms}s + K_{nms}} \tag{1.19}$$

Experiments were conducted with eight subjects with limbs relaxed, and tensed, giving a range of parameter values for the intrinsic limb natural frequency and damping. System natural frequency averaged 0.9 Hz with limbs relaxed, and 3.7 Hz with limbs tensed. Damping ratio averaged $\xi = 0.43$ for relaxed limbs, and $\xi = 0.24$ for tensed limbs.

Pick also derived a detailed model of the neuromuscular system, and coupled it to an LQR model to represent the driver. Pick [36] showed that including the driver's reflex loop did not alter the transfer function of the limb dynamics dramatically from that of (1.19), but did cause a slight reduction in system damping.

1.3.4   Identification of steering control

Ljung [47] set out principles for identification of systems operating in closed loop in the presence of noise. Drivers operating in closed loop with a vehicle can only be identified under specific conditions if mis-identification (called bias) of the identified parameters is to be avoided [48]. These conditions and Ljung's system identification equations are reviewed in detail in chapter 5.

Identification of driver control has been attempted by several authors. McRuer [49] fitted his crossover model to recorded driver data. MacAdam [41] simulated closed loop driving using his preview control model and compared the results to those of real drivers. However, neither of these authors used the system identification methods described by Ljung to minimise bias.

Recently Rix [48] tested drivers on a fixed-base simulator to identify compensatory control transfer functions. Rix carried out the experiments in closed loop driving scenarios designed using the principles set out in Ljung [47]. A side-wind disturbance was used to excite both the heading error and lateral error control loops, and transfer functions for both of these loops were derived. Rix only carried out tests for straight line driving tasks, so a preview controller was not identified. The tests did involve step changes in the vehicle dynamics, to monitor how drivers adjusted their transfer function, however, changes in vehicle dynamics arising from speed changes were not studied.

Pick [36] examined Sharp's preview model and compared its performance in lane-change manoeuvres to those found in driver tests. He used trial and error to identify parameters of the LQR controller to match the driver, but did not use Ljung's system identification methods to minimise bias. Also, the driver tests involved repetition of the same lane-change manoeuvre, so it is possible that the driver could have learnt open loop steering inputs, rather than rely on preview and compensatory control.

Peng [50] fitted cost function weights of vehicle lateral and heading error for his model predictive controller to driver data gathered in simulator experiments involving

lane changes. However again this did not take account of system identification theory to minimise the bias of the parameters.

1.4 Objectives of research

The findings from the literature review into driver speed and steering control can be summarised as follows:

At low speed drivers choose their speed to keep below a threshold lateral acceleration [12]. For high speed driving curvature error (and hence path error) based models like Reymond's [23] can predict the reduction of lateral acceleration. However, measurements of path error from drivers have not been linked to speed choice. Van Winsum [24] measured steer angle error, and proposed a speed choice mechanism based on this steering angle error and a constant T_{LC}. However when this model was tested by Reymond [23], it did not give the correct reduction of lateral acceleration at high speeds.

An understanding of the driver closed loop steering control is required in order to model the link between steering angle error and the path error generated by the driver. Models of compensatory and preview control by drivers are well developed, but few are well validated. Models of driver preview control have been developed which are based on minimising a cost function of vehicle and driver performance parameters [27, 36, 41, 50]. These cost function weights can be varied to change the control strategy of the driver. Cost function weights have been fitted to measured driver data for lane-change manoeuvres [36, 50], but only in an ad-hoc way. Bias free estimates of the controller weights used by drivers have not been published. As a result the changes in controller weights which could be used to model changes in driver control strategy with speed or road width are not well validated.

Prokop [28] proposed a driver internal model with simplified vehicle dynamics, and Peng [50] a model with a simplified cost function, to represent the less sophisticated preview control of a novice driver. However, these 'simplified' preview models have not been shown to fit data collected from novice drivers better than a preview model without these simplifications. Neuromuscular systems have been studied, and included in driver models [36], but have not been incorporated into the driver's

internal model to represent a driver who modifies their control to take account of knowledge of their own neuromuscular system.

Based on the review of literature on speed choice and steering control, the following research objectives have been identified:

- To test the link between path error and speed choice by performing simulator experiments. Experiments should measure driver speed choice and path error as a function of road geometry, and allow the assessment of a path error based speed choice model.

- To develop driver models which incorporate the effect of the NMS into the driver's internal model to assess the effect of including the driver's knowledge of their own bandwidth limitation on their chosen control. Also to incorporate simplified driver internal models to represent novice drivers.

- To validate models of preview driver steering using simulator data. Experiments and identification procedures will need to be designed to minimise identification bias.

- To identify how the steering control of drivers changes with speed and road geometry in order to quantify how driver steering control influences the generation of path following error.

Chapter 2 addresses the modelling of speed choice by testing existing models against simulator data, and assesses a path error based speed choice hypothesis by examining a subject's path error and speed choice during a simulator experiment. Chapter 3 describes and compares driver steering models developed from Sharp's LQR steering model. These include simplified internal models for novice drivers, and a model of the neuromuscular system. Chapter 4 describes the design and validation of identification algorithms and simulator experiments for the identification of driver preview models from closed loop driver data. Chapter 5 describes the results of this driver preview model identification from measured simulator data comparing different driver preview models, test subjects, speeds and road widths. Finally chapter 6 draws conclusions from the work, and suggests directions for future work.

Chapter 2: Driver speed choice modelling

In this chapter, the existing driver speed choice models reviewed in chapter 1 are compared using results from simulator experiments carried out at CUED. A path error based hypothesis for driver speed choice is then proposed and is assessed using path error and speed choice data measured during the same simulator experiments.

The simulator and experiments are described in section 2.1 and the existing models are fitted to the simulator data in section 2.2. A new path error based speed choice model is described in section 2.3, and the path error and speed choice measured during the simulator experiments is analysed in section 2.4. The results of this analysis led to the revision of the simulator tests and modelling approach, which is discussed in section 2.5.

2.1   Simulator design and experiments

A fixed-base driving simulator was developed for carrying out the speed choice and steering experiments described in this chapter, and for the experiments described in chapter 5. This section describes the requirements for the simulator, and how the CUED simulator was designed to fulfil these requirements. The tests carried out on driver speed choice using the simulator are then described in section 2.1.7.

2.1.1   Requirements

The simulator is a development of the fixed base simulator first set up by Andrew Pick and Julius Rix at CUED [36, 48]. In order to be used for speed selection experiments the simulator had to fulfil the following requirements:

1. To avoid simulator sickness, and achieve sufficient fidelity, the time delay for the visual system should not exceed 40 - 60 ms [51] (see section 2.1.2)
2. The simulator must provide sufficient information for accurate speed estimation (see section 2.1.3)
3. The driver must be able to select their speed freely, using familiar brake and accelerator controls (see section 2.1.4).
4. An accurate lateral error constraint must be provided to the driver (see section 2.1.6).
5. The simulator should be able to display the required horizontal road profile, such as those detailed in section 2.1.7.

Solutions to these requirements are described in the following sections.

2.1.2   Hardware configuration

The simulator hardware shown schematically in Figure 2.1 is based around MATLAB^{TM} xPC Target software using a target computer, and a host computer. The target computer runs the vehicle model using xPC at a cycle rate fast enough to communicate with the steering wheel hardware at the required 500 Hz. This computer also runs an A/D card, which reads the pedal position and a D/A card, which outputs

two signals for sound generation. The first output signal is a voltage proportional to speed, which is used to generate a sound with frequency proportional to speed; the second signal switches on the path constraint buzzer. The host computer performs the graphics rendering to a projection screen using MATLAB's virtual reality toolbox. The required vehicle model is downloaded to the target computer before each test run, and the recorded variables (position, yaw angle etc.) can be uploaded after the test is complete.

During the test, some of the variables (position, yaw angle, and speed) are passed to the host computer at a lower sample rate using a TCP/IP connection. These state variables are then used to move the driver's viewing position within a VRML (Virtual Reality Modelling Language) virtual world which is created before each test to define the particular path to be driven.
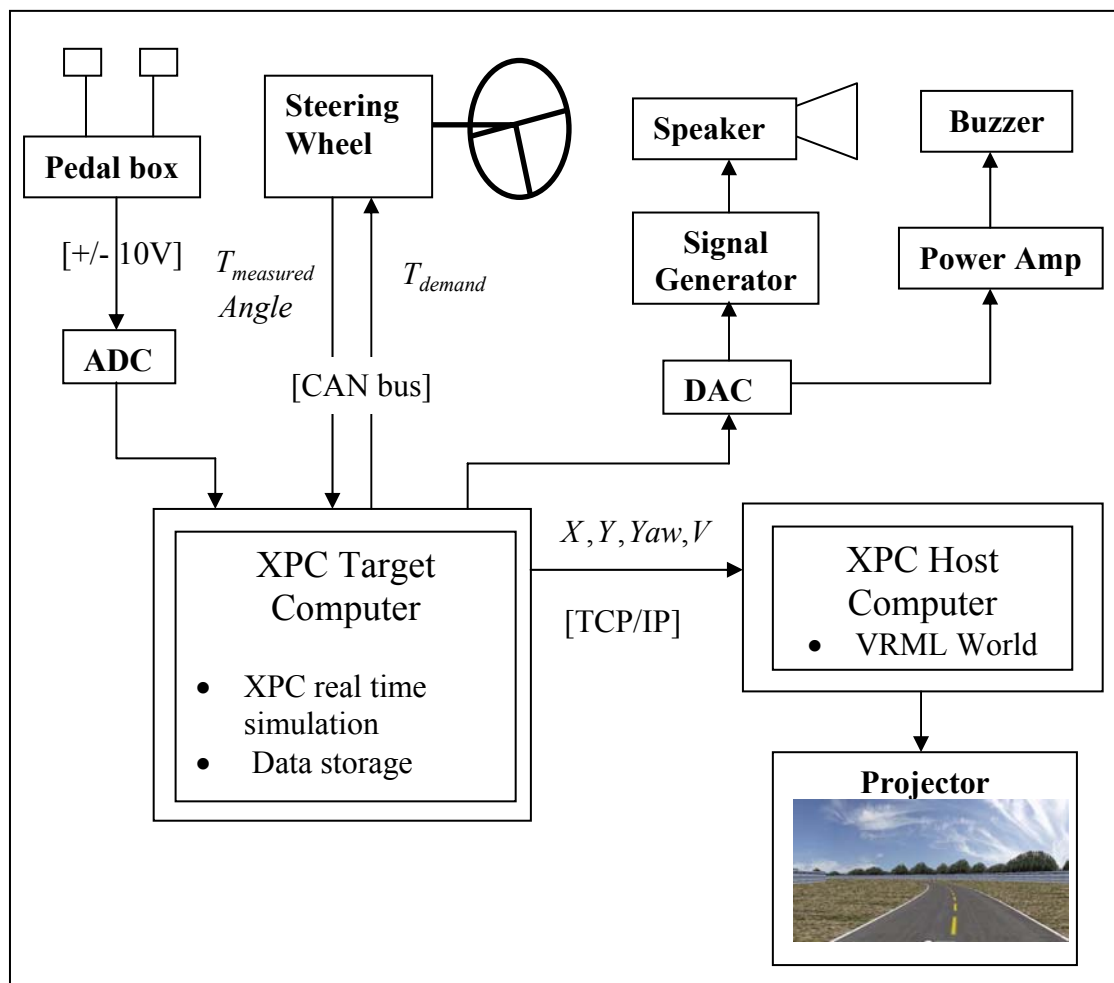
Figure 2.1: Simulator Hardware

The simulator was commissioned with three screens giving a 180º visual field as shown in Figure 2.2. However, with three screens to display, the update rate of the graphics card was found to be only 20 Hz, and was judged insufficient for use in these tests. As a result, one screen was used, giving approximately 50 Hz update rate, and a 60º visual field. Using one screen, time delays in the simulator are estimated to average 20 ms. Approximately ten candidates were tested throughout preliminary and final testing and of these, two could not be used for prolonged testing due to simulator sickness. The sickness became apparent within 5 minutes, and worsened to acute nausea with prolonged testing. None of the five subjects used in final testing (chapter 5) suffered any noticeable simulator sickness.
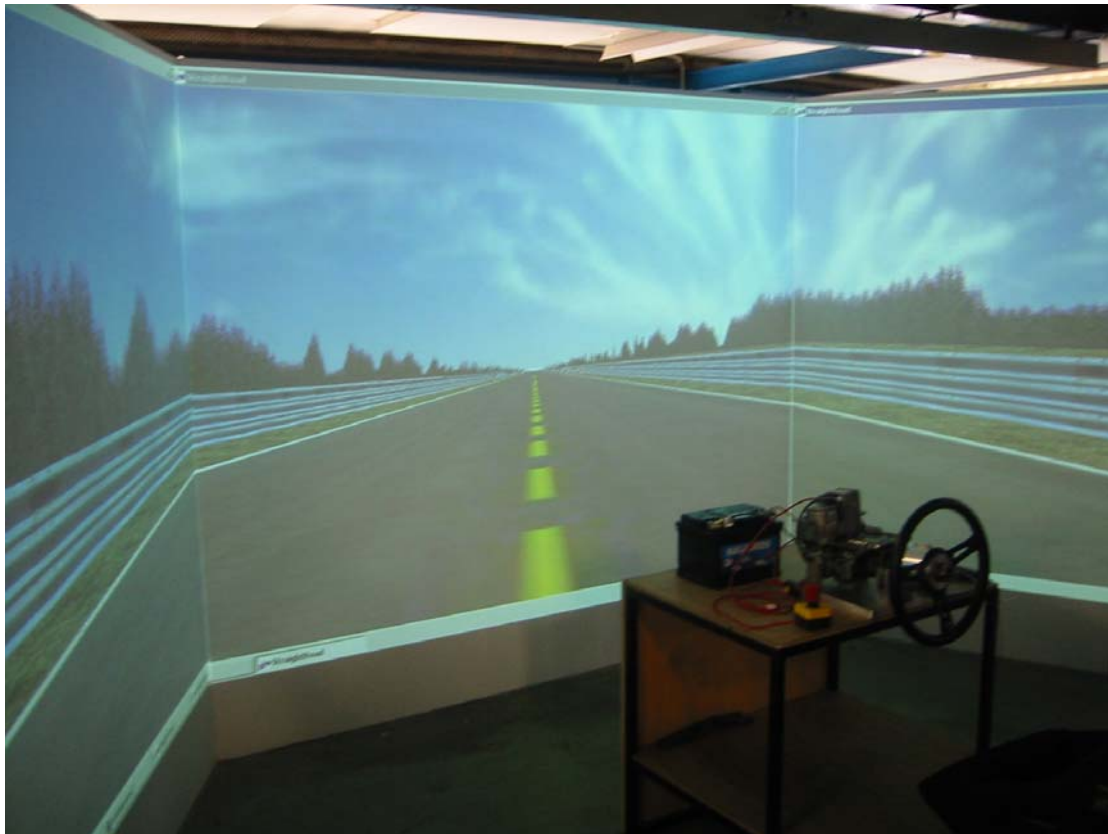
Figure 2.2: CUED fixed base simulator, showing steering hardware, and three screen display (only the central screen was used during experiments)

2.1.3   Speed perception

Three speed cues were provided to the driver. First, a large speedometer on the simulator screen giving quantitative speed information. Secondly, an audible 'tone' whose frequency was proportional to vehicle speed, to imitate the speed dependent

road and engine noises of a real vehicle. Thirdly 'Visual flow' provides a cue to the driver, for example, the growth rate of trees as they are approached in the virtual world.

2.1.4 Vehicle model

A two degree of freedom linear bicycle model was used for the yaw and lateral vehicle dynamics. The bicycle model, as used by many researchers [52-55], is defined with the parameters shown in Figure 2.3.
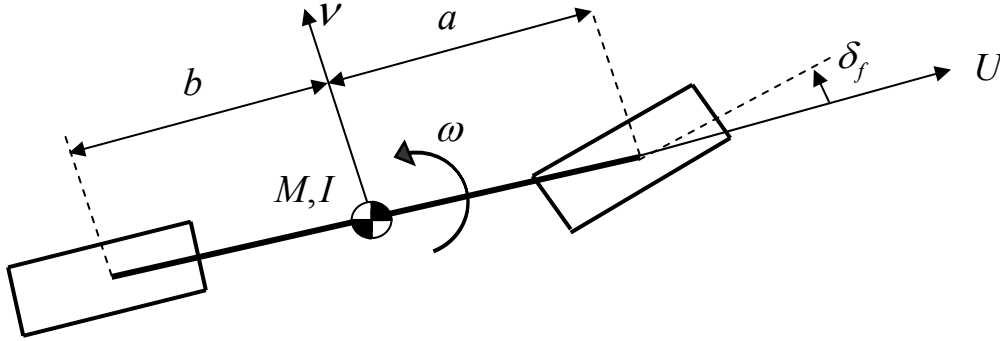
Figure 2.3: Bicycle model of vehicle.

The equations of motion are shown in state space form in equation (2.2). The same formulation is used by Cole [55]. Driver steering wheel angle δ is given by:

$$\delta = \delta_f K_{sw} \tag{2.1}$$

Where K_{sw} is the gain between steering wheel angle and front wheel angle.

$$\begin{bmatrix} \dot{v} \\ \dot{\omega} \end{bmatrix} = \begin{bmatrix} -\left(\dfrac{C_f + C_r}{MU}\right) & -\left(\dfrac{aC_f - bC_r}{MU} + U\right) \\ -\left(\dfrac{aC_f - bC_r}{IU}\right) & -\left(\dfrac{a^2 C_f + b^2 C_r}{IU}\right) \end{bmatrix} \begin{bmatrix} v \\ \omega \end{bmatrix} + \begin{bmatrix} \dfrac{C_f}{MK_{sw}} \\ \dfrac{aC_f}{IK_{sw}} \end{bmatrix} [\delta] \tag{2.2}$$

Roll dynamics were not included in the model, so there was no lateral load transfer. Also, tyre saturations were not included, giving a linear vehicle model. The model was implemented using MATLAB's Simulink software, which was then compiled to

the xPC computer prior to testing. The bicycle model parameters used in testing are listed in appendix A. For these tests, the vehicle parameters were based on those of a Vauxhall Vectra as used by Pick [36], but CG position and tyre stiffness were slightly modified to give a neutral steering vehicle. Steering wheel torque feedback was proportional to steer angle for all tests.

As well as the lateral-yaw model, a longitudinal model was introduced to allow the driver to set the vehicle speed using brake and accelerator pedals. Details of the longitudinal vehicle model are included in appendix B. No interactions between longitudinal and lateral dynamics were included. The longitudinal model included influences of engine power, rolling friction, and aerodynamic drag to make the process of keeping a constant speed as familiar as possible to the driver. The engine and brake power was set very high (1000 kW) to allow rapid acceleration or deceleration to a chosen speed. Aerodynamic drag was also high, limiting the vehicle speed to approximately 65 m/s, but this only had significant effect at high speeds, as drag force was proportional to U^2.

2.1.5 Road profile construction

Construction of the VRML world through which the subject drove was performed using a MATLAB function written for this purpose. The function was passed a 'spine' vector for the desired road centre line, from which the function created a road whose left hand lane centre was defined by the spine vector. The road width W refers to the width of the left hand lane of the road. The road spine equations and widths used for these tests are discussed in section 2.1.7. Each world included a road, verges, barriers, and trees of random height, to give visual flow, helping the driver to perceive their speed.

2.1.6 Lateral error constraint

The width of the left hand lane indicated in the visual system provided the lateral error constraint to the driver. To reinforce this, buzzers sounded whenever the vehicle left the left hand lane. This occurred when lateral error exceeded $(W - W_v)/2$ where

W_v is the vehicle width of 2 metres. In order to activate these buzzers, lateral error had to be calculated within the xPC target computer.

Lateral error was defined as perpendicular distance from the intended path (road spine). Lateral error is defined as perpendicular to the path, rather than the vehicle as this avoids problems when large yaw errors occur.

For the tests described in this chapter, lateral error calculation required an iterative procedure, which is described in appendix C. This iterative procedure was carried out 'offline' i.e. not on the xPC target computer during the testing. To provide a lateral error constraint during testing, lateral error was pre-calculated for a grid of points on the x-y plane over which the car drove. This lateral error information was used as a lookup table to define lateral error as a function of x-y position, and was loaded into the xPC computer before each test. The xPC computer used this lateral error lookup table to interpolate a lateral error for the vehicle's current x-y position, giving a lateral error accuracy of 0.07m with a 10m lookup table grid resolution.

In the tests described in chapter 5 an algorithm for online lateral error estimation was developed based on the road spine expressed in intrinsic co-ordinates. This method is described in appendix D.

2.1.7 *Speed choice experiments*

The simulator experiments whose results are described later in this chapter were carried out using the fixed-base driving simulator described in the preceding parts of section 2.1. Each experiment consisted of the test subject driving the vehicle around twenty-five curves, comprising all permutations of five lane widths (2.4m, 2.8m, 3.2m, 3.6m, and 4.2m), and five radii (66m, 94m, 129m, 190m, and 262m). These curves were presented in random order so that the driver did not learn the sequence of speeds necessary. Instead the driver had to choose a speed for each curve based on their perception of the road ahead.

The road curves consisted of five parts: inward and outward straights, inward and outward transition sections and a constant curvature section, as shown in Figure 2.4. Transitions had a linear increase in curvature with distance, giving the curvature

profile shown in Figure 2.5. Curves were 180°, with 150° constant curvature sections in order to maximise the amount of data collected at the specified curve radius.
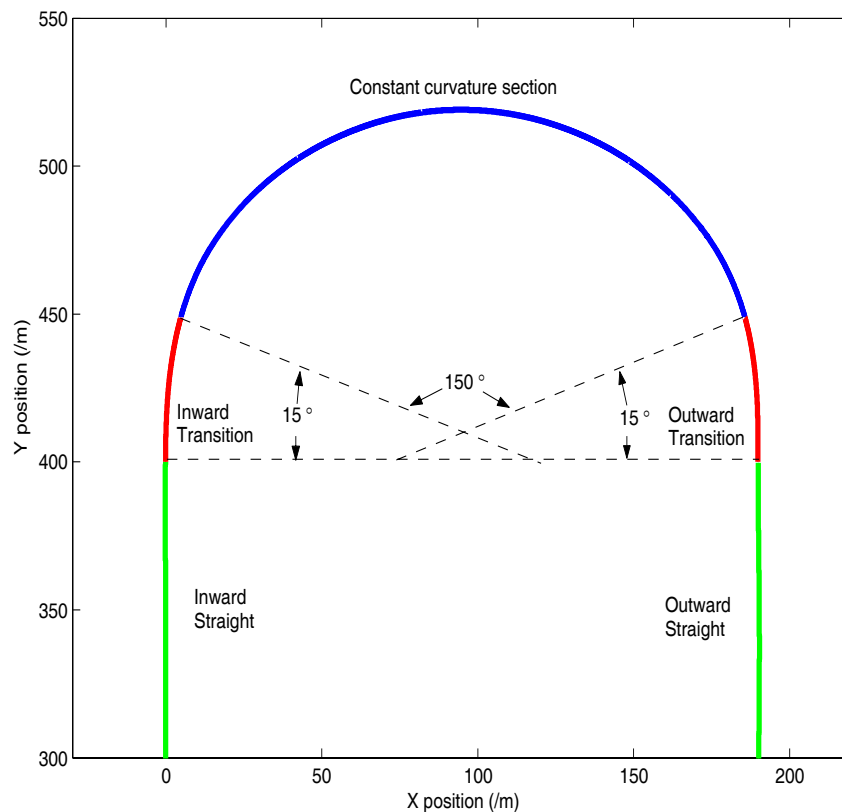
Figure 2.4: 180° curve used for speed choice test (94m radius shown)

Curves were separated by 400m straights, long enough for the subject to re-attain the vehicle's maximum speed between curves. This attempt to reach the same high speed was encouraged by instructions to the driver, in order that the speed for each curve was not influenced by that on the preceding straight (as noted by McLean [16]). Width was changed at the end of the straight, so that choice of speed happened in response to curve geometry and width at the same time.

The driver was instructed to 'drive as fast as possible without leaving the track' to encourage the use of a consistent speed choice strategy. Results presented in the following sections are those of one twenty-five curve experiment on one test subject. A training period, also consisting of twenty-five similar curves, preceded the experiment, during which the driver became familiar with the task.

The data shown in this chapter are from a single test subject, so limited conclusions can be drawn about the speed choice of a population of drivers. However, the data allows comparison of the existing models, and examination of the speed choice trends present in the simulator experiment. Also, the single driver's data is able to illustrate important trends in the path error and speed choice of drivers which led to the revision of the modelling approach, and a change of experimental technique for the remaining chapters of the thesis. Other data were collected with this subject and other subjects that were consistent with the findings shown in this chapter for the single test subject.

2.2 Data analysis

A typical measured speed profile is shown in Figure 2.5. On first entering the curve, an 'open loop' speed is achieved, and is the driver's choice of speed based on preview of the approaching curve. The driver then modifies this speed once in the constant curvature section to a (sometimes lower) 'closed loop' speed.
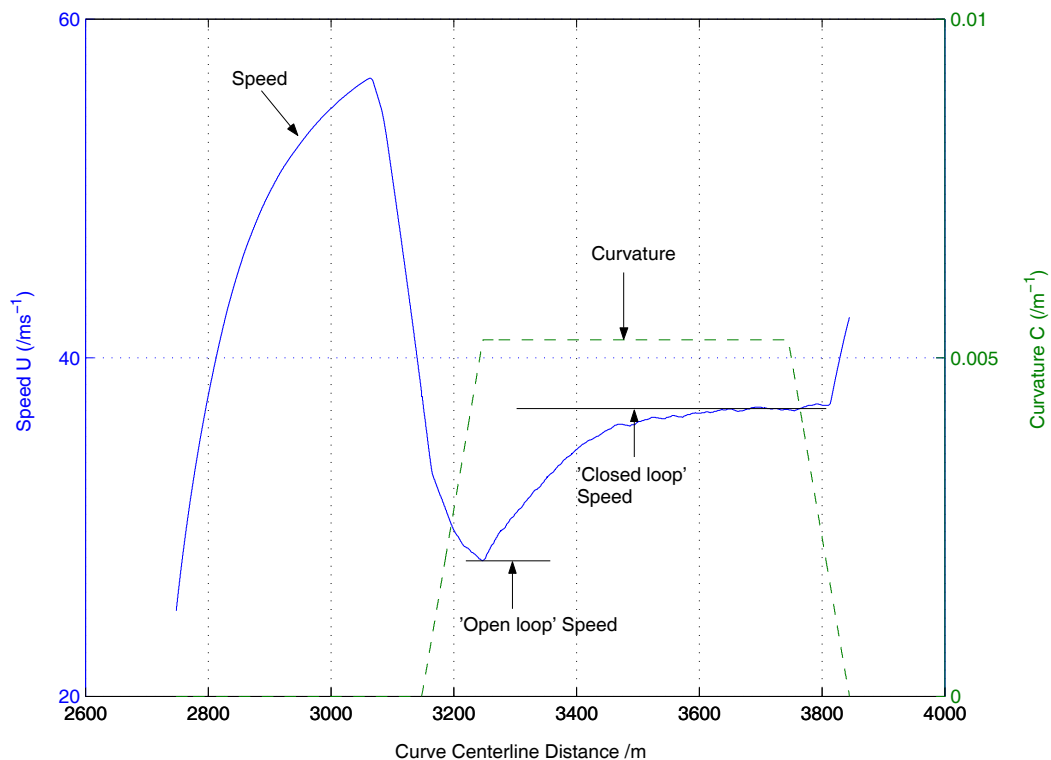
Figure 2.5: Speed and curvature profile for a typical curve

The open loop speed may be different from the closed loop speed for several reasons:

- The driver may have poor speed control of the vehicle, so the driver's intended speed on entry to the constant curvature section is not attained.
- The speed chosen for a transition may be intentional, but different from the constant curvature speed due to the presence of changing curvature, or the uncertainty of the final bend curvature.
- The driver may not be familiar with the simulated vehicle's lack of lateral acceleration limit, so may be able to increase their speed beyond their initial estimate. However, this effect should be eliminated by the training period.

36

The difference between open and closed loop speed choice was not investigated further. Instead, to be consistent with previous studies, the speed and lateral acceleration data recorded in the constant curvature section (U_{cc} and Γ_{cc}) were used in the analysis.

2.2.1 Effect of combined width and radius on speed choice

In order to show the effect of both curve width and radius on the driver's speed a simple model taking into account both variables was fitted first. The model is shown in equation (2.3), and is similar to Taragin's model [17] (equation (1.3)) but includes an extra interaction term (W/R).

$$U_{cc} = a_4 + b_4 . \frac{1}{R} + c_4 . W + d_4 . \frac{W}{R} \qquad (2.3)$$

Where a_4, b_4, c_4 and d_4 are constants. Note that curvature, rather than radius is used to provide the reduced gradient for larger radii as shown in figure 1.5 in chapter 1. Least squares regression of this surface was performed on the data from the experiment and the results are shown in Table 2.1 and Figure 2.6.

a_4 /10ms^{-1}	b_4 /10^{3}m^{2}s^{-1}	c_4 /s^{-1}	d_4 /10^2 ms^{-1}	r^2
3.23	-2.75	8.45	2.55	0.81

Table 2.1: Least square surface fit
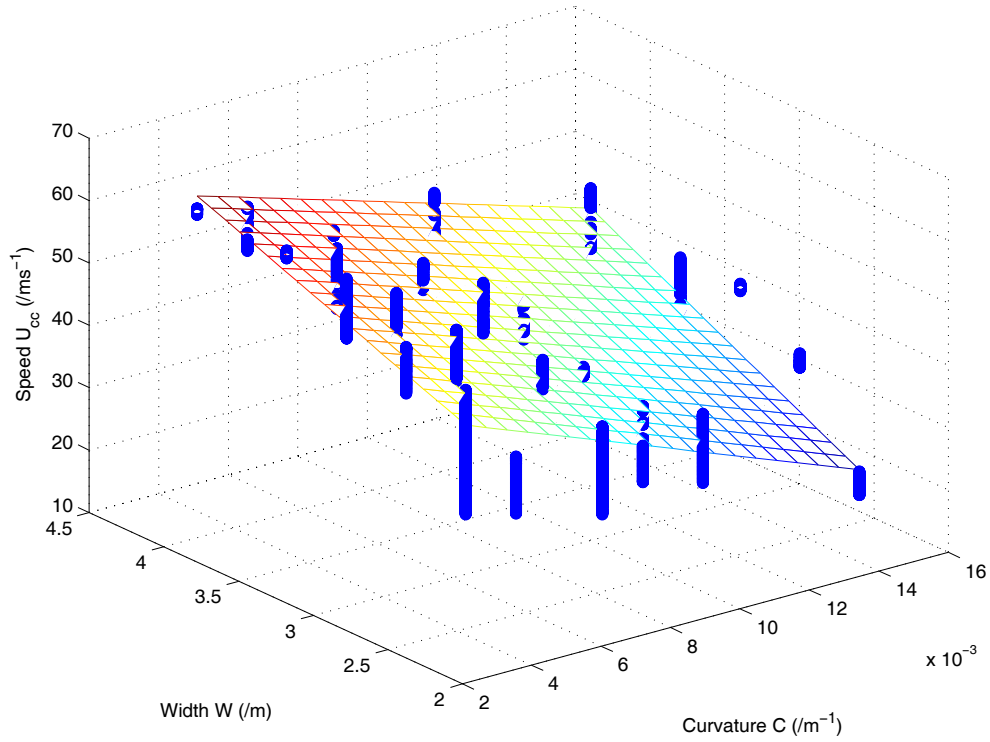
Figure 2.6: Speed U_{cc} vs. curvature C vs. width W

Fit is good ($r^2 = 0.81$), showing increasing speed with increasing width and decreasing curvature. There is not much surface warping, suggesting that the interaction term in (2.3) could be omitted. Fitting this surface without the interaction term gave similarly good fit ($r^2 = 0.80$). This implies that the dependence of speed on width was similar irrespective of the curvature.

2.2.2 *Effect of lateral acceleration on speed choice*

Reymond's lateral acceleration margin model [23] (equations (1.14) and (1.15)) was fitted to the measured data. Results for the narrowest (2.4m) and widest (4.2m) curves are shown in Figure 2.7 and Figure 2.8. The data points show measured Γ_{cc} vs. U_{cc}. For comparison, radius contours for 66m and 262m are also shown as dashed lines. An envelope of maximum lateral acceleration at each speed (as used by Reymond) is shown as a solid line, and a least squares fit of the Reymond model to this envelope is shown as a dotted line. The fitted values of the model parameters and the correlation coefficient are shown in Table 2.2 for each curve width.
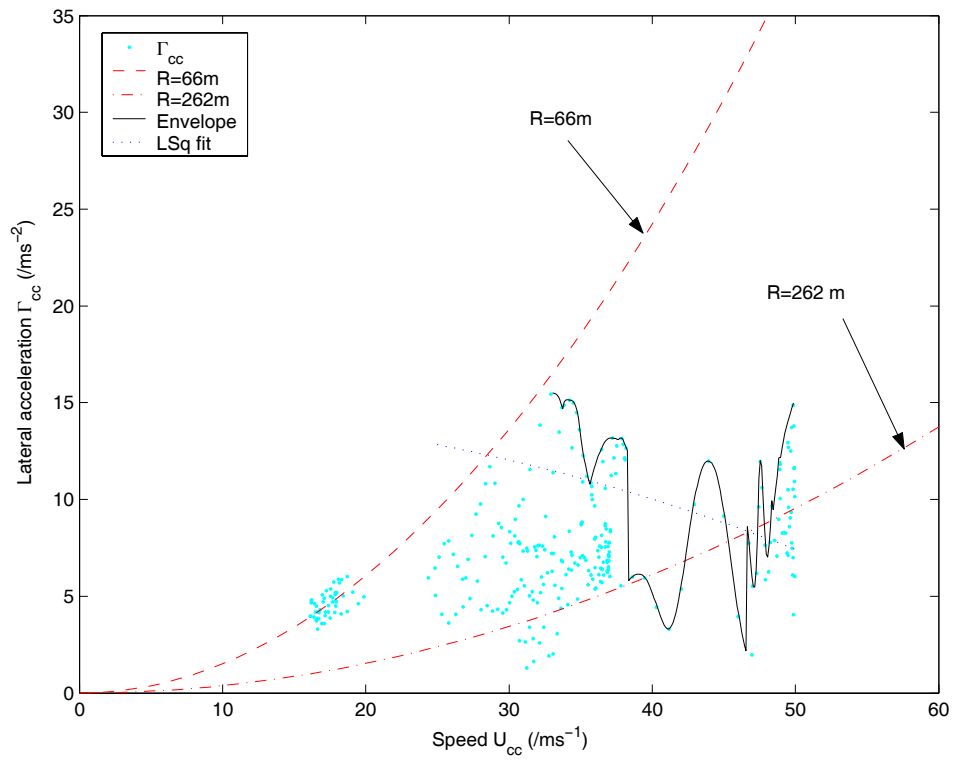
Figure 2.7: Reymond model, Γ vs. speed, 2.4m width
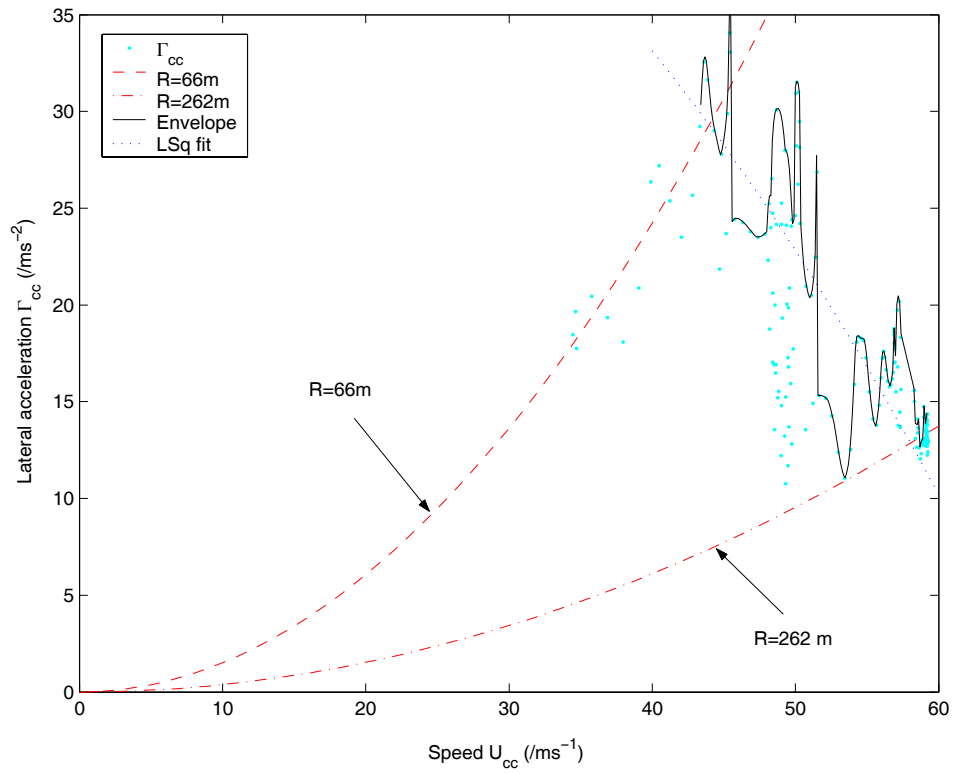
Figure 2.8: Reymond model, Γ vs. speed, 4.2m width

The correlation coefficients are low except for the widest road, so the model coefficients derived for the narrowest four roads are not reliable. However, the widest three roads do show a clear drop-off in lateral acceleration with speed similar to that in Figure 2.8. The maximum lateral acceleration parameter Γ_{max} is much larger than the 10 ms^{-2} recorded by Reymond, presumably because there is no tyre saturation in the simulator vehicle model, and no lateral acceleration cue to the driver. Also the maximum lateral acceleration (Γ_{max}) is seen to increase appreciably for the wider roads. The curvature margin ΔC_{max} is of similar magnitude to that of Reymond, who found $\Delta C_{max} = 3.82\,km^{-1}$ with a standard deviation of $0.77km^{-1}$ for his static simulator tests. This demonstrates that lateral acceleration reduced with speed even though there was no tyre saturation.

Width /m	2.4	2.8	3.2	3.6	4.2
Γ_{max} /m s^{-2}	14.6	9.61	23.9	24.2	51.5
ΔC_{max} / (km)$^{-1}$	2.88	-1.83	3.09	2.48	11.5
r^2	0.09	0.05	0.13	0.08	0.65

Table 2.2: Reymond lateral acceleration model

2.2.3 *Effect of curve radius on speed choice*

The T_{LC} criterion [24] suggests a direct relationship between speed choice and curve radius [23]. Reymond's lateral acceleration margin model can also be rearranged to give such a relationship (eqn (2.4)). In this section, these two models are fitted to the mean speed ($\mu(U_{cc})$) and curve radius (R) data. An envelope function such as that shown Figures 2 and 3 is not used.

2.2.3.1 **Reymond lateral acceleration margin model**

Recorded mean speed and radius for each of the twenty-five curves is shown in Figure 2.9, along with a least squares fit of equation (2.4) for each curve width.

$$\frac{1}{\mu(U_{cc})^2} = \frac{\Delta C_{max}}{\Gamma_{max}} + \frac{1}{\Gamma_{max}}\left(\frac{1}{R}\right) \qquad (2.4)$$
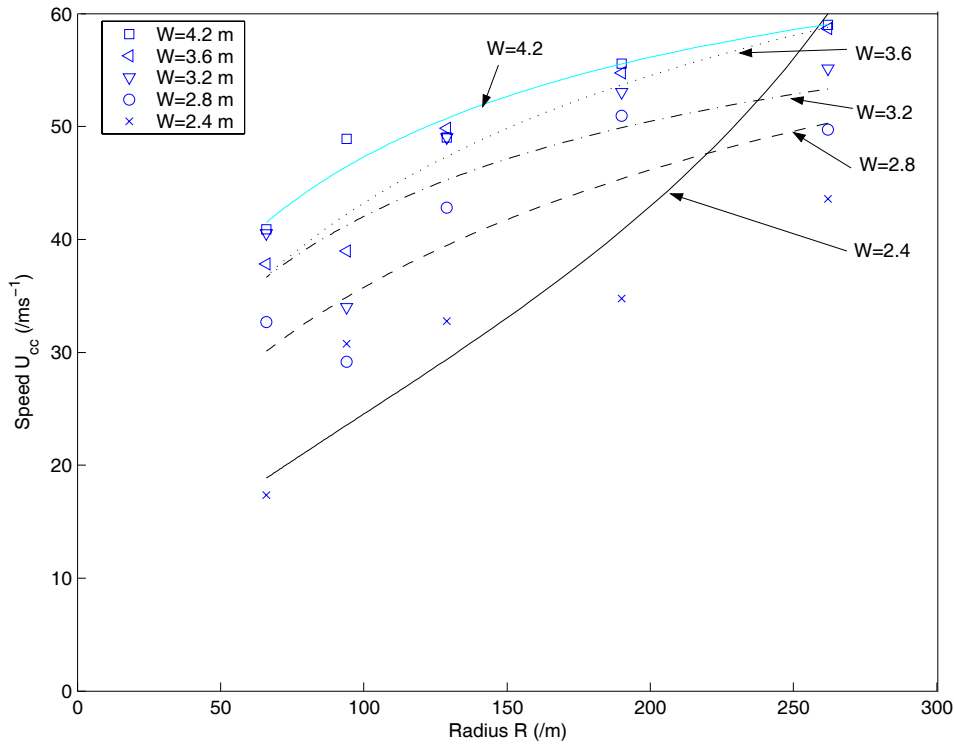
Figure 2.9: Reymond model, speed vs. radius, widths 2.4 to 4.2m

The correlation coefficients (Table 2.3) are much better than those in Table 1, largely because the mean speed $\mu(U_{cc})$ has been used, rather than the maximum lateral acceleration envelope. Also the effect of radius on speed is clearer on these axes. ΔC_{max} and Γ_{max} are similar in magnitude to those of section 2.2.2, and again both increase with increasing curve width. It is clear that curve width affects speed significantly, although curve width is not included in this lateral acceleration based model.

The least squares fitted line for the 2.4m width road in Figure 2.9 does not seem to fit the points well, despite having $r^2 = 0.81$. The reason for the apparently poor fit is that the regression was performed to minimise the least squares error of $1/U^2$, rather than U. The fitted line has increasing gradient at large radii in contrast to all of the other widths, and a trend which is not apparent in the data. This gives rise to negative curvature margin ΔC_{max}, which would imply increased lateral acceleration with increased speed.

Width / m	2.4	2.8	3.2	3.6	4.2
Γ_{max} /m s^{-2}	4.47	16.0	28.9	25.1	38.6
ΔC_{max} /(km)$^{-1}$	-2.57	2.50	6.33	3.45	7.24
r^2	0.81	0.64	0.49	0.91	0.95

Table 2.3: Reymond speed vs. radius model

2.2.3.2   Time to lane crossing model

Reymond's model [23] of Van Winsum's constant T_{LC} hypothesis [24] (equation (1.13)) leads to the following:

$$\mu(U_{cc}) = a_7 + \frac{1}{T_{LC}(1+k)}.[\alpha.R] \tag{2.5}$$

For this model, and all models in section 2.2.4, the mean speed $\mu(U_{cc})$ for each curve is used. Figure 2.10 shows the resulting fit of equation (2.5).
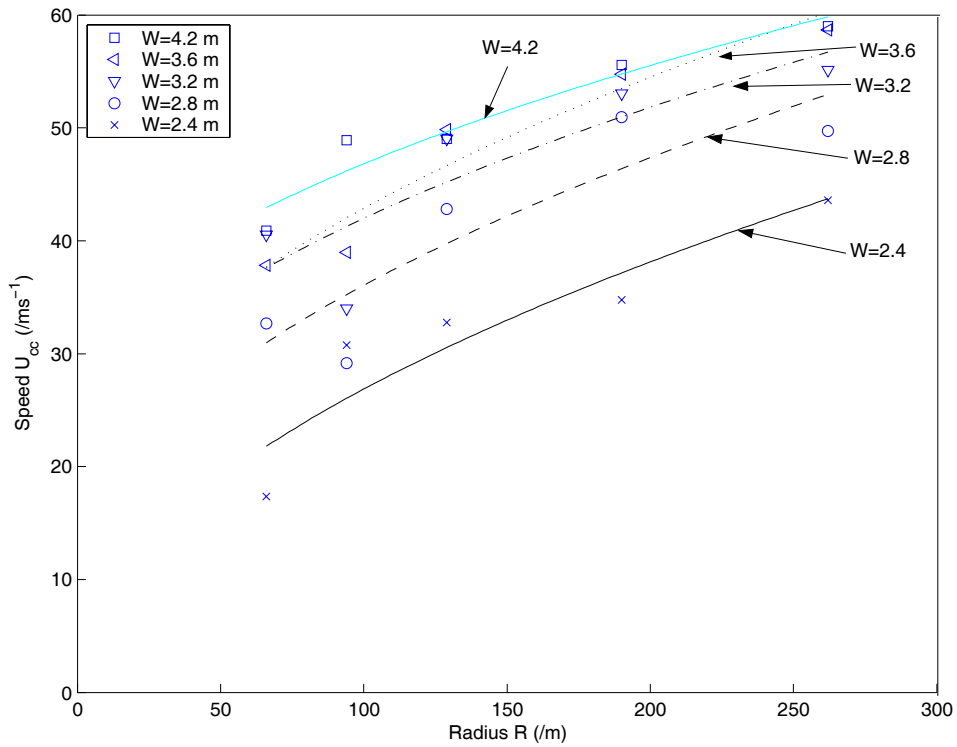
Figure 2.10: $\mathbf{T_{LC}}$ model, speed vs. radius, widths 2.4 to 4.2m

The fitted lines are curved because α is a function of radius. The velocity offset value a_7 was not present in Reymond's model [23], but is necessary to allow a regression

42

coefficient to be calculated, and should be zero if the model is correct. However, the value of a_7 ranges from 0 to 25 ms^{-1}, nearly half of the total speed change (see Table 2.4). The theoretical T_{LC} calculated from the fitted model is also listed. Van Winsum found T_{LC} to average 2.7 seconds over a range of radii. The T_{LC} values in Table 2.4 are similar to those found by Van Winsum [24] for the widest road, but significantly less for the narrowest road. So although curve fit is good (see Figure 2.10), the coefficients a_7 do not fit the assumptions in the T_{LC} hypothesis [24].

Width /m	2.4	2.8	3.2	3.6	4.2
a_7 /ms^{-1}	-0.40	8.64	18.1	14.5	25.5
T_{LC} /s	0.73	1.03	1.46	1.42	2.22
r^2	0.85	0.79	0.74	0.93	0.93

Table 2.4: Reymond T_{LC} model

Fitting the same model without the extra coefficient a_7 forces the curves through the origin. The resulting fits are shown in Figure 2.11.
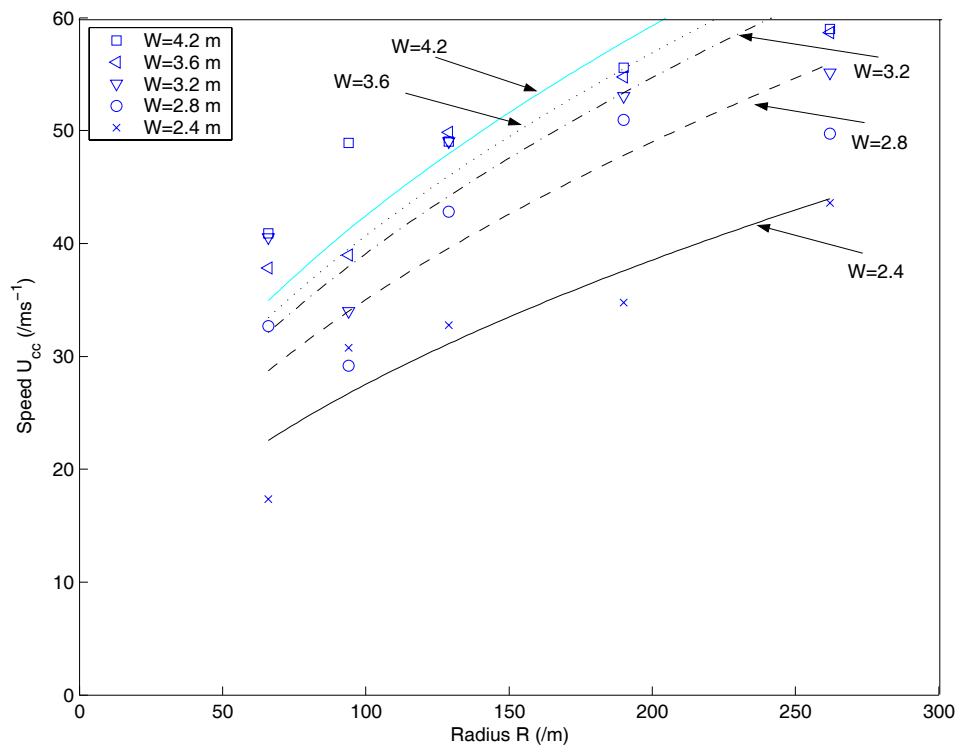
Figure 2.11: T_{LC} model, speed vs. radius, widths 2.4 to 4.2m, fitted without the offset a_7

Eliminating the coefficient a_7 leads to an undefined r^2 value in the regression, so goodness of fit cannot be quantified. However, Figure 2.11 reveals a qualitatively poorer agreement with the data, especially for the wider roads. Also, if $a_7 = 0$ had given a better fit, it would have been chosen in the previous regression. The T_{LC} values derived are listed in Table 2.5. The values are more consistent than those of Table 2.4, but are significantly less than those found by Van Winsum [24].

Width /m	2.4	2.8	3.2	3.6	4.2
T_{LC} /s	0.74	0.83	0.91	1.00	1.13

Table 2.5: Reymond T_{LC} model

2.2.4 Effect of curve width on speed shoice

2.2.4.1 De Fazio et al linear model

De Fazio et al's linear model [21] of speed vs. width (equation (1.9)) is fitted to each radius separately in Figure 2.12.
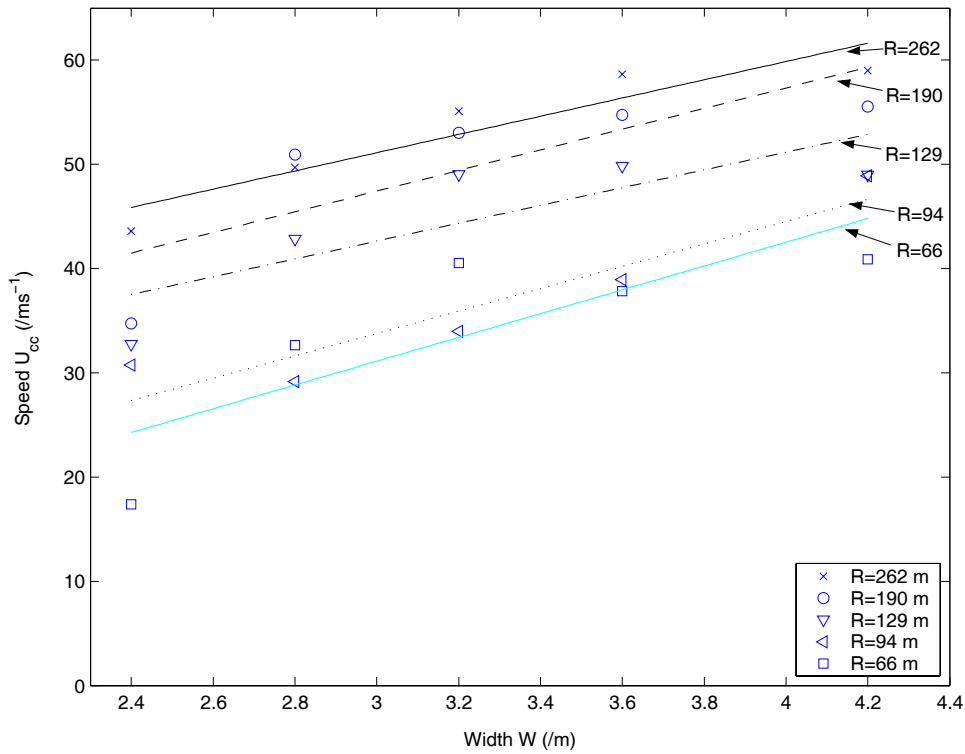
Figure 2.12: Linear model speed vs. width, radii 66 m to 262 m

Fitted coefficients a_2 and b_2 are shown in Table 2.6. Fit is not as good as that observed by De Fazio [21], with r^2 from 0.66 to 0.89. Close examination suggests that a curve would fit the points better than this straight line, such that less increase in speed is seen at higher widths.

Radius /m	66	94	129	190	262
a_2 /ms^{-1}	-3.12	1.58	17.0	17.7	24.9
b_2 /s^{-1}	11.4	10.7	8.54	9.91	8.75
r^2	0.66	0.89	0.69	0.65	0.87

Table 2.6: De Fazio et al linear model

2.2.4.2   Tracking difficulty model

Fitting of the measured data to Bottoms' tracking difficulty model [20] (equations (1.10) and (1.11)), is shown in Figure 2.13.
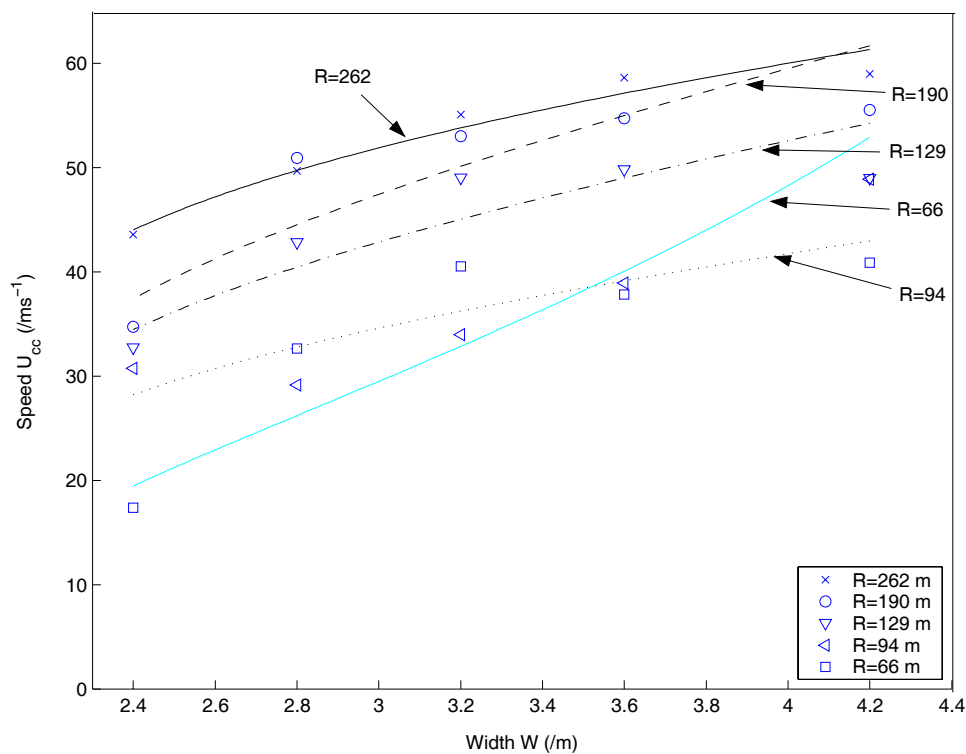
Figure 2.13: Bottoms' model, speed vs. width, radii 66 m to 262 m

Unlike De Fazio et al's linear model, the curves show the appropriate reduction of gradient at high speed, and a corresponding improvement in r^2 (Table 2.7). The curve

with 66m radius does not seem to fit the data well, but the regression of this model minimises $1/U$, rather than U. Tracking difficulty T_d was much lower than that recorded by Bottoms since the road is much wider relative to the vehicle than in his experiments with tractors. However, the model's intended mechanism based on driver limited cognitive capacity still applies since the instructions were to go as fast as the driver was capable.

Radius /m	66	94	129	190	262
a_3 /10^{-2}m^{-1}s	0.75	1.90	1.47	1.25	1.41
b_3 /10^{-2}m^{-1}s	1.90	0.71	0.62	0.62	0.38
r^2	0.80	0.72	0.86	0.80	0.97

Table 2.7: Bottoms' tracking difficulty model

2.2.4.3   Time to lane crossing model

Reymond's T_{LC} model from section 2.2.3.2 can be fitted to the data to predict the dependence of speed on road width, because the angle α is a function of road width. Reymond's derivation of the T_{LC} model assumed that road edge collision occurred when the vehicle's CG crossed the road edge i.e. when lateral error reached $W/2$. However, in testing, the road edge constraint (when the buzzers sounded) was for lateral error exceeding $(W - W_v)/2$ i.e. when the edge of the vehicle crossed the road edge. The available width $(W - W_v)$ was therefore used in equation (1.13) in place of W. The available width $(W - W_v)$ was also used in section 2.2.3.2 to calculate angle α. Figure 2.14 shows the fit of Reymond's T_{LC} model to the measured data. Again the velocity offset a_7 was included to allow a regression coefficient to be calculated.
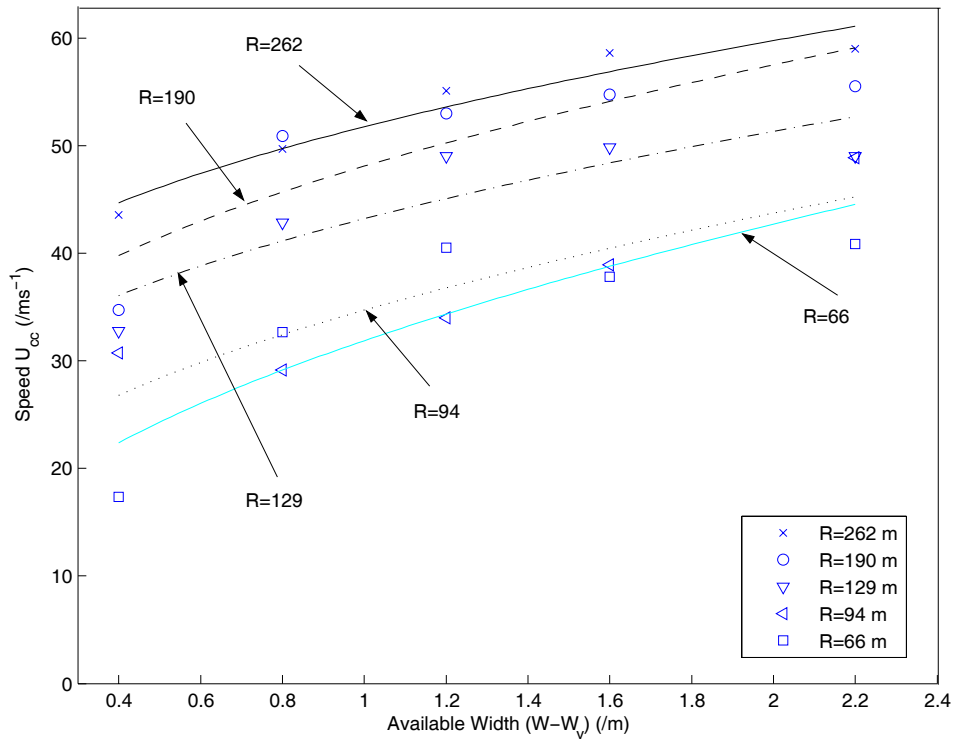
Figure 2.14: T_{LC} **model, speed vs. available width, radii 66 m to 262 m**

The resulting curves are nearly linear, having r^2 (see Table 2.8) only slightly better than De Fazio et al's (Table 2.6). Unlike Van Winsum's result [24] the time to lane crossing T_{LC} is not constant with radius, but increases with increasing radius. The velocity offset a_7 indicates the model's prediction of the driver's speed with zero available width, and the model predicts that the driver would still have significant speed even with a road the same width as the car.

Radius /m	262	190	129	94	66
a_7 /ms^{-1}	32.6	25.5	23.8	13.3	6.20
T_{LC} /s	2.67	1.93	1.86	1.43	1.00
r^2	0.93	0.75	0.78	0.80	0.76

Table 2.8: Reymond T_{LC} **model based on width**

As in section 2.2.3.2, the fit was repeated with the velocity offset a_7 omitted, and the result is shown in Figure 2.15 and Table 2.9.
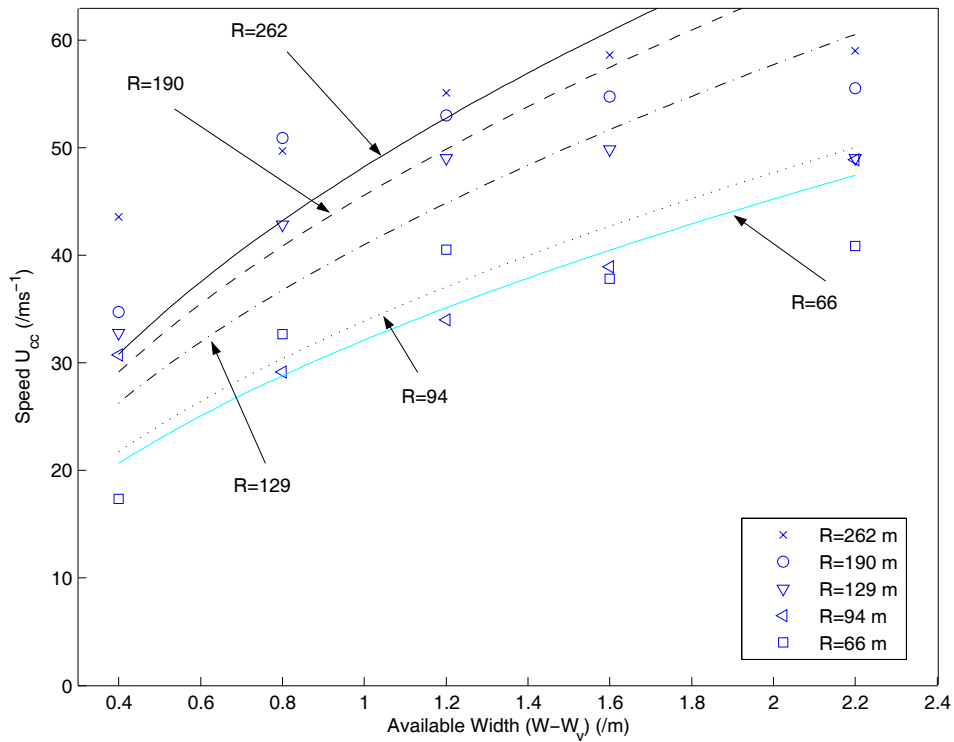
Figure 2.15: T_{LC} model, speed vs. available width, radii 66 m to 262m , fitted without the offset a_7

Again no r^2 value can be provided because of the lack of velocity offset a_7, but the fit must be worse, as otherwise the previous regression would have yielded $a_7 = 0$. As in section 2.2.3.2 omitting the velocity offset a_7 gives more consistent T_{LC} values.

Radius /m	262	190	129	94	66
T_{LC} /s	1.08	0.98	0.90	0.94	0.83

Table 2.9: Reymond T_{LC} model based on width

2.2.5   Summary of data analysis with existing speed choice models

Limited simulator data is used for this analysis, so limited conclusions can be drawn from the r^2 coefficients. However, the following conclusions can be drawn.

Driver speed increased with both radius and width. A linear surface model fitted this behaviour well, even with no interaction (W/R) term. However, such a model gave no insight into the mechanism of speed choice.

48

The driver data showed a reduction of lateral acceleration at high speed for widest three roads despite the vehicle model including no tyre saturations. This lends weight to a curvature error or path error based explanation for the reduction in lateral acceleration such as Reymond's lateral acceleration margin model.

Mean speed increased with increasing radius such that reduced gradient occurred at larger radii. Reymond's lateral acceleration margin model was able to predict this behaviour well for most widths, but did not take account of the curve width. Speed increased with width such that a reduced gradient of speed vs. width was seen for wide roads. De Fazio's linear model could not provide the required reduction in gradient at large widths. Bottoms' model was able to provide this reduction in gradient giving improved fit, but was unable to model radius dependence.

Reymond's T_{LC} model was able to predict both the radius and width dependence of speed with similarly good fit to other models. However, the speed offset a_7 was significantly greater than the zero that was predicted by Van Winsum. Omission of a_7 gave poorer fit, but more consistent T_{LC}. Good fit of this model was therefore not achieved with the assumptions of Van Winsum's original model.

From this analysis, none of the models could provide all three requirements of:
- Good fit
- A mechanistic model whose assumptions were met by the fitted parameters
- An ability to predict both width and radius dependence.

A new model of speed choice should incorporate the successful features from the existing models. Firstly, lateral acceleration dependence should be included, as it conveniently models the driver's low speed behaviour found in real driving experiments in the presence of lateral acceleration and tyre saturations [12]. Secondly, the use of anticipated driver error (such as curvature error or path error) is the most promising mechanistic model of driver speed choice. A model which could include this feature and also predict the influence of path width (unlike Reymond's model) would be desirable.

2.3 Speed choice model hypothesis

A hypothesis (Figure 2.16) is proposed in this section based on speed choice as a function of both lateral acceleration [10, 12, 15, 16, 23, 34], and path error [10, 13, 16, 20, 22, 34] as follows:

(1) Upon approach to a corner, its curvature is assessed by the driver, and an estimate of the path error allowable on the corner is made.

(2) Previous experience allows the driver to anticipate lateral acceleration and path error on the corner for a given speed. Experience is stored in the form of lookup tables of speed vs. path error, and speed vs. lateral acceleration

(3) The driver decides on what speed to negotiate the corner by minimising a cost function based on travel time through the corner, lateral acceleration, and path error. The weights of the three components are dependent on the motivation of the driver.

(4) After negotiating the corner, the driver uses the actual lateral acceleration and path error achieved for that curve to update their experience.

Though lateral acceleration is important to the speed choice of drivers its influence is reasonably well understood. This work concentrated on identifying the part of the speed choice decision arising from path error estimation, rather than from lateral acceleration effects. This enabled the use of a fixed base driving simulator, and linear tyre models. The effects of path error on speed choice could then be studied in the absence of lateral acceleration cues and limits, and without the more complex changes in vehicle handling brought about by tyre saturations (e.g. understeer to oversteer transitions at high lateral acceleration).
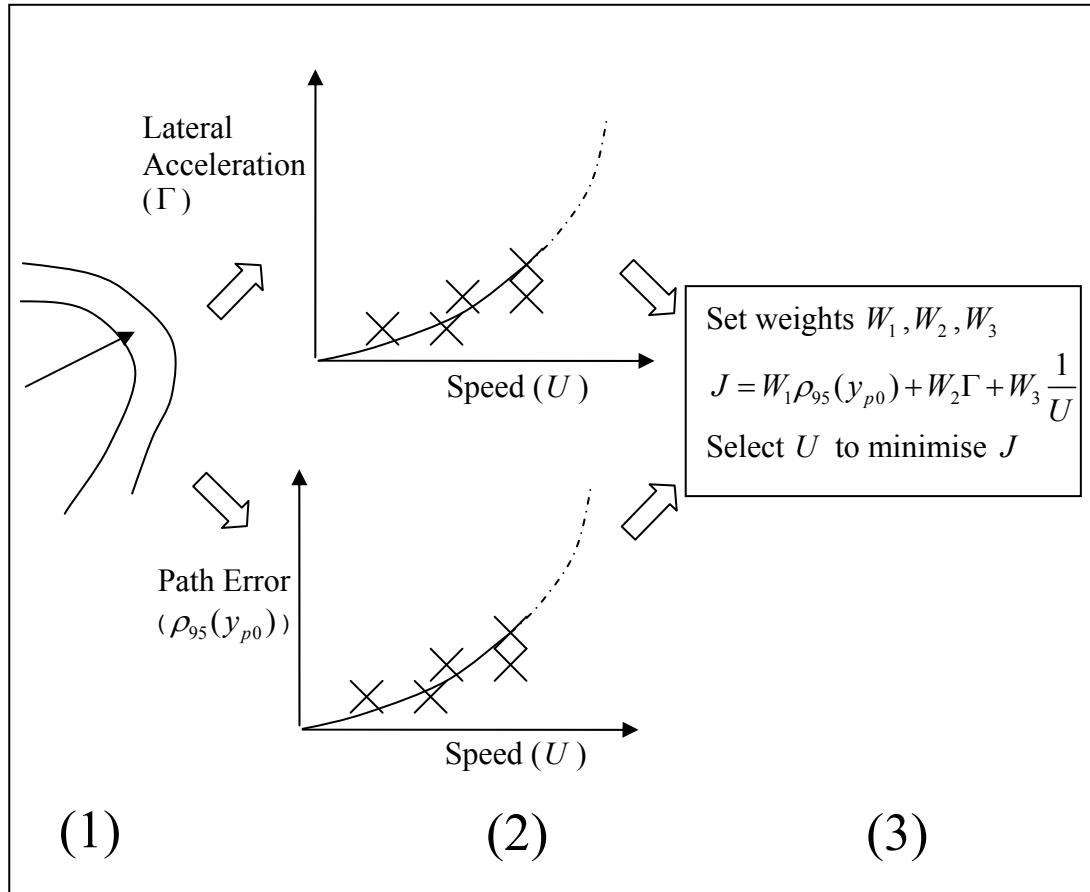
Figure 2.16: Speed selection hypothesis overview

Sources of path error are proposed as follows:

    (1) External sources e.g. side winds, road roughness.

    (2) Internal Driver sources

        a) Imperfect feedforward control, from incomplete learning of the vehicle dynamics.

        b) Driver measurement and actuation noise e.g. Perception of path, motor control.

        c) Intentional driver (open loop) inputs.

No external noise sources were provided to the driver during testing, so external noise sources (1) were not present. This work concentrated on the driver internal noise sources a) and b), and assumed that intentional (open loop) inputs by the driver were not present. An empirical model for path error prediction by the driver is proposed as follows.

The prediction of path error by the driver in order to select speed is assumed to take the form of a lookup table, or surface, as shown in Figure 2.17. The surface reflects the drivers' estimate of their own probable error, and assumes that the path error is a function of speed and the curvature of the bend perceived by the driver [24]. Limits to the surface exist due to tyre saturations, maximum steer angle, and maximum speed. The surface is fitted from the combinations of curvature, speed and resulting path error experienced by the driver. The term 'path error' encompasses both lateral error and heading error. However, for the further development of this hypothesis, the driver's measure of path error is assumed to be a percentile of lateral error from the intended path, for example 95th percentile lateral error.
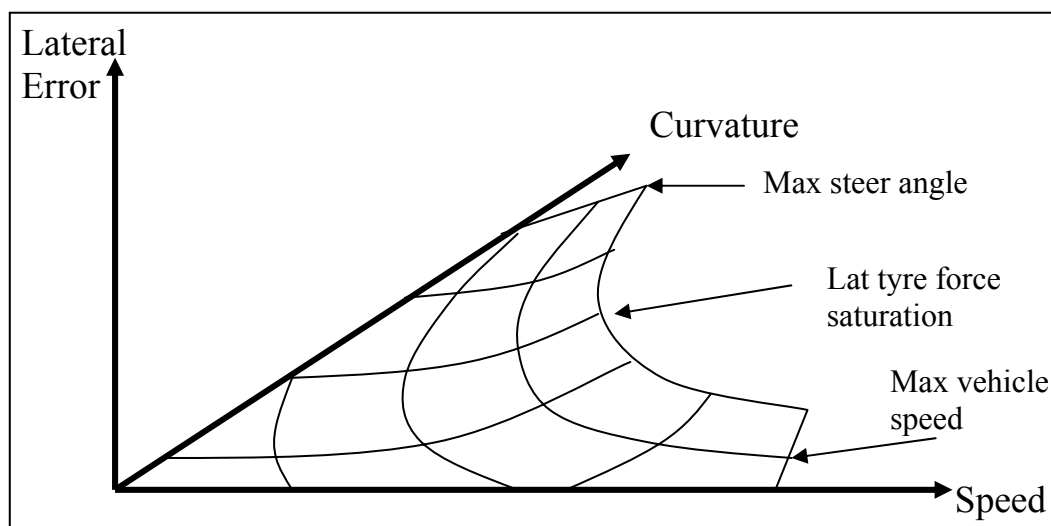
Figure 2.17: Lateral error as a function of vehicle speed and bend curvature

The driver's prediction of lateral error (and hence speed) for an upcoming bend is based on an extrapolation or interpolation of the known surface. There will be variability present in the data, so the driver must make a best-fit estimate of the surface. Figure 2.18 shows a section through the surface along a plane of constant curvature. 'x' marks show data gathered by the driver upon which they base their surface, one mark representing one corner. Variability in the data means that the driver can only estimate the probability of achieving a certain lateral error. The solid line shows the driver's estimate of the median of the data. The median line indicates a 50% probability of achieving a given lateral error. The dashed lines represent higher, and lower probabilities of achieving a given lateral error.

The variability of lateral error is inherent due to its nature as a sample of a noise signal, but also because the driver's perception of curvature, speed, and lateral error may not be consistent. The driver may be able to reduce their lateral error by increased effort or by experience. Reduction in lateral error with increased experience could be accounted for with a forgetting factor such that old experiences have less relevance than more recent ones when fitting the surface.
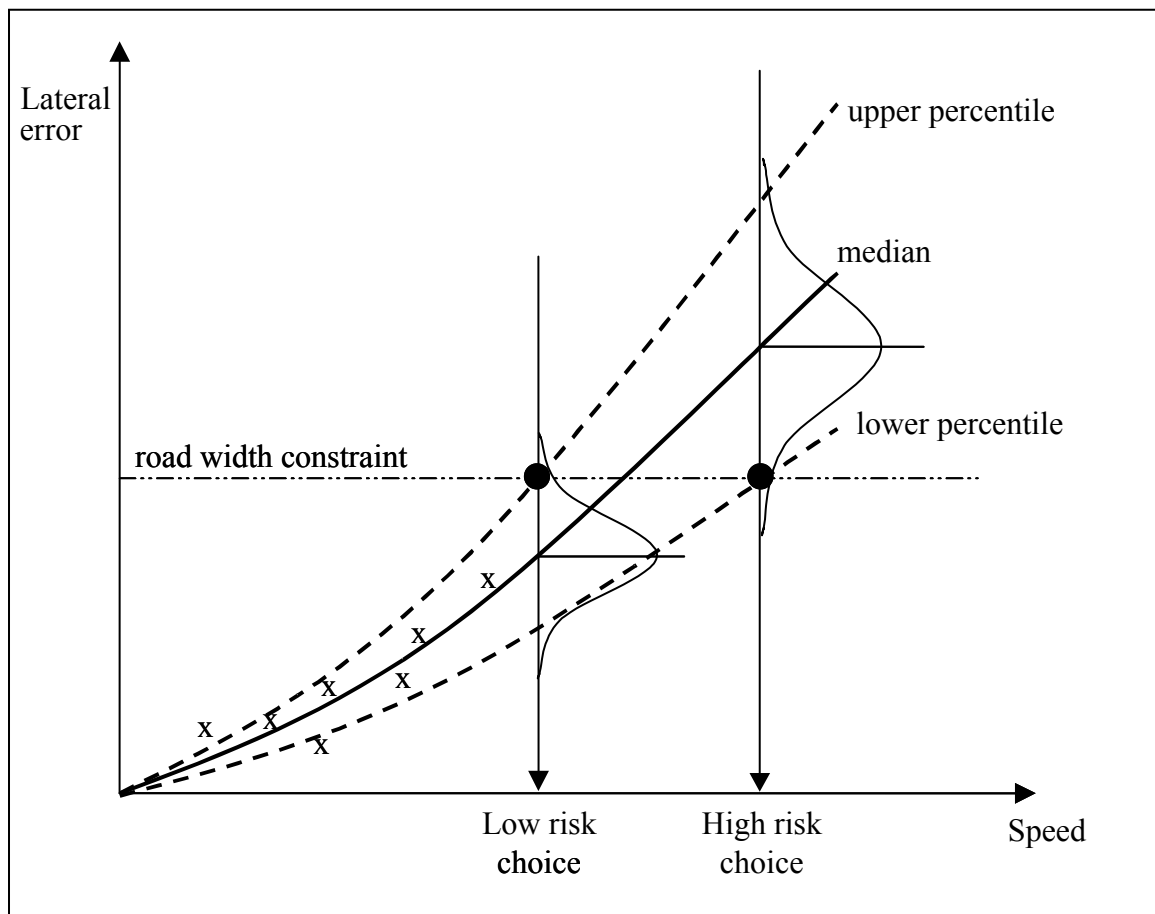
Figure 2.18: Lateral error vs. speed prediction function showing development of the surface

In the absence of lateral acceleration dependence, the choice of speed will be based purely on the allowable lateral error, through the road width constraint. The driver therefore selects a speed with an acceptable probability of achieving the given lateral error. A high-risk strategy would be to select a high speed and accept a high risk that lateral error will exceed that available. A low risk strategy would be to select a lower speed in order to ensure a lower probability of exceeding the road width, but at the expense of slower progress, and slower learning of the full surface.

Data from the simulator tests described in section 2.1.7 were used test this hypothesis, the results are presented in the next section. During tests instructions were given to try and keep the risk strategy constant, so it was assumed that the driver would have a consistent risk strategy independent of road width.

2.4   Data analysis for path error model

The speed choice hypothesis presented in the previous section (2.3) relies on establishing the dependence of the driver's lateral error on speed, radius and width. This lateral error dependence is therefore investigated in sections 2.4.1 to 2.4.6.

Limited data from only one subject are used to illustrate the dependence of lateral error on speed, so it is not possible to validate the hypothesis based on these results. A single driver's data is shown as it is able to illustrate important features of the dependence of the driver's lateral error on road width, without the complexity of comparison between subjects. More importantly, the results of one subject are able to illustrate the need for a revision of the modelling approach, and a change of experimental technique. This change of approach meant that only a limited number of subjects were tested using this method. However, other data from this subject and from the two other subjects tested was consistent with the results shown in this section.

The new modelling approach was required in order to identify the steering behaviour of the test subjects. The results of this section show that an ability to quantify the driver's steering behaviour is an important part of a speed choice model.   The identification of driver steering behaviour is the subject of the remaining chapters of the thesis.

2.4.1   Lateral error vs. time histograms

Figure 2.19 shows histograms of the lateral error vs. number of samples (at 500 Hz) for the constant curvature part of the curve, for each of the 25 curves in the test. The curves are sorted by width and radius, with the largest radius, widest road at the lower right of the figure, and the smallest radius, narrowest road on the upper left. 95th percentile lateral error ($\rho_{95}(y_{p0})$) is shown on each plot as a dashed red line.
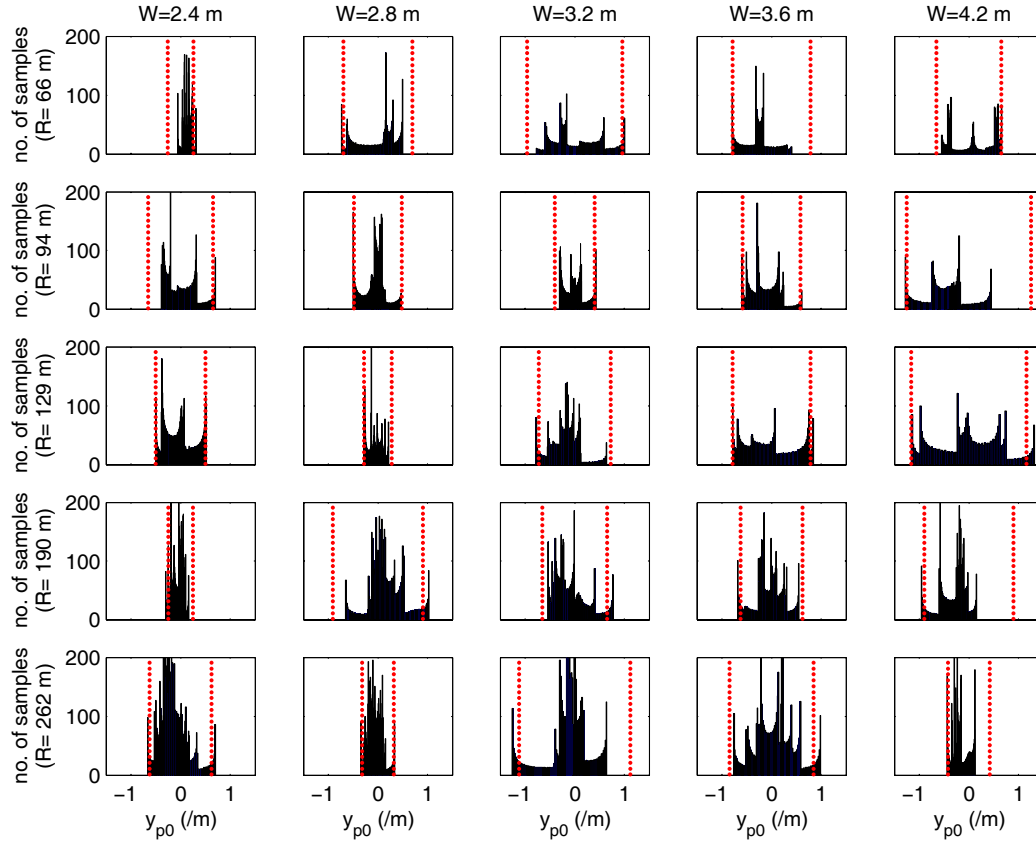
Figure 2.19: Lateral error histogram for each curve

The distribution of lateral error for most of the curves is non-normal, and the peaks caused by individual excursions from the centre line are visible in the histograms. Finding the 95th percentile lateral error $\rho_{95}(y_{p0})$ (or other percentiles) of these distributions is therefore an inaccurate representation of the true statistics of the data.

Ideally, more data would be gathered for each radius and width to provide a normal distribution for each radius and width combination. However, in the absence of this data another approach was taken, in which several curves were grouped together by either radius or width. This approach is shown in sections 2.4.3 and 2.4.4. The disadvantage of grouping data by width or radius is that some variable interactions are not visible, so first the lateral error vs. speed vs. curvature surface proposed in the hypothesis was fitted to the 'ungrouped' curve data as shown in section 2.4.2.

2.4.2 Lateral error vs. speed vs. curvature

Although the histograms of section 2.4.1 showed 95th percentile lateral error $\rho_{95}(y_{p0})$ for individual curves to be unreliable, it is useful to plot a surface of the form given in equation (2.6) to illustrate the interactions of the three variables. The surface relates a percentile (λ) of lateral error ($\rho_\lambda(y_{p0})$) to the mean speed in the constant curvature part of the curve ($\mu(U_{cc})$), and curve curvature ($1/R$) including an interaction term ($\mu(U_{cc})/R$).

$$\rho_\lambda(y_{p0}) = a_5{}^\lambda + b_5{}^\lambda \frac{1}{R} + c_5{}^\lambda \mu(U_{cc}) + d_5{}^\lambda \frac{\mu(U_{cc})}{R} \qquad (2.6)$$

Where $a_5{}^\lambda$, $b_5{}^\lambda$, $c_5{}^\lambda$ and $d_5{}^\lambda$ are constants for a particular lateral error percentile λ. Figure 2.20 shows the 95th percentile lateral error ($\lambda = 95$) surface from equation (2.6) fitted to the data from the simulator experiment.
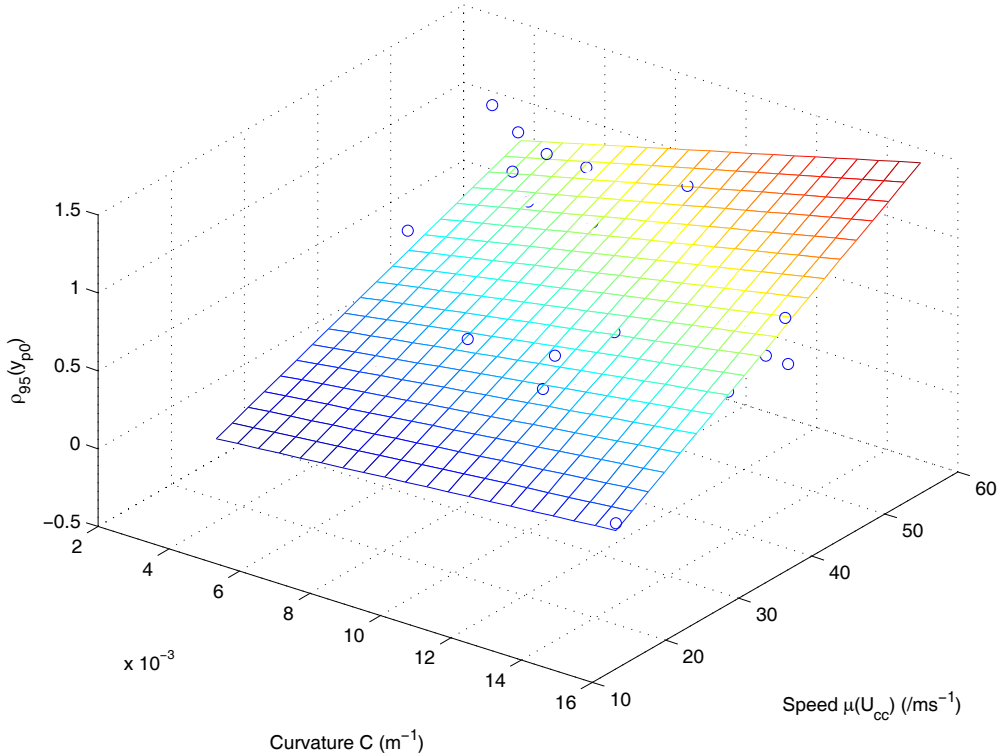
Figure 2.20: $\rho_{95}(y_{p0})$ vs. curvature C vs. speed $\mu(U_{cc})$, with surface fitted from equation (2.6)

57

The regression coefficient for the surface ($r^2 = 0.44$) was poor but this was to be expected given the non-normal distribution of the lateral error for each curve.

The dependence of speed on curvature demonstrated in Figure 2.6 has led to the driver only using a part of the surface in the lateral error vs. speed vs. radius axes. There are therefore no points for low curvature at low speed, or high curvature at high speed. In order to fully populate this surface, an experiment with speed as a controlled variable would be required.

2.4.3 Lateral error vs. curvature

Figure 2.21 shows the same lateral error data as the histograms of Figure 2.19 grouped by curve radius. Again $\rho_{95}(y_{p0})$ for each radius is shown as a dashed red line. Each group contains data from all five widths, so any dependence on width will not be visible in these plots.
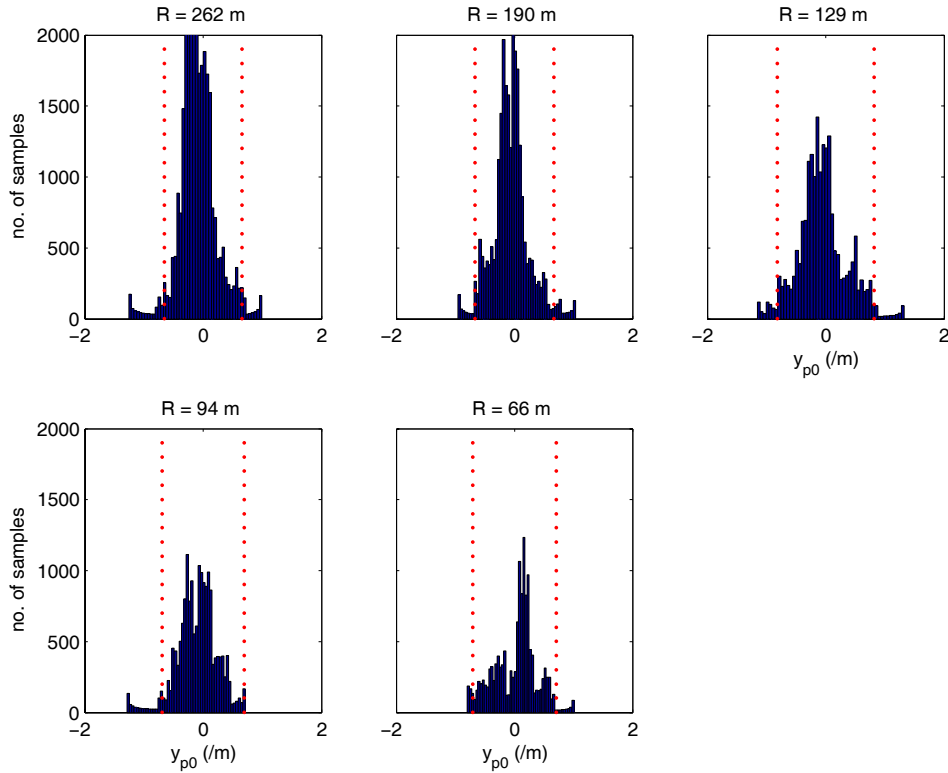
Figure 2.21: Histograms of lateral error (y_{p0}) samples at 500 Hz, grouped by radius. Red dashed line shows $\rho_{95}(y_{p0})$

Grouped by radius, the data is more like a normal distribution, so percentiles of these histograms become more meaningful. The smaller radius bends take less time, so have less data, giving a less normal distribution. 95th percentile lateral error ($\rho_{95}(y_{p0})$) from Figure 2.21 is plotted against curve curvature in Figure 2.22.
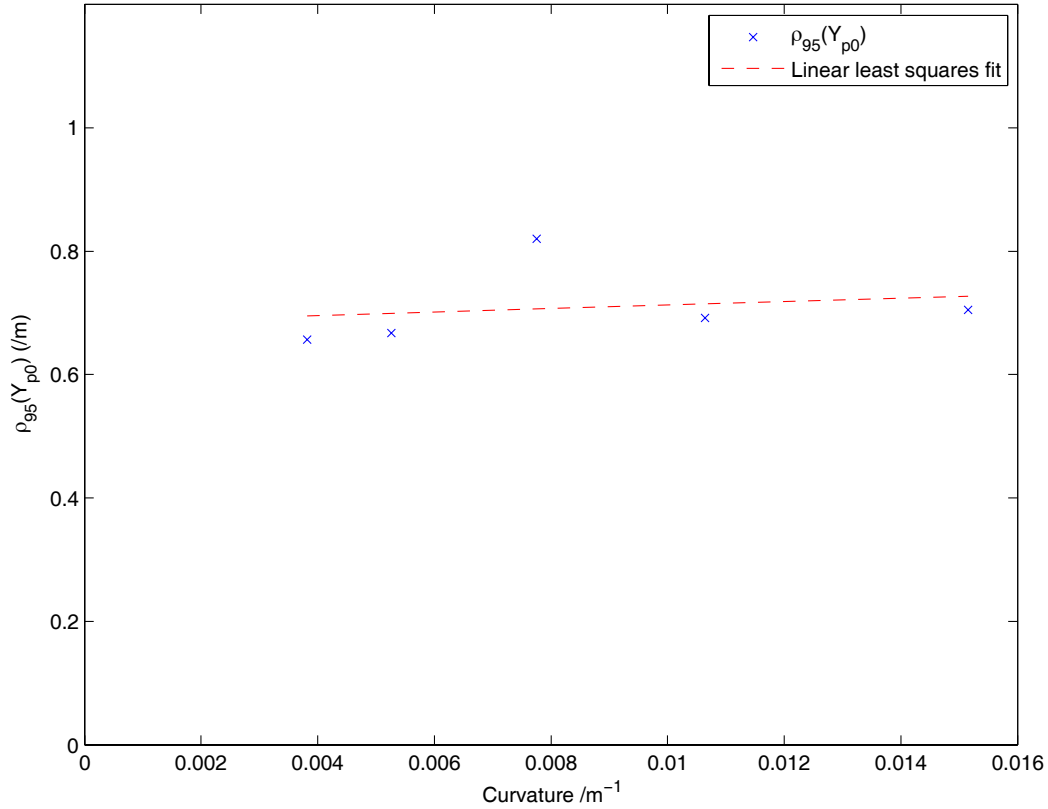
Figure 2.22: Lateral error $\rho_{95}(\mathbf{y_{p0}})$ vs. curvature C

Figure 2.22 shows that lateral error $\rho_{95}(y_{p0})$ is nearly independent of curvature. Speed $\mu(U_{cc})$ is dependent on curvature (see Figure 2.6) therefore Figure 2.22 supports the hypothesis of the driver attempting to keep $\rho_{95}(y_{p0})$ constant by changing speed.

If Figure 2.20 is viewed along the direction of the speed axis the same independence of lateral error and curvature can be seen.

2.4.4   Lateral error vs. width

Figure 2.23 shows the same lateral error data as Figure 2.19 grouped by curve width. Again $\rho_{95}(y_{p0})$ for each width is shown as a dashed red line.
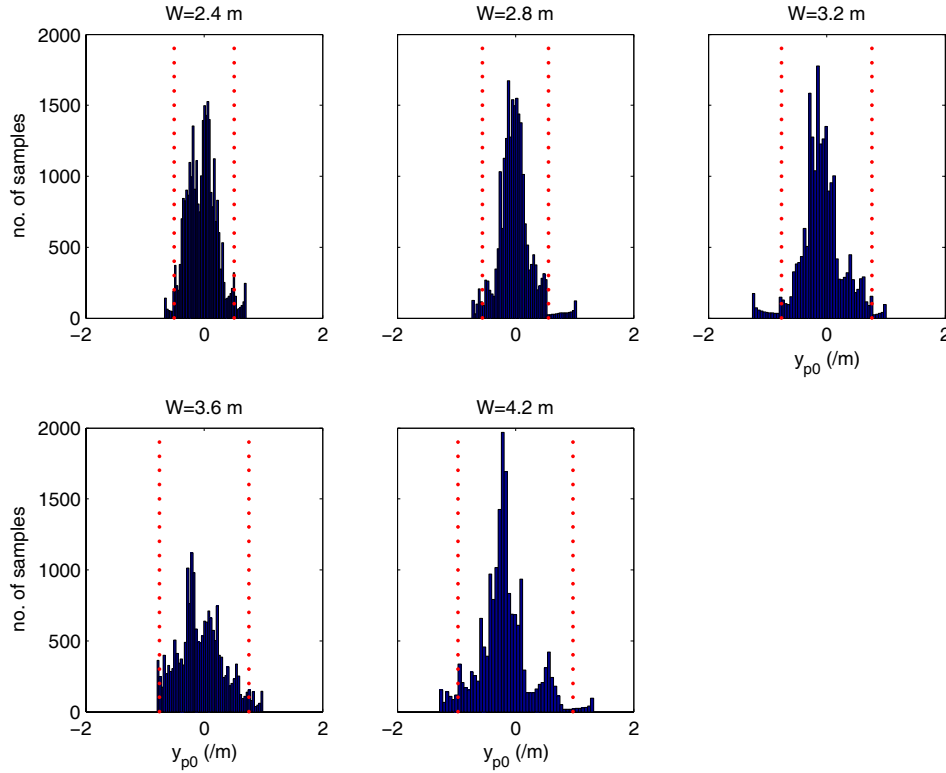
Figure 2.23: Histograms of y_{p0} samples at 500 Hz, grouped by width. Red dashed line shows $\rho_{95}(y_{p0})$

Distributions are again nearly normal, but with distortions still visible in the tails of the distributions due to individual excursions from the road centre. Figure 2.24 shows 95th percentile lateral error $\rho_{95}(y_{p0})$ from Figure 2.23 plotted against the 'available tolerance' $(W - W_v)/2$. The solid black line indicates lateral error equal to available tolerance ($\rho(y_{p0}) = (W - W_v)/2$).
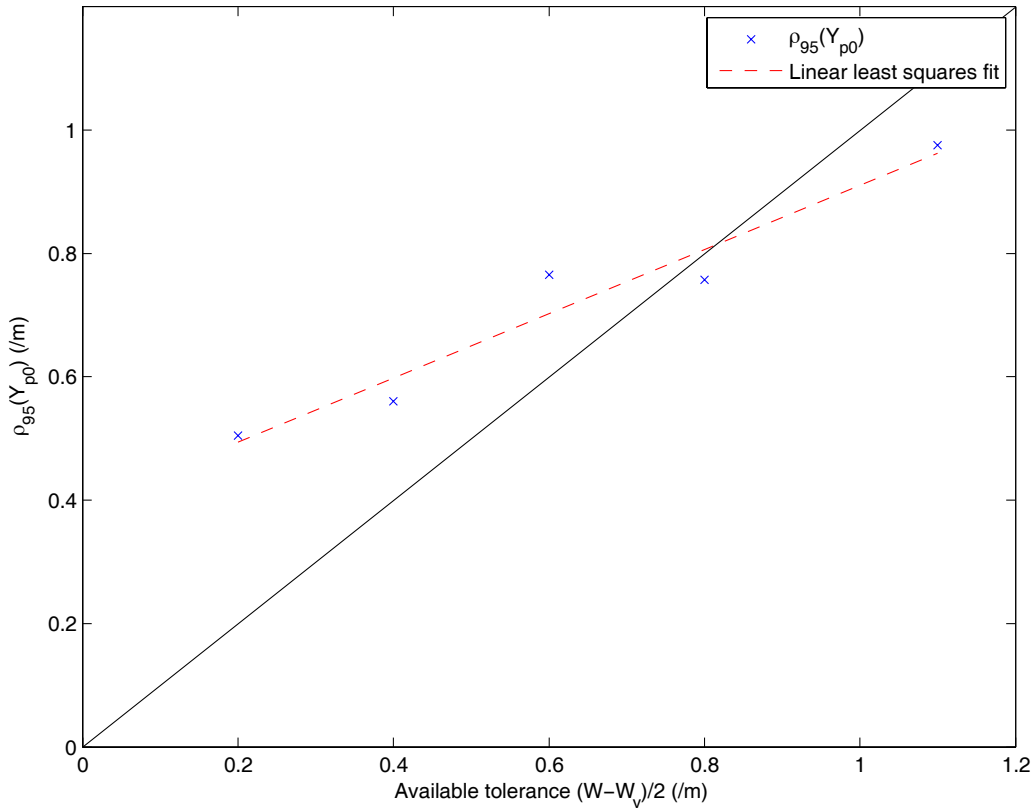
Figure 2.24: Lateral error $\rho_{95}(y_{p0})$ vs. available tolerance ($(W - W_v)/2$) for radii 66m to 262m

The assumption of the hypothesis of section 2.3 was that lateral error would match the available tolerance as a result of the driver adjusting his speed to use the whole road width. As a result, the driver would aim for the same lateral error percentile for all widths.

The results of Figure 2.24 support the hypothesis that lateral error is altered to take advantage of road width. However, Figure 2.24 shows that $\rho_{95}(y_{p0})$ exceeds the available tolerance for narrow roads, but is less than the available tolerance for wide roads.

This implies that the driver is not changing his speed enough to make $2.\rho_{95}(y_{p0})/(W - W_v)$ independent of W. Two possible reasons have been identified for this behaviour:

1. It may be a risk strategy inherited from road driving, given that accidents more severe at high speed.

2. The driver may change their steering control strategy in response to width. It would then be possible for the driver to achieve different lateral error for the same radius and speed by using different steering control strategies (requiring different amounts of control effort).

Changes in driver control strategy (or effort) would require a different version of the lateral error vs. speed curve in Figure 2.18 for each level of driver effort. In order to quantify the steering strategy parameter, it is necessary to look more closely at the driver's steering control to quantify how it changes with speed, width, or between drivers. This is the subject of the work in chapters 3, 4 and 5, and is discussed in section 2.5.

The path error hypothesis can be modified to take account of the 'risk' part of the behaviour observed in Figure 2.24, so that the driver aims to achieve a different lateral error percentile (λ) for each width. This modification is examined in section 2.4.6.

2.4.5 Lateral error vs. speed

It is not as easy to plot lateral error as a function of speed, because speed was not a controlled variable of the experiment. The data from the constant curvature section of the curves was therefore grouped in speed bands of 10m/s width, and histograms of these bands are shown in Figure 2.25.
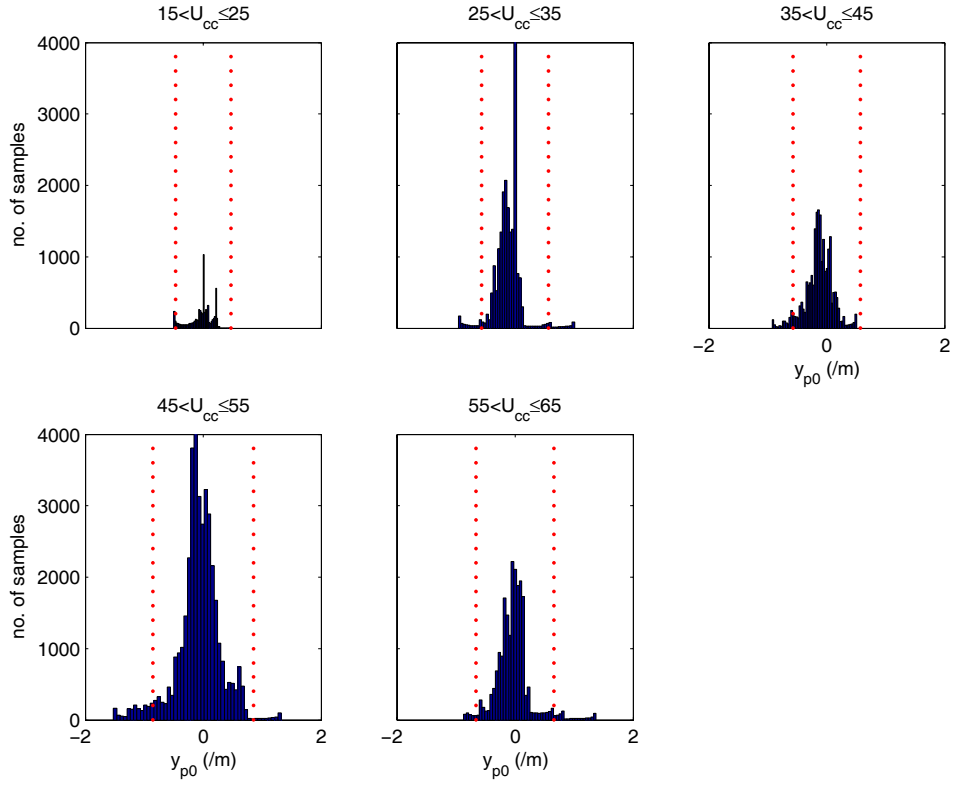
Figure 2.25: Histograms of y_{p0} samples at 500 Hz, grouped by U_{cc}. Red shows $\rho_{95}(y_{p0})$

There are different amounts of data in each speed band, and as a result, the poorly populated distributions are not as normal as those for grouping by width or radius. 95th percentile lateral error $\rho_{95}(y_{p0})$ was plotted against the speed at the centre of each speed band in Figure 2.26.
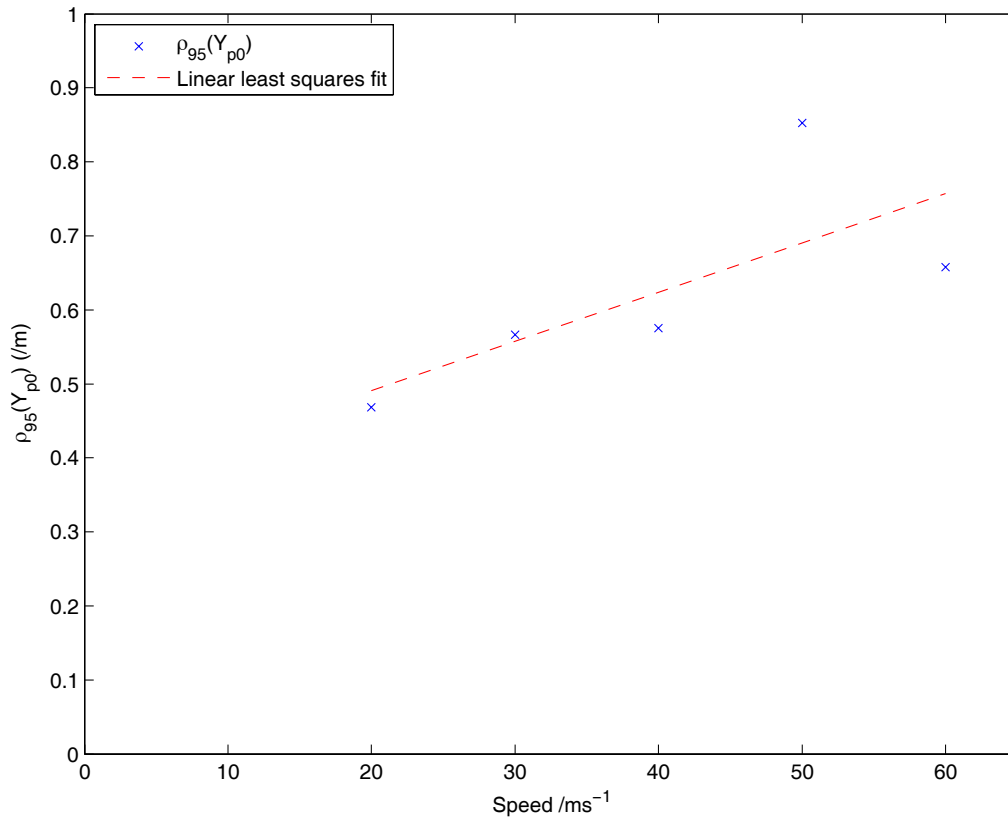
Figure 2.26: $\rho_{95}(\mathbf{y_{p0}})$ vs. speed $\mathbf{U_{cc}}$

Figure 2.26 shows that $\rho_{95}(y_{p0})$ was dependent on speed, as expected from the hypothesis.

The dependence of lateral error on speed is consistent with the expectation from the results of Figure 2.24, where lateral error $\rho_{95}(y_{p0})$ was dependent on width, and Figure 2.6 where the speed was dependent on width. These together imply that the driver changed his or her speed to achieve different lateral errors for different road widths.

The dependence of lateral error on speed is also consistent with the expectation from the results of Figure 2.6 where speed was dependent on curvature, and Figure 2.22 where lateral error was independent of curvature. These together implied that the driver changed their speed to achieve consistent lateral error for different curvatures.

2.4.6 Speed prediction using hypothesis

The hypothesis of section 2.3 can be modified to take account of the risk/effort behaviour observed in section 2.4.4 by assuming that the driver aimed to achieve a different lateral error percentile (λ) for each width. The fitting of this modified 'variable risk' hypothesis is described in the sections 2.4.6.1 to 2.4.6.3.

In order to fit this modified hypothesis it must be assumed that the driver effort is constant, and that the driver's risk behaviour accounts for the change in lateral error percentile λ with width. The reasons for this are described in section 2.4.6.2. Although constant effort was encouraged by instructions to the driver, the possibility that the driver effort was not constant cannot be discounted. This modified 'variable risk' speed choice hypothesis can therefore not be considered a complete solution to the problem identified in section 2.4.4, as driver effort must be quantified. Defining the driver effort through modelling of driver steering control is the subject of the work in chapters 3, 4 and 5.

The 'variable risk' path error based speed choice hypothesis was fitted to the driver data, and its prediction of speed was compared with the linear surface model shown in section 2.2.1. The model of section 2.2.1 was chosen for comparison as this predicts the influence of both radius and width. Speed prediction using the 'variable risk' path error hypothesis involved the following steps.

1. Establish the lateral error percentile λ_W chosen for each width (risk behaviour).
2. Fit a lateral error ($\rho_\lambda(y_{p0})$) vs. speed vs. curvature surface for each percentile λ_W.
3. Predicted speed can then be determined from the fitted surface.

2.4.6.1   Lateral error percentile vs. width

First, the lateral error percentile λ chosen for each width was established as discussed in section 2.4.4 . This was carried out using an optimisation routine in MATLAB to solve equation (2.7) for each width W_1 to W_5.

$$\lambda_{W_1} = \arg\min_{\lambda} \left\{ \left\| \frac{(W_1 - W_v)}{2} - \rho_\lambda(y_{p0}(W_1)) \right\| \right\} \qquad (2.7)$$

Where $\rho_\lambda(y_{p0}(W_1))$ is the λth percentile of the lateral error recorded for width W_1 in the constant curvature section (shown in Figure 2.23). This yields five percentiles λ^{W_1} to λ^{W_5}. The five percentiles λ^{W_1} to λ^{W_5} are plotted against the widths W_1 to W_5 in Figure 2.27.
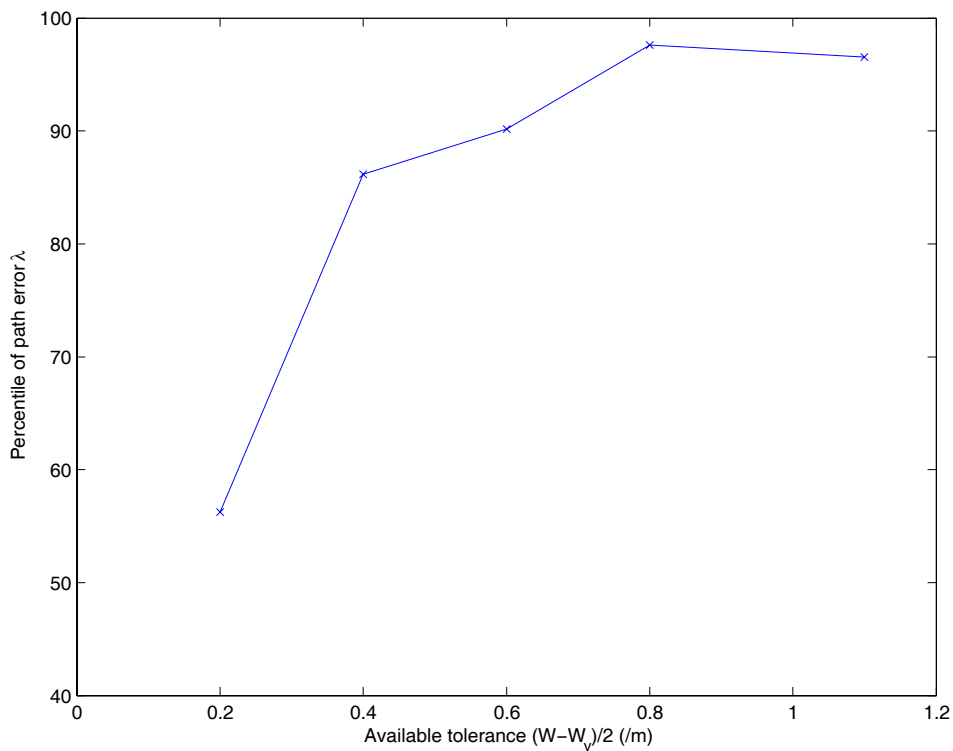
Figure 2.27: Percentile (λ) of $\mathbf{y_{p0}}$ vs. available tolerance $\left(\mathbf{W - W_v}\right)\!\big/\mathbf{2}$

The result is consistent with that of Figure 2.24, and shows that the subject was within the road for 55% of the time on the narrowest road, but 96% of the time on the widest road.

2.4.6.2 Lateral error surface fitting

Next, for each of the widths, a lateral error vs. speed vs. curvature surface must be fitted using equation (2.6) as demonstrated in section 2.4.2. For example, for width W_1 the surface for the 55th percentile lateral error ($\rho_\lambda(y_{p0})$ where $\lambda = \lambda^{W_1} = 0.55$),

66

yielding four surface coefficients $[a_5^{W_1}, b_5^{W_1}, c_5^{W_1}, d_5^{W_1}]$. This procedure is repeated for each of the percentiles λ^{W_1} to λ^{W_5} to establish four surface coefficients for each of the widths W_1 to W_5.

This is can be thought of as plotting contours of λ for the three dimensional field $\rho(y_{p0})\{\lambda, C, U\}$. Fitting of a λ surface to this field uses all the data, rather than just that for the width corresponding to λ. This presumes that the field $\rho(y_{p0})\{\lambda, C, U\}$ is independent of width.

However, this may not be the case if driver control strategy is being changed between widths. It would then be possible for the driver to achieve different lateral error $\rho(y_{p0})\{\lambda\}$ for the same curvature and speed $\{C, U\}$ point by using different control strategies. It would then be necessary to define a 4th dimension to the field, to take account of this control strategy (or effort) parameter Θ, giving a field $\rho(y_{p0})\{\lambda, C, U, \Theta\}$. A constant effort Θ was assumed for this model. However, to better understand the driver speed choice, a means of defining this driver effort parameter Θ will be important. Defining the driver steering strategy (or effort) through modelling of driver steering control is the subject of the work in chapters 3, 4 and 5 and is discussed in section 2.5.

2.4.6.3 Speed prediction

Predicted speed (U_{cc}') for each curve can then be determined from the surface corresponding to the correct width for that curve. For example, for width W_1, the surface coefficients $[a_5^{W_1}, b_5^{W_1}, c_5^{W_1}, d_5^{W_1}]$ are used in equation (2.8) (a rearrangement of (2.6)) to yield the predicted speed for the five curves of width W_1.

$$U_{cc}{}'^{(W_1)} = \frac{((W_1 - W_v)/2 - a_5^{W_1} - \dfrac{b_5^{W_1}}{R})}{c_5^{W_1} + \dfrac{d_5^{W_1}}{R}} \qquad (2.8)$$

This procedure is repeated for each of the widths W_1 to W_5 to establish the speeds for the curves at each of these widths. The speed predictions U'_{cc} from this path error model are plotted against the driver's recorded speed $\mu(U_{cc})$ as red circles in Figure 2.28. Speed predictions U'_{cc} from the speed vs. width vs. radius surface prediction model of equation (2.3) are shown as blue crosses, and the solid line indicates perfect prediction.
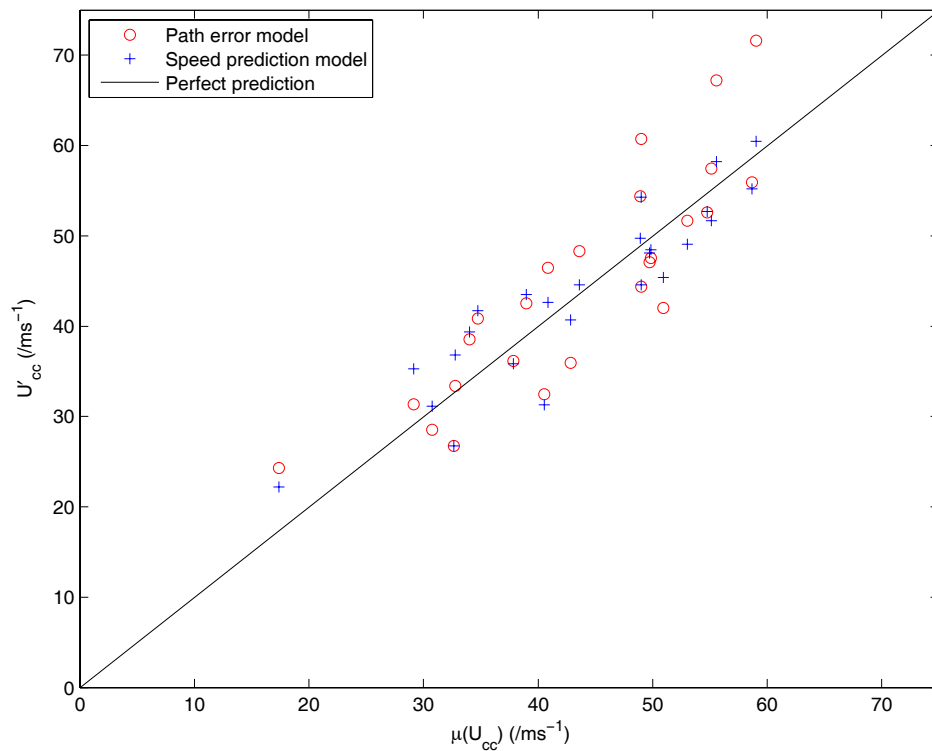
Figure 2.28: Predicted speed (U'_{cc}) vs. actual speed ($\mu(U_{cc})$)

Figure 2.28 shows that the individual speed predictions of the two models do differ, so the two are not just amounting to same model. Table 2.10 shows the mean and variance of prediction error for both models.

	$\mu(U'_{cc} - \mu(U_{cc}))$	$\sigma(U'_{cc} - \mu(U_{cc}))$
Speed prediction model eqn. (2.3) (/ms^{-1})	0.00	4.31
Path error model (/ms^{-1})	-1.14	6.10

Table 2.10: Speed prediction errors from speed prediction model and path error model

The speed prediction model has zero mean prediction error because the surface was fitted to ensure that the mean error of the residuals is zero. The mean prediction error for the path error model is low considering the non-normal data used to populate the $\rho(y_{p0})\{\lambda, C, U\}$ field.

The path error model is significantly more complicated than the speed prediction model, and gave no benefit in prediction accuracy. The assumption of constant driver effort necessary to fit this model also renders it less useful. To validate this model properly, different data should be used for fitting the model to that used for evaluating the model. Instead of collecting this data, it was preferred to spend time on a new set of experiments, designed to resolve the issue of changing driver effort.

2.5 Discussion

The experiments described in this chapter were not designed to enable the driver's steering control strategy (or effort level) to be quantified. In order to enable the driver's steering strategy to be determined, the fitting (identification) of a driver steering model with an appropriate 'effort' parameter to driver steering data was required. An identified steering model would allow the variation of steering control (or effort) with speed and track width to be quantified.

Sharp's LQR preview model allows driver steering strategy to be modelled using cost function weights on lateral error and heading error, so was chosen as a suitable driver model. The development of driver models based on Sharp's LQR controller is described in chapter 3.

A revised set of experiments were undertaken in order to quantify the changes in the driver steering strategy with speed and road width. A range of fixed speeds and road widths was used so that the variation of driver performance (including path error) and steering control (effort) could be measured as a function of speed and road width. A group of five subjects was used in order to quantify the variation in steering strategy between drivers.

In order to identify the preview driver model without bias, notice had to be taken of the system identification theory set out by Ljung [47]. A suitable experimental design using a random road input to excite the driver's preview control had to be validated. The validation of this method is described in chapter 4, and the results of the driver identification are described in chapter 5.

2.6   Conclusions

The conclusions for the existing speed choice models were covered in the summary in section 2.2.5, leading to the proposal of the new path error based speed choice hypothesis. Conclusions from assessment of the path error based speed choice hypothesis using measured simulator data are as follows:

Lateral error histograms for individual curves were non-normal, so fitting percentiles to these provided poor statistics. Data was therefore 'lumped' together to examine lateral error as a function of width, radius, and speed separately. This led to more normal distributions. Lateral error was independent of bend curvature, but speed was not, indicating that speed and/or steering control was changed in order to keep lateral error constant. Lateral error changed with width, but not by enough to keep the ratio of lateral error to available tolerance constant. The cause of non-constant lateral error to available tolerance ratio could be a risk strategy, or a change in steering control strategy (effort) by the driver. Although only one test subject's results are shown here, data from earlier tests showed similar trends.

A variable percentile of lateral error with width was added to the path error based speed choice model to take account of this behaviour, but it was necessary to assume constant driver effort. The prediction of speed using this modified 'variable risk' hypothesis gave poorer fit than the linear speed vs. width vs. curvature surface model of equation (2.3), despite the path error model's increased complexity. Although the limited data does not enable the speed choice model to be validated, the results illustrate the importance of the relationship between path error and speed in the modelling of speed choice.

It was concluded that changes in driver steering control (effort) could affect the speed choice of drivers. Because of this possibility new experiments were proposed to examine the changes in the steering control of drivers with speed and road width. The experiments proposed involved driving random roads at a range of fixed speeds, and

road widths. The driver steering strategy was to be determined by fitting preview steering control models to the measured steering control action of the driver.

Chapter 3: Models of driver steering control

Chapters 3 to 5 deal with the possibility of modelling the driver's steering control as a linear quadratic regulator (LQR). This chapter introduces a set of candidate LQR models with varying degrees of sophistication, while chapter 4 introduces and validates identification procedures for fitting these models to measured data. The results of fitting the LQR models to driver data are then presented in chapter 5.

This chapter is split into four sections. Firstly, the LQR controller concept and the way it is implemented is explained. Secondly, a set of LQR models with varying degrees of sophistication is proposed. Thirdly, the preview and state gains of these controllers are investigated, including how they change with speed. Finally closed loop control with each controller is implemented and the performance of the controllers is compared.

A set of LQR models with varying degrees of sophistication was required for two reasons. Firstly it was unclear at this stage how sophisticated a model was required to reflect a 'typical' human driver. A model set with a range of complexities was used to find out the minimum complexity required to fit the 'typical' driver's behaviour closely. Secondly there may be significant variability between drivers due to different levels of competence at steering. Steering competence may be affected by experience, natural ability, or attentiveness of the driver. A range of driver models was required to ensure that each driver can be matched closely enough by one of the models of the set.

Ideally an infinitely large model set would be used, but this work was limited to LQR models. LQR models were chosen as they incorporate many of the important features known to be present in control by real drivers, but are simple to implement as they have linear time invariant gains.

3.1 Introduction to Sharp's LQR controller

Sharp proposed an LQR controller with road preview as a model of the driver for moderate steering manoeuvres [43]. In this section the derivation of Sharp's model is explained and modifications are proposed to make the model more representative of real driver behaviour.

3.1.1 The LQR controller

The derivation of the LQR controller involves a vehicle model coupled to a road model via a cost function. This cost function is chosen to reflect the priorities of the driver in terms of path following, heading error minimisation, or steer angle minimisation. Derivation of the controller begins with a description of the bicycle model of the vehicle (Figure 2.3) in state space form:
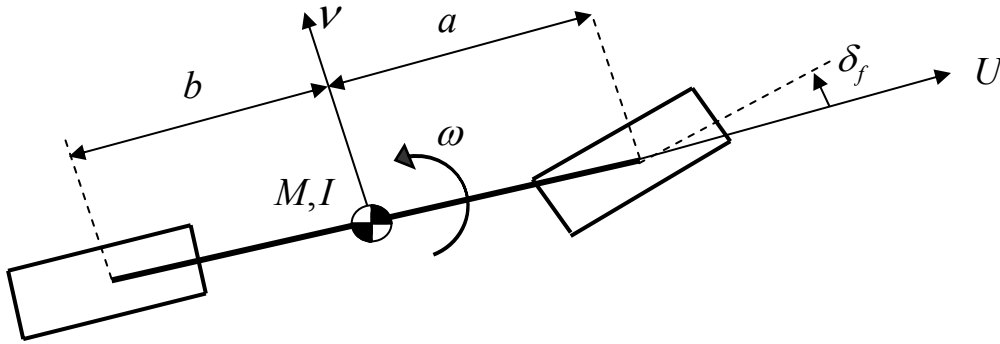
Figure 3.1: Bicycle model of vehicle

$$\delta_f = \delta / K_{sw} \tag{3.1}$$

Where δ is the driver's steering wheel angle, and K_{sw} is the gain between steering wheel angle and front wheel angle.

$$\dot{\mathbf{x}}_v = \mathbf{A}\mathbf{x}_v + \mathbf{B}\delta \tag{3.2}$$

For a 2DOF bicycle model this takes the form [55]:

$$\mathbf{x}_v = \begin{bmatrix} v & \omega & y_v & \theta \end{bmatrix}^T \tag{3.3}$$

$$\mathbf{A} = \begin{bmatrix} A_{11} & A_{12} & 0 & 0 \\ A_{21} & A_{22} & 0 & 0 \\ 1 & 0 & 0 & U \\ 0 & 1 & 0 & 0 \end{bmatrix} \text{ and } \mathbf{B} = \begin{bmatrix} B_1 \\ B_2 \\ 0 \\ 0 \end{bmatrix} \tag{3.4}$$

$$\begin{bmatrix} A_{11} & A_{12} \\ A_{21} & A_{22} \end{bmatrix} = \begin{bmatrix} -\left(\dfrac{C_f + C_r}{MU}\right) & -\left(\dfrac{aC_f - bC_r}{MU} + U\right) \\ -\left(\dfrac{aC_f - bC_r}{IU}\right) & -\left(\dfrac{a^2 C_f + b^2 C_r}{IU}\right) \end{bmatrix} \text{ and } \begin{bmatrix} B_1 \\ B_2 \end{bmatrix} = \begin{bmatrix} \dfrac{C_f}{MK_{sw}} \\ \dfrac{aC_f}{IK_{sw}} \end{bmatrix} \tag{3.5}$$

Secondly, the road is described in ground-fixed axes (x, y) in terms of offsets y_{ri} from the x-axis shown in Figure 3.2.
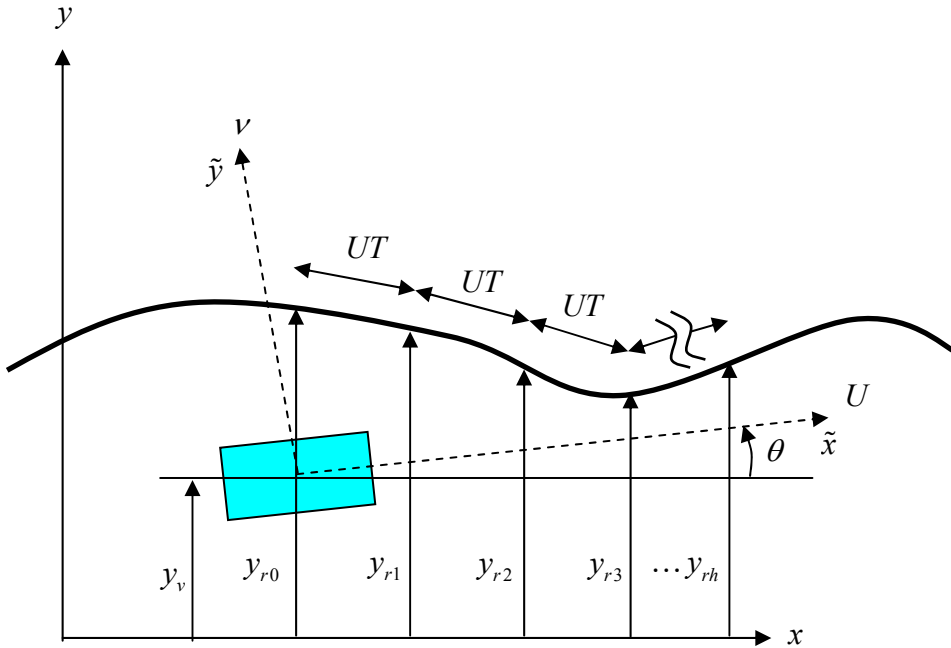
Figure 3.2: Road and preview offsets in ground-fixed $(\mathbf{x}, \mathbf{y})$ axes

The road is modelled in discrete state space form such that each timestep T a new road point y_{rh} is introduced at the end of the vector of preview offsets $\mathbf{y_r}$ and the remaining points move down the vector $\mathbf{y_r}$ by means of a shift register:

$$\mathbf{y_r}(k+1) = \mathbf{D}\mathbf{y_r}(k) + \mathbf{E}y_{rh} \tag{3.6}$$

$$\mathbf{D} = \begin{bmatrix} 0 & 1 & 0 & \cdots & 0 \\ 0 & 0 & 1 & \cdots & 0 \\ \vdots & & & & \vdots \\ 0 & 0 & 0 & \cdots & 1 \\ 0 & 0 & 0 & \cdots & 0 \end{bmatrix} \quad \text{and} \quad \mathbf{E} = \begin{bmatrix} 0 \\ 0 \\ \vdots \\ 0 \\ 1 \end{bmatrix} \tag{3.7}$$

Discretising $\mathbf{A}$ and $\mathbf{B}$ from equation (3.4) using MATLAB function C2D gives $\mathbf{A_d}$ and $\mathbf{B_d}$. The vehicle and road discrete state space models can then be amalgamated:

$$\begin{bmatrix} \mathbf{x_v}(k+1) \\ \mathbf{y_r}(k+1) \end{bmatrix} = \begin{bmatrix} \mathbf{A_d} & 0 \\ 0 & \mathbf{D} \end{bmatrix} \begin{bmatrix} \mathbf{x_v}(k) \\ \mathbf{y_r}(k) \end{bmatrix} + \begin{bmatrix} 0 \\ \mathbf{E} \end{bmatrix} y_{rh} + \begin{bmatrix} \mathbf{B_d} \\ 0 \end{bmatrix} \delta \tag{3.8}$$

The two models are not linked in (3.8), but are linked by the introduction of a cost function. The cost function proposed by Sharp is as follows:

$$J = \lim_{n \to \infty} \sum_{k=0}^{n} \{ \mathbf{z}^T(k) . \mathbf{R_1} . \mathbf{z}(k) + \delta(k) . \mathbf{R_2} . \delta(k) \} \tag{3.9}$$

Where:

$$\mathbf{z} = \begin{bmatrix} \mathbf{x_v} \\ \mathbf{y_r} \end{bmatrix} = \begin{bmatrix} v & \omega & y_v & \theta & y_{r0} & y_{r1} & \cdots & y_{rh} \end{bmatrix}^T \tag{3.10}$$

The parameter $\mathbf{R_2}$ sets the driver's cost on steer angle, while the matrix $\mathbf{R_1}$ sets the driver's cost on combinations of states. In Sharp's formulation, the cost on steer angle ($\mathbf{R_2}$) is kept constant:

$$\mathbf{R_2} = 1 \tag{3.11}$$

The vehicle states cost matrix $\mathbf{R_1}$ is then varied (relative to $\mathbf{R_2}$) to set the driver's preferences. In Sharp's formulation, the state cost matrix $\mathbf{R_1}$ is formulated as follows:

$$\mathbf{R_1} = \mathbf{C_1}^T \mathbf{Q} \mathbf{C_1} \tag{3.12}$$

$$\mathbf{C_1} = \begin{bmatrix} 0 & 0 & 1 & 0 & -1 & 0 & 0 & 0 & \cdots & 0 \\ 0 & 0 & 0 & 1 & \dfrac{1}{UT} & \dfrac{-1}{UT} & 0 & 0 & \cdots & 0 \end{bmatrix} \tag{3.13}$$

$$\mathbf{Q} = \begin{bmatrix} q_y & 0 \\ 0 & q_\theta \end{bmatrix} \tag{3.14}$$

The parameters q_y and q_θ set driver's cost of lateral error and heading error respectively. The driver can therefore vary their costs on lateral error (q_y) and heading error (q_θ) independently to set his or her driving strategy preference. The MATLAB function DLQR is then used to calculate an LQR controller from equations (3.8), (3.12) and (3.13), yielding a controller of the type:

$$\delta = \mathbf{K_{LQR}} \mathbf{z} = k_v v + k_\omega \omega + k_y y_v + k_\theta \theta + \sum_{i=0}^{h} k_{ri} y_{ri} \tag{3.15}$$

This controller can then be reformulated in terms of preview offsets $\mathbf{y_{pi}}$ measured in the driver reference frame (offsets measured from the driver's 'optical lever' as shown in Figure 3.3), as detailed by Sharp and later Cole [43, 55]. In this vehicle reference frame, equation (3.15) simplifies to equation (3.16) (for the 2DOF bicycle model above):

$$\delta = k_v v + k_\omega \omega + \sum_{i=0}^{h} k_{pi} y_{pi} \tag{3.16}$$
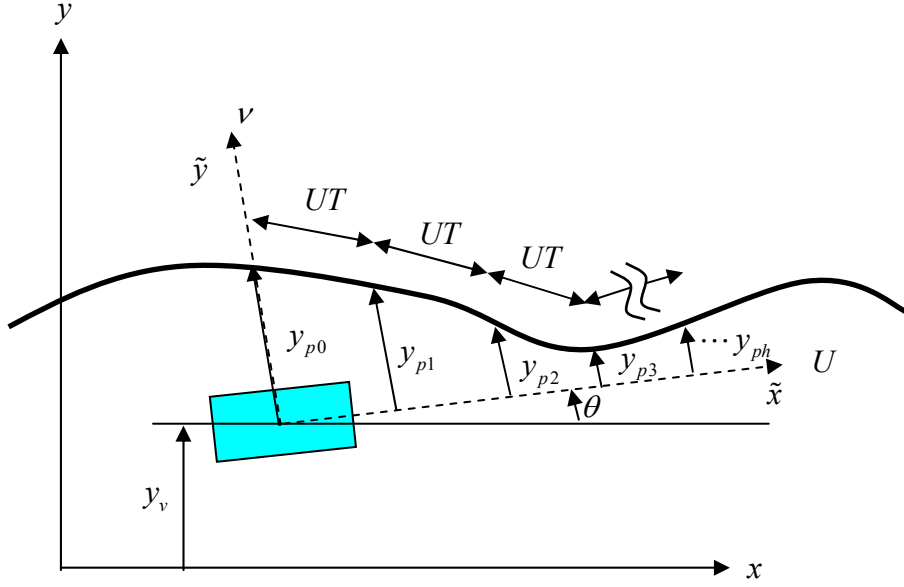
Figure 3.3: Preview offsets measured in vehicle reference frame $(\tilde{\mathbf{x}}, \tilde{\mathbf{y}})$

The resulting controller uses the same preview gains ($\mathbf{k_{pi}} = \mathbf{k_{ri}}$) and vehicle state gains (k_v, k_ω), but the gains k_y and k_θ become zero and can be removed from the controller. The elimination of (k_y, k_θ) was found by Cole [55] to be conditional on the preview being sufficiently long for the preview gains to decay to zero at the furthest point ($k_{ph} = 0$). Care needs to be taken therefore when selecting preview length for controllers.

3.1.2 Proposed modifications to LQR controller

Sharp's LQR controller [43] provides most of the features necessary in a good driver model, namely: preview of the future road path; feedback of present vehicle states; an internal model of the system to be controlled; and parameters to specify the control priorities (effort level) of the driver. However, certain limitations of Sharp's model were identified which could be remedied with modifications to the LQR formulation. Each of these modifications was incorporated into one or more models of the set to provide greater or sophistication than Sharp's model. The limitations, and the modifications made to Sharp's formulation are as follows.

Firstly, the LQR controller presumes perfect knowledge of the vehicle by the driver. This may not be the case for novice drivers, who might assume a simplified vehicle model and be able to use this to control the vehicle in relatively benign situations (i.e. low sideslip and yaw acceleration conditions). This means of modelling a novice driver was used by Prokop [28]. Two LQR controllers based on simplified vehicle models are described in sections 3.2.2 and 3.2.3.

Secondly the controller assumes infinite bandwidth of driver control, whereas in fact the driver's control is band-limited. The use of a second order filter to approximate the neuromuscular system (NMS) models proposed by Pick [36] was discussed in chapter 1. A second order filter NMS model is incorporated into the LQR formulation in sections 3.2.5 and 3.2.6.

Finally, the driver is subject to significant time delay between measurement of vehicle states and actual steer angle application. These delays occur during perception, decision making and actuation of the neuromuscular system and are thought to total between 0.15 and 0.3 seconds [36, 39, 41]. These delays are not represented in the LQR formulation as explained so far. An LQR formulation taking account of delay was proposed by Pick [36] and this model is detailed in section 3.2.4.

A limitation that could not be remedied with modifications to Sharp's model was the restriction of linear time invariant (LTI) control inherent in the LQR controller. A real driver is not restricted to LTI control, and may act non-linearly in the presence of constraints such as road edges. A model predictive controller could provide this feature, but requires a different modelling approach than that used here for the LQR controller. Study of model predictive controllers may be carried out in future work, but was not attempted as part of this thesis. Instead, an LQR controller must model the presence of a more restrictive road edge constraint by using a higher controller weighting on lateral and/or heading error. There may be other limitations of LQR controllers, so one objective of this work was to see how well the LQR controller fits to driver data.

3.2 Description of Models

A range of LQR models was necessary to cover all of the possible modifications above. In this section eight models are proposed. All models are intended to control the same vehicle (second order bicycle model in equation (3.4)), but each model represents a different level of control sophistication of the driver.

Model G_I is that proposed by Sharp [43] as detailed in section 3.1. Models G_{II} and G_{III} are of reduced complexity compared to the plant being controlled, to represent the simplified controller of a novice driver. The concept of a reduced complexity model for novice drivers was as proposed by Prokop [28], who used a point mass vehicle model. Model G_{IV} includes the inherent driver delay as formulated by Pick [36]. Models G_V to G_{VIII} include a neuromuscular system (NMS) model. In three of these models (G_{VI} to G_{VIII}) the driver is aware of the neuromuscular system and changes their LQR control to compensate, whereas in model G_V the driver is not aware of its presence and uses a controller optimised with no NMS. The eight models and their equations are described in sections 3.2.1 to 3.2.6.

3.2.1 Model G_I *: Second order bicycle model*

Model G_I is the LQR controller detailed by Sharp [43] and in section 3.1. The model represents an experienced driver with full knowledge of the yaw and sideslip behaviour of the vehicle.
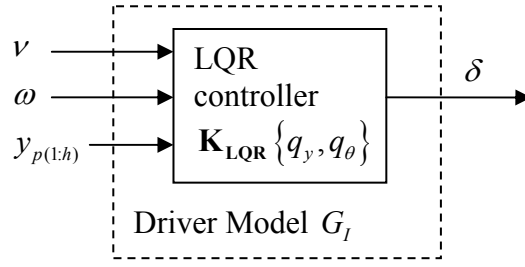
Figure 3.4: State and preview inputs and output of model $\mathbf{G_I}$

The resulting controller shown in Figure 3.4 requires preview, but also both yaw and sideslip (v, ω) states of the vehicle. This model is parameterised by the two weights $\{q_y, q_\theta\}$ on lateral error and heading error respectively.

3.2.2   Model $\mathbf{G_{II}}$: Zero order model

Model G_{II} is a simplified version of the real vehicle system intended to characterise a novice driver with a simplified internal model of vehicle. This vehicle is modelled as a point-mass, as shown in Figure 3.6 and behaves according to equation (3.18) from Prokop [28]. Figure 3.5 and equation (3.17) show the derivation of equation (3.18) .
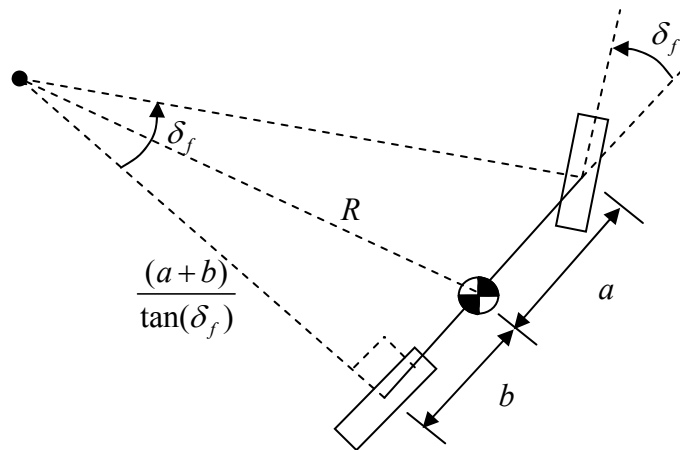
Figure 3.5: Derivation of Prokop's point mass model

From the lengths marked in Figure 3.5, applying Pythagoras leads to:

$$R = \sqrt{b^2 + \frac{(a+b)^2}{\tan^2(\delta_f)}} \qquad (3.17)$$
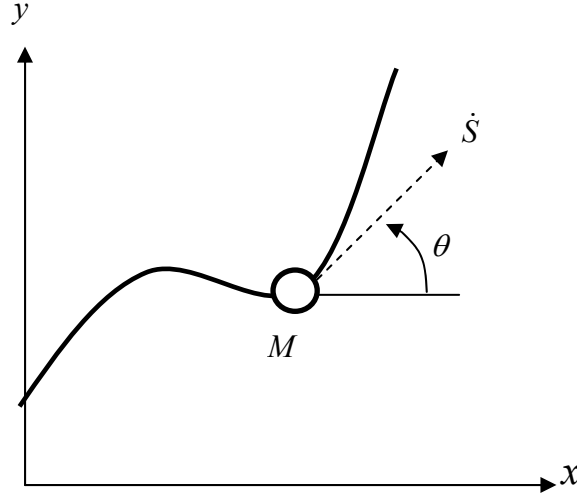
Figure 3.6: Point mass model as proposed by Prokop [28]

$$\frac{d\theta}{dS} = \frac{1}{R} = \frac{\tan \delta_f}{\sqrt{(a+b)^2 + b^2 \tan^2 \delta_f}} \qquad (3.18)$$

Equation (3.18) implies a vehicle with no yaw inertia whose path curvature ($d\theta/dS$) responds instantaneously to steer angle (a zero order system). Equation (3.18) can be linearised with little loss of accuracy below 40° of front wheel steer angle (1.8 steering wheel revolutions) as shown in Figure 3.7. Figure 3.7 shows $d\theta/dS$ calculated from equation (3.18) as a solid line and a linear approximation with the same initial gradient as a dashed line.
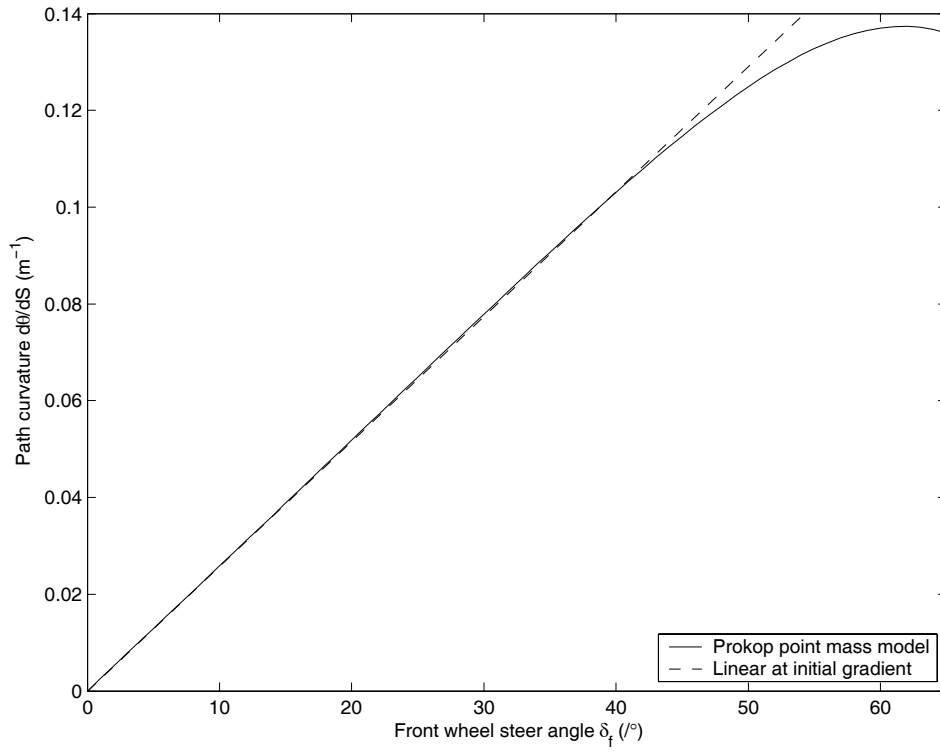
Figure 3.7: Front wheel steer angle δ_f vs. path curvature $d\theta/dS$ in Prokop's point mass model

Linearising equation (3.18) gives yaw rate as shown in equation (3.19):

$$\omega = \frac{d\theta}{dt} = \frac{d\theta}{dS}\frac{dS}{dt} = \frac{\dot{S}}{\sqrt{(a+b)^2 + b^2 \tan^2 \delta_f}} \tan \delta_f \approx k_1 \delta \tag{3.19}$$

If yaw rate gain k_1 is chosen to be consistent with the 2DOF system of equation (3.4), then the system equation (analogous to that of equation (3.2)) is:

$$\begin{bmatrix} \dot{y} \\ \dot{\theta} \end{bmatrix} = \begin{bmatrix} 0 & U \\ 0 & 0 \end{bmatrix} \begin{bmatrix} y \\ \theta \end{bmatrix} + \begin{bmatrix} 0 \\ \dfrac{B_2}{A_{22}} \end{bmatrix} \delta \tag{3.20}$$

The resulting LQR controller derived from equations (3.8) to (3.15) and (3.20) is shown schematically in Figure 3.8.
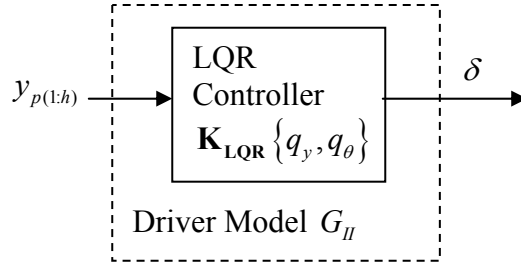
Figure 3.8: State and Preview inputs and output of LQR controller for model $\mathbf{G_{II}}$

The resulting model (G_I) has no vehicle state inputs, only path preview, so the novice driver being modelled takes no account of the vehicle's present velocity states in his or her control. Model parameters are $\{q_y, q_\theta\}$ as for Sharp's controller (G_I).

3.2.3   Model $\mathbf{G_{III}}$: 1DOF model

As for model G_{II}, G_{III} is a simplified vehicle model intended to mimic a novice driver, but of slightly more sophistication. Model G_{III} is based on the 2 DOF bicycle model of equation (3.4), but with the sideslip (v) degree of freedom removed. Zero sideslip can be achieved with various rear wheel steering strategies [52], which are not under the control of the driver, therefore ensure that drivers do not need to take account of sideslip in their control of the vehicle. Sideslip is small in most normal driving situations, so model G_{III} might be used by a normal driver with little experience of tyre saturation conditions.

The system equation for model G_{III} is shown in equation (3.21). Steady state yaw rate gain is the same as that of equation (3.4) (model G_I).

$$\begin{bmatrix} \dot{\omega} \\ \dot{y} \\ \dot{\theta} \end{bmatrix} = \begin{bmatrix} A_{22} & 0 & 0 \\ 0 & 0 & U \\ 1 & 0 & 0 \end{bmatrix} \begin{bmatrix} \omega \\ y \\ \theta \end{bmatrix} + \begin{bmatrix} B_2 \\ 0 \\ 0 \end{bmatrix} \delta \qquad (3.21)$$

Figure 3.9 shows the driver model controller for model G_{III} :
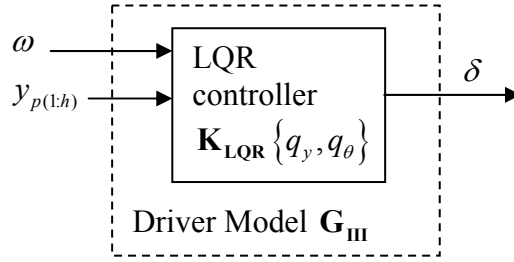
Figure 3.9: State and preview inputs and output of model $\mathbf{G}_{\text{III}}$

The 'model G_{III}' driver requires both preview and vehicle yaw rate (ω) state information to decide on steer angle, but not sideslip velocity (v). Again the model is parameterised by two controller weights $\{q_y, q_\theta\}$.

3.2.4 Model $\mathbf{G}_{\text{IV}}$: Delay state model

Model G_{IV} was proposed by Pick [36] as a means of including the driver's knowledge of his or her own cognitive and actuation delay (τ) in the driver's internal model. The model includes extra 'delay states' for delay of steer angle into the vehicle. This allows modelling of a driver who is aware of his or her own delay and changes their control accordingly.

The state space equations to be used in the LQR controller are shown in discrete form in equation (3.22). Input steer angle δ_{N_d} is delayed by its passage down a shift register before it is applied to the vehicle. The number of delay states (N_d) corresponds to number of time steps of delay.

$$
\begin{bmatrix} \delta_{N_d-1}(k+1) \\ \delta_{N_d-2}(k+1) \\ \vdots \\ \delta_1(k+1) \\ \delta(k+1) \\ v(k+1) \\ \omega(k+1) \\ y(k+1) \\ \theta(k+1) \end{bmatrix} = \begin{bmatrix} 0 & 0 & \cdots & 0 & 0 & 0 & 0 & 0 & 0 \\ 1 & 0 & \cdots & 0 & 0 & 0 & 0 & 0 & 0 \\ \vdots & \vdots & \ddots & \vdots & \vdots & \vdots & \vdots & \vdots & \vdots \\ 0 & 0 & \cdots & 0 & 0 & 0 & 0 & 0 & 0 \\ 0 & 0 & \cdots & 1 & 0 & 0 & 0 & 0 & 0 \\ 0 & 0 & \cdots & 0 & B_{d1} & A_{d11} & A_{d12} & 0 & 0 \\ 0 & 0 & \cdots & 0 & B_{d2} & A_{d21} & A_{d22} & 0 & 0 \\ 0 & 0 & \cdots & 0 & B_{d3} & 1 & 0 & 0 & U \\ 0 & 0 & \cdots & 0 & B_{d4} & 0 & 1 & 0 & 0 \end{bmatrix} \begin{bmatrix} \delta_{N_d-1}(k) \\ \delta_{N_d-2}(k) \\ \vdots \\ \delta_1(k) \\ \delta(k) \\ v(k) \\ \omega(k) \\ y(k) \\ \theta(k) \end{bmatrix} + \begin{bmatrix} 1 \\ 0 \\ 0 \\ 0 \\ 0 \\ 0 \\ 0 \\ 0 \\ 0 \end{bmatrix} \delta_{N_d} \quad (3.22)
$$

The resulting driver model in Figure 3.10 shows that the controller needs to be supplied with steer angle states $(\delta_{N_d-1},\ldots,\delta)$ which are internal states of the steer angle shift register. Pick [36] proposed that this be thought of as a steer angle filter.
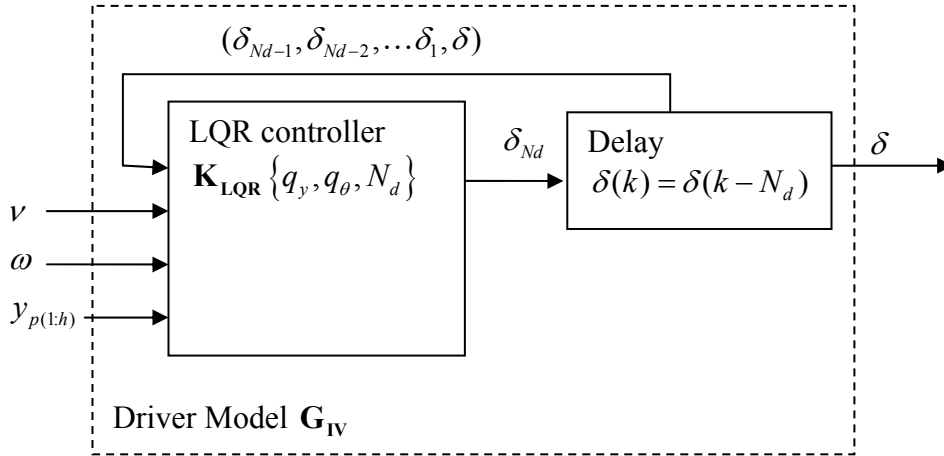
Figure 3.10: State and preview inputs and outputs of model $\mathbf{G_{IV}}$

3.2.5 Model $\mathbf{G_V}$: 4 state NMS model

For the following three models it was intended to use a simple band-limiting second order filter $\mathbf{N_1}(s)$ as a model of the driver's neuromuscular system (NMS) as shown in equation (3.23).

$$
\mathbf{N_1}(s) = \frac{\delta(s)}{\delta_{nms}(s)} = \frac{1}{\dfrac{s^2}{\omega_n^2} + \dfrac{2\xi}{\omega_n} s + 1} \quad (3.23)
$$

However, filter $\mathbf{N}_1(s)$ was not used because when discretised it did not closely match the intended continuous transfer function. Figure 3.11 shows a bode plot of the continuous filter $\mathbf{N}_1(s)$ in green and the discretised version $\mathbf{N}_1(z)$ in blue. $\mathbf{N}_1(z)$ was discretised using the MATLAB function C2D using a zero order hold approximation with timestep $T = 0.05$ s.
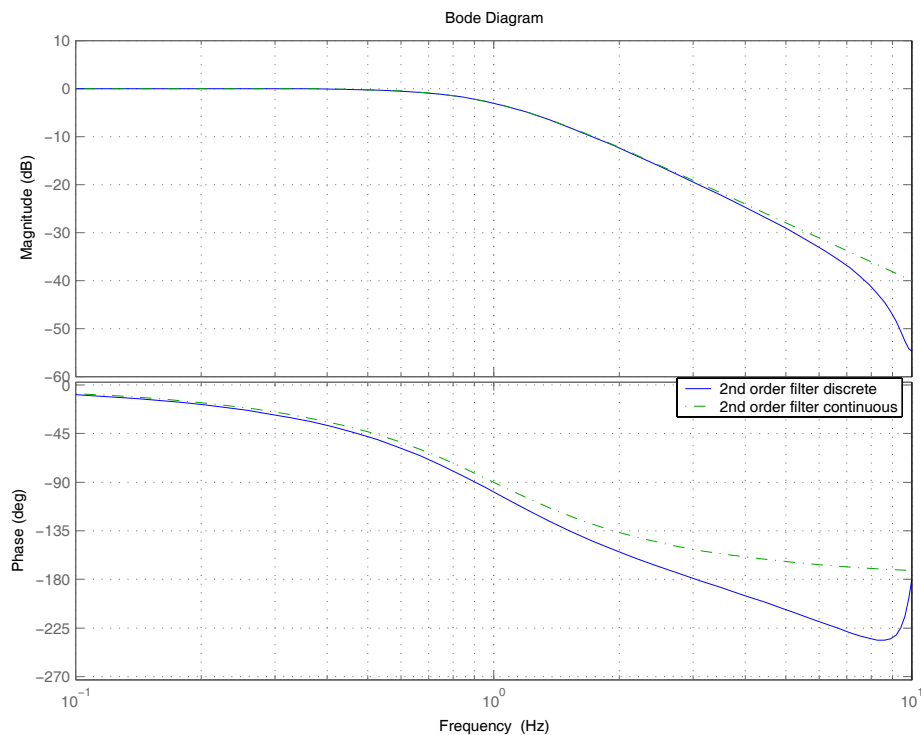
Figure 3.11: Comparison of filter $\mathbf{N}_1$ in continuous and discretised form

The transfer functions can be seen to differ markedly in both magnitude and phase close to the Nyquist frequency of 10 Hz. The filter was modified to include a second order lead term as shown in equation (3.24) to alter its response near the Nyquist frequency.

$$\mathbf{N}(s) = \frac{\delta_{out}(s)}{\delta_{nms}(s)} = \frac{\dfrac{s^2}{\omega_{cut}^2} + \dfrac{2\xi_{cut}}{\omega_{cut}}s + 1}{\dfrac{s^2}{\omega_n^2} + \dfrac{2\xi}{\omega_n}s + 1} \tag{3.24}$$

Figure 3.12 shows a bode plot of the continuous filter $\mathbf{N}_1(s)$ in green and the discretised lead-lag filter $\mathbf{N}(z)$ in blue. $\mathbf{N}(z)$ was discretised using the MATLAB function C2D using a zero order hold approximation with timestep $T = 0.05$ s.
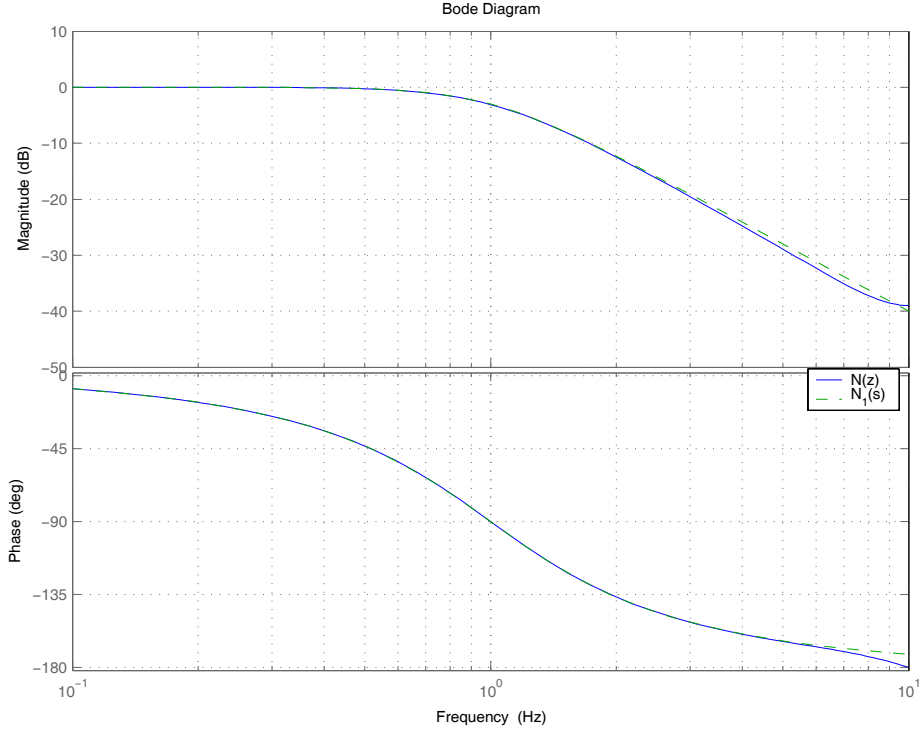
Figure 3.12: Bode plot of $\mathbf{N(z)}$ and $\mathbf{N_1(s)}$ frequency response

The discretised filter $\mathbf{N}(z)$ is a much closer approximation to the continuous filter $\mathbf{N}_1(s)$ than the discretised $\mathbf{N}_1(z)$. Parameters for the neuromuscular system shown in the figure are $\omega_n = 1.0$ Hz and $\xi = 0.707$, with lead compensator parameters $\omega_{cut} = 9$ Hz, $\xi_{cut} = 0.707$. The lead compensator cut-on frequency $\omega_{cut} = 9$ Hz was chosen to be close to the Nyquist frequency so that the lead compensator did not affect the performance of the filter near the NMS cut-off frequency. The lead compensator parameters were fixed at $\omega_{cut} = 9$ Hz, $\xi_{cut} = 0.707$ for all models which include a neuromuscular system (G_V to G_{VIII}).

The inclusion of this filter $\mathbf{N}$ in model G_V is shown in Figure 3.13. The LQR controller outputs a desired steer angle δ_{nms} but this must pass through the NMS filter

before being applied to the vehicle as a steer angle δ_{out}. The neuromuscular system ($\mathbf{N}$) is parameterised by a natural frequency ω_n and damping ξ. Only neuromuscular system natural frequency ω_n was identified for model G_V. NMS damping for G_V was assumed to be $\xi = 0.707$.
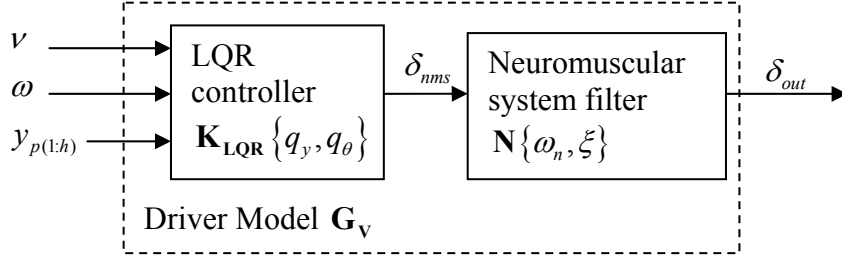
Figure 3.13: State and preview inputs and outputs of model $\mathbf{G_V}$

Model G_V is the simplest realisation of a system with an NMS filter. It is assumed that the neuromuscular system limits the output bandwidth of driver, but that driver does not take account of the filter in tuning the LQR. The driver's internal vehicle model is the same as G_I in equation (3.2) and therefore parameterised by only $\{q_y, q_\theta\}$.

3.2.6   Models $\mathbf{G_{VI}}$ $\mathbf{G_{VII}}$ and $\mathbf{G_{VIII}}$: 6 state NMS model

Models G_{VI} G_{VII} and G_{VIII} also include a neuromuscular system filter, but in addition incorporate the neuromuscular filter into the LQR formulation as shown in equation (3.26). The simpler second order filter $\mathbf{N_1}$ defined in equation (3.23) was used for the LQR controller. The filter $\mathbf{N_1}$ is shown in state space form in equation (3.25).

$$\begin{bmatrix} \dot{\delta} \\ \ddot{\delta} \end{bmatrix} = \begin{bmatrix} 0 & 1 \\ -\omega_n^2 & -2\xi\omega_n \end{bmatrix} \begin{bmatrix} \delta \\ \dot{\delta} \end{bmatrix} + \begin{bmatrix} 0 \\ \omega_n^2 \end{bmatrix} \delta_{nms} \tag{3.25}$$

In the state space model of equation (3.26), the filter $\mathbf{N_1}$ is coupled to vehicle, such that steer angle (δ) applied to the vehicle must first have passed through the NMS.

$$
\begin{bmatrix} \dot{\delta} \\ \ddot{\delta} \\ \dot{v} \\ \dot{\omega} \\ \dot{y} \\ \dot{\theta} \end{bmatrix} = \begin{bmatrix} 0 & 1 & 0 & 0 & 0 & 0 \\ -\omega_n^2 & -2\xi\omega_n & 0 & 0 & 0 & 0 \\ B_1 & 0 & A_{11} & A_{12} & 0 & 0 \\ B_2 & 0 & A_{21} & A_{22} & 0 & 0 \\ 0 & 0 & 1 & 0 & 0 & U \\ 0 & 0 & 0 & 1 & 0 & 0 \end{bmatrix} \begin{bmatrix} \delta \\ \dot{\delta} \\ v \\ \omega \\ y \\ \theta \end{bmatrix} + \begin{bmatrix} 0 \\ \omega_n^2 \\ 0 \\ 0 \\ 0 \\ 0 \end{bmatrix} \delta_{nms} \qquad (3.26)
$$

Models G_{VI} G_{VII} and G_{VIII} describe a driver who is aware of their NMS limitations and adapts his or her control strategy accordingly. The resulting driver models G_{VI} G_{VII} and G_{VIII} are shown in Figure 3.14. Note that parameters of the LQR controller now include $\{\omega_n, \xi\}$ as well as $\{q_y, q_\theta\}$. Also, the states required by the controller include δ and $\dot{\delta}$ and it is assumed that these could be measured by the driver.
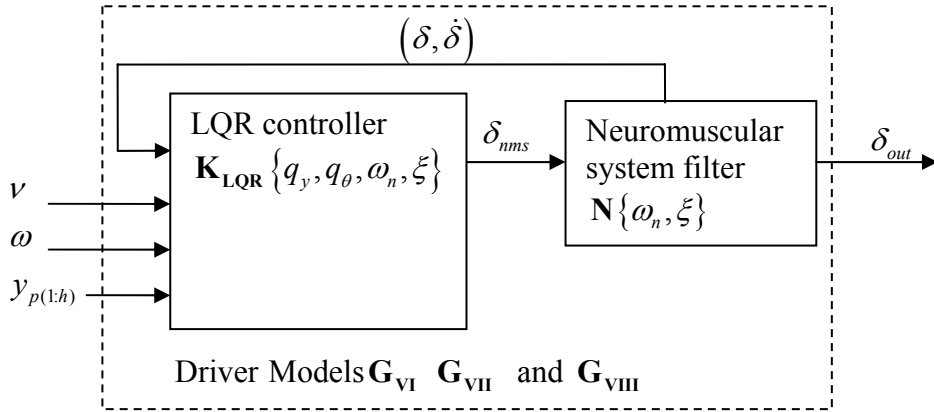
Figure 3.14: State and preview inputs and outputs of models $\mathbf{G_{VI}}$ $\mathbf{G_{VII}}$ and $\mathbf{G_{VIII}}$

Models G_{VI} G_{VII} and G_{VIII} use the same driver model, but differ in which of the neuromuscular system parameters $\{\omega_n, \xi\}$ is identified. For model G_{VI} both of the neuromuscular system parameters $\{\omega_n, \xi\}$ were identified. For model G_{VII} only the NMS natural frequency $\{\omega_n\}$ was identified, while the NMS system damping was assumed to be $\xi = 0.45$, based on that of Pick [36] as discussed in chapter 1. For model G_{VIII} only the NMS damping $\{\xi\}$ was identified and NMS natural frequency was set to $\omega_n = 1\,\mathrm{Hz}$, again based on that of Pick [36].

3.3 Comparison of preview and state gains

The preview and state gains of models G_I to G_{VIII} were evaluated to enable comparison between them. The cost function weights used for the study are $\{q_y, q_\theta\} = \{0.05, 5\}$ for all models.

The NMS natural frequency ω_n was 1 Hz for models G_V to G_{VIII}, consistent with the 0.9 Hz to 3.7 Hz range found by Pick [36]. The NMS damping for model G_V was set to $\xi = 0.707$ to provide a NMS with attenuation, but no resonance. The NMS damping for models G_{VI} to G_{VIII} was set to $\xi = 0.45$ which is consistent with Pick's value for relaxed limbs [36] and parameter values identified for this model in chapter 5. For model G_{IV}, $N_d = 4$ was used corresponding to 0.2 seconds of delay, consistent with values used by previous researchers [36, 39, 41] as discussed in section 3.1.2.

Vehicle parameters were the same as those used for simulator testing in chapter 5 and are listed in appendix A. Preview time (T_p) was 4 s, with 0.05 s timestep (T), giving 80 preview points. Controllers were evaluated at both low speed (20 m/s) and high speed (50 m/s) and are shown in sections 3.3.1 and 3.3.2 respectively.

3.3.1 Low speed controllers (20 m/s)

Preview and state gains for models G_I to G_{VIII} were evaluated first at 20m/s, the lowest speed used in testing in chapter 5. Preview gains against preview time for models G_I to G_{III} are shown in Figure 3.15.
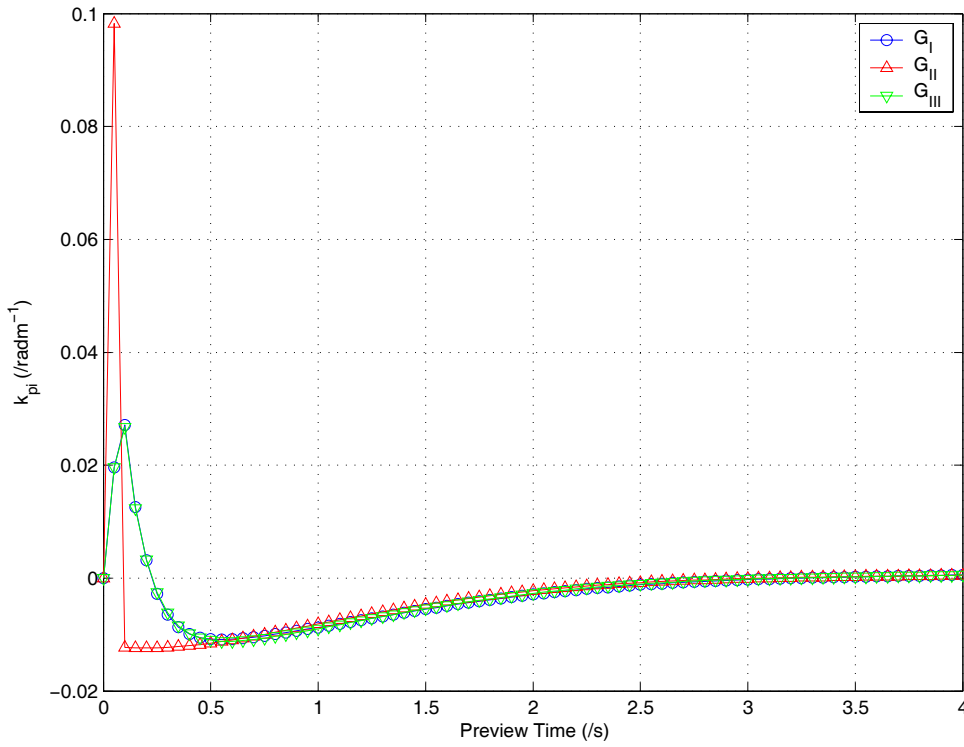
Figure 3.15: Preview gains for models $\mathbf{G_I}$ to $\mathbf{G_{III}}$ at 20 m/s with $\left\{\mathbf{q_y}, \mathbf{q_\theta}\right\} = \left\{\mathbf{0.05, 5}\right\}$

Model G_I shows that preview points further ahead of the vehicle have less significance to the driver. Preview points closer to the vehicle have positive gain (steering the 'wrong' way i.e. away from the direction of the curve), while points further ahead have a negative gain (steering the 'correct' way i.e. towards the direction of the curve).

This particular set of $\left\{q_y, q_\theta\right\}$ weights gives a controller with preview gains somewhere between what Sharp refers to as 'heading error weighted' and 'steer angle weighted' cases. The controller tends to steer the correct way first (towards the curve) as in the 'steer angle weighted' case, to cut corners and reduce steer angle effort. However, it also steers the 'wrong' way (away from the curve) close to the driver as is the case with 'heading error weighted' controller.

The preview gains for model G_{II} have similar shape to those for G_I except for the 0.5 seconds nearest the vehicle. Very close to the vehicle, the preview points are much

less 'smoothed' than model G_I, with the 'wrong way' steering restricted to a single preview point with large positive gain. This is consistent with Sharp's assertion [43] that preview gains reflect an inverse of the vehicle dynamics; as model G_{II}, with no yaw inertia, will tend to have much higher frequency inverse dynamics.

Model G_{III} has such similar preview gains to G_I as to be indistinguishable in Figure 3.15. At 20m/s vehicle sideslip will be small, so its omission from G_{III} makes little difference to the controller.

Figure 3.16 shows preview gains of models G_{IV} and G_{VII} compared to model G_I. Model G_V is not included as its controller is identical to that of model G_I. Models G_{VI} and G_{VIII} are not included as they are identical to G_{VII}.
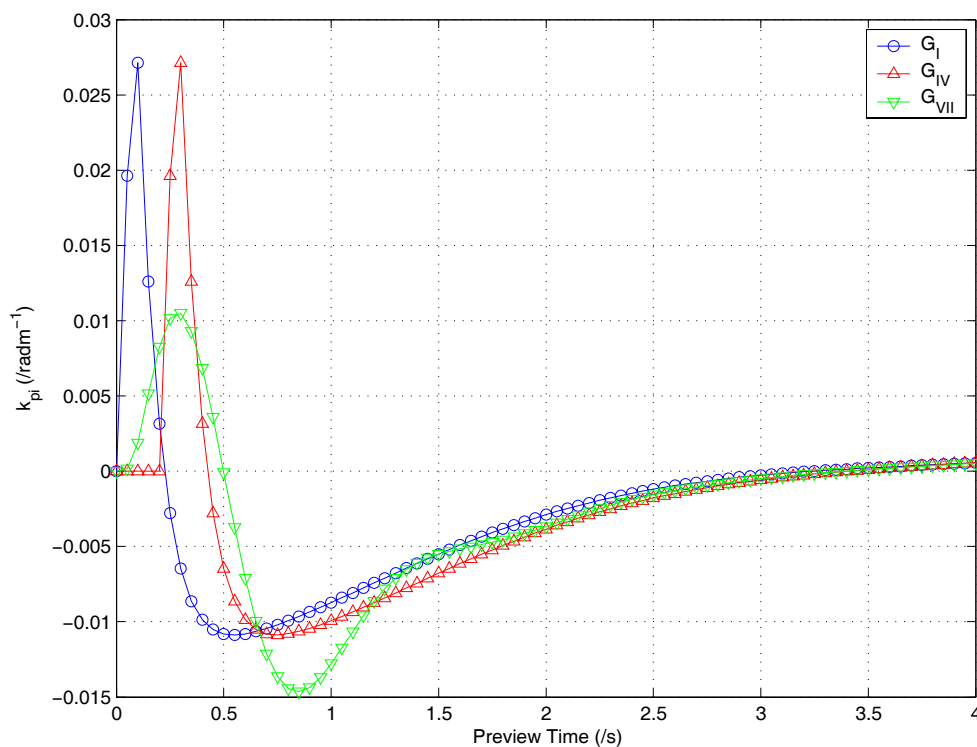
Figure 3.16: Preview gains for models $\mathbf{G_I}, \mathbf{G_{IV}}$ and $\mathbf{G_{VII}}$ at 20m/s with $\left\{\mathbf{q_y}, \mathbf{q_\theta}\right\} = \left\{\mathbf{0.05, 5}\right\}$ and $\mathbf{N_d = 4}$ for model $\mathbf{G_{IV}}$

Model G_{IV} has identical gains to model G_I, but shifted forward by N_d timesteps to compensate for the delay in the driver, as previously observed by Pick [36]. It seems intuitively correct that the driver should compensate for delay by looking further ahead of the vehicle.

Model G_{VII} has broadly similar preview gains to G_I, but the presence of a neuromuscular system filter causes the preview gains to be 'smoothed', appearing more sinusoidal than those of G_I. These gains represent the inversion of the slightly oscillatory NMS. Sharp [56] suggested that a sinusoidal variation of preview gains may provide a form of feed-forward damping to compensate for the low damping in the NMS. Also, the gains are shifted further ahead of driver, which will compensate for the phase-delaying effect of the neuromuscular system.

In all cases, preview gain drops to zero well within the preview length, so assumption of rotation into the driver reference frame (equation (3.16)) is valid.

Figure 3.17 shows the state gains k_v and k_ω for all of the models. G_V has the same state gains as G_I. Also shown are the k_δ and $k_{\dot\delta}$ gains for model G_{VII} and the delay state gains $k_{\delta(N_d-i)}$ for model G_{IV}. Model G_{II} has no state gains and model G_{III} has only k_ω.
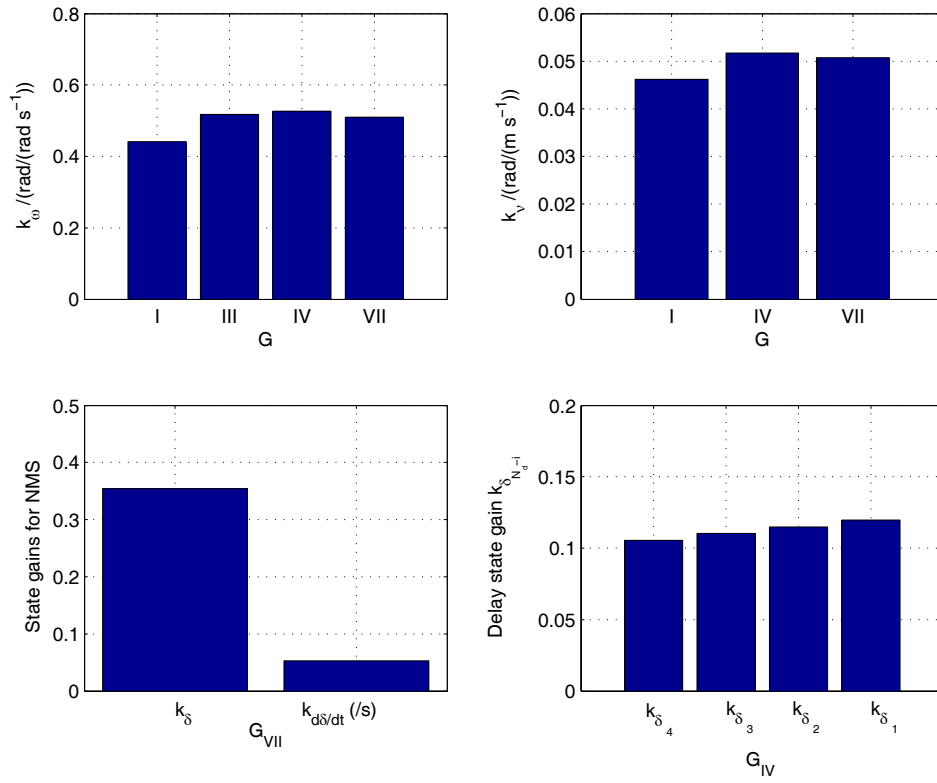
Figure 3.17: State gains for models G_I to G_{VII} at 20 m/s, with $\{q_y, q_\theta\} = \{0.05, 5\}$ and $N_d = 4$ for model G_{IV}

State gains for k_v and k_ω are broadly similar for all models, with some up to 20% higher than model G_I. Pick [36] noted that the LQR state gains are analogous to the compensatory controller gains of Weir and McRuer [40]. The similarity in state gains for all models therefore implies that the compensatory controller gains are similar for all of the driver models at 20 m/s.

Models G_{IV} and G_{VII} have increased delay. In these models k_ω and k_v are greater than model G_I and may help to increase damping of the vehicle motion in the presence of the destabilising delay.

The steer angle delay state gains of model G_{IV} are all of similar magnitude and increase as the steer angle progresses down the shift register (at the end of which, it is applied to the vehicle). Pick [36] suggested viewing this as a discrete filter on steer angle.

3.3.2 High speed controllers (50 m/s)

Controllers G_I to G_{VII} were then re-evaluated at 50 m/s (112 mph). The preview gains of models G_I to G_{III} are shown in Figure 3.18 and models G_I, G_{IV} and G_{VII} in Figure 3.19.
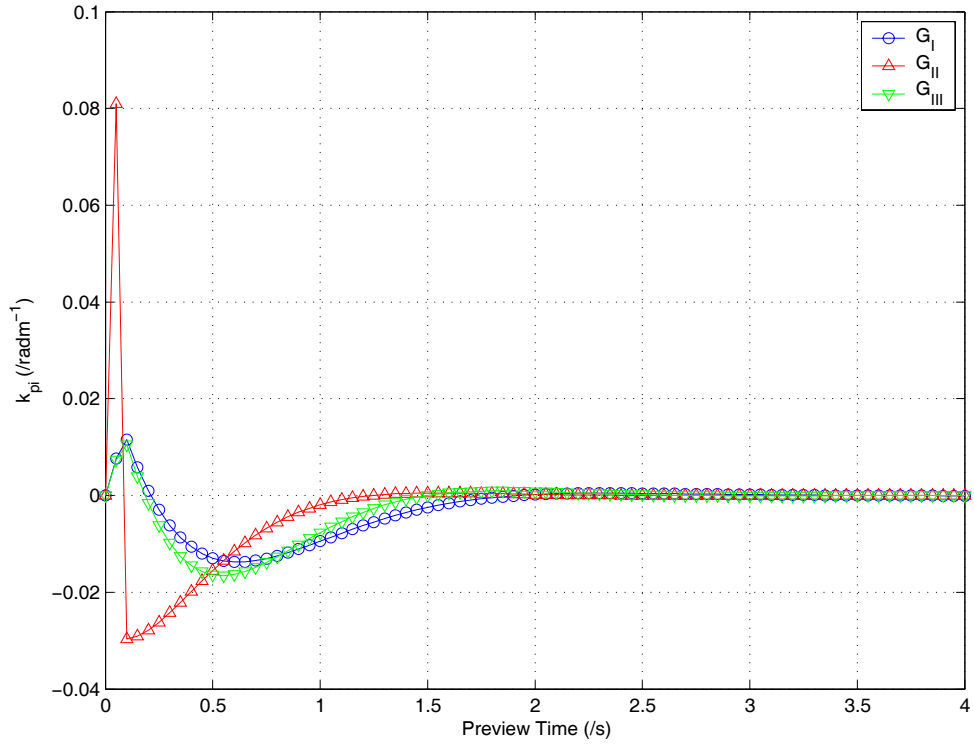
Figure 3.18: Preview gains for models $\mathbf{G_I}$ to $\mathbf{G_{III}}$ at 50 m/s with $\left\{ \mathbf{q_y}, \mathbf{q_\theta} \right\} = \left\{ \mathbf{0.05, 5} \right\}$
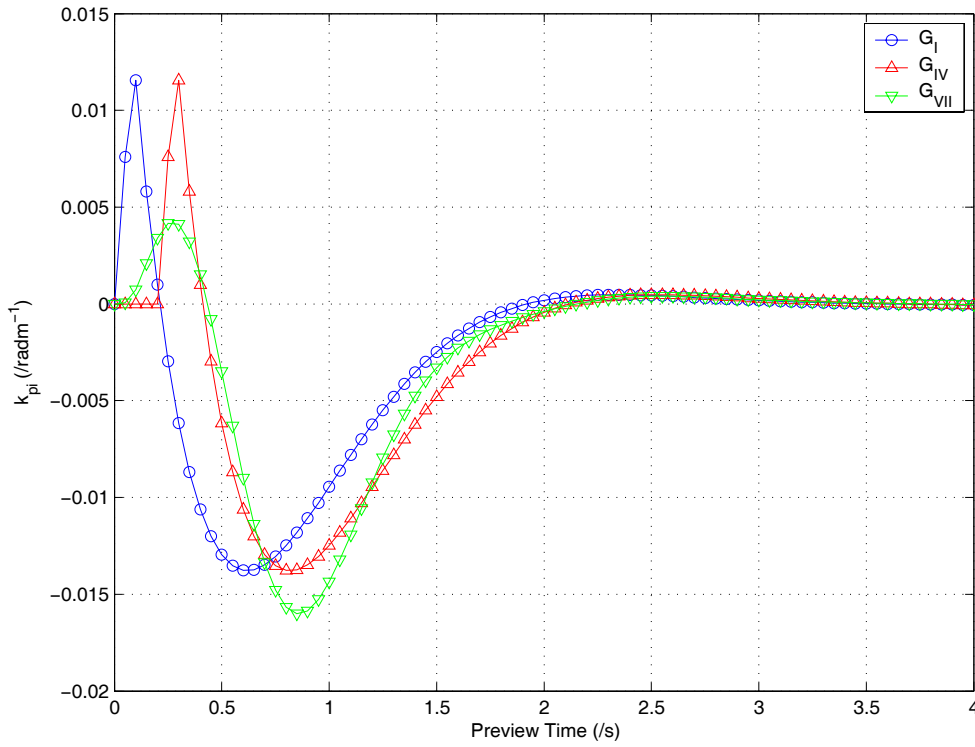
Figure 3.19: Preview gains for models G_I, G_{IV} and G_{VII} at 50 m/s with $\{q_y, q_\theta\} = \{0.05, 5\}$ and $N_d = 4$ for model G_{IV}

For all controllers preview gains as a function of time are of broadly similar shape to those at 20m/s, but have shifted toward more negative gains such that the driver steers more in the 'correct' direction i.e. toward a previewed curve. The fact that this has happened to all models including G_{II} suggests that it is an effect of speed on the 'track dynamics' (those remaining in model G_{II}, equation (3.20)), rather than on the vehicle dynamics.

For all models except G_{II} the preview gains fall to zero a shorter time ahead of the vehicle at 50 m/s than at 20 m/s. This can be viewed as a reduction in preview time from approximately 2.5 seconds at 20 m/s to approximately 2 seconds at 50 m/s. Preview distance therefore increased from 50m to 100m. The preview length of model G_{II} has remained nearly constant for both speeds, so this preview lengthening is likely to be a vehicle dynamics effect, rather than a 'track dynamics' effect, because G_{II} assumes a vehicle with no lateral or yaw dynamics. The fact that G_{III} displays

increased preview length suggests that the increase may be due to a change in vehicle yaw dynamics with speed.

At 20m/s the preview gains for model G_{III} were nearly the same as G_I, but this is not the case at 50m/s. This suggests that sideslip v is more significant at the higher speed.
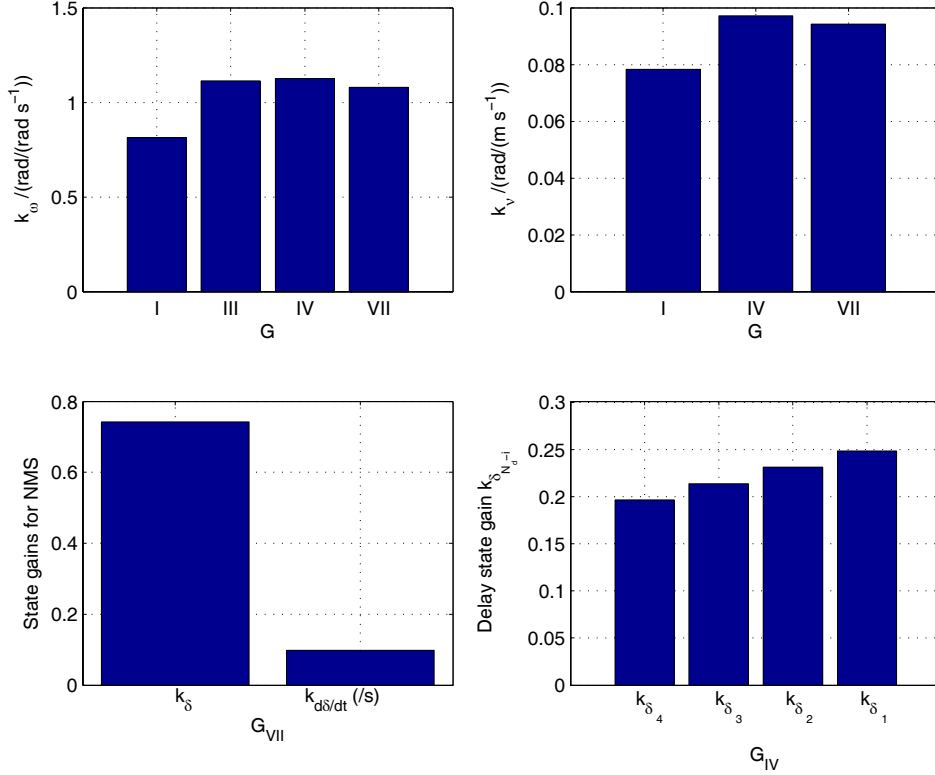
Figure 3.20: State gains for models G_I to G_{VII} at 50 m/s, with $\{q_y, q_\theta\} = \{0.05, 5\}$ and $N_d = 4$ for model G_{IV}

Figure 3.20 shows state gains for all models at 50m/s. For all models k_v and k_ω are related to each other in a similar way to the 20m/s gains, but are all approximately twice the magnitude. Gains for states k_δ and $k_{\dot{\delta}}$ for G_{VII} also double, as do the delay state gains for G_{IV}.

98

3.4   Comparison of closed loop driving

Models G_I to G_{VII} are to be used to model drivers' control of vehicles in closed loop. A comparison of the closed loop control of each of the models G_I to G_{VII} is therefore made in this section. All models G_I to G_{VII} were used to control the same plant: the 2 DOF vehicle model in equations (3.2) to (3.5). All models were compared with G_I, which was used as the baseline case, since this has the LQR controller model equal to the vehicle being controlled.

The road profile followed by each controller was the same, to allow direct comparison. The profile was randomly generated, but band-limited by filtering. Details of how this profile was generated are given in chapter 4. Each model G_I to G_{VII} was 'driven' at both 20 m/s and 50 m/s.

Each model was run with and then without a delay (τ) of 0.2 seconds incorporated into the closed loop. This was to test how realistically each driver model could cope with the unavoidable delays present in the driver. A delay of 0.2 seconds is consistent with that used by other researchers [36, 39, 41] as discussed in section 3.1.2.

Section 3.4.1 describes the simulation method for closed loop modelling, then each model's performance is described in sections 3.4.3 to 3.4.7.

3.4.1   Simulation method

Closed loop vehicle simulation was carried out in MATLAB using a discrete time model. Time steps were $T = 0.05$ seconds, fast enough to represent the vehicle dynamics, but without creating too many preview points. Creating too many preview points tends to slow down the calculation of the LQR controller in MATLAB to a prohibitive degree. Closed loop simulation involves four parts as shown in Figure

3.21, namely the driver model, vehicle model, trajectory algorithm and preview offset algorithm.

Figure 3.21 shows the driver model G outputting steer angle δ to the vehicle model $F(q)$, from which vehicle states (v, ω, θ) are fed back to the driver and to the trajectory calculation algorithm. The Trajectory algorithm calculates current vehicle position (x_v, y_v) from vehicle states (v, ω, θ). The vehicle position (x_v, y_v) and the track input $(\mathbf{x_t}, \mathbf{y_t})$ are then used by the Preview algorithm to calculate the preview offsets $y_{p(1:n)}$ which in turn are used by the driver model G to calculate steer angle δ.
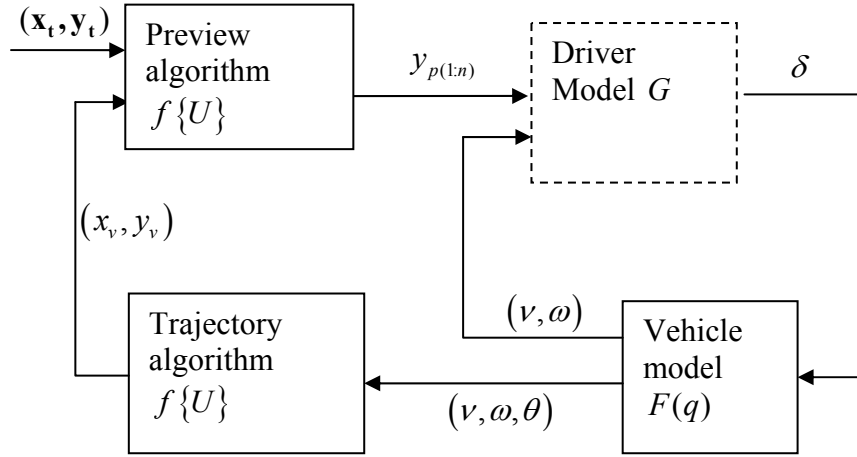
Figure 3.21: Generalised model of closed loop simulation, showing appropriate feedback for model G_I

The driver model G was described in the previous sections and once its preview and state gains are determined, involves only the evaluation of equation (3.16) each time step. The preview offset algorithm is described in sections 3.4.2. Each driver model G_I to G_{VII} has different states fed back so a diagram of the closed loop system for each of G_I to G_{VII} is included in sections 3.4.3 to 3.4.7.

The vehicle model used for simulation is the bicycle model shown in equations (3.2) to (3.5) and Figure 2.3. The state space vehicle model was discretised using MATLAB's C2D function with a time step of $T = 0.05\,\text{s}$.

The vehicle trajectory algorithm shown in Figure 3.21 is defined in equation (3.27). Vehicle trajectory is calculated in global co-ordinates (x_v, y_v) as shown in Figure 3.22.

$$\dot{x}_v(t) = U \cos \theta(t) - v \sin \theta(t)$$
$$\dot{y}_v(t) = U \sin \theta(t) + v \cos \theta(t)$$
(3.27)

Numerical integration is then used to establish vehicle position (x_v, y_v).

In reality there would be noise present within the control loop when a driver controls a real vehicle, but for ease of comparison this is omitted from simulations in this chapter. Driver noise and its consequences are discussed in chapter 4. Weights on lateral and heading errors were set to $\{q_y, q_\theta\} = \{0.05, 5\}$ as in the previous section.

3.4.2 Preview offset algorithm

The preview offset algorithm is designed to operate under the same small angle approximation inherent in the linearised discrete track equation (3.6). However, some curves will exceed these small angles and the algorithm must be robust to this. The preview offset algorithm also deals with the problem of interpolating road path data points of arbitrary spacing. The algorithm used is as follows:

1. Cartesian representation of the track $(\mathbf{x_t}, \mathbf{y_t})$ in the global reference frame is rotated into the vehicle reference frame as shown in Figure 3.22 using equation (3.28).

$$\tilde{\mathbf{x}}_t(t) = (\mathbf{x_t} - x_v(t)) \cos \theta(t) + (\mathbf{y_t} - y_v(t)) \sin \theta(t)$$
$$\tilde{\mathbf{y}}_t(t) = -(\mathbf{x_t} - y_v(t)) \sin \theta(t) + (\mathbf{y_t} - y_v(t)) \cos \theta(t)$$
(3.28)

Where $(\mathbf{x_t}, \mathbf{y_t})$ represents two column vectors of track position points (x_{ti}, y_{ti}) in the global reference frame. Also $(x_v(t), y_v(t))$ represents the current vehicle position in global co-ordinates and $\theta(t)$ represents the vehicle's current yaw angle.
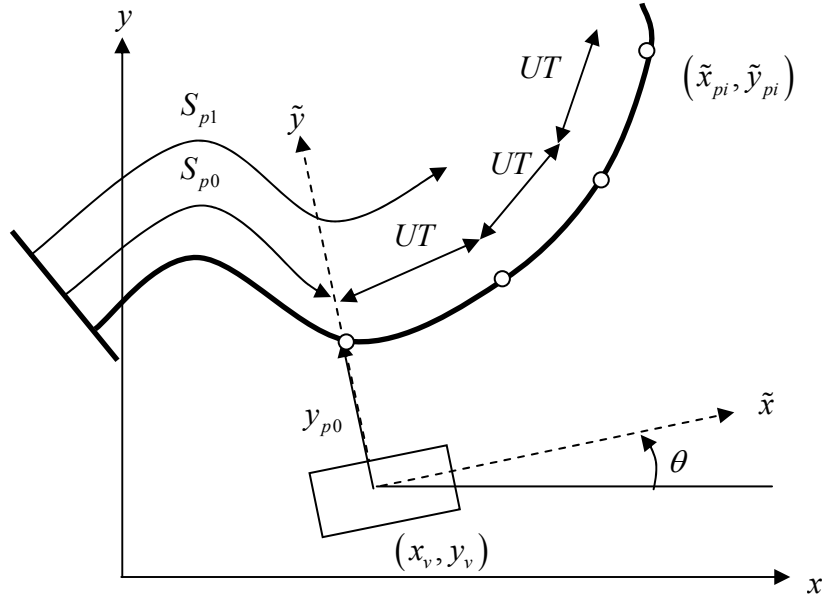
Figure 3.22: Global and vehicle reference frames for expressing track location. Preview points equally spaced along track are illustrated

2. The point on the road path perpendicular to the vehicle is established (the point at $\tilde{x} = 0$ in the vehicle ref. frame). Interpolation was used as there will not be a point exactly at $\tilde{x} = 0$ (brackets $\{\ \}$ denote interpolation).

$$\tilde{y}_{p0} = \tilde{y}_t \{\tilde{x}_t = 0\}$$
$$S_{p0} = S_t \{\tilde{x}_t = 0\}$$

(3.29)

An array of points is generated equally spaced along the track, starting at S_{p0} (the point perpendicular to vehicle). $T = 0.05\,\text{s}$ is the time step used to discretise the LQR controller.

$$S_{pi} = S_{p0} + UTi$$

(3.30)

3. Cartesian positions $\left(\tilde{x}_{pi}, \tilde{y}_{pi}\right)$ of the array of points defined by equation (3.30) are interpolated at these locations along the track (S_t is same for both reference frames):

$$\tilde{x}_{pi} = \tilde{x}_t \{S_t = S_{pi}\}$$
$$\tilde{y}_{pi} = \tilde{y}_t \{S_t = S_{pi}\}$$

(3.31)

102

This gives rise to a two column vector of Cartesian positions $\left(\tilde{\mathbf{x}}_{\mathbf{pi}}, \tilde{\mathbf{y}}_{\mathbf{pi}} \right)$ of the previewed points on the path which are equally spaced along the path a distance UT apart as shown in Figure 3.22. These previewed points can be joined with straight sections of track as shown in Figure 3.23.

4. Angles between the straight sections of track shown in Figure 3.23 are determined from the list of Cartesian positions $\left(\tilde{\mathbf{x}}_{\mathbf{pi}}, \tilde{\mathbf{y}}_{\mathbf{pi}} \right)$ (in vehicle reference frame) as shown in Figure 3.23 and equation (3.32).

$$\psi_{pi} = \arctan\left(\frac{\tilde{y}_i - \tilde{y}_{i-1}}{\tilde{x}_i - \tilde{x}_{i-1}} \right) \tag{3.32}$$
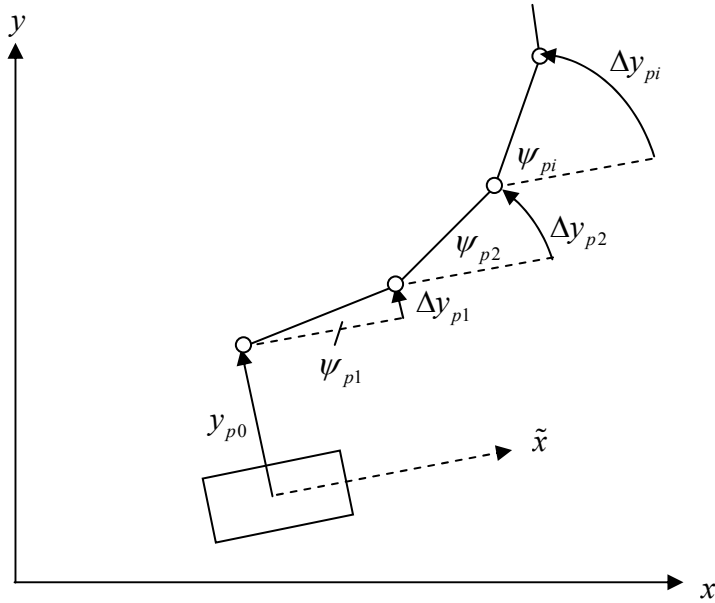
Figure 3.23: Small angle approximation method for preview offset determination, applied to case with large angles

5. Preview offsets y_{pn} are then determined from the angles between these discrete sections using a small angle approximation:

$$y_{pn} = y_{p0} + \sum_{i=1}^{n} \Delta y_{pi} = y_{p0} + \sum_{i=1}^{n} UT\psi_{pi} \tag{3.33}$$

103

This procedure is repeated every time step to establish new preview offsets. Equation (3.33) is based on the same small angle assumption as the track model (equation (3.6)) so is consistent with way the LQR controller model is formulated. The algorithm above avoids the problem which can arise if preview points are spaced equally along the preview optical lever, instead of along the track. If preview points are spaced evenly along the preview lever, then infinite preview offsets can arise, for example when previewing a 90° bend as shown in Figure 3.24.
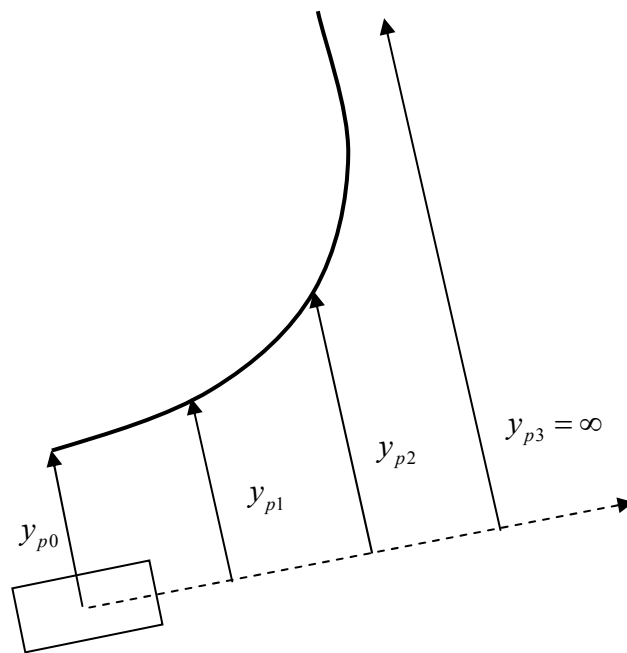
Figure 3.24: Problem of infinite preview offset when preview points are evenly spaced along the preview lever

3.4.3 Model G_{II}

Model G_{II} was simulated in closed loop with the 2DOF bicycle model. The system is shown in Figure 3.25. Note that a delay block was added to driver model of Figure 3.8 which shifts the steer angle by a whole number of time steps to represent the driver's internal delay τ.
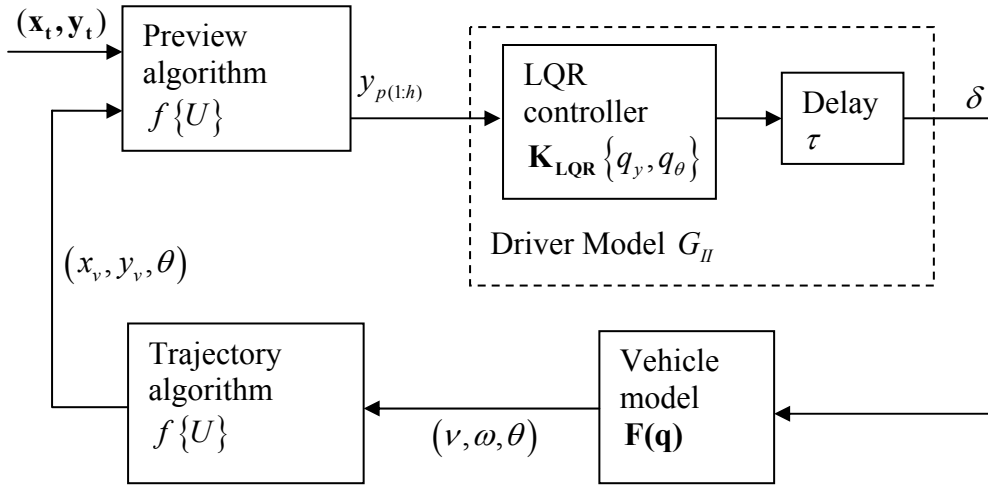
Figure 3.25: Closed loop driving of model $\mathbf{G}_{II}$ with possibility of delay

Poor control was expected for G_{II} for two reasons. Firstly only preview information is fed back to the driver model G_{II}, (no vehicle states) so all of the feedback information to the driver must pass through the integration within the trajectory algorithm. In the trajectory algorithm sideslip velocity v and yaw rate ω are integrated to give position (x_v, y_v) and yaw angle θ. This feedback path will therefore have more phase lag than direct feedback of sideslip velocity and yaw rate. Secondly the LQR controller for model G_{II} is derived from a simplification of the vehicle so will not be optimal for the vehicle $F(q)$.

The steer angle of driver model G_{II} operating in closed loop with the vehicle was compared with that of model G_I. Model G_I was shown in closed loop with the vehicle in Figure 3.21. Model G_I also includes a delay τ in series with the LQR controller shown in Figure 3.4.

Figure 3.26 shows a comparison of steer angle vs. distance of model G_I and G_{II} on the same track. The model was operated in four configurations; two speeds, $U = 20\,\text{m/s}$ and $U = 50\,\text{m/s}$; and two delay settings, $\tau = 0$ and $\tau = 0.2$ seconds (4 time steps). For all models in this section, the left hand plots show the case with zero delay ($\tau = 0$) and the right hand plots with delay $\tau = 0.2\,\text{s}$. The upper plots show 20m/s and

the lower plots 50m/s. The controllers G_I and G_{II} for these two speeds were shown in section 3.3.
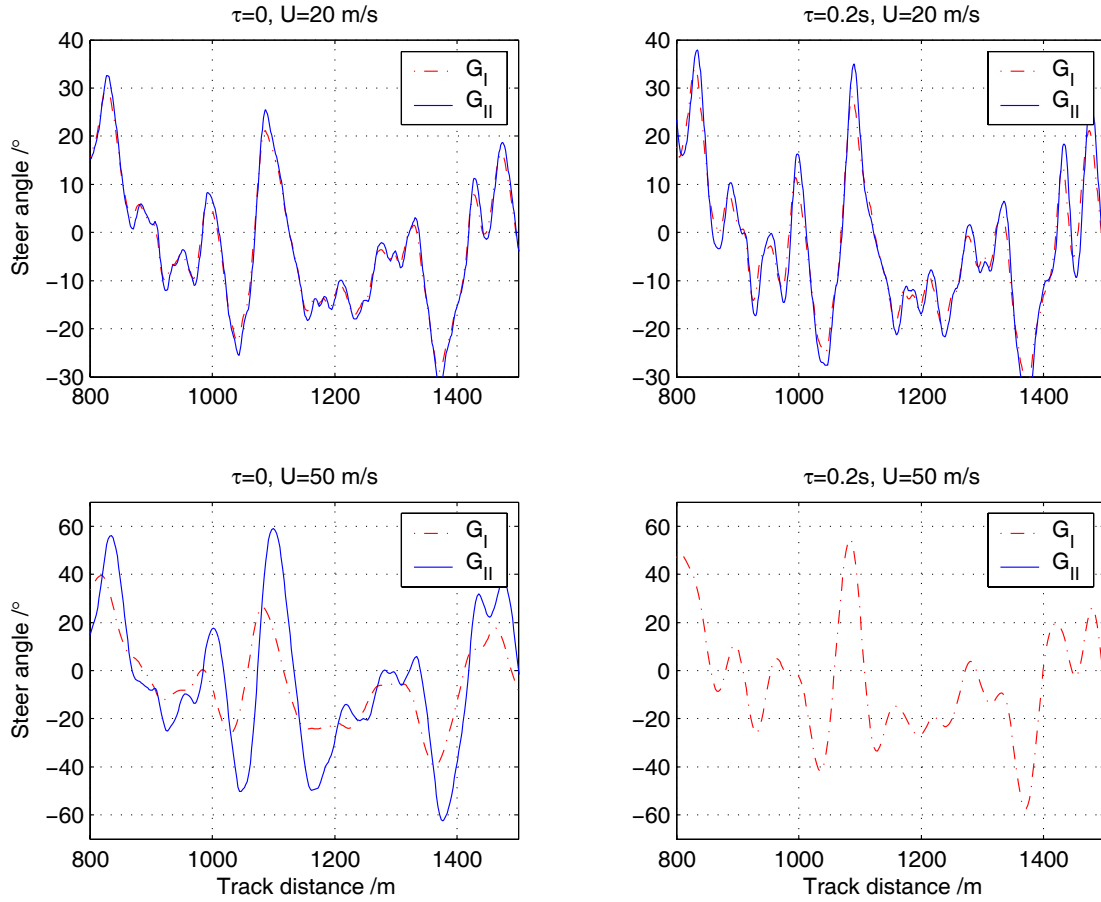
Figure 3.26: Steer angle vs. time for model $\mathbf{G_{II}}$ and model $\mathbf{G_I}$ on same random track $\left(\mathbf{x_t,y_t}\right)$. Left hand plots show $\boldsymbol{\tau = 0}$, right hand plots $\boldsymbol{\tau = 0.2}$. Upper plots U=20m/s, lower plots U=50m/s

At low speed ($U = 20\,\text{m/s}$), both controllers G_{II} and G_I give similar steer angles. With no delay ($\tau = 0$), model G_{II} has slightly more overshoot than G_I, which would lead to slightly poorer control of the vehicle. With $\tau = 0.2\,\text{s}$ at $U = 20\,\text{m/s}$ both controllers generate more steer angle for a given point in the track. Also G_{II} and G_I both show more overshoot in their steer angle output with delay present. Model G_{II} gives slightly more overshoot than model G_I, perhaps because it has no state gains to provide yaw rate feedback.

At high speed ($U = 50$ m/s), the closed loop responses for G_{II} and G_I are quite different from their counterparts at low speed. Firstly comparing model G_I to its performance at low speed, the steer angle δ resembles a low-pass filtered version of the steer angle at low speed, with fewer short wavelength steer angle inputs. This is a result of the longer preview length at $U = 50$ m/s as discussed in section 3.3.2.

With no delay ($\tau = 0$) and at high speed ($U = 50$ m/s), the steer angle for model G_{II} is quite different to that of G_I. The steer angles for G_{II} appear to be delayed from those of G_I. This is a result of the shorter length of preview for model G_{II} (Figure 3.18) leading to later steering for a given feature in the track. This in turn gives poorer closed loop control of the system, leading to much larger steer angles for G_{II} than for G_I.

With delay $\tau = 0.2$ s, model G_{II} is unstable in closed loop control. Although instability in a steering controller is undesirable, the modelled behaviour could conceivably be consistent with that of a poor human driver.

3.4.4   Model $\mathbf{G_{III}}$

Model G_{III} is the next most sophisticated driver model and performance should be better than G_{II} because yaw rate feedback is included. As discussed in section 3.3.1 model G_{III} has a very similar controller to G_I at low speed. Similar results would therefore be expected at $U = 20$ m/s, but not necessarily at $U = 50$ m/s. Figure 3.27 shows a diagram of closed loop control with model G_{III}.
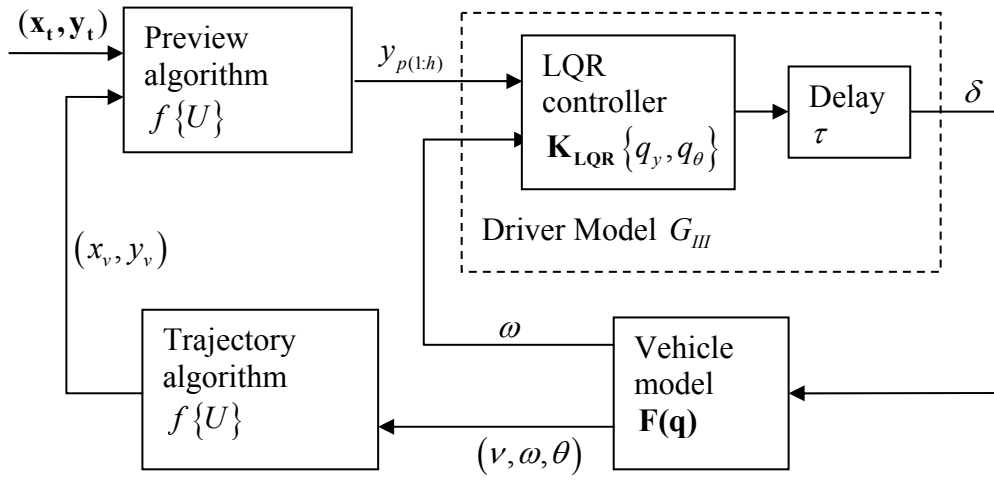
Figure 3.27: Model G_{III} operating in closed loop, including delay

Figure 3.28 shows steer angle vs. distance for models G_{III} and G_I, with $\tau = 0$ and $\tau = 0.2\,\text{s}$. The upper two plots are at 20 m/s, the lower at 50 m/s.
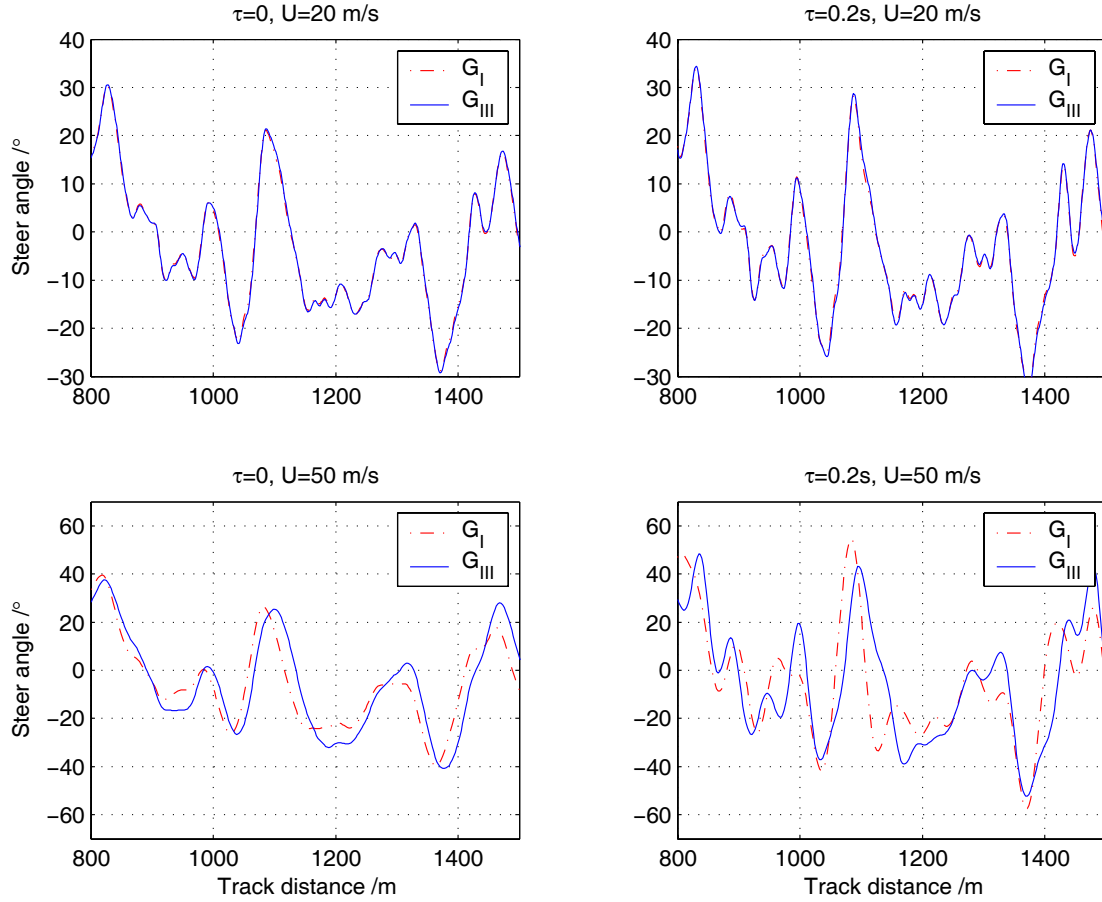
Figure 3.28: Steer angle vs. time for model $\mathbf{G_{II}}$ and model $\mathbf{G_{I}}$ on same random track $(\mathbf{x_t}, \mathbf{y_t})$. Left hand plots show $\tau = 0$, right hand plots $\tau = 0.2$. Upper plots U=20m/s, lower plots U=50m/s

At low speed the controllers G_{III} and G_I show almost identical performance with and without delay, as predicted. The high speed cases again show an apparent delay in steering between G_{III} and G_I. The amount of delay is consistent with the slightly shorter preview time used by G_{III} than G_I.

The simplification of the controller G_{III} from that of G_I has only degraded its performance at high speed, where sideslip velocity (v) becomes important. Model G_{III} is able to keep control of the vehicle even with delay $\tau = 0.2$ s, assisted by yaw rate feedback (which was not present for G_{II}). Also, for G_{III} the vehicle model on

109

which the LQR controller is based is closer to that of the vehicle being controlled than was the case for G_{II} .

3.4.5 Model G_{IV}

Model G_{IV} in closed loop is shown in Figure 3.29. The coupled steering-vehicle system shown in the dotted box is modelled using the discretised equation (3.22). The states of (3.22) are then fed to the driver as states of vehicle (v, ω) and delay states $(\delta_{Nd-1}, \ldots, \delta)$.

As with models G_I to G_{III} , a delay τ is added, but this time to represent any delay which the driver has not taken account of within their LQR controller. This 'uncompensated' delay τ may arise, for example, if the driver cannot perceive the steer angle delay states $(\delta_{Nd-1}, \ldots, \delta)$ instantaneously. There are therefore two sources of delay within the closed loop: the N_d timesteps which are accounted for in the LQR controller, and the 'uncompensated' delay τ .
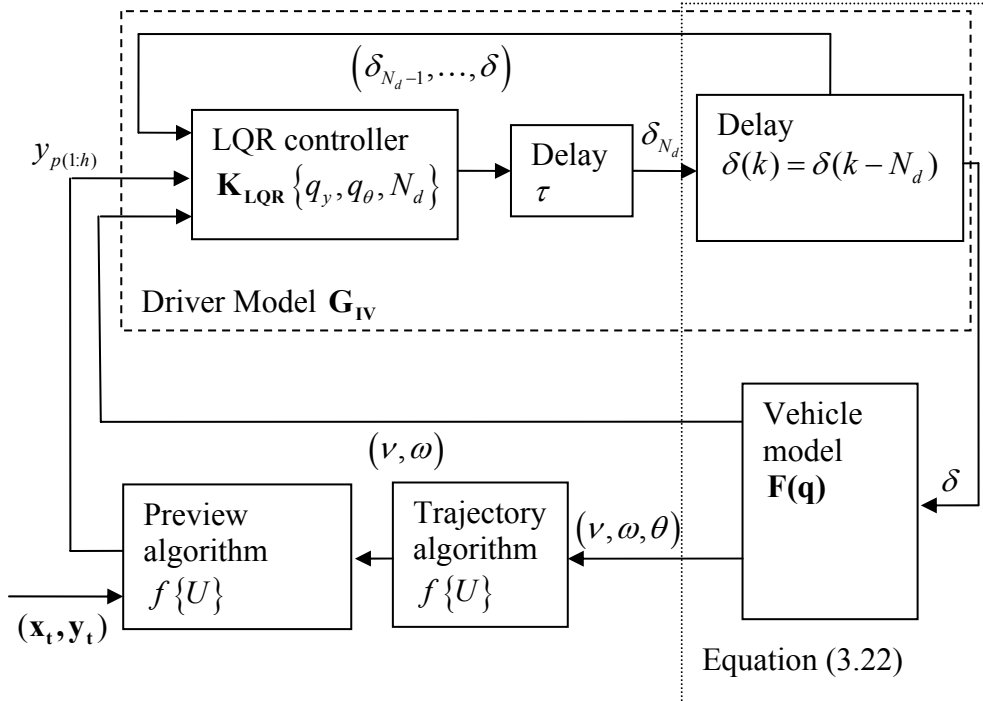
Figure 3.29: Model G_{IV} operating in closed loop, including uncompensated delay τ

Figure 3.30 shows the steer angles of model G_{IV} compared with those of G_I. Model G_{IV} is shown with $N_d = 4$ (corresponding to 0.2 seconds of delay) in all four plots. Note that model G_{IV} with $N_d = 0$ would be the same as model G_I, but this case is not shown here.
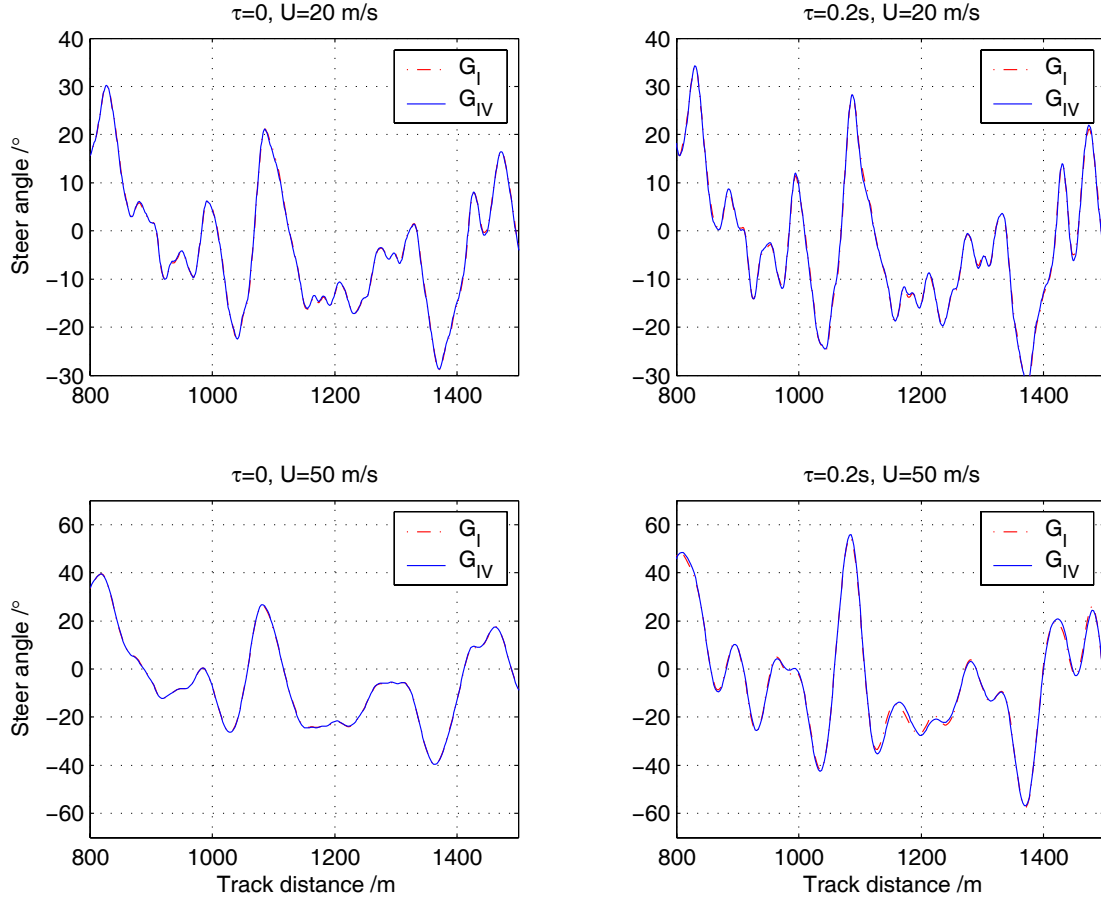
Figure 3.30: Steer angle vs. time for model $\mathbf{G_{IV}}$ and model $\mathbf{G_I}$ on the same random track $(\mathbf{x_t, y_t})$. Left hand plots show $\boldsymbol{\tau = 0}$ for both models with $\mathbf{N_d = 4}$. Right hand plots $\boldsymbol{\tau = 0.2}$ s for both models with $\mathbf{N_d = 4}$. Upper plots at $\mathbf{U = 20}$ m/s, lower plots at $\mathbf{U = 50}$ m/s

For all four plots of Figure 3.30 the steer angles of models G_I and G_{IV} are nearly identical, despite G_{IV} having an extra $N_d = 4$ steps of time delay within the closed loop. This means that the LQR controller has been able to nearly perfectly compensate for the delay N_d by shifting its preview points forward in time (Figure

3.19) and by including the steer angle delay states $\left(\delta_{Nd-1},\ldots,\delta\right)$. The similarity between G_I and G_{IV} is clear for both values of τ and for both speeds.

Slight differences are visible between the steer angles of G_I and G_{IV} for all four cases in Figure 3.30. This is because G_{IV} will have an extra N_d steps of time delay in its state feedback information $\left(v,\omega\right)$ compared with model G_I. This effect was anticipated by Pick [36] when deriving this controller. The extra delay in state feedback does not seem to significantly degrade the controller performance even at high speed.

3.4.6 Model G_V

In model G_V the driver does not take account of the NMS in their formulation of the LQR controller. As with model G_{II}, this case has significant mismatch between the LQR controller and the coupled NMS-vehicle system being controlled. Also the introduction of an NMS will increase phase lag in the closed loop and reduce bandwidth of control. For both of these reasons poor performance might be expected.
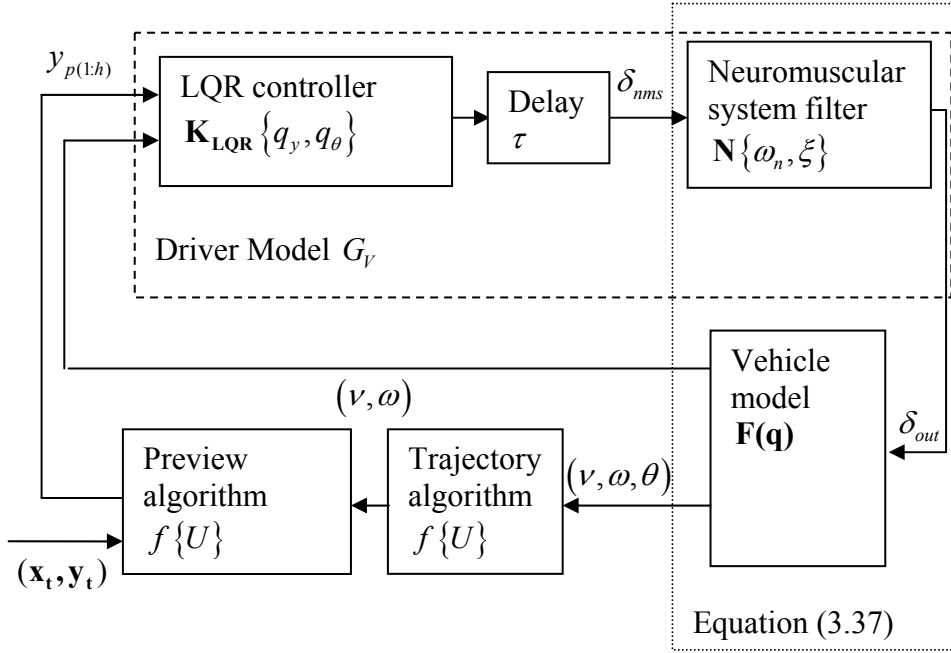
Figure 3.31: Model $\mathbf{G_V}$ operating in closed loop, including delay τ

Figure 3.31 shows closed loop operation of model G_V. States passed to the driver model are both of the vehicle states (v, ω) as for G_I, but none of the neuromuscular system states. When simulating the system in closed loop, the neuromuscular system filter $\mathbf{N}$ is coupled to the vehicle state space model in a similar way to equation (3.26) . The state space model of the filter $\mathbf{N}$ is given by equations (3.34) to (3.36).

$$\begin{bmatrix} \dot{\delta} \\ \ddot{\delta} \end{bmatrix} = \begin{bmatrix} 0 & 1 \\ -\omega_n^2 & -2\xi\omega_n \end{bmatrix} \begin{bmatrix} \delta \\ \dot{\delta} \end{bmatrix} + \begin{bmatrix} 0 \\ \omega_n^2 \end{bmatrix} \delta_{nms} \tag{3.34}$$

$$\delta_{out} = \begin{bmatrix} a_{lead} & b_{lead} \end{bmatrix} \begin{bmatrix} \delta \\ \dot{\delta} \end{bmatrix} + \begin{bmatrix} c_{lead} \end{bmatrix} \delta_{nms} \tag{3.35}$$

Where:

$$a_{lead} = 1 - \left(\frac{\omega_n}{\omega_{cut}} \right)^2$$

$$b_{lead} = \frac{2}{\omega_{cut}} \left(\xi_{cut} - \xi \frac{\omega_n}{\omega_{cut}} \right) \tag{3.36}$$

$$c_{lead} = \left(\frac{\omega_n}{\omega_{cut}} \right)^2$$

This state space model is then coupled with the vehicle state space model of equation (3.4) to give equation (3.37). A discretised version of the coupled vehicle-NMS system in equation (3.37) is used in the MATLAB simulation to model the part of the system shown in the dotted box of Figure 3.31. This method is also used for simulation of model G_{VII} in section 3.4.7.

$$
\begin{bmatrix} \dot{\delta} \\ \ddot{\delta} \\ \dot{v} \\ \dot{\omega} \\ \dot{y} \\ \dot{\theta} \end{bmatrix} = \begin{bmatrix} 0 & 1 & 0 & 0 & 0 & 0 \\ -\omega_n^2 & -2\xi\omega_n & 0 & 0 & 0 & 0 \\ a_{lead}B_1 & b_{lead}B_1 & A_{11} & A_{12} & 0 & 0 \\ a_{lead}B_2 & b_{lead}B_2 & A_{21} & A_{22} & 0 & 0 \\ 0 & 0 & 1 & 0 & 0 & U \\ 0 & 0 & 0 & 1 & 0 & 0 \end{bmatrix} \begin{bmatrix} \delta \\ \dot{\delta} \\ v \\ \omega \\ y \\ \theta \end{bmatrix} + \begin{bmatrix} 0 \\ \omega_n^2 \\ c_{lead}B_1 \\ c_{lead}B_2 \\ 0 \\ 0 \end{bmatrix} \delta_{nms} \qquad (3.37)
$$

The steer angle time history of model G_V is compared with that of model G_I in Figure 3.32.
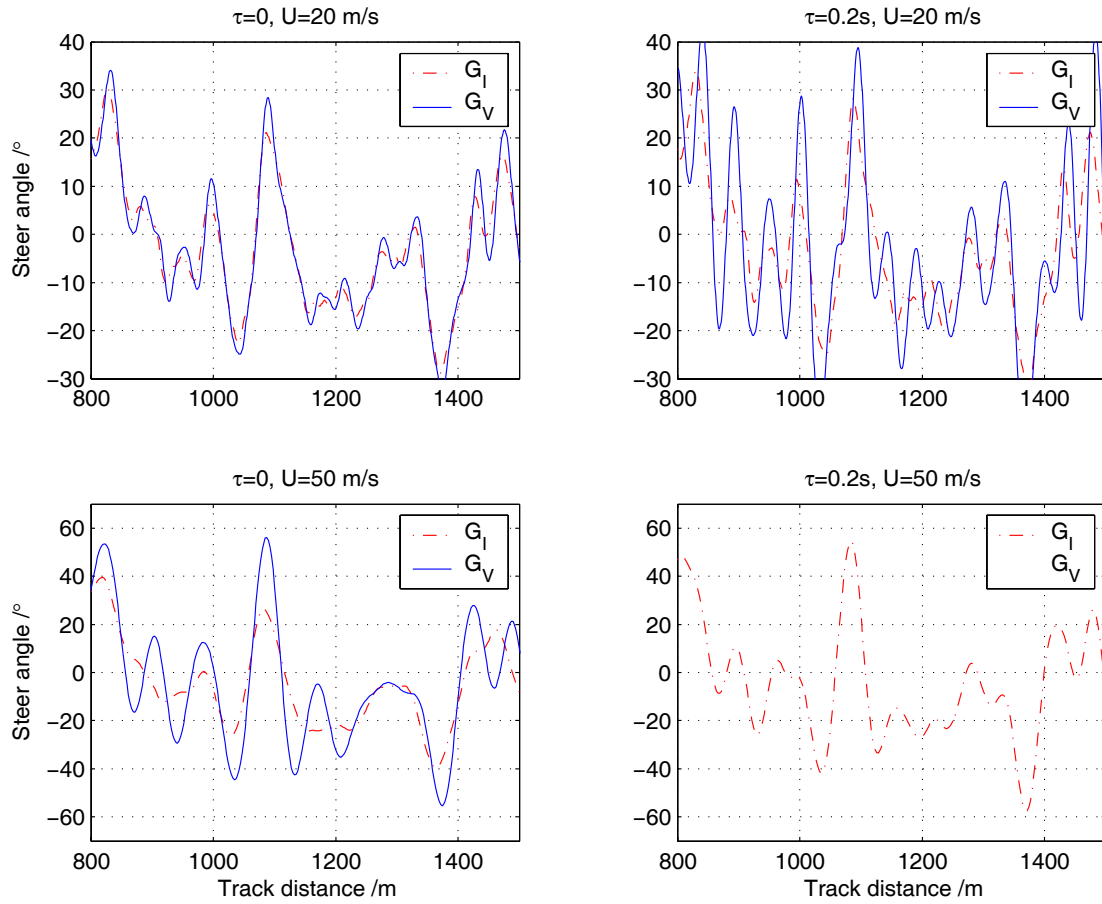
Figure 3.32: Steer angle vs. time for model $\mathbf{G_V}$ and model $\mathbf{G_I}$ on same random track $\left(\mathbf{x_t}, \mathbf{y_t}\right)$. Left hand plots show $\tau = 0$, right hand plots $\tau = 0.2$. Upper plots U=20m/s, lower plots U=50m/s

At low speed ($U = 20\,\text{m/s}$) with no delay ($\tau = 0$), steer angle only overshoots mildly from that of model G_I. However, when the delay $\tau = 0.2\,\text{s}$ is introduced, the steer angle of model G_V becomes very oscillatory compared to model G_I. This is due to the destabilising effect of the phase delay from the neuromuscular system, which is not present in G_I.

At high speed ($U = 50\,\text{m/s}$), oscillatory steering is evident even without delay in the loop ($\tau = 0$). When delay $\tau = 0.2\,\text{s}$ is introduced, the closed loop is unstable. From these results it seems unlikely that a driver could adequately control a car without

adjusting the cost function weights to improve high speed stability, or using a more sophisticated LQR controller such as model G_{VII}, as shown in the next section.

3.4.7 Models G_{VI} G_{VII} and G_{VIII}

Models G_{VI}, G_{VII} and G_{VIII} form the same closed loop system shown in Figure 3.33.
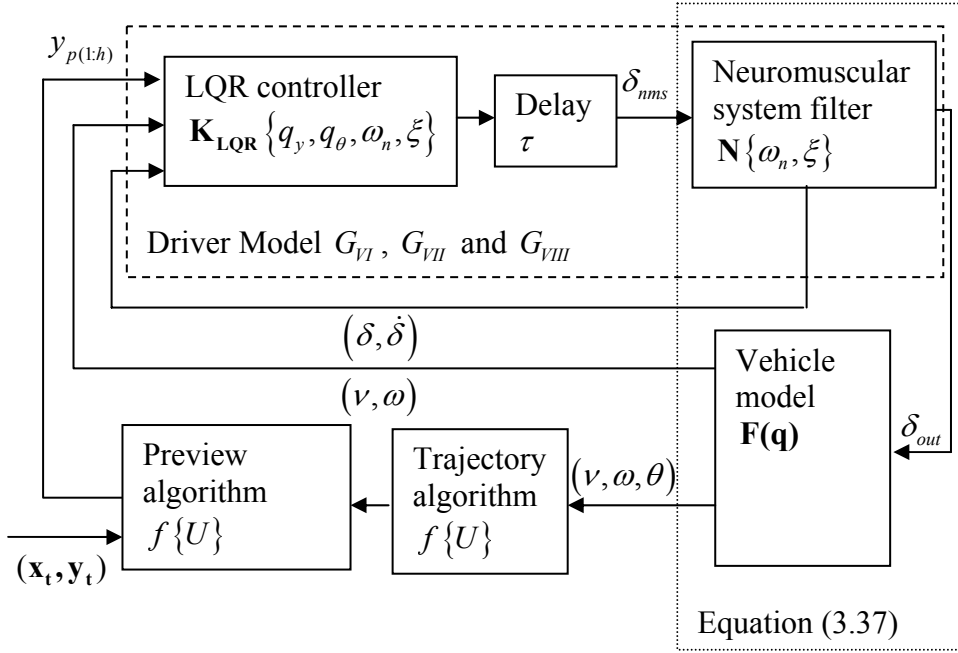
Figure 3.33: Models G_{VI} G_{VII} and G_{VIII} operating in closed loop, including delay τ

For models G_{VI}, G_{VII} and G_{VIII}, as well as vehicle states (v, ω), the NMS states δ and $\dot{\delta}$ are passed to the driver model. As for G_V, a discretised version of the state space model in equation (3.37) is used for MATLAB simulation of the coupled NMS-vehicle system shown in the dotted box. Figure 3.34 shows the steer angle performance of model G_{VII} and G_I.
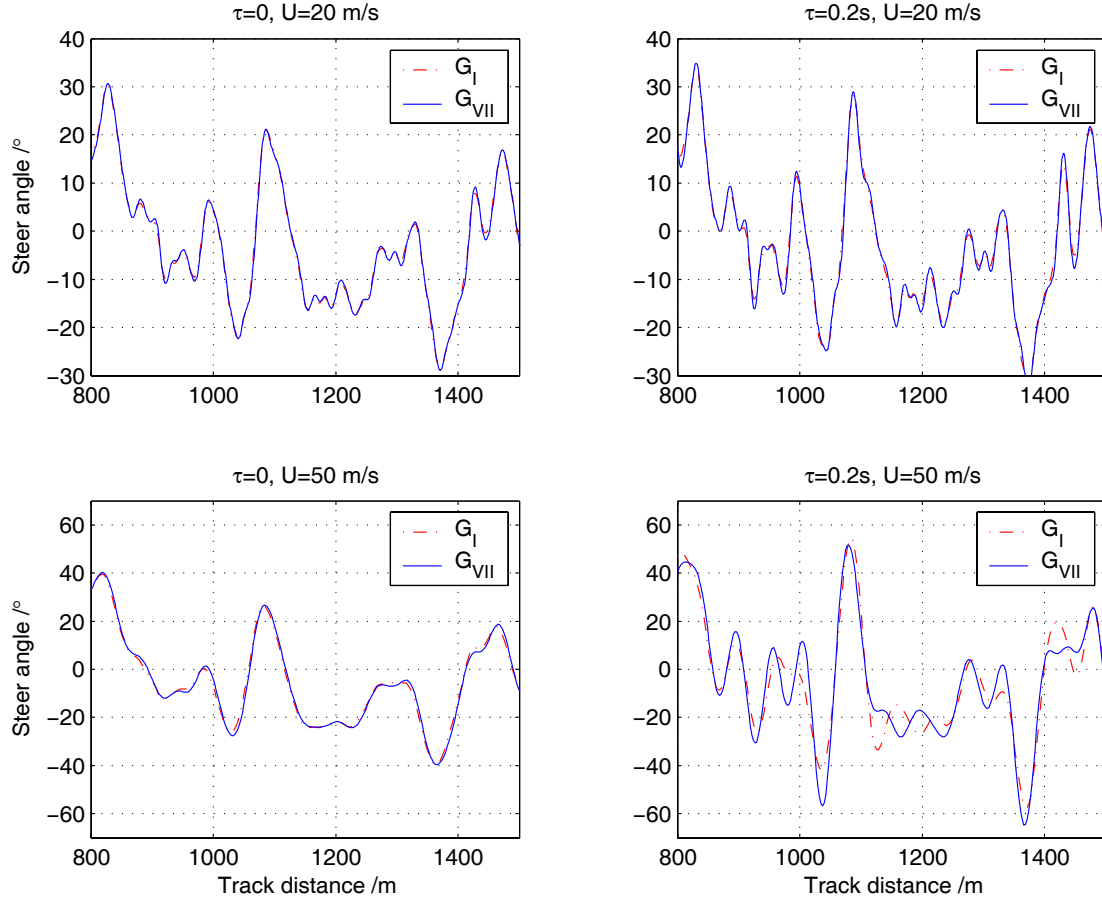
Figure 3.34: Steer angle vs. time for model G_{VII} and model G_I on same random track $\left(x_t, y_t\right)$. **Left hand plots show** $\tau = 0$, **right hand plots** $\tau = 0.2$. **Upper plots U=20m/s, lower plots U=50m/s**

Figure 3.34 shows that for both low speed ($U = 20\,\text{m/s}$) and high speed ($U = 50\,\text{m/s}$) without delay ($\tau = 0$), the steer angle of model G_{VII} is almost identical to model G_I. The inclusion of the NMS within the LQR controller has enabled the driver to nearly fully 'compensate' for the effect of the NMS that was evident in model G_V. This is achieved by the feedback of NMS states and the shifting forward of the preview gains. If delay $\tau = 0.2\,\text{s}$ is included at high speed ($U = 50\,\text{m/s}$), only a slight difference in steer angles between G_{VII} and G_I can be seen.

3.5 Conclusions

A requirement was identified in chapter 2 for a driver model which includes a steering strategy parameter, so models of the driver were developed based on Sharp's LQR controller structure. The models included cost function weights to allow the driver's strategy to be altered in favour of lateral error minimisation, heading error minimisation, or steer angle minimisation. In chapter 1 the need was identified for models to represent the novice driver, and to incorporate the effect of the NMS into the driver's internal model. A driver model with simplified vehicle dynamics has been developed to represent novice drivers, and a range of models including the driver's neuromuscular system have also been developed. The preview and state gains of the controllers developed in this chapter have been compared as well as their steer angles in closed loop driving. The important features of each model were:

Model G_I used an LQR controller based on Sharp's 2DOF bicycle model. The closed loop steer angles for model G_I during high speed driving resembled a low pass filtered version of its steer angles at low speed. This is because the preview length of the high speed controller was double that of the low speed controller. Adding a delay $\tau = 0.2\,\text{s}$ within the closed loop increased the steer angle used.

Model G_{II} used an LQR controller based on a point mass model to represent a novice driver. Model G_{II} had abrupt changes in its preview gains with preview time because the vehicle model had no yaw dynamics. Model G_{II} gave closed loop steer angles similar to G_I at low speed, but was unstable at high speed in the presence of delay ($\tau = 0.2\,\text{s}$), possibly due to its lack of a yaw rate state gain.

Model G_{III} used an LQR controller based on a single degree of freedom second order model with no sideslip so only the yaw rate state is fed back to the driver. Model G_{III} gave closed loop steer angles very similar to G_I at low speed but at high speed, steer angles resembled those of G_I 'delayed' due to preview being shorter.

Model G_{IV} used an LQR controller with delay states. Model G_{IV} with $N_d = 4$ gave nearly identical steer angles to G_I for both $U = 20\,\text{m/s}$ and $U = 50\,\text{m/s}$ and for both $\tau = 0$ and $\tau = 0.2\,\text{s}$. Preview shifting and steer angle delay state gains were able to nearly completely compensate for the delay N_d.

Model G_V used the same 4 state LQR controller as model G_I, but its output steer angle was filtered through an NMS. Model G_V gave more oscillatory closed loop steer angles than G_I. At high speed in the presence of the delay $\tau = 0.2\,\text{s}$ the closed loop controller G_V was unstable.

Models G_{VI}, G_{VII} and G_{VIII} used a six state LQR controller based on a coupled vehicle and neuromuscular system model and an NMS filter on its output steer angle. Model G_{VII} was able to closely reproduce model G_I's performance despite the NMS filter being present within the closed loop. This was due to the NMS state gains and the preview shifting.

Increasing vehicle speed from 20m/s to 50 m/s doubled the state gains of all controllers and shifted preview gains toward more negative values corresponding to steering more toward the direction of a curve. Increasing speed from 20 to 50 m/s also reduced the preview time of all controllers due to changes in vehicle dynamics.

Chapter 4: Identification of driver steering models

In this chapter, the procedure for identification of driver models from recorded data is explained and validated. In the first half of the chapter, two possible methods for identification of the driver model are explained, namely the direct, and indirect methods. The direct method was chosen for further development and the algorithms developed for driver identification using the direct method are described. The second half of the chapter describes the way in which the direct method was validated by identifying models from artificially created data. Validation of the method for each of the models in chapter 3 is described, and a study of the available parameters is carried out. This parameter study assisted in the design of the identification experiment to be carried out on drivers in chapter 5.

4.1 Identification procedure

In the previous chapter, each of the controllers G_I to G_{VIII} was operated in closed loop to investigate its performance, however, in order for these models to represent a driver more accurately, they must be modified to include the noise inherent in a driver's control [24]. This driver internal noise may have many sources e.g. inaccuracies in the reproduction of intended steer angle by the neuromuscular system; or noise arising from misperception of system parameters (preview offsets, or vehicle states). All of these sources can be modelled together by 'referring' the noise to the driver's output (steer angle δ) as a random coloured additive noise signal as shown in Figure 4.1.
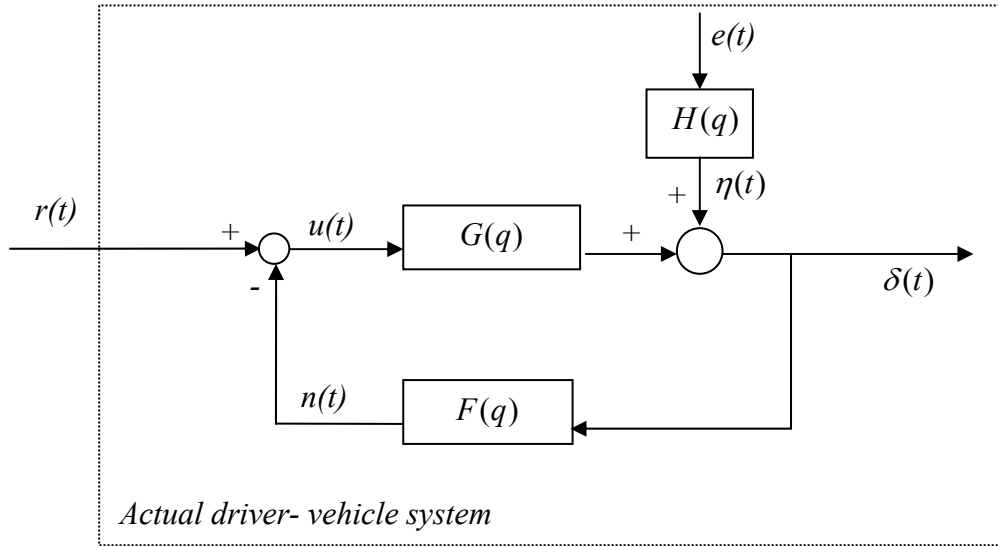
Figure 4.1: Driver-vehicle closed loop system including added driver noise η(t)

In Figure 4.1, driver noise is represented by a coloured noise signal $\eta(t)$ which is produced from a white noise signal $e(t)$, filtered with a noise filter $H(q)$. For the driver system, $r(t)$ represents the road path input, $G(q)$ is the driver model, and $F(q)$ is the vehicle model.

The method used for identification of G must be chosen to take account of the noise (η) entering at a point within the closed loop. Ljung [47] describes two methods for

identification of such systems based on the prediction error method (PEM), namely the direct, and indirect methods. Both methods involve comparing output (steer angle δ) recorded from the driver during simulator tests, to the output (δ') from a proposed driver model which is subject to the same inputs. A suitable model of the driver can then be found by choosing model parameters which give the minimum prediction error ($\delta - \delta'$). The two methods differ in whether they operate the driver model (G') in open or closed loop. In the following sections 4.1.1 and 4.1.2, the direct and indirect methods are explained, and the choice of the direct method is justified in section 4.1.3.

4.1.1 Indirect method

The indirect method of system identification reported by Ljung [47] is shown in Figure 4.2. In this method, the 'actual driver-vehicle system' output δ is compared to the output δ' from a 'modelled driver-vehicle system' (see Figure 4.2). The 'modelled driver-vehicle system' consists of a driver model estimate $G'(q)$ operating in closed loop with a vehicle model $F(q)$. The input to the closed loop system $r(t)$ is the same as was experienced by the actual driver during testing. This 'modelled driver-vehicle system' contains no noise (see Figure 4.2), so is similar to the closed loop models of chapter 3.
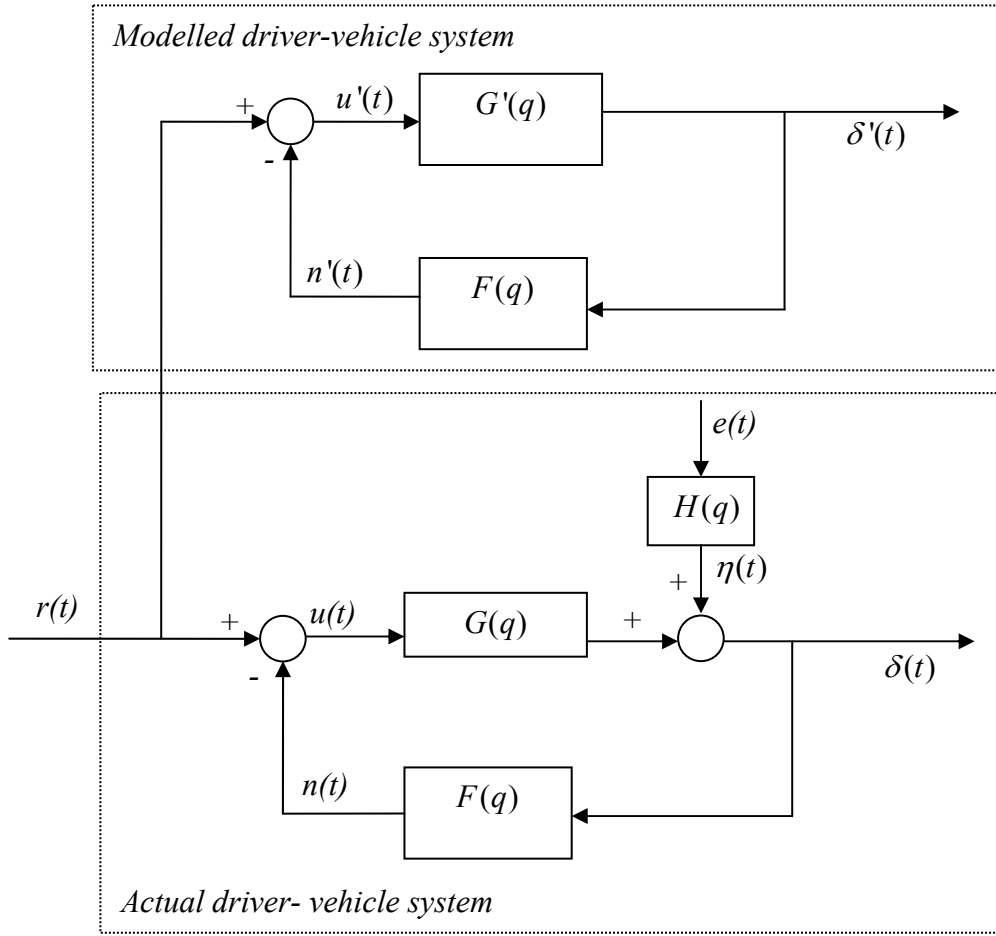
Figure 4.2: Indirect method identification of driver-vehicle closed loop system

For the 'actual driver-vehicle system' in Figure 4.2:

$$\delta(t) = G(q)u(t) + H(q)e(t) = G(q)r(t) - G(q)F(q)\delta(t) + H(q)e(t) \qquad (4.1)$$

Hence:

$$\delta = GS_f r + HS_f e \qquad (4.2)$$

Where S_f is the sensitivity function:

$$S_f = \frac{1}{1 + GF} \qquad (4.3)$$

The steer angle δ' of the modelled driver-vehicle system is given by:

$$\delta' = G'u' = G'S_f 'r \qquad (4.4)$$

123

Where S_f' is the sensitivity function:

$$S_f' = \frac{1}{1+G'F} \qquad (4.5)$$

Prediction error (υ) is therefore:

$$\upsilon = \delta - \delta' = Gu - G'u' + He = (GS_f - G'S_f')r + HS_f e \qquad (4.6)$$

A weighted prediction error ε is given by:

$$\varepsilon = \left(H'S_f'\right)^{-1}(\delta - \delta') = \left(H'S_f'\right)^{-1}\left(GS_f - G'S_f'\right)r + \left(H'S_f'\right)^{-1}HS_f e \qquad (4.7)$$

Where H' and S_f' are estimates of the initially unknown H and S_f. The weighting of prediction error (υ) using $\left(H'S_f'\right)^{-1}$ causes the noise term $\left(H'S_f'\right)^{-1}HS_f e$ to approximate white noise. The purpose of adding this frequency weighting is to minimise the misidentification of the driver model G', also known as bias.

Ljung [47] states that if the input (r) and noise (e) are uncorrelated, then minimising the variance of ε will minimise $\left(H'S_f'\right)^{-1}\left(GS_f - G'S_f'\right)$. The resulting estimate G' is given by [47]:

$$G' = \arg\min_{G'} \int_{-\pi}^{\pi} \left|\frac{G-G'}{1-FG'}\right|^2 \frac{|S_f|^2 \Phi_r}{|H'|^2} d\omega \qquad (4.8)$$

Where $\arg\min_x f(x)$ is the value of x that minimises $f(x)$, and Φ_r is the spectrum of the input $r(t)$. The 'model set' is the range of possible driver models used in the optimisation of equation (4.8) to give the estimate G'. The estimate G' will be a compromise between making G' close to G, and making $1/(1-FG')$ small. However, if the true system (G) exists within the model set, then the bias of the system estimate G' will be zero.

4.1.2 Direct method

In the direct method reported by Ljung [47], the driver's open loop response δ to inputs $u(t)$ is modelled, as shown in Figure 4.3.
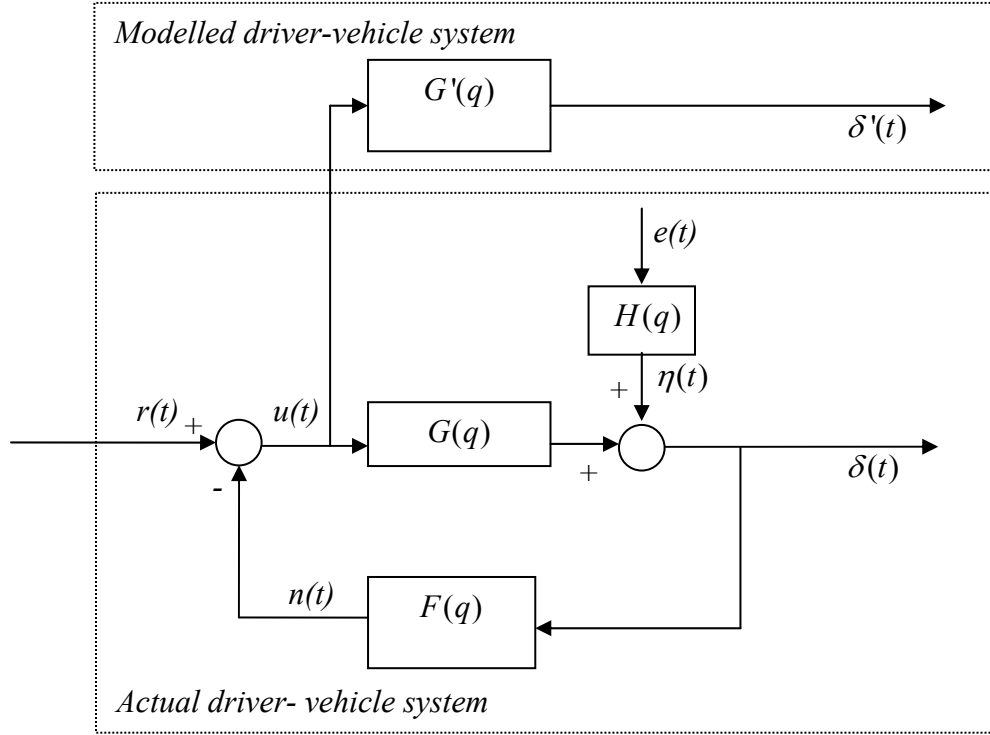
Figure 4.3: Direct method identification of driver-vehicle closed loop system

The recorded system inputs $u(t)$ are fed into the estimated system model $G'(q)$, then estimated output steer angle $\delta'(t)$ is compared to the recorded driver output $\delta(t)$. Driver system output $\delta(t)$ is the summation of model output $(G(q)u(t))$, and the noise $\eta(t)$:

$$\delta(t) = G(q)u(t) + H(q)e(t) \qquad (4.9)$$

The model prediction δ' is given by:

$$\delta'(t) = G'(q)u(t) \qquad (4.10)$$

Prediction error is therefore a function of the model error $(G - G')$, and the noise (e):

$$\upsilon = \delta - \delta' = (G - G')u + He \qquad (4.11)$$

In the special case of white driver noise ($H = 1$), G' can be determined by minimising prediction error (υ), and no bias would result. However, if driver noise (He) is non-white ($H \neq 1$), minimising prediction error (υ) would lead to bias in G'. For $H \neq 1$ a weighted prediction error ε must be minimised to reduce bias:

$$\varepsilon = H'^{-1} \upsilon = H'^{-1} (\delta - \delta') = H'^{-1} (G - G')u + H'^{-1} He \qquad (4.12)$$

The prediction error (υ) is weighted by an inverse noise model H'^{-1}, which must be estimated to ensure that ($H'^{-1} He$) is white noise. However, even if H' is a good estimate, minimising ε does not minimise the error in the model G', because ε is correlated with e via the closed loop. Ljung [47] states that minimising ε leads to the following estimate of G':

$$G' = \arg\min_{G'} \int_{-\pi}^{\pi} \left| G(\omega) + B(\omega) - G'(\omega) \right|^2 \frac{\Phi_u(\omega)}{\left| H'(\omega) \right|^2} d\omega \qquad (4.13)$$

Where Φ_u is the spectrum of $u(t)$ and the bias term $B(\omega)$ is given by:

$$\left| B(\omega) \right|^2 = \frac{(\sigma(e))^2}{\Phi_u(\omega)} \frac{\Phi_u^e(\omega)}{\Phi_u(\omega)} \left| H(\omega) - H'(\omega) \right|^2 \qquad (4.14)$$

Where $\Phi_u^e(\omega)$ is the spectrum of the input $u(t)$ resulting from noise $e(t)$ fed back through the vehicle. Identification bias ($B(\omega)$) in the frequency range of interest will be small if either (or all) of the following hold:

1. The noise model is good ($H - H'$ is small).

2. The feedback contribution to the input spectrum ($\dfrac{\Phi_u^e(\omega)}{\Phi_u(\omega)}$) is small.

3. The signal to noise ratio is good ($\dfrac{(\sigma(e))^2}{\Phi_u(\omega)}$ is small).

These three conditions will need to be satisfied for a successful identification experiment. Note from equation (4.13) that the identified model G' is frequency weighted by $\Phi_u / \left| H' \right|^2$ (called the prediction 'norm'). This frequency weighting is

dependent on the input spectrum Φ_u, and on the estimated noise model H'. Although the input spectrum Φ_u can be designed as part of the experiment, the noise model H' is dependent on the driver's internal noise colour H and so cannot be specified freely.

4.1.3 Choice of identification method

The direct method was chosen to identify the driver models from experimental data. The direct method was chosen as it used significantly less CPU time due to simulating the 'modelled driver-vehicle system' (Figure 4.3) in open loop rather than in closed loop (Figure 4.2). It was possible for the direct method to be just as accurate (bias free) as the indirect method if the conditions set out in section 4.1.2 were met.

In the driver models G_I to G_{VIII} there were additional feedback loops for the states $\left(v, \omega, \delta, \dot{\delta}, \delta_{Nd-1}, \ldots, \delta_1\right)$ which were not considered in Ljung's derivation. Validation was undertaken to ensure that these extra feedback loops did not introduce bias into the identification procedure. This validation is reported in section 4.2. The identification procedure developed using Ljung's direct method is described in section (4.1.4).

4.1.4 Identification procedure

Direct method identification was carried out using the equations of the previous section with an algorithm written in MATLAB. Validation of the identification procedure is described in section 4.2. The procedure consists of two processes; optimum model (G') selection as in equation (4.13), and noise model (H') identification. These processes are covered in section 4.1.4.1 and 4.1.4.2 respectively. The complete identification algorithm is then explained in section 4.1.4.3.

4.1.4.1 Optimum model selection

Optimum model selection is summarised by equation (4.13). A minimisation search function available in MATLAB (fminsearch) was used to perform the optimisation. The function was used to find the model parameter estimates $\{q_y', q_\theta', \tau'\}$ which minimised $\Xi(\varepsilon)$, the RMS of the weighted prediction error ε (defined in (4.12)) as shown in (4.15). The parameters $\{q_y, q_\theta, \tau\}$ were defined in chapter 3 for the driver models G_I to G_{VIII}.

$$\left(q_y', q_\theta', \tau'\right) = \text{fminsearch}_{q_y, q_\theta}\left[\Xi\left(\varepsilon\left\{q_y, q_\theta, H'\right\}\right)\right] \qquad (4.15)$$

The optimum time delay (τ') was not found by including it as a parameter of the 'fminsearch' optimisation. Instead τ' was determined for each $\{q_y, q_\theta, H'\}$ point evaluated, by shifting δ' a whole number of time steps until $\Xi(\varepsilon)$ was minimised. Equation (4.12) becomes:

$$\varepsilon\left\{q_y, q_\theta, H'\right\} = H'^{-1}\left(\delta - \delta'\left\{q_y, q_\theta\right\} q^{-\tau'}\right) \qquad (4.16)$$

Where:

$$\tau' = \arg\min_\tau\left[\Xi\left(H'^{-1}\left(\delta - \delta'\left\{q_y, q_\theta\right\} q^{-\tau}\right)\right)\right] \qquad (4.17)$$

This time shifting is quick to compute compared to additional function evaluations by fminsearch, which involve the slow step of deriving a new LQR preview controller $K_{LQR}\{q_y, q_\theta\}$.

4.1.4.2 Determination of noise model

A noise model estimate H' is fitted by using the non-weighted prediction error υ as an estimate of the noise signal η (see equation (4.11)). The noise model H' is fitted using the MATLAB built-in function 'ARMAX'. 'ARMAX' calculates an Auto-Regressive Moving Average model for the time series $\upsilon\{q_y, q_\theta, \tau\}$ of the form shown in equation (4.18):

$$A(q)\upsilon\{q_y, q_\theta, \tau\} = C(q)e(t) \tag{4.18}$$

where $e(t)$ is a white noise signal. $A(q)$ and $C(q)$ are combined to determine the identified discrete transfer function $H'(q)$ (the noise model) as in equation (4.19):

$$H'(q) = \frac{C(q)}{A(q)} \tag{4.19}$$

4.1.4.3 Identification algorithm combining optimum model selection, and noise model identification

The complete identification algorithm combines 'optimum model selection' (section 4.1.4.1 and equation (4.20)), and 'noise model identification' (section 4.1.4.2 and equation (4.21)).

$$\left(q_{yi}', q_{\theta i}', \tau'_i\right) = \text{fminsearch}_{q_y, q_\theta}\left[\Xi\left(\varepsilon\{q_y, q_\theta, H'_i\}\right)\right] \tag{4.20}$$

$$H_i' = ARMAX\left[\upsilon\{q_{yi}', q_{\theta i}', \tau'_i\}\right] \tag{4.21}$$

The algorithm is iterative, because optimum model selection (4.20) is dependent on the noise model estimate $H'_i\{\upsilon\{q_{yi}', q_{\theta i}', \tau'_i\}\}$ used. In turn H'_i (eqn. (4.21)) is dependent on the parameter estimates $\{q_{yi}', q_{\theta i}', \tau'_i\}$ which are the result of the previous 'optimum model selection' (eqn (4.20)). On the first iteration a noise model is not available, so $H'_0 = 1$ is assumed. Figure 4.4 summarises the algorithm.
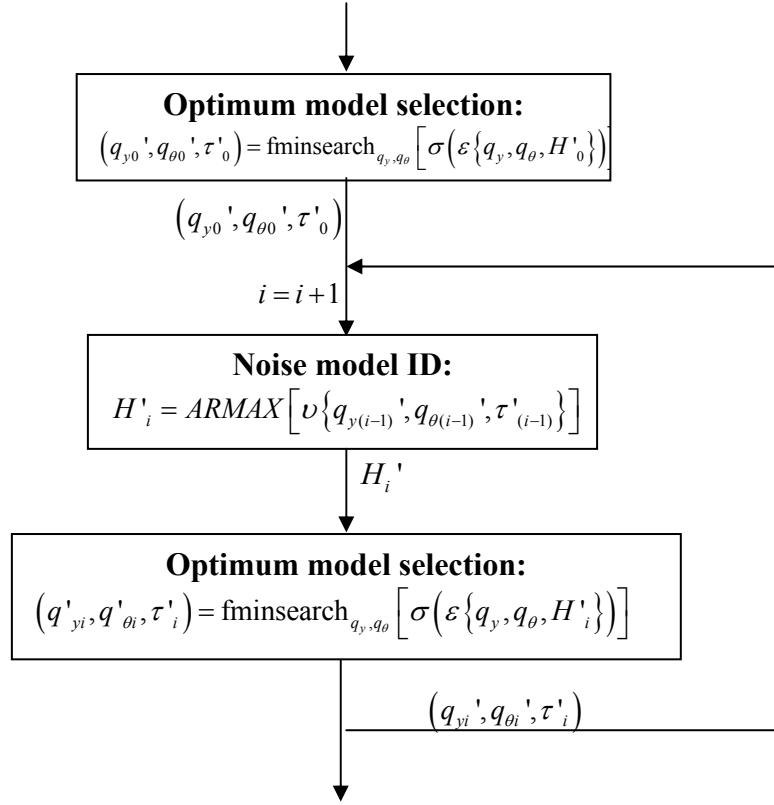
Figure 4.4: Iterative identification procedure used in Matlab algorithm

The algorithm functions as follows:

1. 'Optimum model selection' is carried out first, using a white noise model $H'_0 = 1$, yielding estimates of the model parameters $(q_{y0}', q_{\theta0}', \tau'_0)$.

2. An estimate of the noise model is made from the prediction error $(\upsilon\{q_{y0}', q_{\theta0}', \tau'_0\})$ of this 'Optimum model selection', yielding an improved noise model estimate H'_1.

3. 'Optimum model selection' is then repeated using this improved noise model H'_1.

Stages 2 and 3 are repeated until the parameter estimates converge, or a maximum number of iterations is reached.

4.2   Validation of direct method identification

The direct method was validated by using the algorithm of section 4.1.4.3 to identify simulated driver data with known parameters $\left\{q_y^G, q_\theta^G, \tau^G\right\}$. The data was generated using a known LQR controller with parameters $\left\{q_y^G, q_\theta^G, \tau^G\right\}$ operating in closed loop, as demonstrated in chapter 3, but with added noise η (as in Figure 4.1). Figure 4.19 shows the simulation carried out during validation with the controller G_I.

The purpose of the validation was to ensure that both the experiment and the identification procedure were suitable for identifying a driver control model. A parameter study was then carried out to assess the sensitivity of the identification to experiment and model parameters. Parameters investigated in the study were:

1. Driver noise colour; defined by the filter $H(q)$
2. Road path signal (r); in terms of magnitude and frequency content.
3. Vehicle speed U from 20 m/s to 60 m/s.
4. Complexity (order) of noise model H'.
5. Time delay of the driver (τ).
6. Complexity and structure of the driver model to be fitted (G_I to G_{VIII}).

These parameter studies are detailed in sections 4.2.1 to 4.2.6 respectively.

Base settings for driver noise colour and magnitude, and driver time delay were selected to reflect those observed during tests on drivers as detailed in chapter 5. Each parameter was then changed in turn to assess its effect, leaving all other parameters at their base settings. Interactions between parameters were not investigated.

The white noise input to the driver model $e(t)$ (see Figure 4.3) was generated as a zero-mean random number in MATLAB, then scaled to give the appropriate RMS value. Note that the noise standard deviation $\sigma(e)$, and the noise RMS $\Xi(e)$ are equivalent because $e(t)$ has zero mean. Unless otherwise stated $\Xi(e) = 10°$. This

value corresponds approximately to the noise observed from drivers during experiments in chapter 5.

The parameters $\{q_y, q_\theta\}$ of the LQR model G (in Figure 4.3) used to create $\delta(t)$ were set at $\{q_y{}^G, q_\theta{}^G\} = \{0.05, 5\}$. For the parameter studies of sections 4.2.1 to 4.2.5, model G_I was used operating in closed loop, as shown in figure 3.21. Parameter values for G_I were $\tau^G = 0$, and $U = 20$ m/s except where explicitly stated. Table 4.1 at the end of the chapter lists the parameters used for the derivation of each figure in sections 4.2.1 to 4.2.5. Track length was varied according to speed to give 100 second track duration, up to a maximum track length of 4 km. Each of the tracks were randomly generated from the spectral density equation (4.24).

4.2.1 Noise colour

The bias effect of noise colour was investigated by identifying the LQR model parameters $\{q_y, q_\theta\}$ with two different noise inputs. The first was a white noise input ($H = 1$) in section 4.2.1.1, the second was a coloured noise input ($H = M$) in section 4.2.1.2.

4.2.1.1 White input noise case ($H = 1$)

A white noise input ($H = 1$), and white noise model ($H' = 1$) is the simplest case for identification, and allows the effect of noise magnitude to be observed. With $H' = H = 1$, equation (4.13) simplifies to:

$$G' = \arg\min_{G'} \int_{-\pi}^{\pi} \left| G(\omega) - G'(\omega) \right|^2 \Phi_u(\omega) d\omega \qquad (4.22)$$

The bias term $B(\omega)$ in equation (4.14) is zero because $H' = H$, so no bias should be evident in the identification of the model estimate G'. The identification norm $\left(\Phi_u(\omega) / \left| H'(\omega) \right|^2 \right)$ is now frequency weighted only by the input spectrum $\Phi_u(\omega)$.

The identification procedure from section 4.1.4.3 was used to identify $\{q_y{}',q_\theta{}'\}$ using the data (y_p,δ,v,ω) generated by G_I operating in closed loop along one track. This procedure was then repeated fifteen times at each of five driver noise ($\Xi(e)$) levels, resulting in 75 different tracks driven. Each of the 75 tracks used a different random noise signal (e).

Results of the identification are plotted in Figure 4.5 with driver noise level $\Xi(e)$ on the x-axis, and identified parameters ($q_y{}'$ and $q_\theta{}'$) on the y-axes. Note that $\Xi(e) = \Xi(\eta)$ for this white noise case ($H = 1$). Each identification is shown as a blue cross, representing one track driven and then identified. The real values of the model parameters ($q_y{}^G$ and $q_\theta{}^G$) are shown as a solid red line, and a least squares fit to the identifications is shown as a dashed blue line.
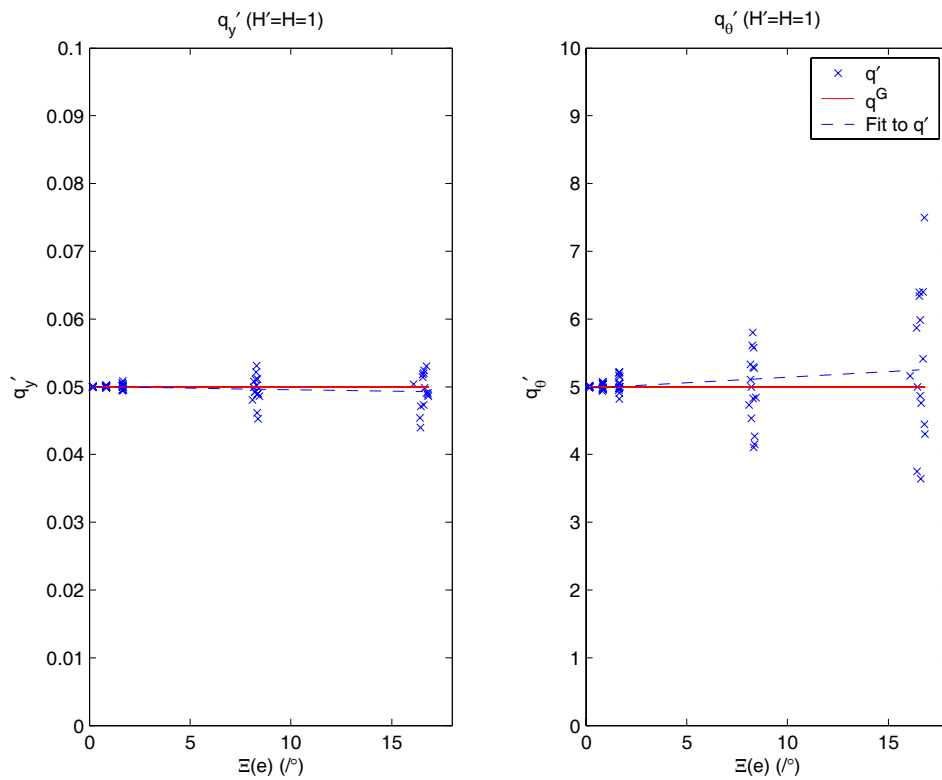
Figure 4.5: Identification of parameters $\mathbf{q_y}$' and $\mathbf{q_\theta}$' vs. RMS noise level $\Xi(\mathbf{e})$ with white noise input, and white noise model ($\mathbf{H' = H = 1}$)

As expected, the results show little bias even at high noise levels, but the variance of the identified parameters increases with noise variance. The variance in $q_\theta{}'$ is greater than that in $q_y{}'$, especially at the highest noise level. As discussed in chapter 3 section 3.3.1 the controller is 'q_θ weighted', and this may be the reason that identification of $q_\theta{}'$ has more variance for a given $\Xi(e)$ than identification of $q_y{}'$.

4.2.1.2 Coloured noise case

For the coloured noise case, a filter $M(q)$ was used as noise filter $H(q)$. A continuous filter $M(s)$ was created then discretised using the 'C2D' function in MATLAB with a Tustin approximation to give $M(q)$. $M(s)$ had two poles and two zeros. The poles were those of a second order Butterworth filter with cut-off at 1Hz. This cut-off was chosen because it was similar to the noise colour observed during experiments on drivers as discussed in chapter 5 p199. This was based on the assumption that the driver noise was equal to the model prediction error υ in equation (4.11) measured during experiments. This assumption is good as long as the contribution from model mismatch $(G-G')$ is small relative to the real driver noise He. The zeros of $M(s)$ were those of an inverted second order Butterworth filter with cut-off at 9 Hz. The resulting filter $M(s)$ is shown in equation (4.23).

$$M(s) = \frac{39.48\ s^2 + 3157\ s + 126200}{3198\ s^2 + 28410\ s + 126200}$$
(4.23)

The zeros ensured that the inverted noise model H'^{-1} was proper, as an improper filter could not be used for the identification procedure. 9 Hz was chosen as the highest possible cut-on frequency which would fall below the 10 Hz Nyquist frequency, but was sufficiently above the 1 Hz cut-off to allow a 38 dB attenuation in $M(q)$ at 10 Hz. The gain plot of the resulting discrete filter $M(q)$ is shown in Figure 4.6.
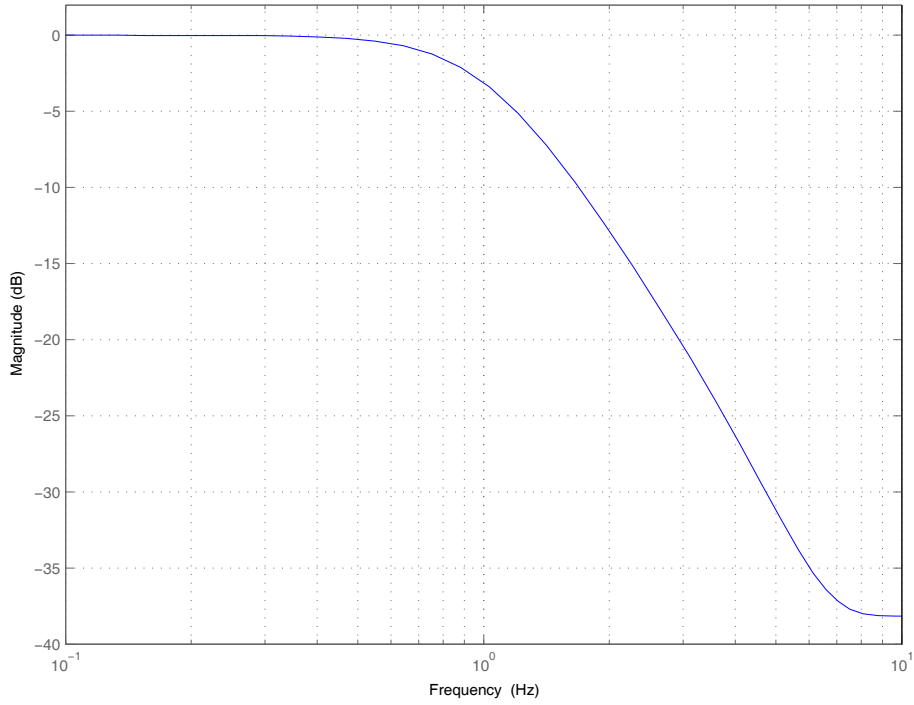
Figure 4.6: Gain plot of noise filter M(q)

Driver noise levels for this section are shown as $\Xi(\eta)$, the RMS of the post-filter noise η. For a given $\Xi(\eta)$, the filter $H = M$ will result in more low frequency content in the signal η than was the case for $H = 1$ (where $\Xi(e) = \Xi(\eta)$).

Identifications were first carried out with coloured noise ($H = M$), but with a white noise model estimate $H' = 1$. The resulting $\{q_y', q_\theta'\}$ estimates are shown in the upper two plots of Figure 4.7. Figure 4.7 uses the same labelling convention as Figure 4.5.
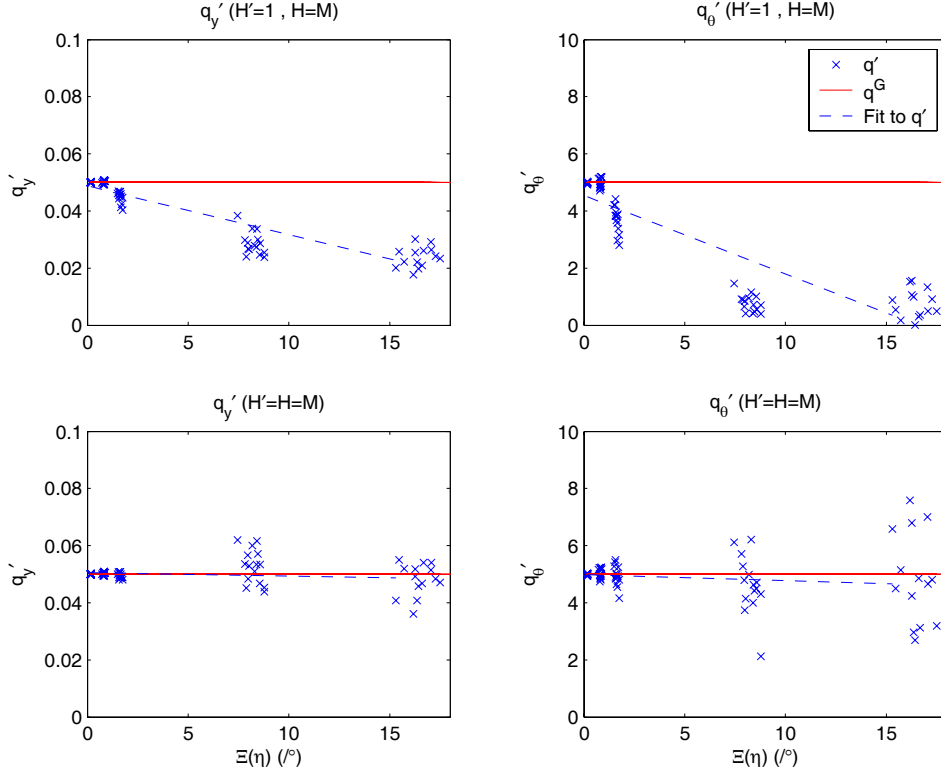
Figure 4.7: Identification of parameter estimates $\mathbf{q_y}'$ and $\mathbf{q_\theta}'$ vs. RMS noise level $\Xi(\mathbf{e})$ with coloured noise input ($\mathbf{H = M}$). White noise model ($\mathbf{H' = 1}$), and perfect coloured noise model ($\mathbf{H' = M}$) shown

Bias is evident in these upper two plots particularly at higher noise levels. For $\Xi(\eta) = 17°$, $\mu(q_y')$ is underestimated by 50%, and $\mu(q_\theta')$ by 82%. Bias is evident even with noise levels as low as $\Xi(\eta) = 2°$.

Identification of $\{q_y', q_\theta'\}$ using a 'perfect' noise model ($H' = H = M$) is shown in the lower plots of Figure 4.7. This perfect noise model is able to reduce the bias significantly at high $\Xi(\eta)$ for both q_y' and q_θ'. For q_y' bias is eliminated, but for q_θ' some slight bias of $\mu(q_\theta')$ remains at high noise levels, though this is to be expected given larger variance and limited number of samples. This result is consistent with equation (4.22) which implies that no bias should be present with $H' = H = M$. Comparison of the variance of q_y' and q_θ' shown in Figure 4.5 and Figure 4.7 is not meaningful because the noise signals e and $\eta\{H = M\}$ are not similarly coloured.

In the following sections, coloured driver noise $H = M$ was used as this more closely reflects the noise present in the real driver identifications. A perfect coloured noise model $H' = M$ was assumed until section 4.2.4 where the identification of this noise model was investigated. A noise level of $\Xi(\eta) = 10°$ was used unless otherwise stated.

4.2.2 Road path input signal

Road input to the model ($r(t)$ in Figure 4.3) was provided using a discrete set of roadway points (S_t, ψ_t) defined in intrinsic coordinates. A study of measured horizontal road profiles by Picardo [57] defined horizontal road profiles using a spectral density of the road angle ψ_t (assuming a constant point spacing). The spectral density of the road profile used for this study is defined in intrinsic coordinates by equation (4.24):

$$\Phi_{\psi_t}(\chi) = \kappa \chi^{-\gamma} = \text{ Spectral density of track angle } (\psi_t) \ \left(/ \, \text{rad}^2 \text{cycles}^{-1} \text{m}\right) \quad (4.24)$$

Where:

$$\chi = \text{Wavenumber (cycles/m)}$$
$$\gamma = \text{Frequency roll off parameter} \quad (4.25)$$
$$\kappa = \text{Magnitude parameter}$$

Equation (4.24) is similar to that used for vertical road roughness profiles in vehicle ride modelling. It describes a frequency spectrum which has a magnitude defined by κ, and which rolls off with a gradient defined by γ, as shown in Figure 4.8 on a log-log scale.
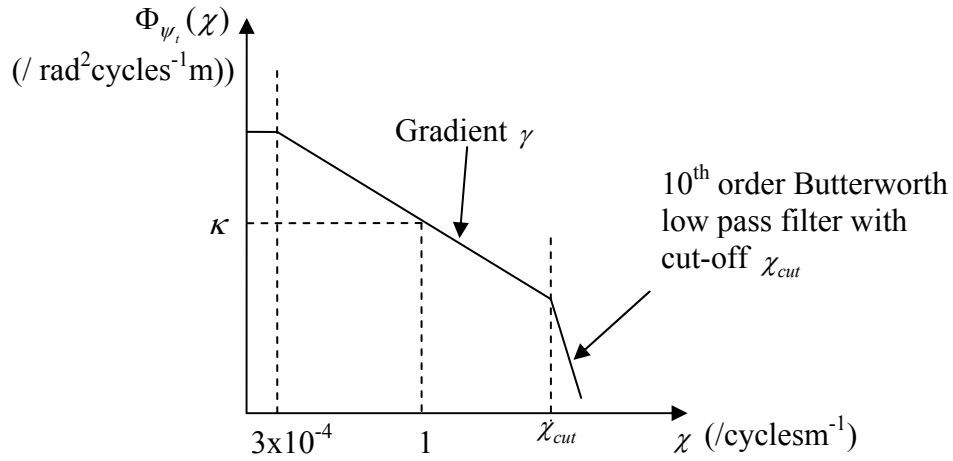
Figure 4.8: Diagram of road spectral density of road path angle (ψ_t). Axes are Log-Log

The PSD of ψ_t was constant below a wavenumber of 3×10^{-4} cycles/m, which is very low compared to the wavenumbers of interest for driver excitation. Equation (4.24) therefore expresses the part of the spectrum which is of interest for driver excitation. The effect of κ and γ on vehicle identification are investigated in sections 4.2.2.1 and 4.2.2.2 respectively. The track is defined using points with finite spacing, so a 10th order Butterworth low pass filter was applied to the track profile to prevent aliasing. The effect of changing the cut-off wavenumber (χ_{cut}) of this filter is investigated in section 4.2.2.3.

4.2.2.1   Effect of κ : signal-to-noise ratio

In the real driver system changing κ could cause a real driver's internal noise level $\Xi(\eta)$ to change. In this section, however, κ is changed with $\Xi(\eta)$ constant, which has the effect of changing the signal-to-noise ratio of the system, and hence $(\sigma(e))^2/\Phi_u(\omega)$ (see section 4.1.2). Decreasing κ would therefore be expected to increase identification bias. However, with a perfect noise model ($H = H'$), the bias term in equation (4.14) should be zero for any $(\sigma(e))^2/\Phi_u(\omega)$, and no bias should result.

The value of parameter κ is not intuitive for assessing the amount of driver input resulting from a track, so a method was used to allow the amount of path input to be measured in degrees of steer angle, making it dimensionally comparable to the steering noise level $\Xi(\eta)$. A separate closed loop track-driving simulation was run with no added noise ($\Xi(\eta) = \Xi(e) = 0$), similar to those in chapter 3, section 4.4. The RMS steer angle of this closed loop simulation ($\Xi(\delta_{e=0})$) was then calculated as the measure of track input.

Identification was repeated twenty times at each of four κ values, the highest of which was that used in the driver experiments of chapter 5 (as shown in Table 5.1 p181). Results are shown in Figure 4.9 on axes of q_y' and q_θ' vs. $\Xi(\delta_{e=0})$.
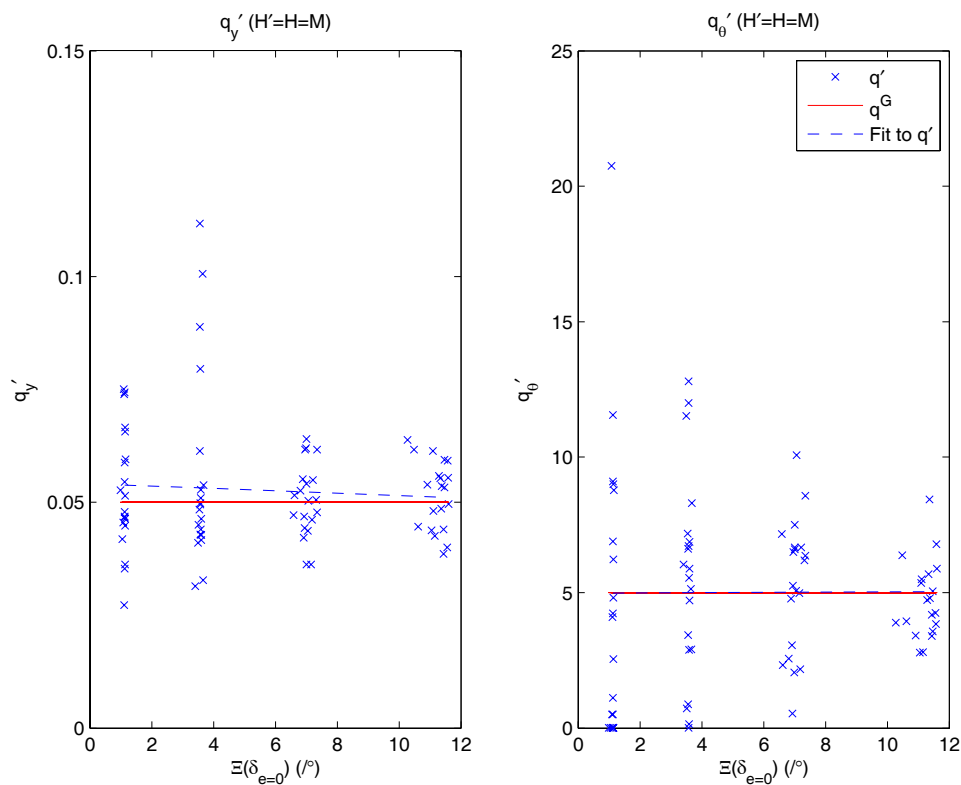
Figure 4.9: Identification of parameters $\mathbf{q_y}$' and $\mathbf{q_\theta}$' vs. $\Xi(\delta_{e=0})$. Perfect coloured noise model ($\mathbf{H'} = \mathbf{H} = \mathbf{M}$) only shown

For both q_y' and q_θ', variance increases as track input magnitude is reduced below that used in tests. Also for $\Xi(\delta_{e=0}) < 7°$ some outliers are evident. These outliers lead

to bias of $\mu\left(q_y{}'\right)$ for $\Xi\left(\delta_{e=0}\right) < 7°$, but this is because the standard deviation $\sigma\left(q_y{}'\right)$ is large compared to the parameter value. For $\Xi\left(\delta_{e=0}\right) > 7°$ the bias for both $q_y{}'$ and $q_\theta{}'$ is small. This result is consistent with the prediction that a perfect noise model ($H = H'$) should ensure zero bias.

4.2.2.2   Colour of track input

The road profile parameter γ specifies the frequency roll-off of the road spectral density. This parameter can be used to modify the colour of the road input to the driver. Road input colour will affect the identification norm $\Phi_u\big/\left|H'\right|^2$ in equation (4.13) and therefore the frequency weighting of the identified model. The input spectrum Φ_u can also affect the bias in equation (4.14), but only in cases where the noise model is not perfect, so should not affect these results.

A range of values $\left(-3.6 \geq \gamma \leq -1\right)$ was therefore investigated. Identification was carried out fifteen times at each of five γ values. Track input magnitude κ was adjusted to keep $\Xi\left(\delta_{e=0}\right) = 11.5°$ for all tracks. Increasingly negative γ values therefore correspond to increased low frequency content, but reduced high frequency content. Results for the identification are shown in Figure 4.10.
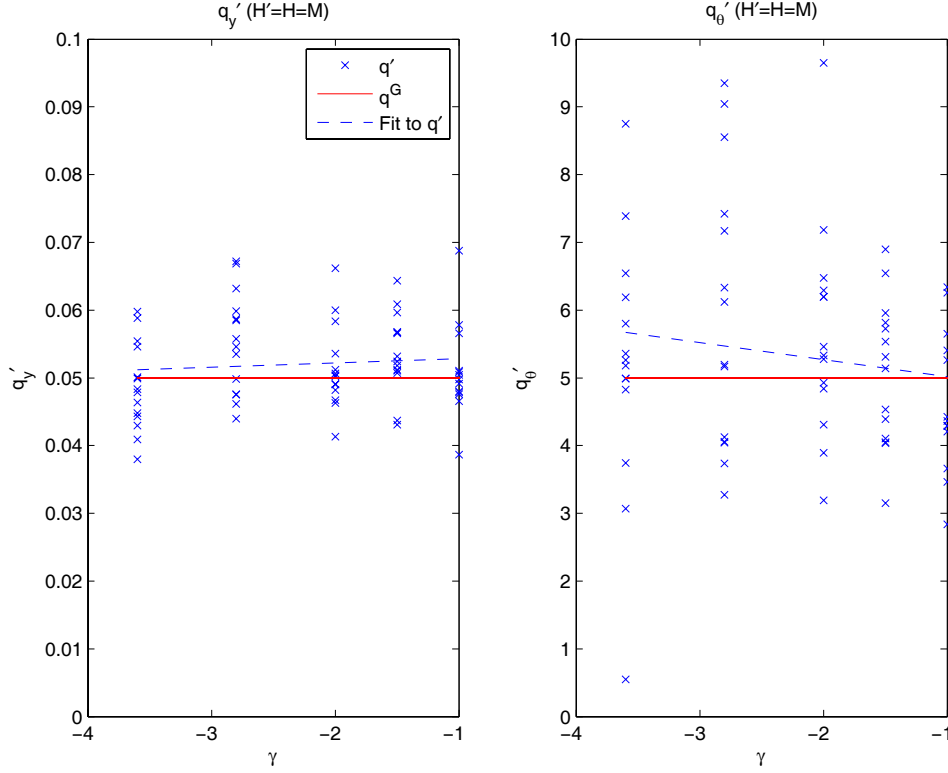
Figure 4.10: Identification of parameters $\mathbf{q_y}'$ and $\mathbf{q_\theta}'$ vs. Track input noise colour (γ). Perfect coloured noise model ($\mathbf{H'=H=M}$) shown

The results of Figure 4.10 show little systematic change in bias with γ in either q_y' or q_θ', as would be expected with a perfect noise model. There seems to be some bias for $\gamma = -3$ for both q_y' and q_θ', but this trend does not extend to the other γ values. The variance of q_θ' does increase for $\gamma < -2$, but this is not the case for q_y'. It seems that reducing the high frequency content of the road too much can increase the variance of q_θ'. Overall the value of $\gamma = -2$ used for experiments presented in the next chapter seems suitable. The value of $\gamma = -2$ corresponds to white noise curvature, as described in appendix E.

4.2.2.3 Frequency cutoff of track input

Track filter cut-off wavenumber (χ_{cut}) is of interest because it affects the bandwidth of the excitation spectrum $\Phi_u(\omega)$. This in turn affects the identification norm

141

$\Phi_u \big/ |H'|^2$, and hence the bandwidth over which the identified model is valid. Also if a lower wavenumber cut-off is used, track point spacing can be increased without aliasing. This would allow tracks on the simulator to be longer (for a given amount of simulator memory), and hence more data to be collected for each trial, giving a larger sample for identification.

A Butterworth filter was used to provide the wavenumber cut-off. A 10th order filter was used where possible, but for tracks with few points (due to increased point spacing) the filter order was reduced to as low as 5th order.

The effect of varying χ_{cut} was investigated by identifying simulated data from tracks with seven values of χ_{cut} fifteen times each. Track point spacing was changed for each χ_{cut} to give a 25% overhead above the Nyquist wavelength. The track magnitude parameter κ was unchanged. The results are shown in Figure 4.11.
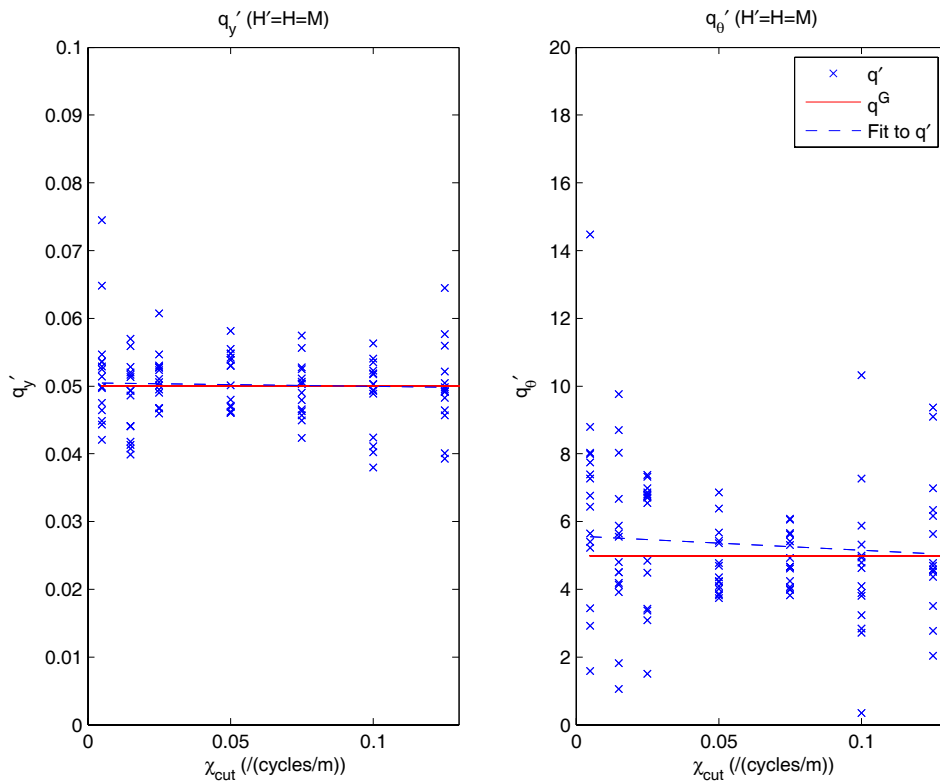
Figure 4.11: Identification of parameters $\mathbf{q_y}'$ and $\mathbf{q_\theta}'$ vs. χ_{cut}. Perfect coloured noise model ($\mathbf{H}' = \mathbf{H} = \mathbf{M}$) shown

The results show little bias in $q_y{}'$ or $q_\theta{}'$ as would be expected for a perfect noise model. Some bias is evident in $q_\theta{}'$ for $\chi_{cut} < 0.025$ cycles/m, but this seems largely due to a single outlier for $\chi_{cut} = 0.005$ cycles/m.

The results do show increased variance for both $q_y{}'$ and $q_\theta{}'$ below $\chi_{cut} = 0.025$ cycles/m. It is helpful to view this result in terms of cut-off wavelength ($L_{cut} = 1/\chi_{cut}$) relative to the driver's preview length (L_{prev}). For this model (G_I), at 20m/s $L_{prev} \approx 50m$ (see chapter 3 section 3.3). If L_{cut} is significantly longer than L_{prev}, little information can be gained about the shape of the preview, so identification may be degraded. Evidence of this is seen in the increased variance of $\{q_y{}', q_\theta{}'\}$ for $\chi_{cut} < 0.025$ cycles/m ($L_{cut} > 40m$).

Conversely if L_{cut} is significantly shorter than the preview, little additional benefit will result from increasing χ_{cut}. Evidence of this is visible for $\chi_{cut} > 0.05$ ($L_{cut} < 20m$) where variance of $q_y{}'$ and $q_\theta{}'$ does not decrease any further than that at $\chi_{cut} = 0.075$. In fact, it seems from these results that the variance of $q_\theta{}'$ for $\chi_{cut} > 0.075$ may increase slightly, but it is unclear why this should be the case based on the previous argument.

During simulator experiments, a track filter with wavenumber cut-off at $\chi_{cut} = 0.1$ cycles/m was used. This would not seem to have the least $\{q_y{}', q_\theta{}'\}$ variance based on these results, but for real tests the perfect noise model H is not available, and H' must be identified from data. In this case it is beneficial to use a track input with as broad-band an excitation as possible to increase the signal to noise ratio for identification of G' in the frequency range of interest, and therefore reduce the likelihood of bias. A wavenumber cut-off of $\chi_{cut} = 0.1$ cycles/m implies a Nyquist point spacing of $5\,m$. The track point spacing was 4m, which gave only 25% over-head from the track Nyquist spacing, but the filter cut-off was sufficiently steep to prevent aliasing. Tracks were tested in the simulator and found to be sufficiently smooth for drivers to follow.

4.2.3 Track speed

The identification algorithm must be reliable for a range of vehicle speeds (U) to be useful for the experiments on drivers. Changing U will alter two aspects of the closed loop driver-vehicle system. Firstly, the frequencies associated with a given road wavelength input will increase as U increases, so the input $\Phi_u(\omega)$ will gain additional high frequency content. This is equivalent to changing the cut-off wavenumber χ_{cut} as discussed in the previous section. Secondly the LQR controller will alter as seen in chapter 3, most notably in terms of preview distance, but also its state gains and preview gain 'shape'.

Identification was carried out twenty times for each of five speeds. The speeds correspond to those used in simulator tests in chapter 5 (as shown in Table 5.1 p181). Results are shown in Figure 4.12.
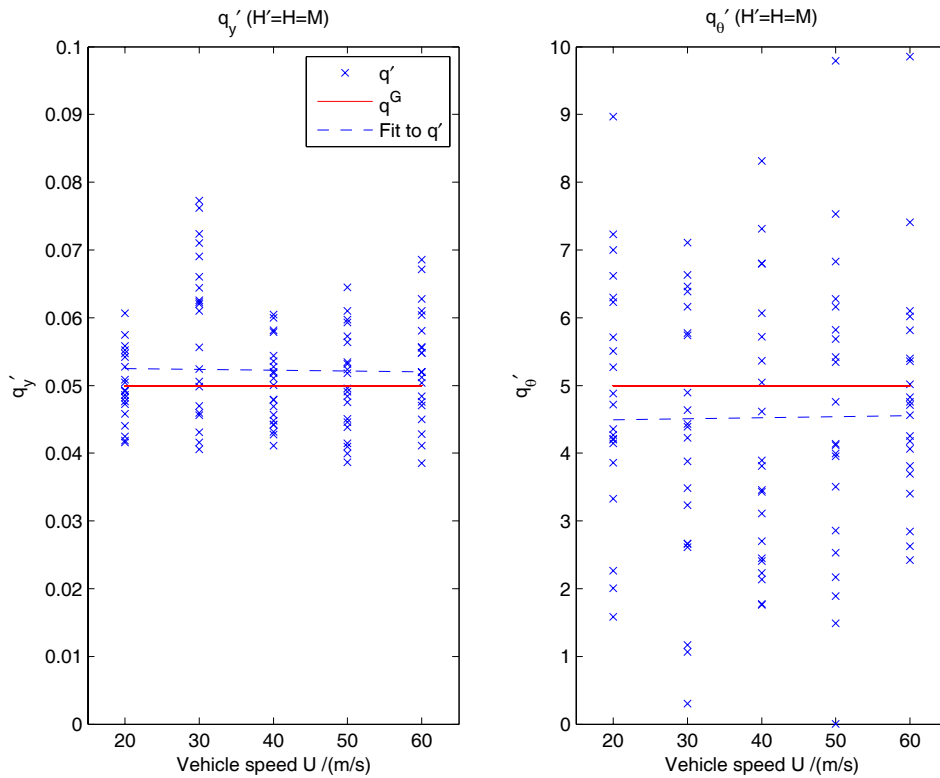
Figure 4.12: Identification of parameters $\mathbf{q_y}'$ and $\mathbf{q_\theta}'$ vs. track speed. Perfect coloured noise model ($\mathbf{H'=H=M}$) shown

The best fit line to the results seem to show a uniform 6% overestimation of $q_y{'}$, and 10% underestimation of $q_\theta{'}$. However, only the results at 30 m/s show any visible bias, and are probably the major cause of the best-fit lines' offsets. The fact that this bias at 30 m/s is not shown at other speeds seems to suggest that the result may be due to a few outliers, and therefore not of major concern.

Significantly there seems to be little change in either bias or variance with speed U. The identification procedure should therefore be suitable for all speeds used in simulator testing, provided an accurate noise model can be identified. The effect of speed on identification of each model (G_I to G_{VIII}) with identified (rather than perfect) noise models is examined in section 4.2.5.3.

4.2.4 Noise model accuracy

During identification using real driver data, the perfect noise model is not available, and must be identified using the ARMAX method described in section 4.1.4.2. Identification of $\{q_y{'}, q_\theta{'}\}$ is improved by an accurate noise model as shown in equation (4.14), so it is desirable to ensure accuracy of the noise model.

Higher order $A(q)$ and $C(q)$ in the noise model $H{'}(q)$ give the opportunity for the model to be more accurate. However, fitting a noise model that is too high an order may be detrimental because the model would tend to fit to features of the sampled dataset, rather than reflecting the ensemble from which the dataset is taken. This possibility is investigated in the following sections.

Section 4.2.4.1 shows the effect of model order on the accuracy of the noise model ($H{'}$). Section 4.2.4.2 then shows how model order affects identification of the driver model.

4.2.4.1   Effect of model order on frequency domain fit.

Models of different orders were fitted to steer angle prediction error data $\upsilon(t)$ from one track. Nine model orders were fitted. These model orders are listed in the caption of the figure, and as titles to the subfigures in Figure 4.13, denoted as [Numerator order/Denominator order], i.e. [order of $C(q)$/order of $A(q)$]. They range from zero order (D.C. gain), to very high order ([20/20]), and include the order [2/2] required to express the real noise model ($H = M$). Figure 4.13 shows each model (in blue) fitted to the spectral density of the same error data (υ) (in magenta) on axes of PSD(υ) vs. frequency.
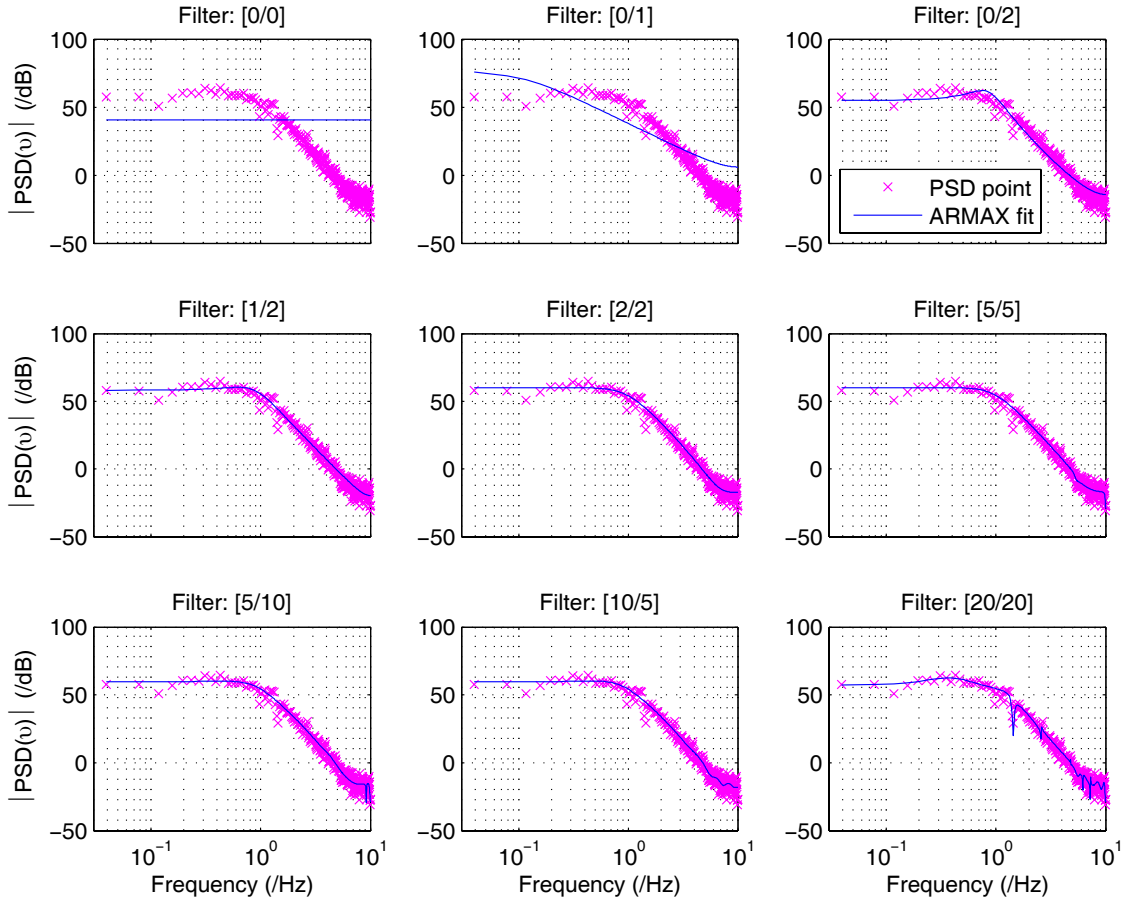
Figure 4.13: Fitting of noise model with increasing model order. $0\mathrm{dB} = 1^{o2}/\mathrm{Hz}$. Model orders [num/den] [0/0, 0/1, 0/2, 1/2, 2/2, 5/5, 5/10, 10/5, 20/20]. $\left|\mathbf{H}.\mathbf{H}^*\right|$ shown in blue.

Both the DC gain ([0/0]) and the single pole ([0/1]) noise models are not able to fit the noise PSD well, and would lead to identification bias. The bias caused by these noise

model inaccuracies is shown in the next section. All other models have two or more poles, and fit the data similarly well, differing only in detail. Having sufficient poles therefore seems to be the most important factor in fitting of the model.

The two-pole, two-zero model ([2/2]) is the correct order for the noise used, and appears to fit the data better than any other model, but there is still mismatch at low frequency. This highlights the fact that the data being fitted is only a sample of a random process, so may not represent the whole ensemble, which the noise model is intended to represent.

The noise models with too few zeros ([0/2], and [1/2]) have different gain from the [2/2] noise model between 5 and 10 Hz and between 0.5 and 1 Hz, but similar gain from 1 to 5 Hz. Increasing the number of poles and zeros to [5/5] does not seem to be detrimental to the fit, but increasing this to [20/20] causes 'spikes' to appear in the fitted PSD. This could be caused by improperly cancelled poles and zeros, or by the model fitting to features that are a facet of this particular data sample. If this is the case the higher order noise models would not be a good representation of the whole ensemble, and a lower order model would help to alleviate this tendency.

4.2.4.2   Effect of model order on identification bias:

The important test for the efficacy of noise model fit is to see how it affects identification bias. The parameters identified by each of the model orders in the previous section are shown on axes of $q_y{}'$ vs. $q_\theta{}'$ in Figure 4.14. The identification domain was restricted to $\{q_y, q_\theta\} = \{0:10, 0:0.1\}$, so that any outliers show up as points on the boundary of the axes.

A zero order model ([0/0] i.e. $H' = 1$) should give significant bias, as was shown in section 4.2.1.1, and it might be expected that bias would reduce as model order was increased. However, it is important to establish whether there is an optimal model order, i.e. whether too high a model order causes inaccuracy.
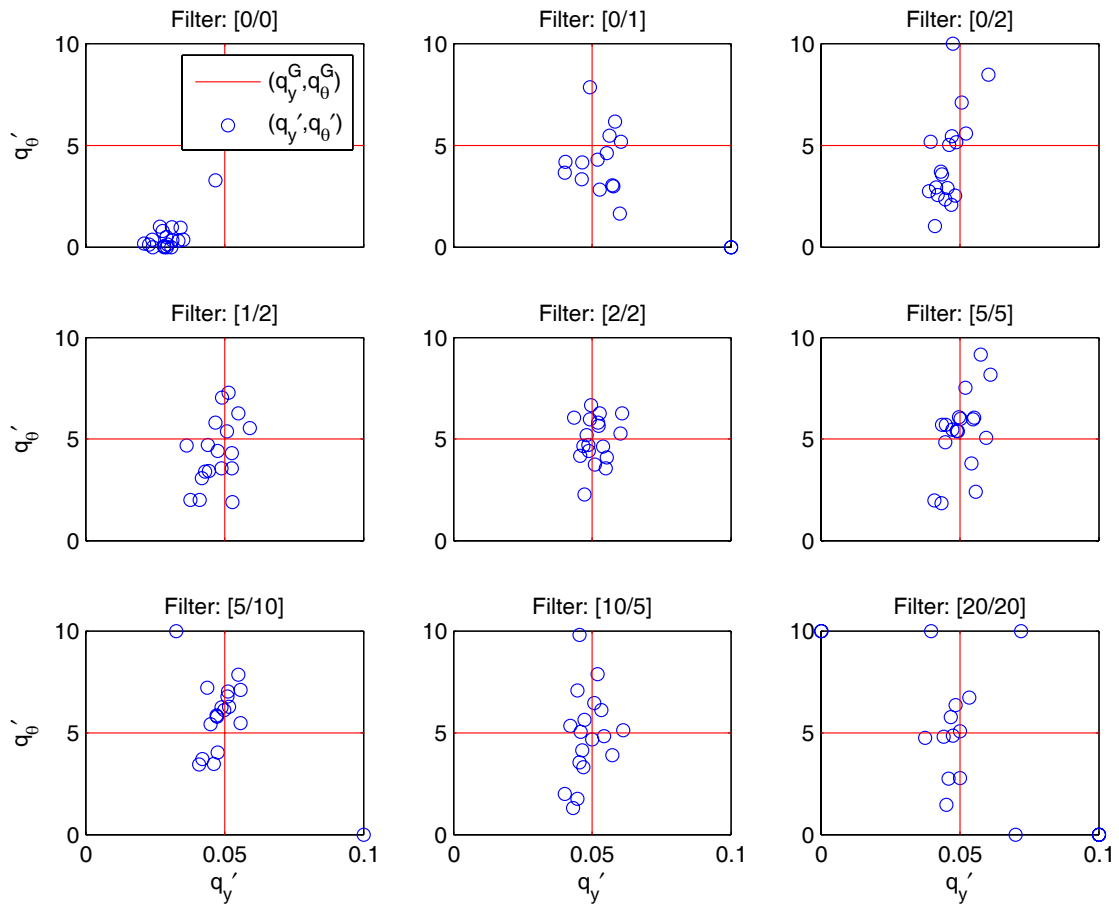
Figure 4.14: Identified model parameters $q_y{}'$ and $q_\theta{}'$ with increasing noise model order. Model orders [num/den] [0/0 , 0/1 , 0/2 , 1/2 , 2/2 , 5/5 , 5/10 , 10/5 , 20/20]

The results show that significant bias is indeed present in the two lowest order cases ([0/0] and [0/1]), where noise model fit was poor. For the next two orders ([0/2] and [2/2]) some bias towards underestimating $q_\theta{}'$ is evident, but for [2/2] identification has little bias. However, as order is increased above [2/2] (that necessary to express the real noise model) outliers begin to appear at the edge of the domain, and become more common as noise model order is increased.

It seems from these results that over-specifying the noise model can be detrimental to the bias and variance of the identification. It will therefore be important to select a model order that is no greater than needed to express the noise spectrum observed

148

during experiments. An over-complicated noise model should be evident from the presence of outliers in $\left(q_y{}', q_\theta{}'\right)$.

4.2.5 Time delay in loop

Incorrectly identified delay could be a source of bias. In this section time delay identification with a perfect noise model ($H' = M$) is investigated. First the effect of incorrect identification of delay τ is illustrated in section 4.2.5.1, then the performance of the time delay identification procedure is demonstrated in section 4.2.5.2. Identification with an identified noise model H' is covered in the section 4.2.5.3.

4.2.5.1   Effect of incorrectly identified delay on bias

Figure 4.19 shows the model G_I with driver delay τ^G included. The effect of incorrect delay identification on bias was explored by fixing $\tau' = 0.2\,\text{s}$ (identified delay in equation (4.16)). The actual delay (τ^G) present in the driver was then varied from 0 to 0.3 seconds. For $\tau^G > 0.3\,\text{s}$ the closed loop model was unstable. $q_y{}'$ and $q_\theta{}'$ were identified for twenty trials at each τ^G value, and are shown in Figure 4.15.
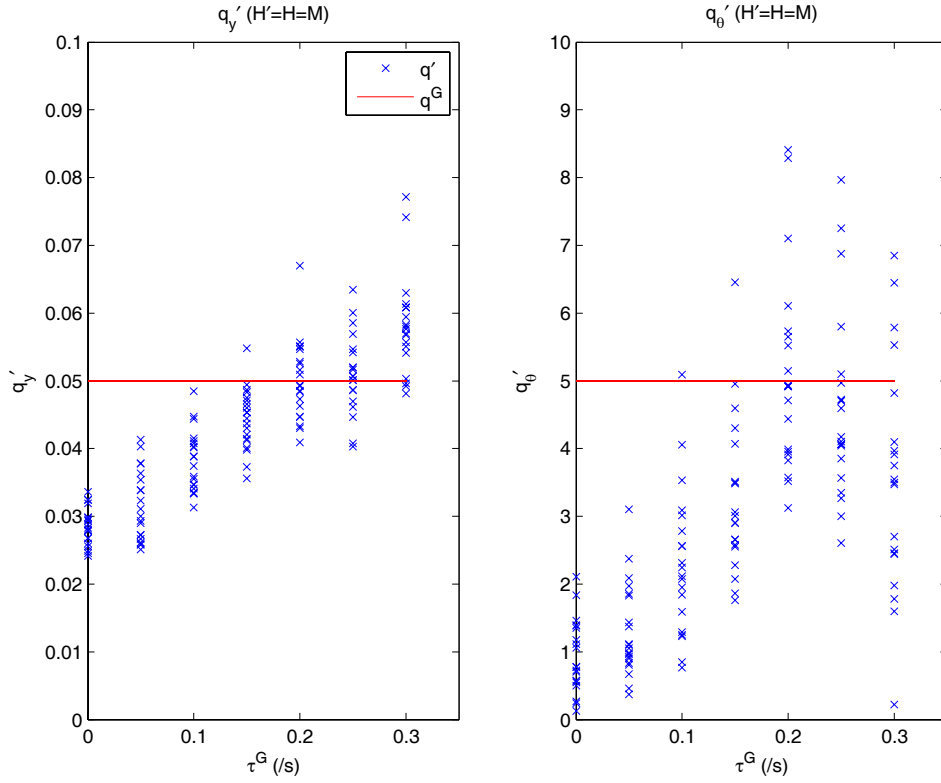
Figure 4.15: q_y' and q_θ' vs. τ^G. $\tau' = 0.2$ seconds for all trials

Figure 4.15 shows that there is little bias when $\tau^G = \tau' = 0.2$ secs (i.e. the real delay matches the identified delay), but significant underestimation of both q_y' and q_θ' when $\tau^G < 0.2$ s (real delay is less than the identified delay). When $\tau^G > 0.2$ secs (real delay exceeds the identified delay), the pattern of bias is less clear, but is non-zero for both q_y' and q_θ'. It is clear that finding the correct delay is very important for avoiding bias.

4.2.5.2 Identification of delay using identification procedure

To demonstrate whether the algorithm correctly identifies delay, identification of $\left(q_y', q_\theta', \tau'\right)$ was attempted on models with a range of τ^G from 0 to 0.3 seconds using the full procedure of section 4.1.4.3. Results for identification of τ' are shown in Figure 4.16. τ' is discrete, so the points are artificially blurred to show number of identifications at each delay point, and the number of points is shown in brackets. A

least squares fit line to the identified delay is shown by the blue dashed line, and perfect delay identification is shown in red.
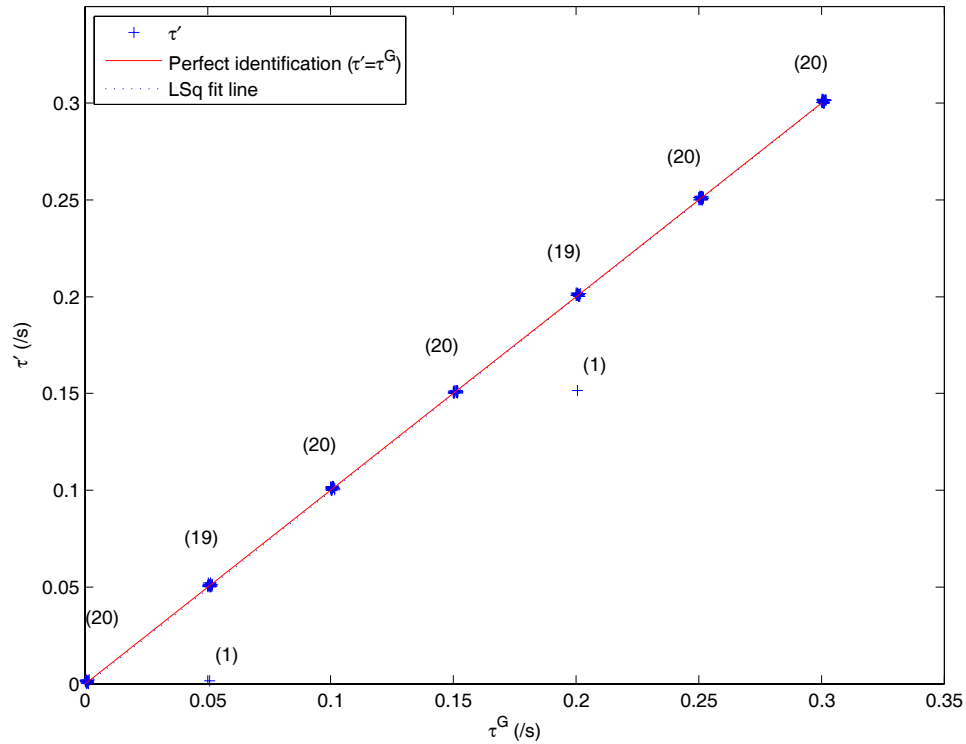
Figure 4.16: identified delay τ' (/secs) vs. actual model delay τ^G (/secs). $\mathbf{H'} = \mathbf{H} = \mathbf{M}$

The result shows perfect identification in all but two cases out of 140 trials. Note, however, that this is for perfect noise model case ($H' = H = M$), and may not be as good with an identified noise model ($H' \neq H$). Results for identification of q_y' and q_θ' for the same trial are shown in Figure 4.17.
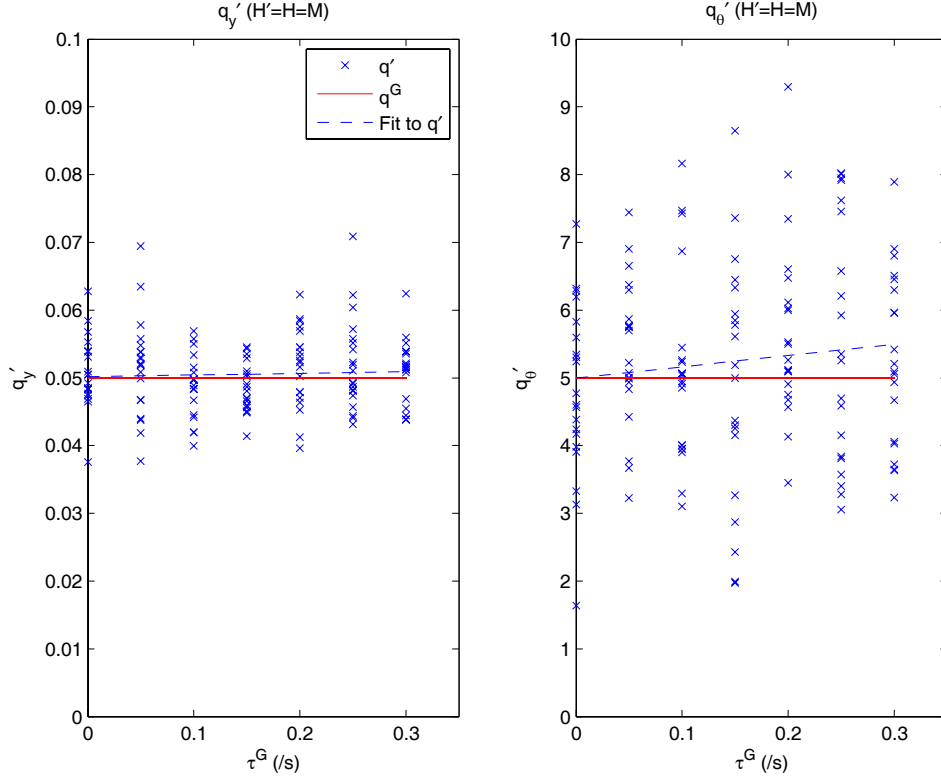
Figure 4.17: Identified parameters $(q_y ', q_\theta ')$ vs. real model delay τ^G (/s) with $H' = H = M$

Best fit lines to these results show little systematic bias in q_y' and little dependence on τ^G. q_θ' seems to show increased bias with increased τ^G, but this is mainly due to outliers for $\tau^G = 0.2$, because of the large variance in q_θ'. Delay in real drivers is likely to be close to 0.2 seconds [36, 39], so if a perfect noise model could be found, the bias in $\{q_y', q_\theta'\}$ would be acceptable.

Bias due to identification of τ' becomes more complicated when H' has to be identified, because the two identifications are interdependent. However, the iterative computation of noise model and model optimisation as explained in section 4.1.4.3 should minimise any resulting bias. Identification of (q_y', q_θ', τ') with an identified H' is covered in the next section (4.2.5.3).

4.2.5.3 Identification of time delay with an identified noise model

Figure 4.16 showed that near perfect identification of τ' was possible with $H' = H$. However, when identifying real data the noise model has to be identified, and the identification of τ' may be degraded as a result. To test this, one iteration of the algorithm from section 4.1.4.3 was carried out to identify $\left(q_y', q_\theta', \tau' \right)$ for a range of $0 \leq \tau'_0 \leq 0.3$ (i.e. the delay assumed when fitting H'_1). The identification was tried at three τ^G values (0, 0.1, 0.2 secs), and three driver noise levels $\Xi(\eta) = [1°, 5°, 10°]$ giving nine combinations shown on the subplots of Figure 4.18. Each subplot shows τ'_1 vs. τ'_0 for 30 trials.

For successful iteration τ' must approach τ^G for successive iterations (i.e. $\tau'_i < \tau'_{i-1}$ for $\tau'_{i-1} > \tau^G$, and $\tau'_i > \tau'_{i-1}$ for $\tau'_{i-1} < \tau^G$). This region is that bounded by the solid and the dashed lines in each of the subplots of Figure 4.18. The algorithm will not iterate toward a correct τ' if $\tau'_i = \tau'_{i-1}$ for $\tau'_i \neq \tau^G$, so any identifications on the dashed line $\tau'_1 = \tau'_0$ indicate that τ', and hence q_y' and q_θ' (see section 4.2.5.1) will be incorrect.
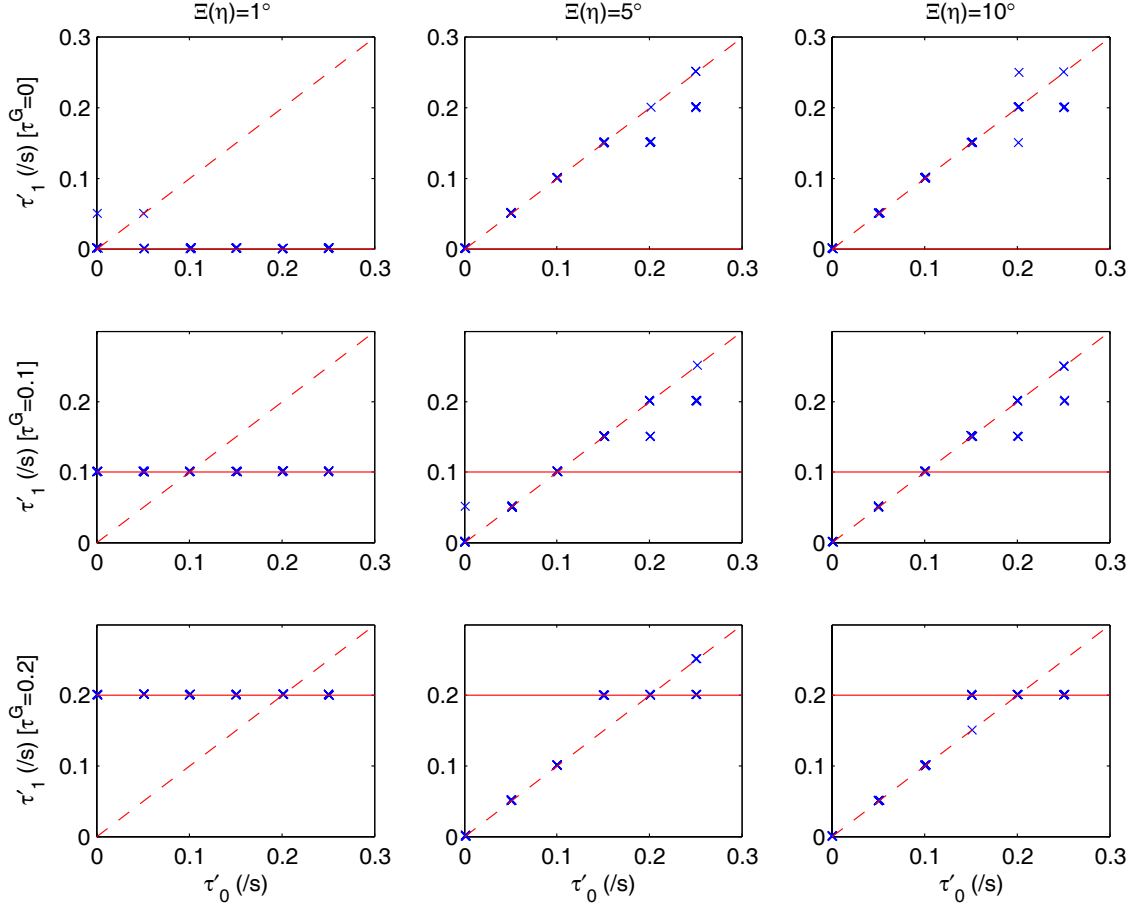
Figure 4.18: delay τ' vs. $0 \le \tau'_0 \le 0.3$ identified for one iteration ($\mathbf{i}_{max} = 1$) of algorithm in section 4.1.4.3. Subplots show $\tau^G = [0, 0.1, 0.2]$, and $\Xi(\eta) = [1^o, 5^o, 10^o]$

The results of Figure 4.18 show that for $\Xi(\eta) = 1^\circ$ (three left hand plots) identification was near-perfect, with $\tau'_1 = \tau^G$. This implies that no iteration is required for correct delay identification for a very low noise level $\Xi(\eta) = 1^\circ$. The exception was $\left(\tau^G = 0, \tau'_0 = [0, 0.05]\right)$, where some mis-identification instances occurred. The cause of this is unclear, but it is unlikely to be significant given that driver delay is non-zero.

Both noise levels $\Xi(\eta) = 5^\circ$ and $\Xi(\eta) = 10^\circ$ show similarly poor identification of τ', with a majority of the identifications falling on the dashed line $\tau'_1 = \tau'_0$. This indicates that there is no tendency to iterate toward a correct solution. The delay

$\tau^G = 0.2$ shows some tendency toward correct convergence, but only in the immediate vicinity of the correct answer $\tau'_0 = \tau^G$ (i.e. for $\tau'_0 = [0.15, 0.2, 0.25]$).

The reason for this poor convergence seems to be error in the noise model. The noise model H'_i incorporates model error ($G - G'_{i-1}$ in equation (4.10)) caused by $\tau'_{i-1} \neq \tau^G$. The subsequent driver model $G'_i\{H'_i\}$ parameter estimates $\left(q_{yi}', q_{\theta i}', \tau'_i\right)$ are found using this erroneous noise model H'_i (equation (4.20)). The parameter estimates $\left(q_{yi}', q_{\theta i}', \tau'_i\right)$ for driver model $G'_i\{H'_i\}$ are then biased toward $\tau'_i = \tau'_{i-1}$ by the incorrect H'_i.

$\Xi(\eta)$ for the real driver is around $10°$ so the algorithm seems to be unsuitable for identification of τ' on real driver data (as tends to give $\tau' = \tau_0$). The approach adopted for the identification of real driver data was therefore to identify $\{q_y', q_\theta'\}$ for a range of feasible delays τ to show a range of feasible $\{q_y', q_\theta'\}$. This work is described in chapter 5.

4.2.6 *Fitted driver model (G_I to G_{VIII})*

In this section identification of $\{q_y, q_\theta\}$ was attempted with each of the models G_I to G_{VIII} proposed in chapter 3. The aim was to fully validate the fitting procedure for each model, and to assess the performance of the algorithm in each case. A realistic driver delay of $\tau^G = 0.2$ secs was used throughout this section. $\tau' = \tau_G$ was assumed because identification of delay was unreliable as illustrated in the previous section. Where possible, trials were conducted at 20 m/s and 50 m/s to check for speed dependence. A maximum of eight iterations of the procedure ($i \leq 8$ in section 4.1.4.3) was used, and a noise model of the correct order was fitted ([2/2] for G_I to G_V and [4/4] for models G_{VI} to G_{VIII}). Identification was attempted with the noise model $H'\{q_y', q_\theta', \tau'\}$ identified by the algorithm of equation (4.21). Mean and standard deviation of the identified parameters of G_I to G_{VIII} and details of the identification

parameters are listed in Table 4.2 at the end of the chapter. Driver noise $\Xi(\eta)=10°$ throughout this section.

4.2.6.1 Model G_I

The simulation for G_I is shown diagrammatically in Figure 4.19. Inputs to the estimated driver model G_I' include both preview offsets y_p and both vehicle states (v,ω), and the parameters to be identified are (q_y', q_θ') as delay was not identified ($\tau'=\tau^G$ for all trials).
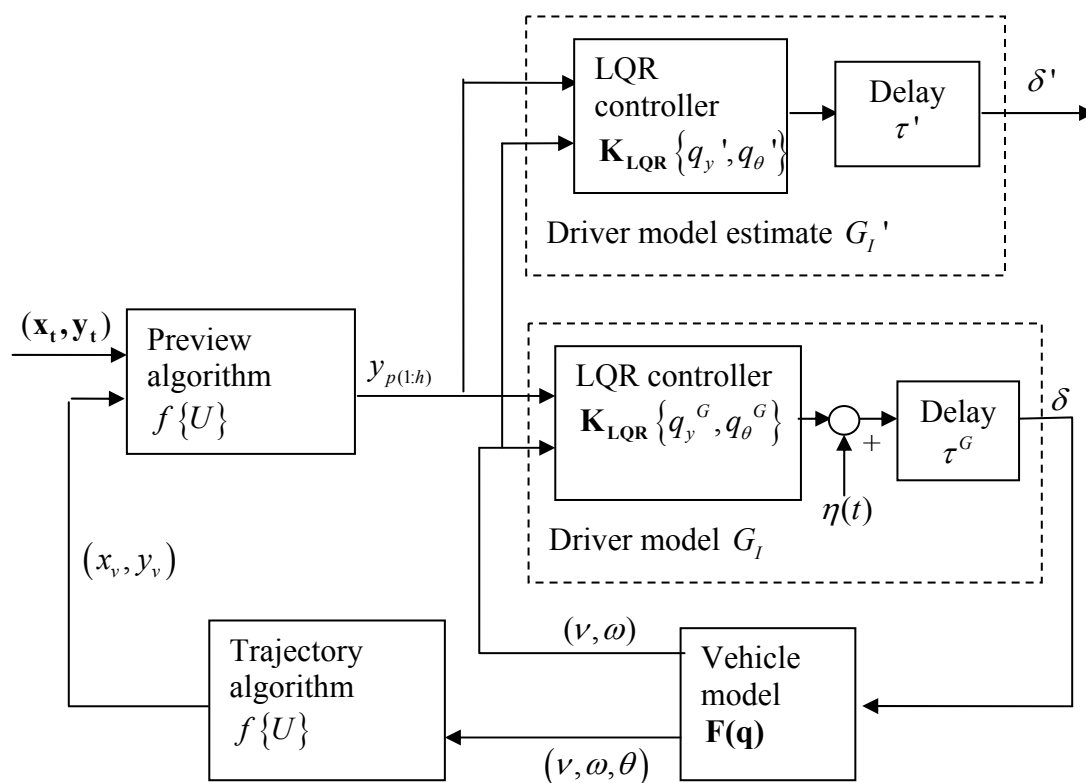
Figure 4.19: Simulation flow diagram for identification validation of G_I

Figure 4.20 shows the results of 50 identification trials at each speed for model estimate G_I'. Each trial is shown as a circle on axes of q_y' vs. q_θ', for both 20 m/s and 50 m/s. The true parameter values (q_y^G, q_θ^G) are shown as red lines.
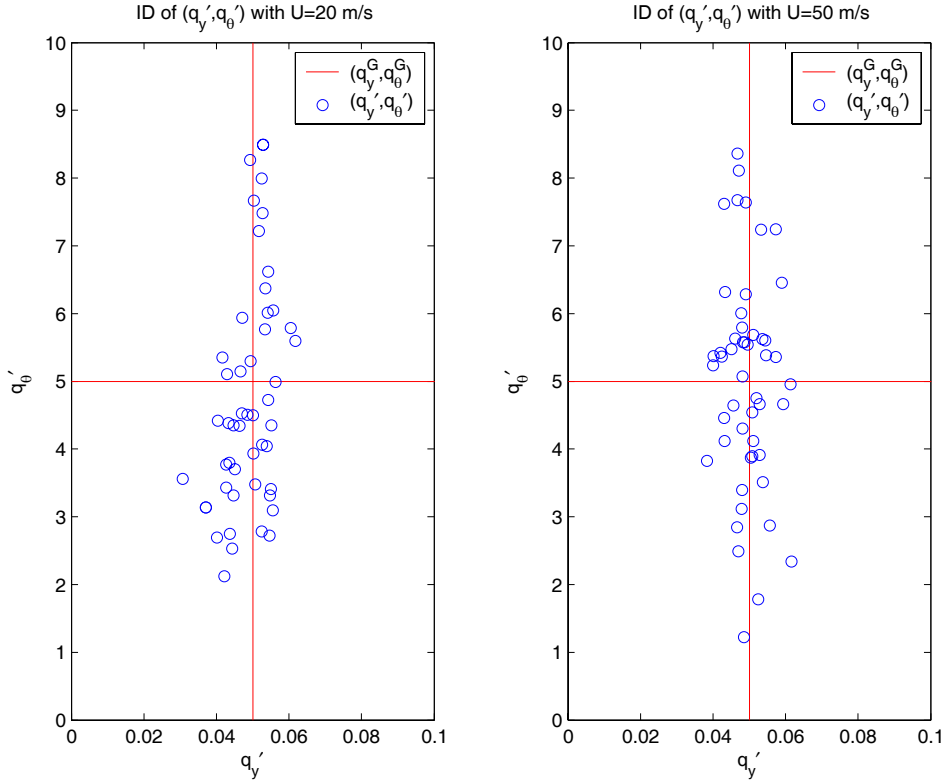
Figure 4.20: Identification of $\mathbf{G_I}$ at 20 m/s and 50 m/s with $\boldsymbol{\tau}' = \boldsymbol{\tau}^{\mathbf{G}} = \mathbf{0.2\ secs}$, using $\mathbf{H}'\{\mathbf{q_y}', \mathbf{q_\theta}', \boldsymbol{\tau}'\}$ (noise model identified using equation (4.21))

Bias in the parameter estimates was measured using the percentage error in the mean of the identified parameters as in equation (4.26). The variance of the identified parameters was measured using the standard deviation of the identified parameters as a percentage of the true parameter value, as shown in equation (4.27).

$$\mu_{err}(q_y', q_\theta') = 100\left(\frac{\left(\mu(q_y') - q_y^G\right)}{q_y^G}, \frac{\left(\mu(q_\theta') - q_\theta^G\right)}{q_\theta^G}\right) \tag{4.26}$$

$$\sigma_{err}(q_y', q_\theta') = 100\left(\frac{\sigma(q_y')}{q_y^G}, \frac{\sigma(q_\theta')}{q_\theta^G}\right) \tag{4.27}$$

At 20 m/s, bias is small for both parameters $\mu_{err}(q_y', q_\theta') = (-2.2, -4.6)\%$. Standard deviation was three times larger for q_θ' than q_y' with $\sigma_{err}(q_y', q_\theta') = (12.8, 33.8)\%$. This result is consistent with that observed for the perfect noise model case. The larger bias for q_θ' is consistent with its larger variance given the limited sample size.

At 50 m/s, slightly less variance was found $\sigma_{err}(q_y', q_\theta') = (10.8, 32.1)\%$, giving even lower bias $\mu_{err}(q_y', q_\theta') = (-1.0, -0.4)\%$. There seems to be little dependence of the identification on speed. Neither of the speeds show a correlation between $\mu(q_y')$ and $\mu(q_\theta')$ so bias of q_y' and q_θ' is independent.

4.2.6.2   Model G_{II}

The same procedure was used to validate identification of G_{II}'. Figure 4.21 shows the simulation for G_{II} where the only input to G_{II} is the preview y_p.   50 trials identifying q_y' and q_θ' were carried out at 20 m/s only. Figure 4.22 shows the identification results for this model.
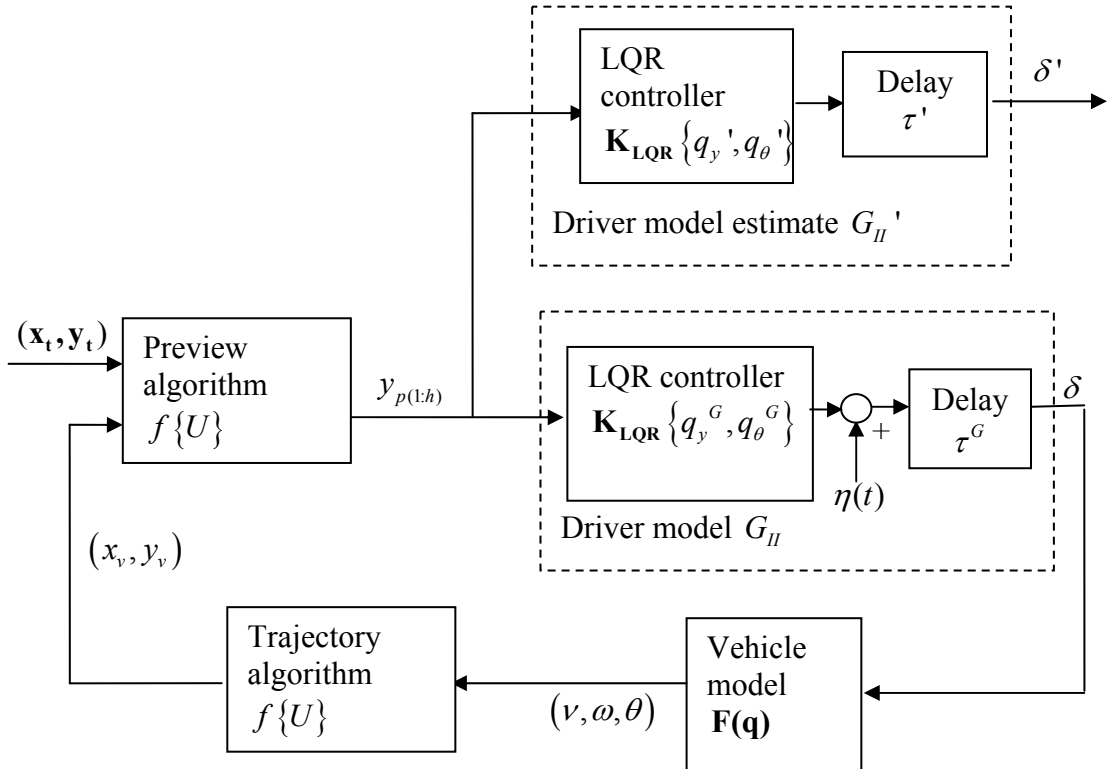
Figure 4.21: Simulation flow diagram for identification validation of G_{II}
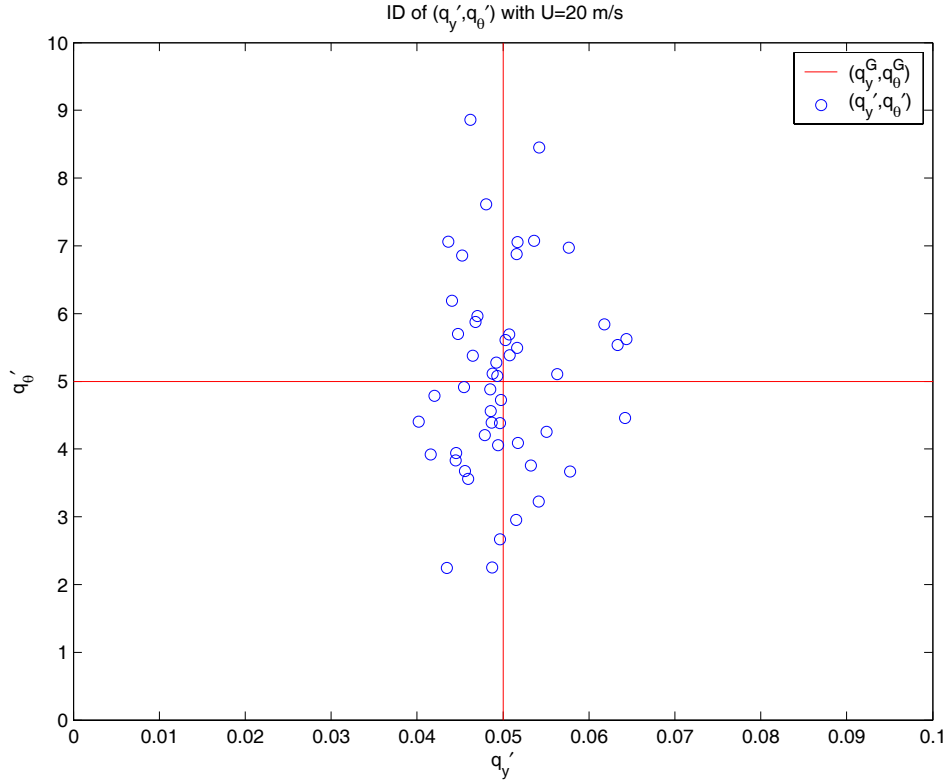
Figure 4.22:Identification of $\mathbf{G_{II}}$ with $\tau^G = 0.2\,\mathrm{secs}$, using $\mathbf{H'}\{\mathbf{q_y}',\mathbf{q_\theta}',\tau'\}$ (noise model identified using equation (4.21))

Bias is less than for G_I for both parameters $\mu_{err}(q_y',q_\theta') = (-1.0, 0.4)\%$ and variance is similar to that for G_I with $\sigma_{err}(q_y',q_\theta') = (11.4, 29.5)\%$.

It was not possible to validate the model at 50 m/s because with delay present, the driver-vehicle system is unstable with these (q_y^G, q_θ^G) values. This does not mean that the model is invalid at high speed, as a driver might use other (q_y^G, q_θ^G). However, if $(q_y', q_\theta') = (0.05, 5)$ were identified from real data at high speed the results would be suspicious, as such a controller is known to be unstable even without noise present.

4.2.6.3   Model G_{III}

The simulation carried out for identification of G_{III}' is shown in Figure 4.23. Driver model inputs are now y_p and ω, and again (q_y', q_θ') must be identified. Results for identification at 20m/s and 50m/s are shown in Figure 4.24.

Figure 4.23: Simulation flow diagram for identification validation of G_{III}
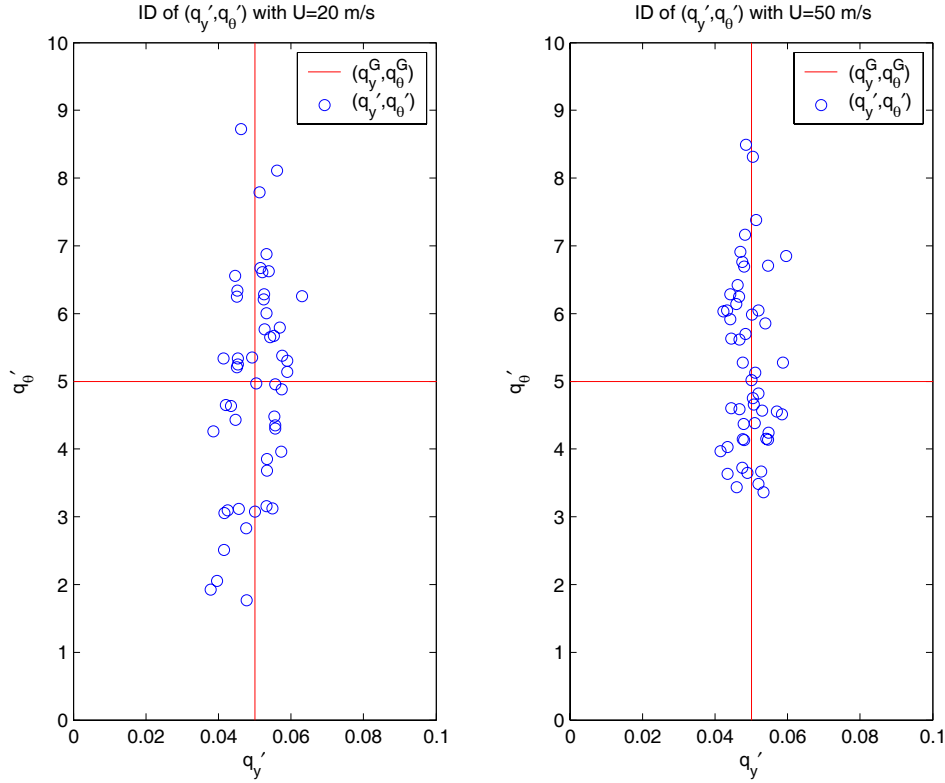
Figure 4.24: Identification of $\mathbf{G}_{\mathrm{III}}$ at 20 m/s and 50 m/s with $\tau' = \tau^G = 0.2\,\mathbf{secs}$, using $\mathbf{H}'\{\mathbf{q_y}', \mathbf{q_\theta}', \tau'\}$ (noise model identified using equation (4.21))

Again acceptable variance is achieved for both speeds. At 20 m/s, bias is very small $\mu_{err}(q_y', q_\theta') = (0.4, -1.0)\%$, and variance is similar to that for G_I with $\sigma_{err}(q_y', q_\theta') = (11.4, 29.5)\%$. At 50 m/s, bias is slightly increased $\mu_{err}(q_y', q_\theta') = (-1.2, 5.4)\%$ but variance is reduced with $\sigma_{err}(q_y', q_\theta') = (8.8, 25.8)\%$.

There is therefore some speed dependence in the identification of G_{III} which was not present for G_I. In chapter 3, section 4.4.3 it was observed that G_{III} gave similar steer angle outputs to G_I at 20 m/s, but differed at 50 m/s due to lack of sideslip feedback. It is likely that this difference in steer angle could explain the difference in identification results for G_I and G_{III} at 50 m/s.

4.2.6.4   Model G_{IV}

Figure 4.25 shows the simulation schematic for G_{IV}. This model involves feedback of the steer angle delay states $\delta_{N_d-1},...,\delta$ as well as y_p and (v,ω).

Identification of N_d was attempted, but was unsuccessful. It was shown in chapter 3 section 4.4.6 that steer angle δ for G_I and $G_{IV}\{N_d=4\}$ are almost identical. Noting also that $G_I = G_{IV}\{N_d=0\}$, this implies that the steer angle time histories $\delta(G_{IV}\{N_d=0\})$ and $\delta(G_{IV}\{N_d=4\})$ are almost identical. This implies that N_d' will have very little effect on δ'. This fact makes identification of N_d' poor because the prediction error ε (where $\varepsilon = H'^{-1}(\delta-\delta')$) will not be affected by N_d', and hence the optimisation routine fminsearch cannot converge to the correct N_d' value. For this reason $N'_d = N_d = 4$ for all identifications in this section.

As for previous models, the parameters to be identified for G_{IV} are (q_y',q_θ'), with $\tau' = \tau^G = 0.2\,\text{s}$. Figure 4.26 shows the results of 50 identifications for 20 m/s and 50 m/s.
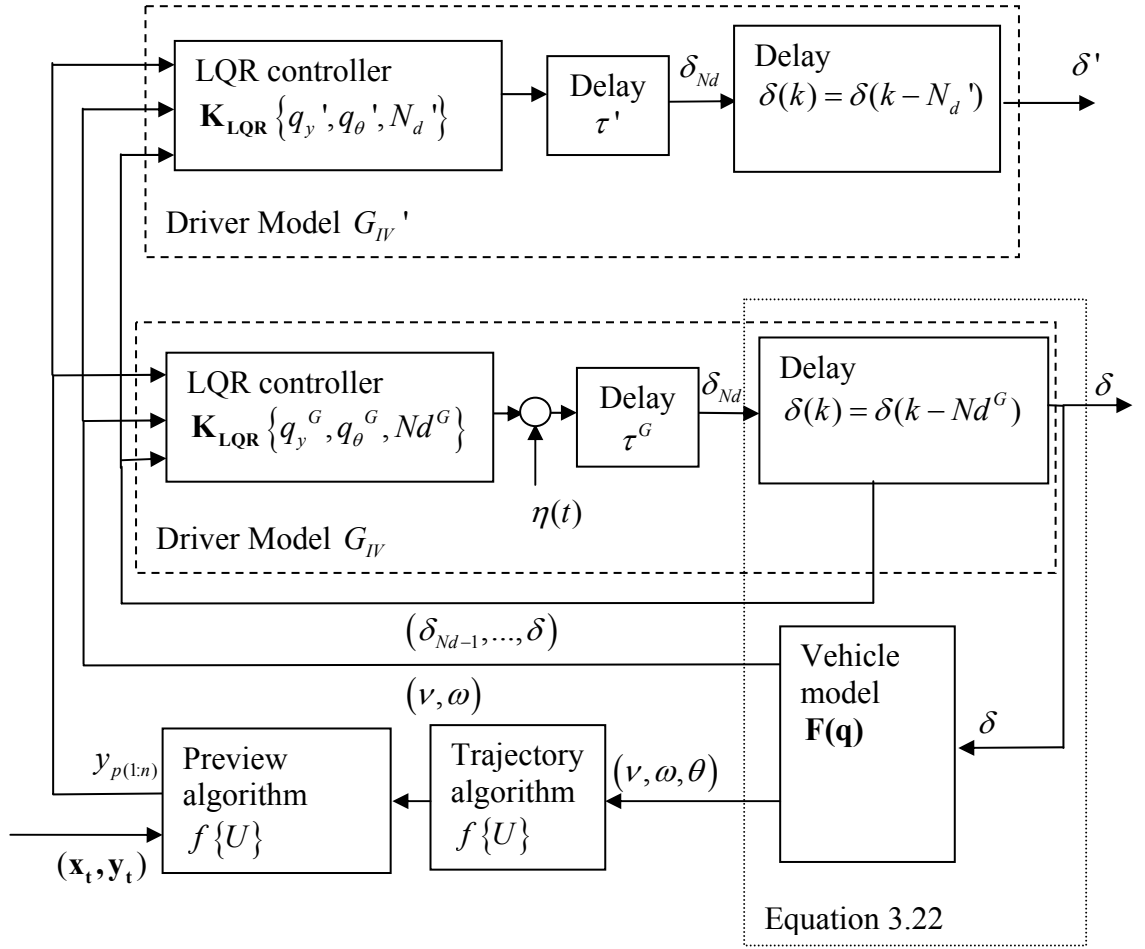
Figure 4.25: Simulation flow diagram for identification validation of G_{IV}
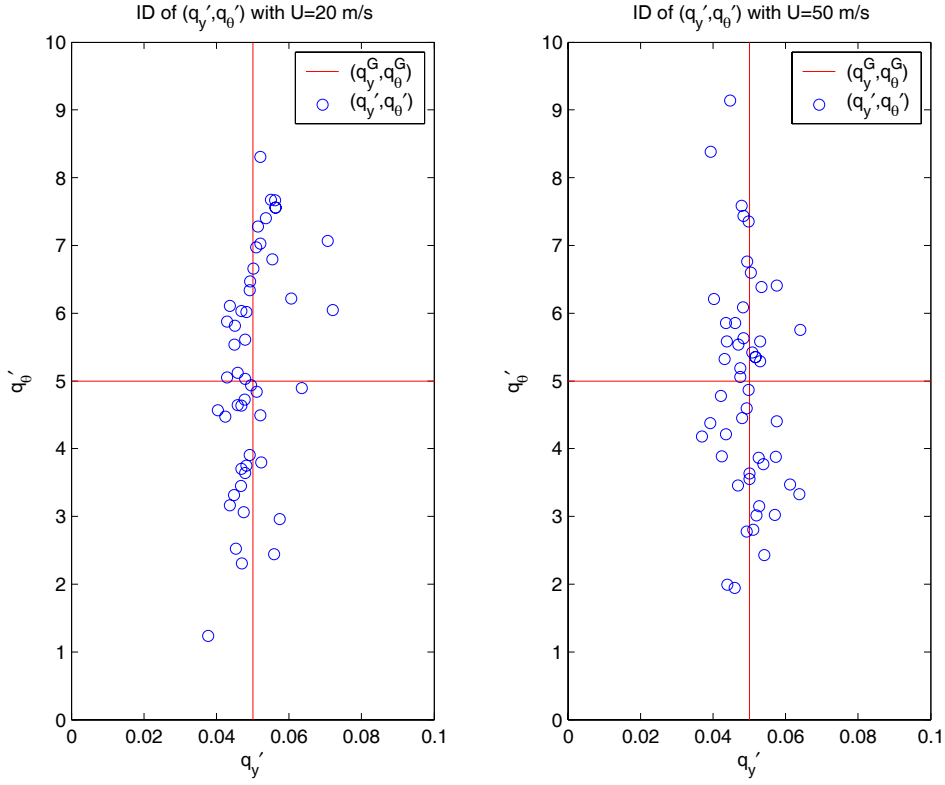
Figure 4.26: Identification of $\mathbf{G_{IV}}$ at 20 m/s and 50 m/s with $\boldsymbol{\tau\,' = \tau^G = 0.2\,\text{secs}}$, $\mathbf{N_d\,' = N_d = 4}$, using $\mathbf{H'\{q_y\,',q_\theta\,',\tau\,'\}}$ (noise model identified using equation (4.21))

At 20 m/s, both bias and variance are slightly larger than those of G_I with $\mu_{err}(q_y\,',q_\theta\,') = (1.0, 6.1)\%$ and $\sigma_{err}(q_y\,',q_\theta\,') = (14.0, 36.7)\%$. At 50 m/s, both bias and variance are similar to G_I with $\mu_{err}(q_y\,',q_\theta\,') = (-1.2, -2.0)\%$ and $\sigma_{err}(q_y\,',q_\theta\,') = (11.8, 32.3)\%$. The similarity of bias and variance at both speeds is consistent with the similarity in steer angle δ for G_I and G_{IV} seen in section 3.4.5.

4.2.6.5   Model $\mathbf{G_V}$

The simulation carried out for identification of G_V' is shown in Figure 4.27. For G_V the parameters $\left(q_y', q_\theta', \omega_n'\right)$ were identified, but only 30 trials were carried out, as the identification was much slower with a three dimensional parameter space to search. ξ' was not identified, but set to $\xi' = \xi^G = 0.707$. A value of $\omega_n^G = 1\,\text{Hz}$ was used. Only results for identifications at 20 m/s are shown in Figure 4.28 because G_V is unstable at $U = 50$ m/s with the parameter values chosen.
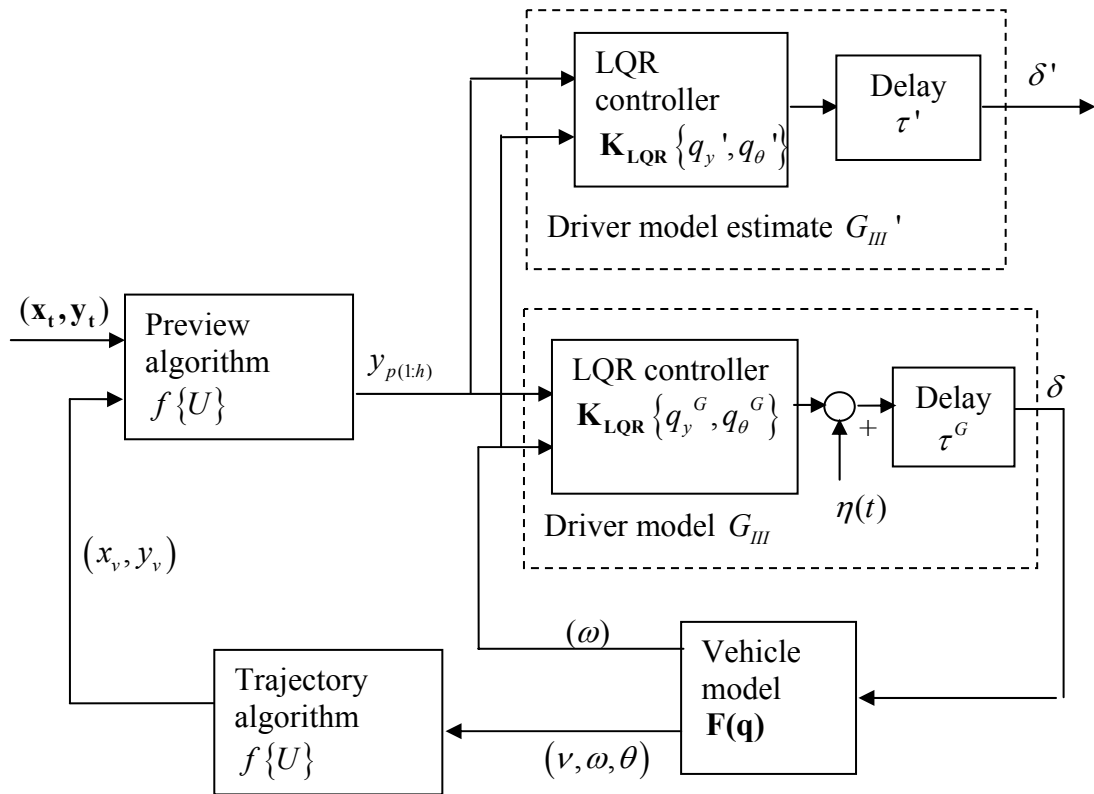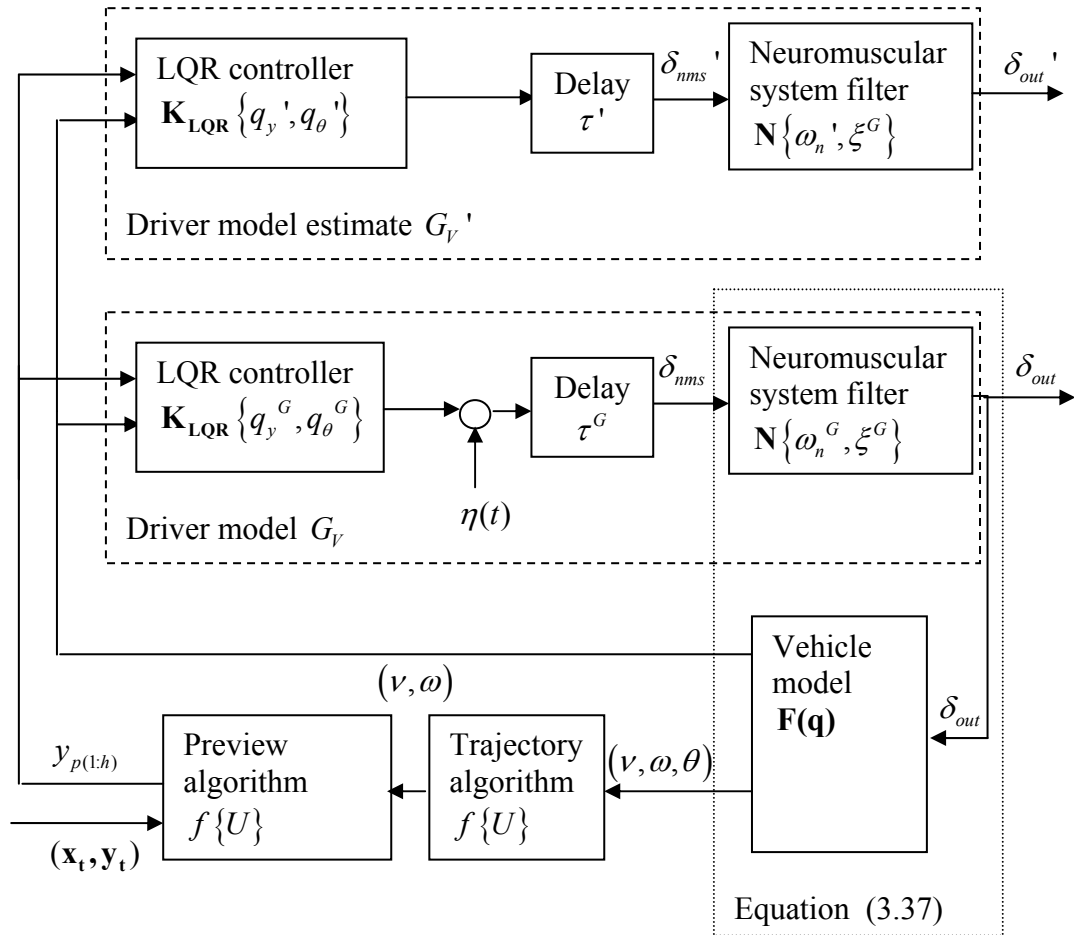

Figure 4.27: Simulation flow diagram for identification validation of $\mathbf{G_V}$
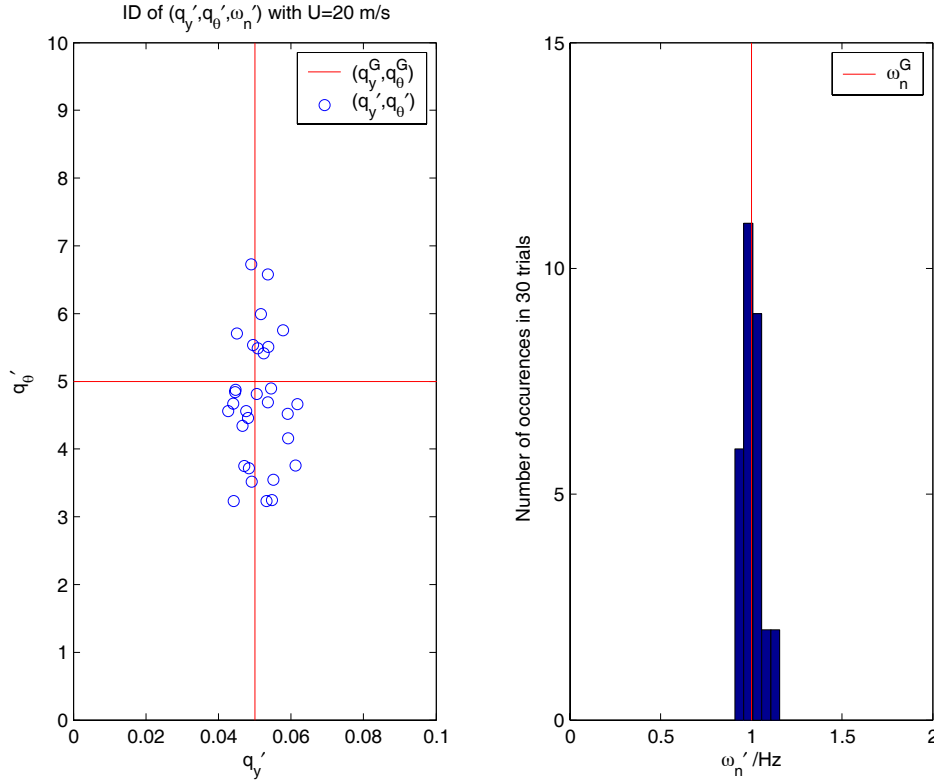
Figure 4.28: Identification of $\mathbf{G_V}$ at 20 m/s with $\tau' = \tau^G = 0.2$ secs, using $\mathbf{H}'\left\{\mathbf{q_y}', \mathbf{q_\theta}', \tau'\right\}$ (noise model identified using equation (4.21))

The results show that bias of $\mu_{err}(q_y', q_\theta') = (2.4, -6.2)\%$ is comparable to that of G_I but with reduced variance of q_θ' with $\sigma_{err}(q_y', q_\theta') = (10.6, 19.1)\%$. This is hard to compare with previous models as there are fewer samples. ω_n', however, is identified with very little bias $\mu_{err}(\omega) = 0.5\%$ and small standard deviation $\sigma_{err}(\omega) = 5.8\%$. It is possible that the very oscillatory steer angle δ demonstrated in chaper 3, section 3.4.6 has aided an accurate identification of the filter frequency ω_n^G responsible for the instability.

166

4.2.6.6 Model G_{VI}

The simulation for identification of G_{VI}' is shown in

Figure 4.29. G_{VI} features an NMS filter but also uses the (ω_n, ξ) parameters in the

derivation of the LQR controller gains. Initially, identification of all parameters

$(q_y', q_\theta', \omega_n', \xi')$ was attempted and is shown for $U = 20$ m/s in Figure 4.30 and

$U = 50$ m/s in Figure 4.31 on axes of (q_y', q_θ') and (ω_n', ξ') . Again $\tau' = \tau^G = 0.2$ s,

$\omega_n{}^G = 1$ Hz, and $\xi^G = 0.45$ as used in chapter 3. Only thirty trials were conducted at

each speed due to much slower convergence of the fminsearch algorithm with a four

dimensional parameter space to search.
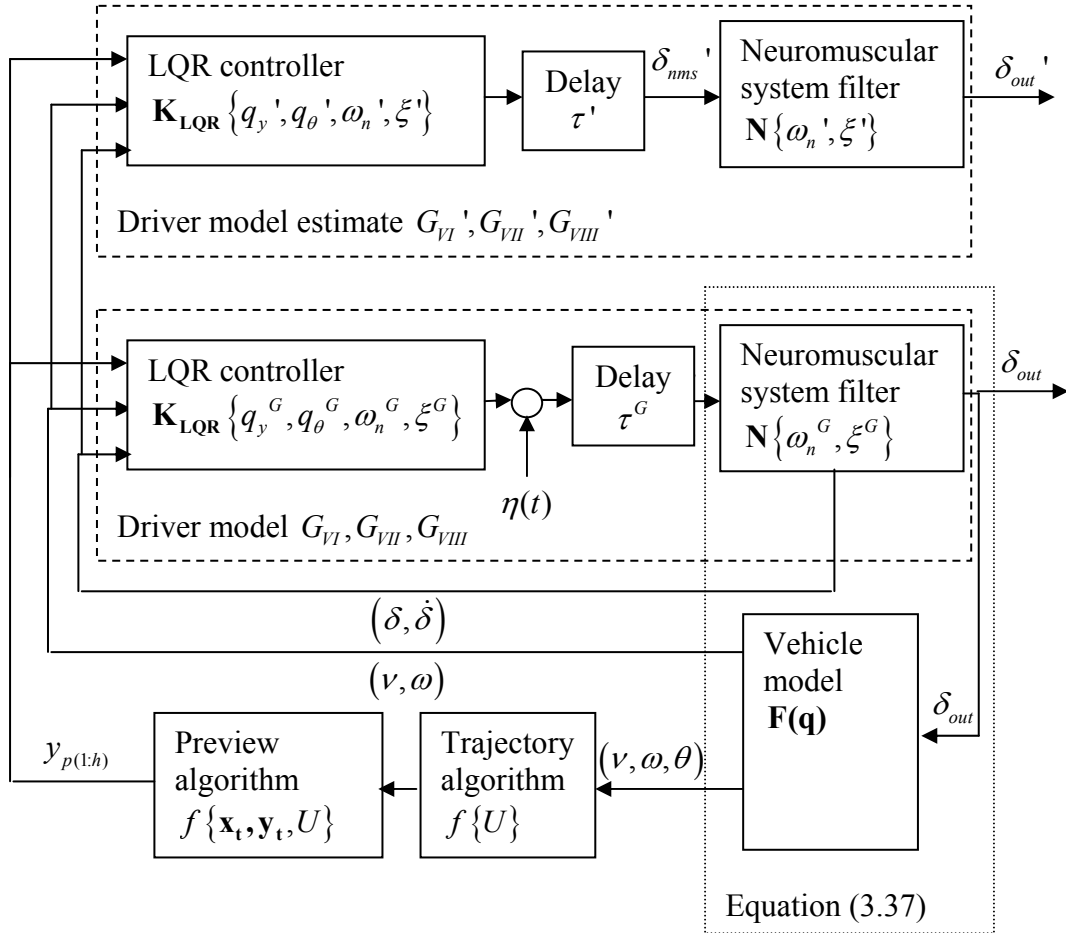
Figure 4.29: Simulation flow diagram for identification validation of $\mathbf{G}_{VI}, \mathbf{G}_{VII}, \mathbf{G}_{VIII}$
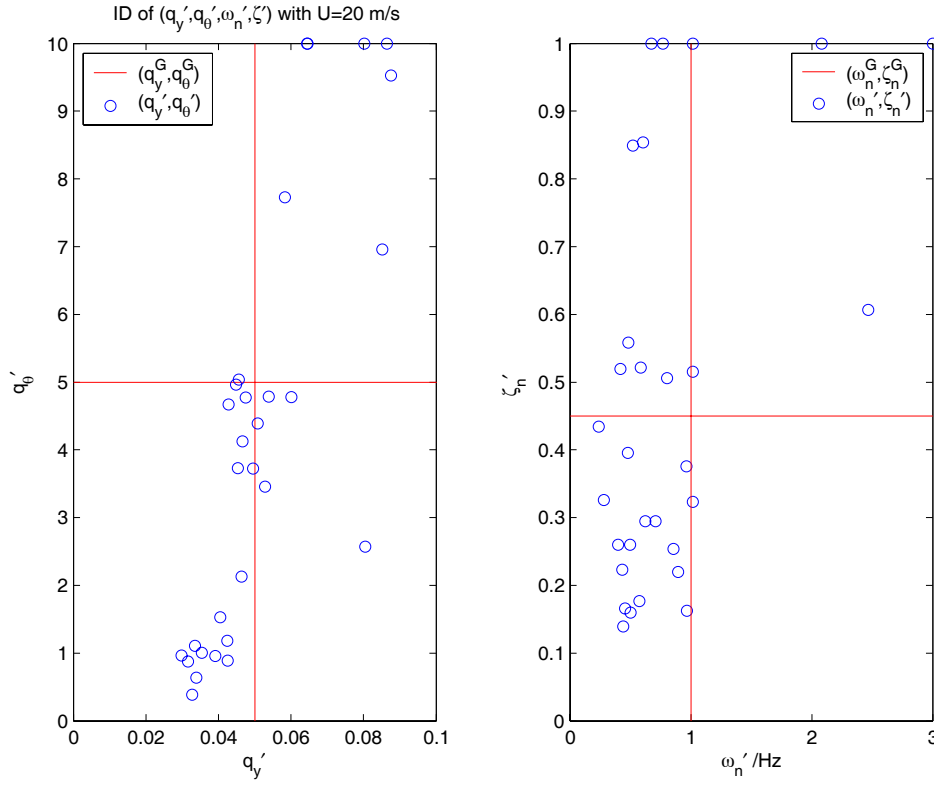
Figure 4.30: Identification of $\mathbf{G}_{VI}$ at 20 m/s with $\tau' = \tau^G = 0.2$ secs, using $\mathbf{H}'\{\mathbf{q_y}', \mathbf{q_\theta}', \tau'\}$ (noise model identified using equation (4.21))

At 20 m/s, although the bias of $\mu_{err}(q_y', q_\theta') = (3.6, -4.7)\%$ seems acceptable, the standard deviation of $\sigma_{err}(q_y', q_\theta') = (34.4, 89.5)\%$ is three times that of G_I, and for (ω_n', ξ') the variance is very large with $\sigma_{err}(\omega_n', \xi') = (81.5, 89.6)\%$. It is clear from Figure 4.30 that a few outliers, shown artificially at the edge of the axes, are correcting the mean. If these outliers were removed from the data set a large bias would be evident.
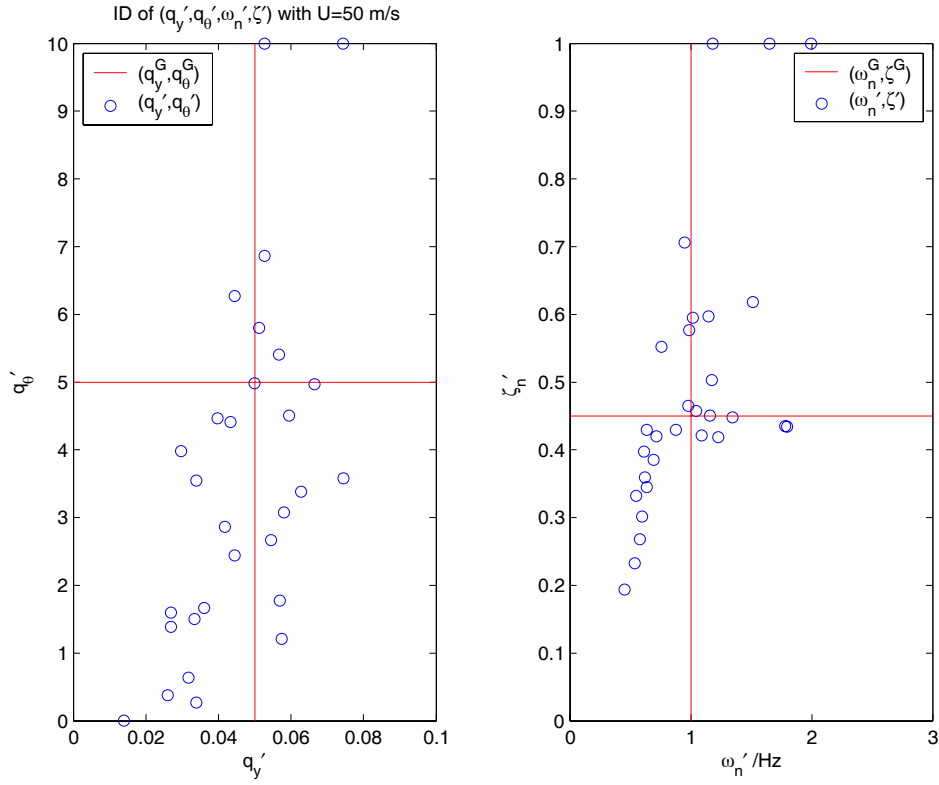
Figure 4.31: Identification of $\mathbf{G}_{VI}$ at 50 m/s with $\boldsymbol{\tau}' = \boldsymbol{\tau}^{\mathbf{G}} = \mathbf{0.2\,secs}$, using $\mathbf{H}'\left\{\mathbf{q}'_y, \mathbf{q}'_\theta, \boldsymbol{\tau}'\right\}$ (noise model identified using equation (4.21))

The results for 50 m/s show fewer outliers, and consequently lower variance than at 20 m/s for most parameters with $\sigma_{err}(q_y', q_\theta', \omega_n', \xi') = (30.8, 62.2, 41.8, 98.4)\%$. However, this means that the means of the estimates $\mu_{err}(q_y', q_\theta', \omega_n', \xi')$ are no longer corrected by the outliers, giving larger bias particularly for q_θ' with $\mu_{err}(q_y', q_\theta', \omega_n', \xi') = (-9.4, -28.5, 1.0, 22.9)\%$.

The variance for identification is much greater than that of G_V, and may be a result of identifying four parameters for G_{VI} with the same amount of information available. In order to test this, identification was attempted for parameters $(q_y', q_\theta', \omega_n')$ with $\xi' = \xi^G$ (model G_{VII} in section 4.2.6.7), then for (q_y', q_θ', ξ') with $\omega_n' = \omega_n$ (model G_{VIII} in section 4.2.6.8).

4.2.6.7 Model G_{VII}

G_{VII} is the same as G_{VI} but only $(q_y', q_\theta', \omega_n')$ were identified, while $\xi' = \xi^G$. Results for identification of parameters $(q_y', q_\theta', \omega_n')$ are shown in Figure 4.32 for $U = 20$ m/s and Figure 4.33 for $U = 50$ m/s.
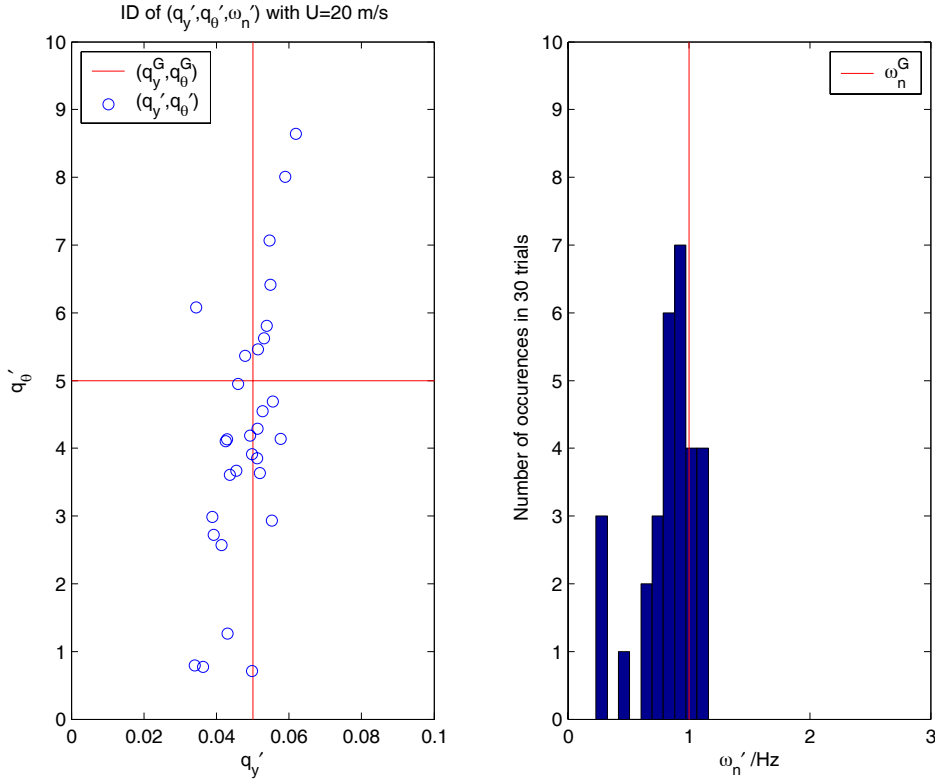
Figure 4.32: Identification of $\mathbf{G_{VII}}$ at 20 m/s with $\boldsymbol{\tau' = \tau^G = 0.2}$ secs , using $\mathbf{H'\{q_y', q_\theta', \tau'\}}$ (noise model identified using equation (4.21))

At 20 m/s, $\mu_{err}(q_y', q_\theta', \omega_n') = (-3.4, -15.4, -17.1)\%$. At first this seems to be worse than the result for G_{VI}, however, from the figure it is clear that the identifications are far more closely gathered around the correct value. This closer grouping is reflected in the standard deviation $\sigma_{err}(q_y', q_\theta', \omega_n') = (24.4, 31.3, 13.7)\%$ being less than half that of G_{VI}.
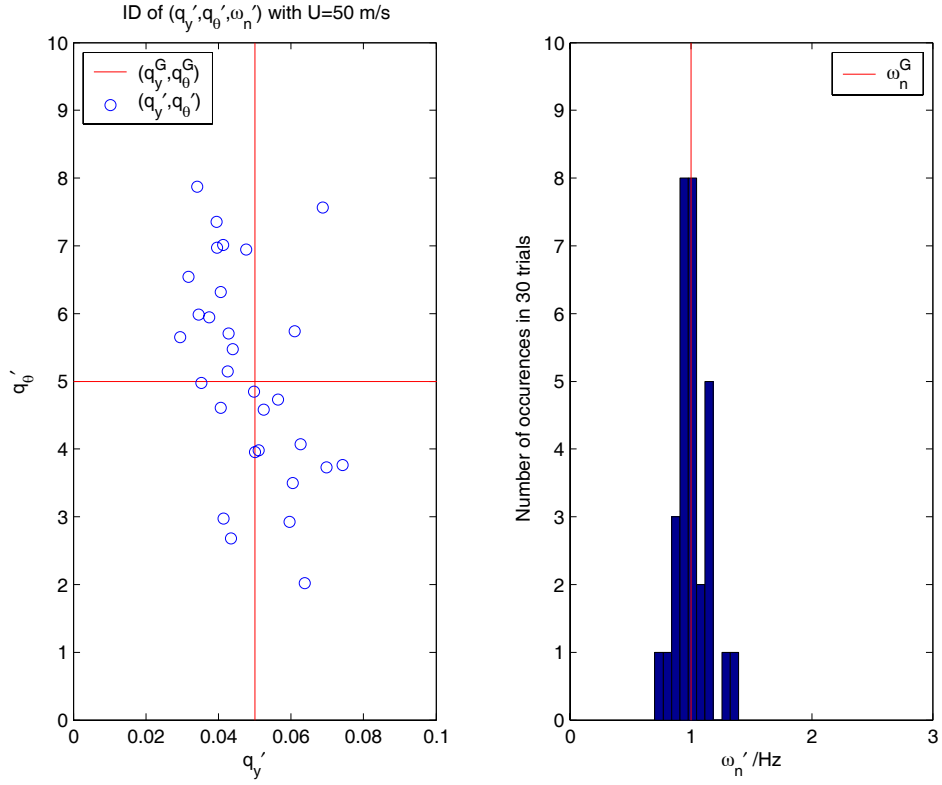
Figure 4.33: Identification of $\mathbf{G_{VII}}$ at 50 m/s with $\tau' = \tau^G = 0.2$ secs, using $\mathbf{H'}\left\{\mathbf{q_y}', \mathbf{q_\theta}', \boldsymbol{\tau}'\right\}$ (noise model identified using equation (4.21))

At $U = 50$ m/s, variance has reduced for (q_θ', ω_n'), but increased slightly for q_y from the $U = 20$ m/s case. However, the bias of the mean of the estimates is much smaller with $\mu_{err}(q_y', q_\theta', \omega_n') = (-3.6, 2.4, 1.8)\%$, so is comparable to that for G_V.

Identification of $(q_y', q_\theta', \omega_n')$ without ξ' is therefore useful in reducing bias and variance of all three parameters.

4.2.6.8 Model G_{VIII}

G_{VIII} is the same as G_{VI} but only (q_y', q_θ', ξ') are identified, with $\omega_n' = \omega_n^G$. Results for identification of parameters (q_y', q_θ', ξ') are shown in Figure 4.34 for $U = 20 \, \text{m/s}$, and Figure 4.35 for $U = 50 \, \text{m/s}$.
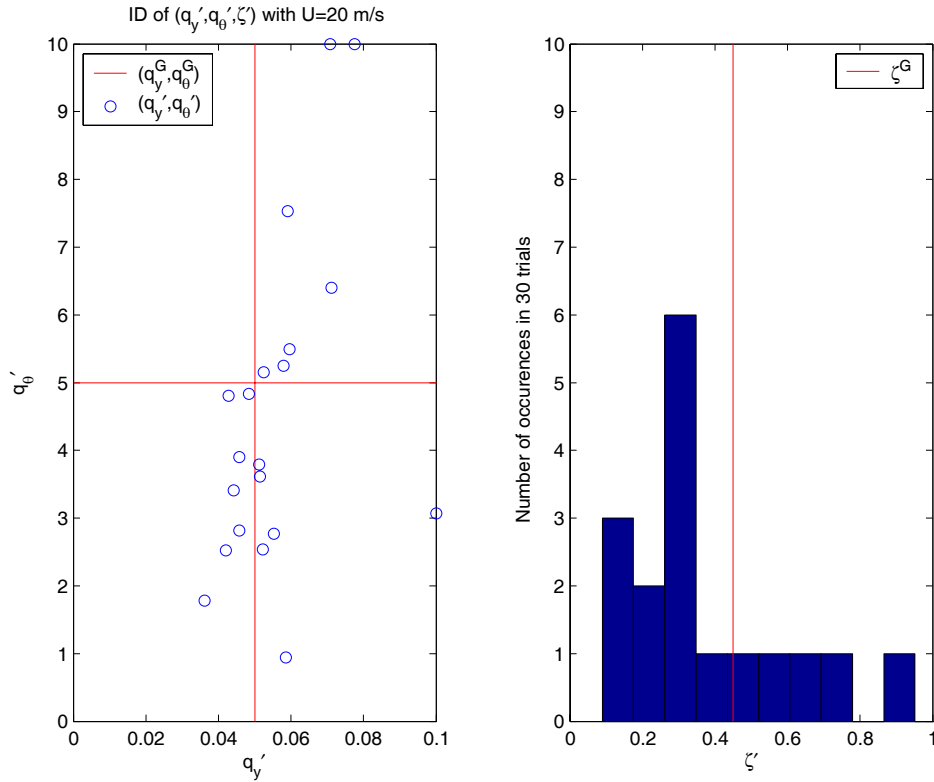
Figure 4.34: Identification of $\mathbf{G_{VIII}}$ at 20 m/s with $\boldsymbol{\tau}' = \boldsymbol{\tau}^{\mathbf{G}} = \mathbf{0.2 \, secs}$, using $\mathbf{H}'\{\mathbf{q_y}', \mathbf{q_\theta}', \boldsymbol{\tau}'\}$ (noise model identified using equation (4.21))

At $U = 20 \, \text{m/s}$ variance was large for all parameters with $\sigma_{err}(q_y', q_\theta', \xi') = (34.2, 66.5, 135.6)\%$, this is particularly true for ξ' meaning many of the 30 identifications of ξ' are outside the axes. This led to poor bias for (q_y', ξ'), with $\mu_{err}(q_y', q_\theta', \xi') = (13.6, -3.1, 31.5)\%$.
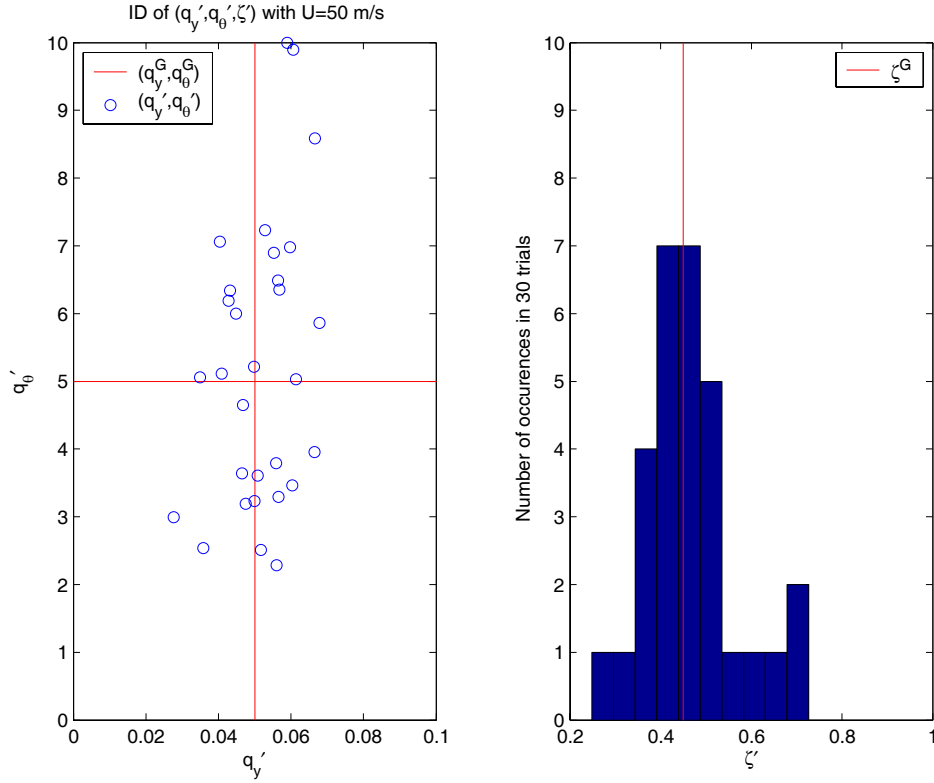
Figure 4.35: Identification of $\mathbf{G}_{\text{VIII}}$ at 50 m/s with $\boldsymbol{\tau}' = \boldsymbol{\tau}^{\mathbf{G}} = \mathbf{0.2}\,\mathbf{secs}$, using $\mathbf{H}'\{\mathbf{q}_y', \mathbf{q}_\theta', \boldsymbol{\tau}'\}$ (noise model identified using equation (4.21))

As for G_{VII}, at $U = 50$ m/s, variance is reduced from the result at $U = 20$ m/s, but $\sigma_{err}(q_\theta') = 45.4\%$ is still somewhat high. Bias for all parameters is low as a result with $\mu_{err}(q_y', q_\theta', \omega_n') = (3.0, 6.3, 3.8)\%$.

It appears that, for a given number of samples, identifying G_{VII} and G_{VIII} results in smaller parameter variance and bias compared to identifying all four parameters $(q_y', q_\theta', \omega_n', \xi')$ at once using G_{VI}. It is possible that identification of the NMS is poor at low speed because the NMS has less effect at this speed. This is shown in Figure 3.34 where the output δ is similar to G_I for $U = 20$ m/s. However, at $U = 50$ m/s, (with $\tau = 0.2$ s) the effect of NMS is more marked (Figure 3.34) so its parameters could be more reliably identified.

4.3 Conclusions

Two possible approaches to driver identification were considered, namely the direct and indirect methods. The direct method was chosen for the identification of real drivers because it involved significantly less CPU time. Weighting the prediction error υ by using a noise model reduces bias in identification of systems operating in closed loop [47], however, a good noise model is required for bias free identification. An iterative procedure was required to determine both the driver model and the noise model, so such a procedure was designed for use in identifying driver model parameters.

A validation was carried out to check that the identification procedure and the road path excitation parameters were suitable for giving an unbiased identification of the driver model. Validation consisted of a known controller driving a road path in closed loop with a vehicle, followed by an identification of the model parameters $\left(q_y{}', q_\theta{}', \omega_n{}', \xi{}' \right)$ using the inputs and outputs of the known LQR controller. Bias of identification was demonstrated when a white noise model ($H' = 1$) was used to identify data created using coloured driver noise ($H = M$). A perfect noise model ($H' = M$) eliminated bias when the driver noise η was coloured using a realistic noise filter ($H = M$).

Validation of the identification bias of $\left(q_y{}', q_\theta{}' \right)$ was carried out for a range of values of each experiment parameter. Experiment parameter values suitable for driver experiments were determined from this validation. It was found that the track PSD amplitude parameter κ should be as large as possible to minimise bias and variance of $\left(q_y{}', q_\theta{}' \right)$ by increasing the signal to noise ratio. Road spectral density roll-off gradient $\gamma \geq -2$ gave improved variance and bias of $\left(q_y{}', q_\theta{}' \right)$. For driver experiments $\gamma = -2$ was used which corresponds to white noise road curvature.

Track wavenumber cut-off values $\chi_{cut} \geq 0.05$ cycles/m gave similar bias and variance of $\left(q_y', q_\theta'\right)$. Driver experiments were carried out using $\chi_{cut} = 0.1$ to give good signal to noise ratio for noise model identification. Bias and variance of $\left(q_y', q_\theta'\right)$ was not affected systematically by vehicle speed U, so the identification procedure was suitable for data gathered from driver experiments at different vehicle speeds. A noise model H' of too low an order led to identification bias, but a noise model of too high an order was prone to outliers of $\left(q_y', q_\theta'\right)$. The order of the noise model H' must therefore be just sufficient to express the noise present.

Time delay τ' was nearly perfectly identified when a perfect noise model was used ($H' = H = M$). However, with an identified noise model H', misidentification of τ' occurred for $\Xi(\eta) \geq 5°$. For a realistic driver noise level ($\Xi(\eta) = 10°$), time delay did not iterate away from its initial value ($\tau'_1 = \tau'_0$). Delay τ' therefore could not be reliably identified, and for the identification using real driver data in chapter 5 a range of realistic driver delays is investigated.

Identification of each of the driver models G_I to G_{VIII} was validated at $U = 20$ m/s and $U = 50$ m/s with an identified noise model H', but with correct time delay ($\tau' = \tau^G$). G_I' to G_{IV}' were all identified with small bias (<6.1%) for both parameters $\left(q_y', q_\theta'\right)$. Standard deviation of q_θ' was approximately three times that of q_y' for these models. Vehicle speed had little effect on identification bias or variance of $\left(q_y', q_\theta'\right)$ for these models.

G_V' was identified with similar bias and variance of $\left(q_y', q_\theta'\right)$ to that found for G_I'. ω_n' had even lower bias (0.5%) and standard deviation (<6%). G_{VI}' had very large variance of q_y' and q_θ', leading to large bias for some parameters and rendering the model G_{VI}' unreliable for use in driver identification in chapter 5. G_{VII}' and G_{VIII}' are more successful at identifying NMS parameters than G_{VI}', giving much smaller variance of q_y' and q_θ'. However, both have large bias of q_y' and q_θ' at 20 m/s.

Figure	sub plot	Model	q_y	q_θ	H	$\Xi(e)$	$\Xi(\eta)$	H'	num	den	χ_{cut} (/1/m)	γ	κ	$\Xi(\delta_{e=0})$	U	τ^G	τ'	τ'_0
Figure 4.5		G_I	5	0.05	1	0 to 16		1	not fitted		0.05	-2	5.0E-05	11.50	20	0	ID	-
Figure 4.7	1	G_I	5	0.05	M		0 to 16	1	not fitted		0.05	-2	5.0E-05	11.50	20	0	0	-
Figure 4.7	2	G_I	5	0.05	M		0 to 16	M	not fitted		0.05	-2	5.0E-05	11.50	20	0	0	-
Figure 4.9		G_I	5	0.05	M		10	M	not fitted		0.05	-2	[5e-7 to 5e-5]	1 to 11.5	20	0	0	-
Figure 4.10		G_I	5	0.05	M		10	M	not fitted		0.05	[-3.6 to -1]	[2e-9 to 0.79e-2]	11.50	20	0	0	-
Figure 4.11		G_I	5	0.05	M		10	M	not fitted		.005 to .13	-2	5.0E-05	11.50	20	0	0	-
Figure 4.12		G_I	5	0.05	M		10	M	not fitted		0.05	-2	5.0E-05	11.50	20 to 60	0	0	-
Figure 4.13		G_I	5	0.05	M		10	M	0 to 20	0 to 20	0.05	-2	5.0E-05	11.50	20	0	0	-
Figure 4.14		G_I	5	0.05	M		10	M	0 to 20	0 to 20	0.05	-2	5.0E-05	11.50	20	0	0	-
Figure 4.15		G_I	5	0.05	M		10	M	not fitted		0.05	-2	5.0E-05	11.50	20	0 to 0.3	0.2	0.2
Figure 4.16		G_I	5	0.05	M		10	M	not fitted		0.05	-2	5.0E-05	11.50	20	0 to 0.3	ID	0
Figure 4.17		G_I	5	0.05	M		10	M	not fitted		0.05	-2	5.0E-05	11.50	20	0 to 0.3	ID	0
Figure 4.18		G_I	5	0.05	M		[1,5,10]	M	2	2	0.05	-2	5.0E-05	11.50	20	[0,0.1,0.2]	ID	0 to 0.3

Table 4.1: Validation parameters for figures of chapter 4

Figure	Subplot	Model	U	$\mu_{err}\left(q_y{}'\right)$	$\mu_{err}\left(q_\theta{}'\right)$	$\mu_{err}\left(\omega_n{}'\right)$	$\mu_{err}\left(\xi'\right)$	$\sigma_{err}\left(q_y{}'\right)$	$\sigma_{err}\left(q_\theta{}'\right)$	$\sigma_{err}\left(\omega_n{}'\right)$	$\sigma_{err}\left(\xi'\right)$
Figure 4.20	1	G_I	20	-2.2	-4.6	-	-	12.8	33.8	-	-
	2	G_I	50	-1.0	0.4	-	-	10.8	32.1	-	-
Figure 4.22		G_{II}	20	0.0	1.4	-	-	11.4	29.5	-	-
Figure 4.24	1	G_{III}	20	0.4	-1.0	-	-	12.4	31.9	-	-
	2	G_{III}	50	-1.2	5.4	-	-	8.8	25.8	-	-
Figure 4.26	1	G_{IV}	20	1.0	6.1	-	-	14.0	36.7	-	-
	2	G_{IV}	50	-1.2	-2.0	-	-	11.8	32.3	-	-
Figure 4.28		G_V	20	2.4	-6.2	0.5	-	10.6	19.1	5.8	-
Figure 4.30		G_{VI}	20	3.6	-4.7	-12.8	17.1	34.4	89.5	81.5	89.6
Figure 4.31		G_{VI}	50	-9.4	-28.5	1.0	22.9	30.8	62.2	41.8	98.4
Figure 4.32		G_{VII}	20	-3.4	-15.4	-17.1	-	14.8	39.4	24.2	-
Figure 4.33		G_{VII}	50	-3.6	2.4	1.8	-	24.4	31.3	13.7	-
Figure 4.34		G_{VIII}	20	13.6	-3.1	-	31.5	34.2	66.5	-	135.6
Figure 4.35		G_{VIII}	50	3.0	6.3	-	3.8	19.8	45.4	-	23.6

Table 4.2: Table of fitted model parameter results. μ_{err} denotes percentage error from true value, σ_{err} is standard deviation as percentage of true parameter value. $\chi_{cut} = 0.05, \gamma = -2, \kappa = 5.0 * 10^{-5}, \Xi(\eta) = 10^{o}, \tau' = \tau^{G} = 0.2s$

Chapter 5: Driver model identification results

In this chapter the results are presented for the identification of LQR models from measured driver data. First the experiment is described, and how it differs from those described in chapter 2. This includes modifications to the simulator and roads driven. In section 5.2 the process of selecting a delay (τ') for each model is described.

In section 5.3 seven of the models G_I to G_{VIII} are compared. G_{VI} was not included because its validation was not successful in chapter 4. The models are compared for goodness of fit and examples of time histories of the fitted models are included to allow the goodness of fit to be illustrated. The model parameters are then compared as well as their preview and state gains. From this analysis, G_I is selected as the most suitable model for evaluating the steering performance of the test subjects.

In section 5.4 the results for the variation of path error (lateral error and heading error) as a function of width and speed are shown, as well as the variation of the derived parameters (q_y, q_θ). The relevance of these results to the speed choice model is then discussed, and finally the variation of (q_y, q_θ) between subjects is shown. Finally conclusions are made.

5.1 Description of experiment

The intention of the experiments for this chapter was to concentrate on identifying the drivers' preview behaviour. Previous experiments have been carried out by Rix [48] to identify driver feedback behaviour. However, these were performed on straight roads, so could not identify any of the preview behaviour used by the driver to perform the steering task on curved roads. Simulator experiments were again used as described in section 5.1.2, but with some modifications to the simulator as described in section 5.1.1.

5.1.1 Simulator modifications

As discussed in chapter 2 the method used to calculate lateral error was modified for these later experiments. Whereas previously lateral error was calculated before each test and encoded into a lookup table, the new algorithm allowed lateral error to be calculated online during the experiment (inside the xPC computer). The algorithm was based on the intrinsic profile of the road (ψ, S), and calculated the lateral offset of the vehicle perpendicular to the road. See appendix D for details of the algorithm used. Buzzers were triggered when the road width was exceeded to discourage drivers from leaving the road. The vehicle model used was a linear bicycle model as described in chapter 2. The parameters of the bicycle model are listed in appendix A. Steering torque feedback was a simple gain of the steer angle with light damping.

5.1.2 Design of experiments

The test subjects drove tracks of 4km length at a fixed speed, and either 2.5m or 3.5m wide. Equations for the random road profiles used were described in chapter 4, and the parameters for these profiles are shown in the caption of Table 5.1.

The driver was given a training period of one complete 4km track at 20 m/s. It was assumed that the subject was able to learn the control of the vehicle in a short time relative to the length of the track. Rix [48] observed that adaptation of driver control

to changes in steer angle gain was very rapid (less than 10 seconds). The first 10 seconds of data from each track was not used, in order to allow for a short learning period at the speed being tested, and for any starting transients to die down. It was therefore assumed that the subject used an optimal LQR controller for the whole of the track length except this initial 10 second period.

The vehicle speed range was changed for each road width. The range was selected to be easy to keep within the road width at lowest speed, and very hard to keep within road width at the highest speed. For the 2.5m wide road, U was varied from 20m/s to 40 m/s in increments of 5 m/s, and for 3.5m width, U varied from 30m/s to 50 m/s in 5 m/s increments. Subjects were instructed to try and keep within the road width.

Experiments were carried out in sessions of 15 different 4km road sections, track 1 to track 15. Each session consisted of 5 speeds with three repetitions of each speed. Experiments were ordered with speed increasing through the test. Three repetitions at each speed allowed data to be averaged for a given speed.

One subject at one width was tested in each experiment session of 15 tracks. Each of these 15 track sessions is shown as a row in Table 5.1. Each session lasted approximately 40 minutes, so was short enough for the driver to maintain their concentration. Two of these sessions were required for each subject (one for each width) giving a total of 10 sessions for the whole experimental programme. This gave a total of 150 (4km) tracks driven, each of which was a different randomly generated track.

Session	Subject	Width /m	Vehicle speed U /ms^{-1}														
			Track 1	Track 2	Track 3	Track 4	Track 5	Track 6	Track 7	Track 8	Track 9	Track 10	Track 11	Track 12	Track 13	Track 14	Track 15
1	1	2.5	20	20	20	25	25	25	30	30	30	35	35	35	40	40	40
2	2	2.5	20	20	20	25	25	25	30	30	30	35	35	35	40	40	40
3	3	2.5	20	20	20	25	25	25	30	30	30	35	35	35	40	40	40
4	4	2.5	20	20	20	25	25	25	30	30	30	35	35	35	40	40	40
5	5	2.5	20	20	20	25	25	25	30	30	30	35	35	35	40	40	40
6	1	3.5	30	30	30	35	35	35	40	40	40	45	45	45	50	50	50
7	2	3.5	30	30	30	35	35	35	40	40	40	45	45	45	50	50	50
8	3	3.5	30	30	30	35	35	35	40	40	40	45	45	45	50	50	50
9	4	3.5	30	30	30	35	35	35	40	40	40	45	45	45	50	50	50
10	5	3.5	30	30	30	35	35	35	40	40	40	45	45	45	50	50	50

Table 5.1: Tests carried out on subjects. Each session consisted one subject on 15 tracks, lasting 40 minutes. Test track parameters: $\chi_{cut} = 0.1\,(/m)$**,** $\kappa = 5.0*10^{-5}$**,** $\gamma = -2$**,** $\Xi(\delta_{e=0}) = 11.5^{o}$**.**

A free speed choice experiment was carried out at the end of each session, whereby the subject was given a road of the same width as that tested throughout the session, and allowed to control their vehicle speed using a set of pedals. The subject was instructed to: 'go as fast as you can without leaving road, then keep constant speed'. i.e. to choose a speed for that track within the first 1 km, then keep to that speed for the rest of the track. Analysis of this data will be the subject of future work.

The test programme gave 150 tracks for each model G_I to G_{VIII} to be fitted to. Showing all this data separately is not feasible, so averaging of the derived parameters was used to determine the effect of each of the independent variables: speed, width, subject, and fitted model (G_I to G_{VIII}).

Details of the five test subjects are shown in Table 5.2. The subjects were selected from students of the university but had a variety of driving experience. Subject 1 was a novice with no road driving experience, whereas subject 2 had experience of both car and HGV driving.

Subject	Age (years)	Experience (years)	Sex	Notes
1	18	0	M	No road experience
2	30	13	M	HGV qualified
3	27	9	F	Car and minibus driver
4	24	6	M	
5	24	6	M	

Table 5.2: Details of subjects used in simulator experiments

5.1.3 Model identification

The fitting procedure validated in chapter 4 was used to identify the data from the 150 tracks with seven of the models (G_I to G_{VIII} excluding G_{VI}). This produced 1050 model identifications. Additional identifications were also carried out to explore the results for a range of time delay τ'. A database was constructed of the parameters derived from these identifications in order that combinations of results could be recalled for later comparison, and to ensure traceability of results.

G_{VI} was not fitted, as chapter 4 showed its fitting to be unreliable. The parameters (ω_n, ξ) for the neuromuscular system were identified individually for models G_{VII} and G_{VIII}. When identifying models G_{VII} and G_{VIII} the driver's internal NMS states $(\delta, \dot{\delta})$ were not measurable, so the driver steer angle and its gradient $(\delta_{out}, \dot{\delta}_{out})$ were used as inputs to the LQR controller.

The maximum number of iteration loops for the identification procedure was set to ten, as most models had converged within this number. Figure 5.1 shows the variation of q_y and q_θ for successive iterations i for 15 identifications. The data was produced by subject 2 on a 2.5m width track, shown as session 2 in Table 5.1. Parameter estimates q_y' and q_θ' are normalised by their final converged value, so that all tend towards 1. Lines are curtailed where the iteration procedure has finished due to convergence being detected.
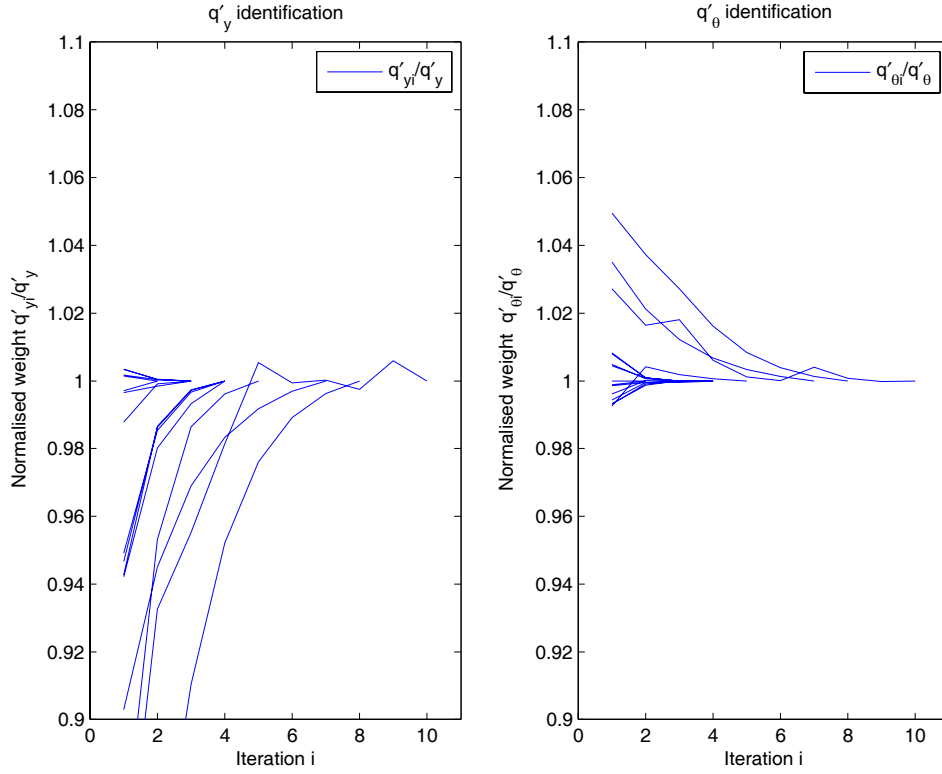
Figure 5.1: $\mathbf{q'_{yi}/q'_y}$ and $\mathbf{q'_{\theta i}/q'_\theta}$ vs number of iterations $\mathbf{i}$, showing convergence toward their final value (unity)

For all of these data q_y' has converged to within 10% of its final value after 3 iterations and q_θ' within 3%. All have converged within 1% afer 7 iterations for both q_y' and q_θ', so ten iterations was judged to be adequate.

The noise model used is of order [5/5] and was found to fit adequately to the noise recorded from real drivers without being too high an order and therefore leading to outliers. Examples of the fitted noise model are shown in section 5.3.2.

5.2 Time delay

In the previous chapter it was shown that driver delay τ could not be reliably identified. The tendency was for $\tau'_{i+1} = \tau'_i$ i.e. delay was identified as that in the previous iteration. It follows that the final delay was the same as the starting delay, giving no useful identification of τ'.

For the identification described in later sections the driver delay was therefore set at a value based on previous literature of $\tau' = 0.2\,\text{s}$ [36, 39]. The exception was model G_V which was found to only identify NMS natural frequency ω_n within the feasible range (0 to 9 Hz) when $\tau' = 0.1\,\text{s}$ was used.

A separate study was undertaken to establish the consequences of presuming this delay $\tau' = 0.2\,\text{s}$ for each model G_I to G_{VIII}. The study examined the 'goodness of fit' of each model G_I to G_{VIII} as a function of the delay τ'. The variation of parameter estimates q_y' and q_θ' as a function of the delay τ' for model G_I was also examined. This study is described in section 5.2.1.

The variation of 'goodness of fit' with τ' was compared for each subject to establish that the same τ' could be used for all subjects. This comparison is shown in section 5.2.2.

There is, however, a problem with how to compare the models' goodness of fit. Ideally $\Xi(\varepsilon)$ would be used because this is the optimisation norm which is minimised during 'model selection' (see chapter 4, section 4.1.4.1). Weighted prediction error ε was defined as follows in equation (4.12):

$$\varepsilon = H'^{-1}\upsilon = H'^{-1}\left(\delta - \delta'\right) = H'^{-1}\left(G - G'\right)u + H'^{-1}He \qquad (4.12)$$

However, H' depends on ε so is particular to the track and model being fitted. This means that $\Xi(\varepsilon)$ cannot be directly compared between G' fitted to different tracks or models. Instead, for this chapter prediction error $\Xi(\upsilon)$ was used for comparison. Unweighted prediction error υ was defined as follows in equation (4.11):

$$\upsilon = (\delta - \delta') = (G - G')u + He \qquad (4.11)$$

5.2.1 Identified parameters vs. delay for each model

To gain an understanding of the variation of parameters q_y' and q_θ' and prediction error $\Xi(\upsilon)$ with delay τ' the identification procedure was carried out with a range of fixed delay τ' varying from 0.05s to 0.3s for model G_I. G_I was fitted to data from all subjects for roads of 2.5m width. The resulting parameter estimates q_y', q_θ', and $\Xi(\upsilon)$ for model G_I are shown in Figure 5.2 and Figure 5.3. Parameters q_y', q_θ', and $\Xi(\upsilon)$ were averaged across all subjects for a given speed. For example for the speed $U = 30$ m/s:

$$\mu_{[1:5]}(q_y'{}_{\{U=30\}}) = \frac{\sum q_y'{}_{[1]\{U=30\}} + \sum q_y'{}_{[2]\{U=30\}} + \sum q_y'{}_{[3]\{U=30\}} + \sum q_y'{}_{[4]\{U=30\}} + \sum q_y'{}_{[5]\{U=30\}}}{15} \qquad (5.1)$$

Where $q_y'{}_{[1]\{U=30\}}$ denotes the three q_y' estimates for the three tracks driven by subject 1 at speed $U = 30$ m/s. The mean parameter values for the range of speeds $U = 20$ m/s to $U = 40$ m/s given by the vectors $\mu_{[1:5]}(q_y')$, $\mu_{[1:5]}(q_\theta')$ and $\mu_{[1:5]}(\Xi(\upsilon))$ should then approximate to the ensemble average of these parameters for a large population of test subjects. Points where $\Xi(\upsilon) > 25°$ were not included as the identification was presumed not to have converged. This led to some missing points for $\tau' = 0.05$ s and $\tau' = 0.1$ s. Figure 5.2 shows the mean prediction error $\mu_{[1:5]}(\Xi(\upsilon))$ plotted against delay τ' for the range of speeds used in the experiments at 2.5m width.
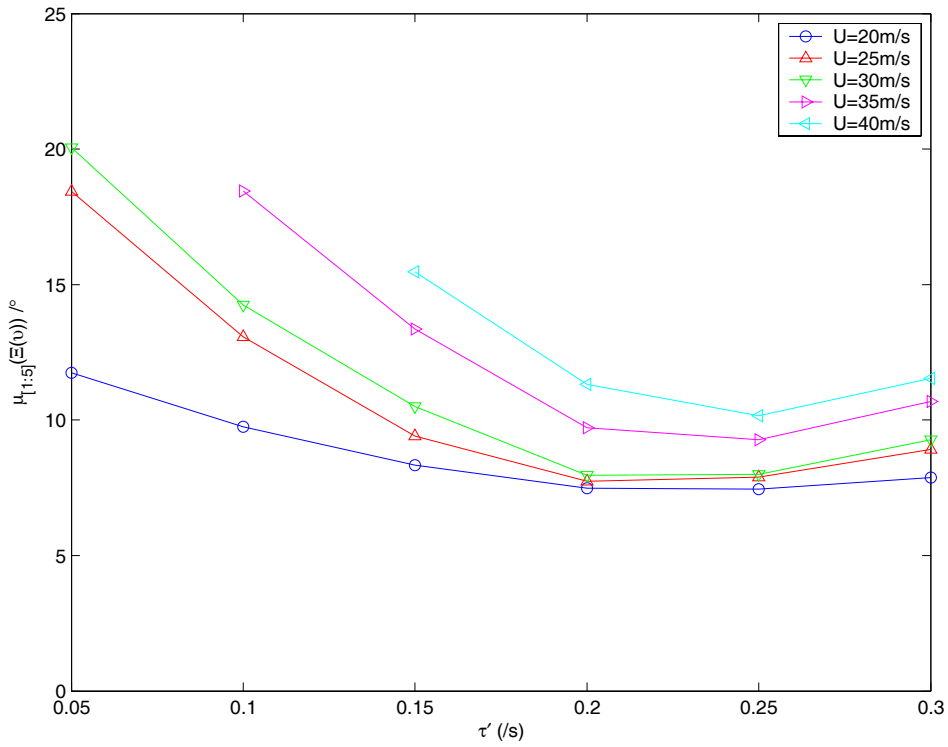
Figure 5.2: G_I , mean of prediction error for subject 1 to 5 , τ' from 0.05s to 0.3s

Figure 5.2 shows that delay τ' of 0.05s and 0.1s have the largest prediction error $\mu_{[1:5]}(\Xi(\upsilon))$ so can be discounted as unfeasible. Delays τ' from 0.15s to 0.3s have similar $\mu_{[1:5]}(\Xi(\upsilon))$ so are all candidates for the correct delay τ'. The lowest prediction error $\mu_{[1:5]}(\Xi(\upsilon))$ is given by a delay of $\tau' = 0.2$ s at low speed, and a delay of $\tau' = 0.25$ s at high speed. It seems that a delay of either $\tau' = 0.2$ s or $\tau' = 0.25$ s would be appropriate choices for G_I.

Figure 5.3 shows the mean parameter values given by $\mu_{[1:5]}(q_y')$ and $\mu_{[1:5]}(q_\theta')$ plotted against speed U for the range of delays τ' using the same data as Figure 5.2.
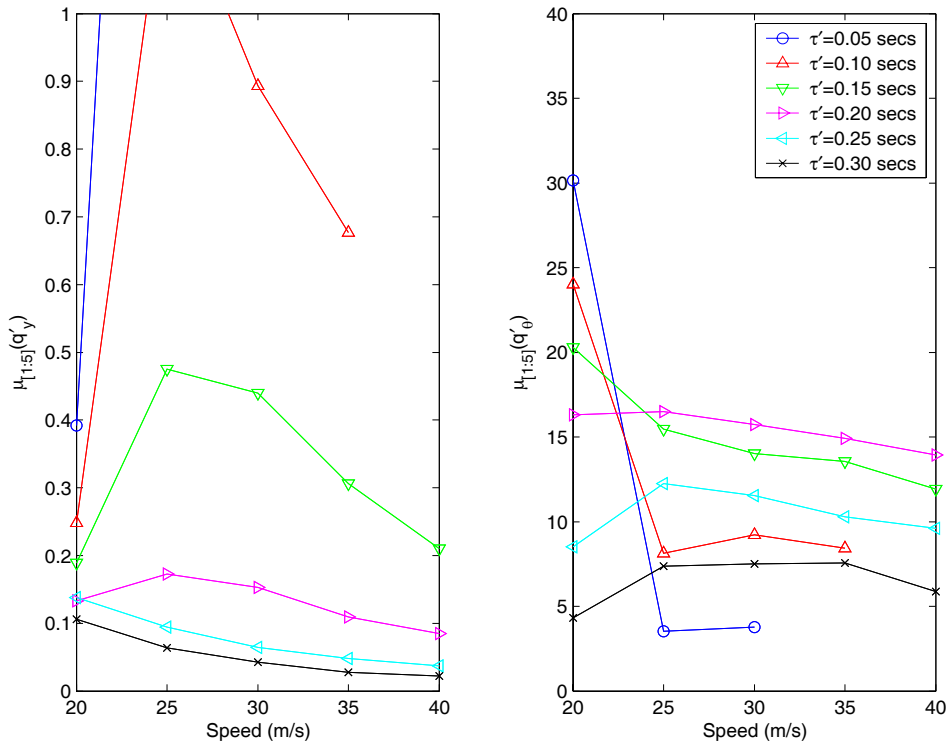
Figure 5.3: G_I, **mean of parameters for subject 1 to 5 ,** τ' **from 0.05s to 0.3s**

Figure 5.2 shows that parameter estimates q_y' and q_θ' tend to reduce with increasing delay τ', but that their variation with speed U is similar independent of τ'. This feature is useful for this analysis, as, if an incorrect τ' is chosen at this stage, then the observed trends for q_y' and q_θ' will still be correct.

A study of the effect of τ' for each of the models G_I to G_{VIII} was carried out. However, examining six values of delay τ' for five subjects with all seven driver models would have been too time consuming (estimated at 96 days on a 3.4 GHz PC). Instead only the data from tests on subject 2 was used. Mean prediction error $\mu_{[2]}(\Xi(\upsilon))$ was plotted against delay τ' in Figure 5.4. The mean prediction error for subject 2 is defined in equation (5.2) for the case of $U = 30$ m/s:

$$\mu_{[2]}(\Xi(\upsilon)_{\{U=30\}}) = \frac{\sum \Xi(\upsilon)_{[2]\{U=30\}}}{3} \tag{5.2}$$

Identification at delay $\tau' = 0.05\,\mathrm{s}$ was not calculated for G_{VII} in order to speed up identification for this model.
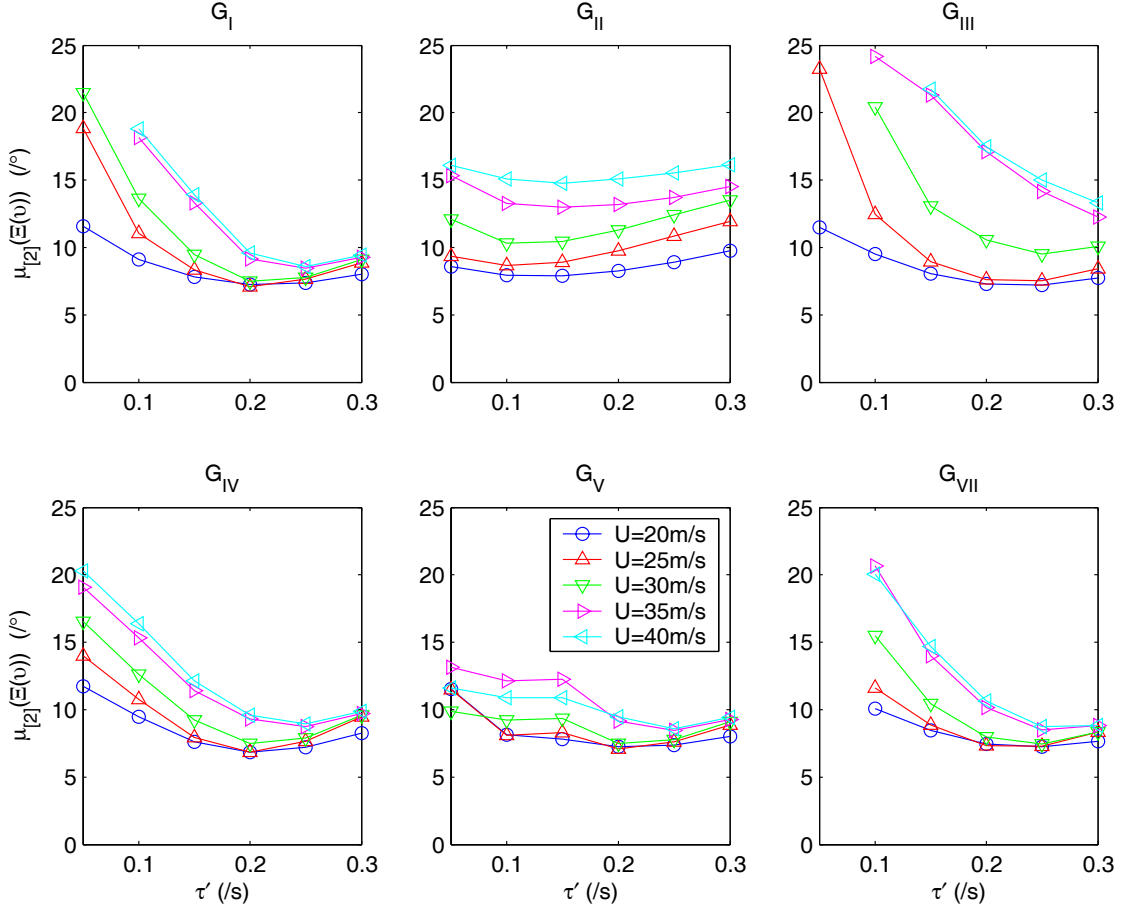
Figure 5.4: $\mu_{[2]}(\Xi(\upsilon))$ for G_I to G_{VII}, subject 2, τ' from 0.05s to 0.3s

Model G_{VIII} is not included in Figure 5.4 because it is based on the same model as G_{VII}, and both have almost identical prediction error $\mu_{[2]}(\Xi(\upsilon))$. Mean prediction error for all subjects $\mu_{[1:5]}(\Xi(\upsilon))$ for G_I shown in Figure 5.2, and mean prediction error for subject 2 $\mu_{[2]}(\Xi(\upsilon))$ shown in Figure 5.4 are very similar. This gives confidence that subject 2 is a good representation of the ensemble of subjects. This is examined more thoroughly in section 5.2.2.

Models G_I, G_{IV} and G_{VII} have similar profiles of prediction error $\mu_{[2]}(\Xi(\upsilon))$ vs. delay τ'. For all three of these models, delay $\tau' = 0.2\,\mathrm{s}$ gives minimum prediction

error $\mu_{[2]}(\Xi(\upsilon))$ at low speed, and $\tau' = 0.25\,\text{s}$ gives minimum prediction error at high speed. For these models either choice of τ' would be suitable.

G_{II} shows very little difference in prediction error $\mu_{[2]}(\Xi(\upsilon))$ for the range of delays τ' investigated. Using $\tau' = 0.2\,\text{s}$ for G_{II} does not give minimum $\mu_{[2]}(\Xi(\upsilon))$, but will not be too detrimental to its goodness of fit.

For model G_V the chosen delay $\tau' = 0.1\,\text{s}$ does not give minimum prediction error $\mu_{[2]}(\sigma(\upsilon))$, however, this was the only delay τ' value which gave a neuromuscular system natural frequency ω_n' within the domain 0 to 9 Hz. This is to be expected, as the neuromuscular filter in G_V provides an extra phase lag within the closed loop meaning that the delay τ' should be reduced. Reduction from $\tau' = 0.2\,\text{s}$ to $\tau' = 0.1\,\text{s}$ is reasonable as it corresponds to $36°$ of phase lag at the anticipated NMS natural frequency ω_n' of 1 Hz.

Models G_{VII} and G_{VIII} do not require a corresponding reduction of delay τ' to ensure a natural frequency ω_n' within the domain. Again this is not unexpected, as the LQR controller includes NMS states, and can therefore provide phase lead to compensate for the NMS phase lag. The chosen delay τ' for each model is shown in Table 5.3.

	G_I	G_{II}	G_{III}	G_{IV}	G_V	G_{VII}	G_{VIII}
τ' (/s)	0.2	0.1	0.2	0.2	0.2	0.2	0.2

Table 5.3: τ' chosen for models G_I to G_{VIII}.

5.2.2 Prediction error vs. delay for each subject

The above comparison this is based only on subject 2, but subjects may differ in their delay. In order to establish if subject 2 was typical of the ensemble, prediction error $\mu(\Xi(\upsilon))$ for delay τ' from 0.05s to 0.3s was plotted for each subject separately in Figure 5.5. The results are those for model G_I.
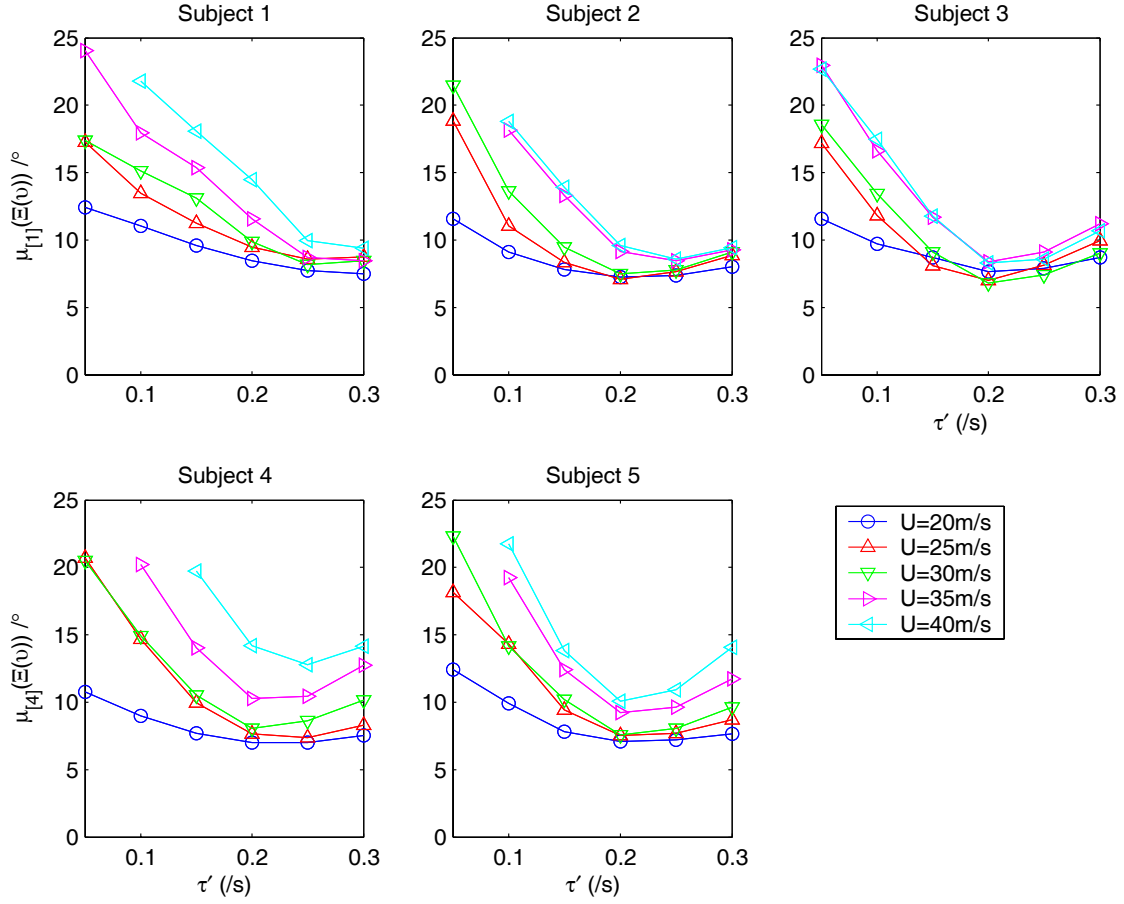
Figure 5.5: $\Xi(\upsilon)$ for $\mathbf{G_I}$, subjects 1 to 5, τ' from 0.05s to 0.3s

Figure 5.5 shows that for subjects 2, 3, 4 and 5, minimum prediction error $\mu(\Xi(\upsilon))$ is for a delay $\tau' = 0.2$ s for the majority of speeds.

Subject 1 is the exception, with minimum prediction error $\mu(\Xi(\upsilon))$ for $\tau' = 0.3$ s. This suggests that Subject 1 had larger delay than average. This was borne out by observations during testing that subject 1 had a noticeably slower response to errors than other subjects. It is also notable that this subject was a novice with no training of driving road cars, though some experience with driving in computer games.

It seems that Subject 2 was a good representative for the ensemble average to use in the previous section (5.2.1) as his results are similar to the majority of subjects. The dependence of goodness of fit $\mu(\Xi(\upsilon))$ on delay τ' for the wider road width was not

examined, but could be undertaken in future work. The difference in parameter estimates $\mu(q_y{}')$ and $\mu(q_\theta{}')$ between subjects is examined in section 5.4.3.

5.3   Comparison of models

Having chosen an appropriate delay for all models, the fit of the models can now be compared to establish which is best to represent the ensemble of drivers. The 'best' model can then be used to investigate differences between subjects, road widths and speeds.

It is worth noting that a particular model may be better for a particular subject, e.g. a novice subject may be better represented with a simpler model. However, the aim at this stage is to try and find which model is best for the ensemble of subjects.

Goodness of fit is compared between the models in section 5.3.1. In section 5.3.2, examples of steer angle time series are shown to illustrate the difference between the models, and calibrate what a given level of prediction error $\Xi(v)$ looks like. Noise models are shown with each of these time series, and also how well the noise model is fitting to the driver's steer angle. The fitted model parameters $q_y{'}$ and $q_\theta{'}$ are compared between models G_I to G_{VIII} in section 5.3.3. Finally, the resulting preview controllers and state gains for G_I to G_{VIII} are compared in section 5.3.4.

5.3.1   Goodness of fit

Having chosen a time delay $\tau{'}$ for each model, the models can now be compared directly. The mean prediction error across all five subjects $\mu_{[1:5]}(\Xi(v))$ is used to assess how well each model fits the ensemble of subjects. Prediction error $\mu_{[1:5]}(\Xi(v))$ vs. speed U for models G_I to G_{VIII} on the 2.5m wide road is shown in Figure 5.6.
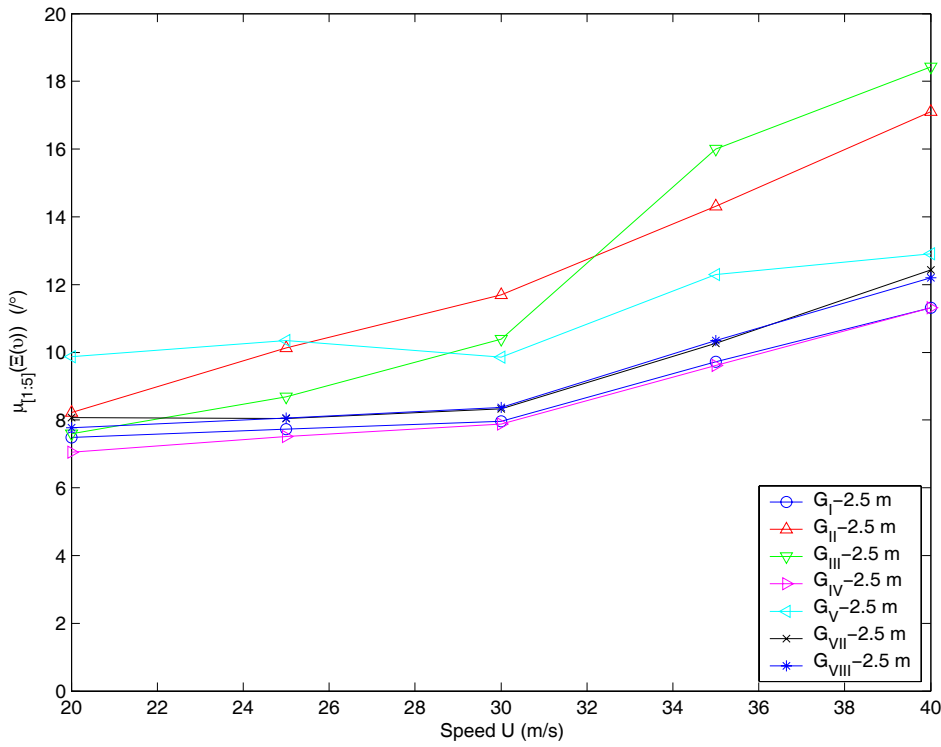
Figure 5.6: $\mu_{[1:5]}(\Xi(\upsilon))$ vs. speed for $\mathbf{G_I}$ to $\mathbf{G_{VIII}}$ with $\boldsymbol{\tau' = 0.2}$ s ($\boldsymbol{\tau' = 0.1}$ s for $\mathbf{G_{II}}$), 2.5m width

Figure 5.6 shows that mean prediction error $\mu_{[1:5]}(\Xi(\upsilon))$ increases with speed for all models fitted. This implies either: worse model fit with increasing speed (increased $(G-G')u$ in equation 4.11), or increasing driver noise with speed (increased *He* in equation 4.11). It is difficult to distinguish the effects of model mismatch from the effects of driver behaviour.

At low speed, all models have similar prediction error $\mu_{[1:5]}(\Xi(\upsilon))$, implying that all are equally able to model driver behaviour at low speed. Additional model complexity does not improve model fit for low speed driving.

At high speed G_{II} and G_{III} give worse fit than G_I. This implies that G_I, which uses both vehicle states (v, ω) reflects the behaviour of the 'mean' driver better than G_{II} with no internal states, or G_{III} with only a yaw rate state (ω). This implies that the 'mean' driver uses a vehicle controller with feedback of both ω and v.

At high speed $G_I, G_{IV}, G_V, G_{VII}$ and G_{VIII} all give similar prediction error $\mu_{[1:5]}(\Xi(\upsilon))$, implying that the increased complexity of these models does not significantly improve the fit over that of G_I. The fact that all of the more complex models reach a similar minimum prediction error $\mu_{[1:5]}(\Xi(\upsilon))$ suggests either that $(G - G') \approx 0$, or that the drivers' controller does not lie within the model set. It is, for example, possible that the driver could be choosing sub-optimal controllers, leading to an increase in $(G - G')u$. Such sub-optimal controllers are not part of the LQR controller model set.

G_{VII} and G_{VIII} give slightly higher prediction error $\mu_{[1:5]}(\Xi(\upsilon))$ than G_I and G_{IV} for all speeds, implying that the inclusion of an NMS model has not helped to improve the fit. Also G_V gives a higher prediction error $\mu_{[1:5]}(\Xi(\upsilon))$ than G_{VII} or G_{VIII}, suggesting that the internal NMS states of G_{VII} and G_{VIII} do improve the model fit. G_{IV} gives the lowest $\mu_{[1:5]}(\Xi(\upsilon))$ of all models, for all speeds, but not by enough to mark it as clearly the best model.

G_I will be chosen to compare road widths and test subjects in the next section, as this model gives nearly as low prediction error $\mu_{[1:5]}(\Xi(\upsilon))$ as G_{IV} but is simpler to implement.

5.3.2 Time domain

Examples of time histories of δ for one driver, on one track are shown in this section. These will not necessarily represent all data but are included to illustrate what is meant by a given prediction error $\Xi(\upsilon)$. The examples also illustrate how the controllers for G_I to G_{VIII} differ, and allow comparison with the time histories of chapter 3. The noise models are also plotted as solid lines in the lower subfigure, with the PSD of the prediction error υ for that driver model shown as crosses of the appropriate colour.

It must be remembered when examining time domain fits that steer angle is unweighted in these plots, and that during optimisation it is the weighted steer angle

error $H'^{-1}(\delta - \delta')$ which is minimised, rather than the unweighted steer angle error $(\delta - \delta')$.

The time histories are for subject 2 at $U = 20\,\text{m/s}$, and at $U = 40\,\text{m/s}$. The 20 m/s track is track 2 of the 15 track session driven on 2.5m wide roads (session 2 in Table 5.1). Steer angles δ'_{G_I} to $\delta'_{G_{VIII}}$ are shown in Figure 5.7, Figure 5.8, and Figure 5.9 for an 1100m to 1400m section of the 4km track.
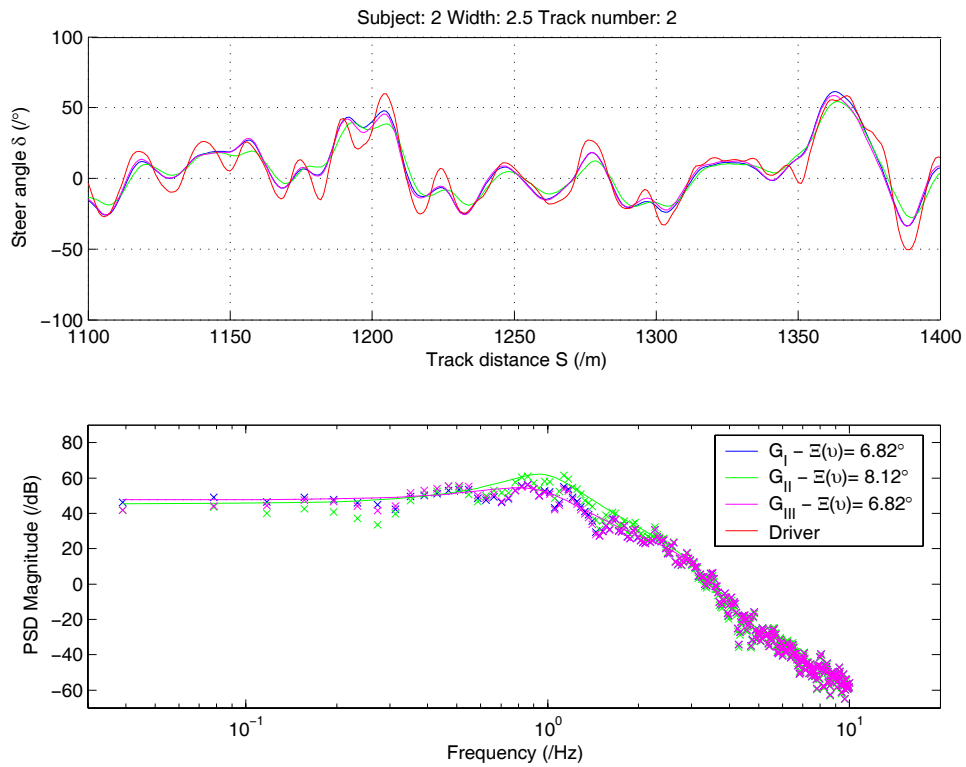
Figure 5.7: Time history for part of track 2, subject 2, 2.5m width, U=20 m/s, showing $\delta'_{G_I}, \delta'_{G_{II}}, \delta'_{G_{III}}$. For PSD magnitude 1dB=1°²/Hz
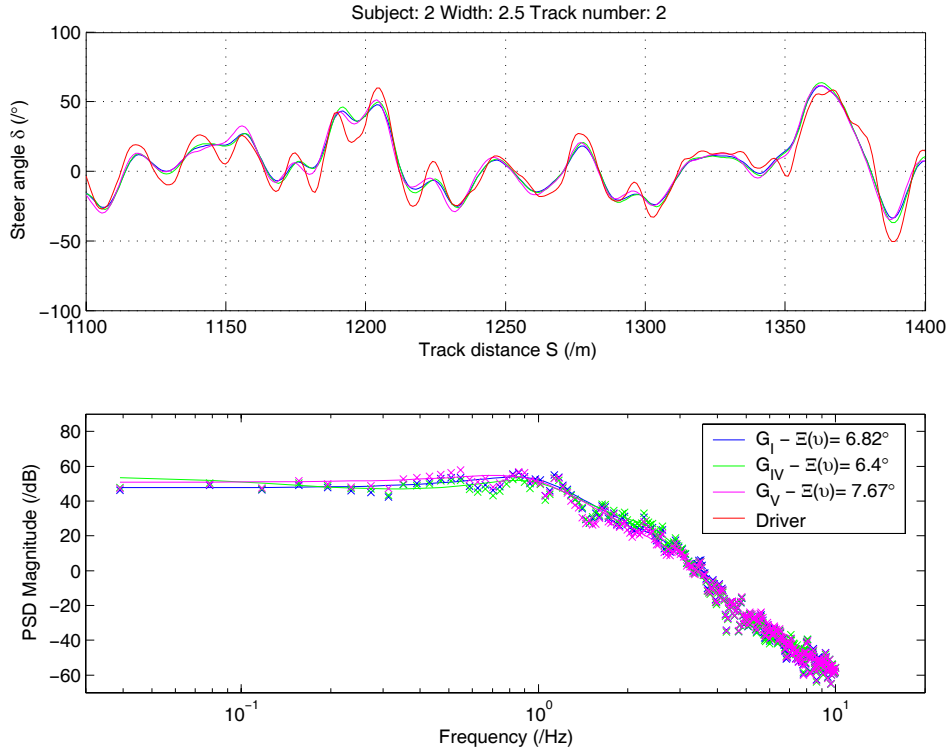
Figure 5.8: Time history for part of track 2, subject 2, 2.5m width, U=20 m/s, showing δ'_{G_I}, $\delta'_{G_{IV}}$, δ'_{G_V}. For PSD magnitude 1dB=1°²/Hz
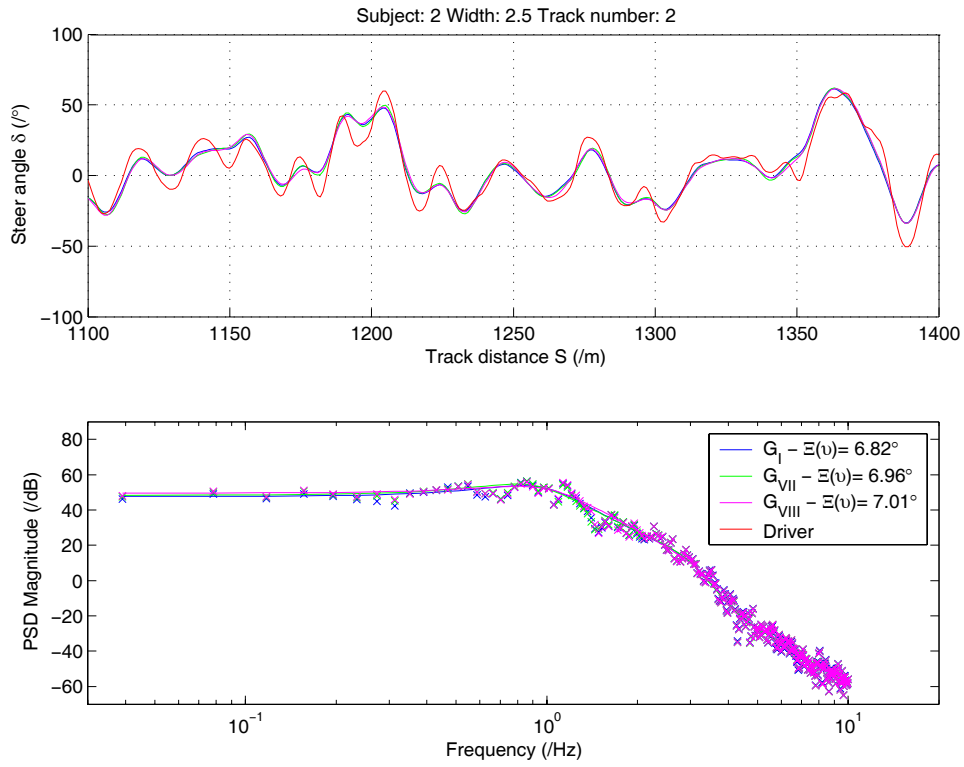
Figure 5.9: Time history for part of track 2, subject 2, 2.5m width, U=20 m/s, showing δ'_{G_I}, $\delta'_{G_{VII}}$, $\delta'_{G_{VIII}}$. For PSD magnitude 1dB=1°²/Hz

Figure 5.7, Figure 5.8, and Figure 5.9 show that there is little difference in steer angle δ' between the identified models at low speed, which explains why all have similar prediction error $\Xi(\upsilon)$.

It appears that oscillations at about 1 Hz in the steer angle δ of the real driver visible in this sample are not being followed by the models, although the lower frequency steer angle is correct. It was hoped that the NMS models could represent this behaviour, but none of models G_V, G_{VII}, or G_{VIII} show an improved fit. There is the possibility that this behaviour may not be within the model set (e.g. be sub-optimal), in which case none of the models could accurately represent it.

All of the noise models appear to fit well, and all of G_I to G_{VIII} give similar noise models at this speed. It appears that a lower order model could be used, but identification does not suffer from (q_y, q_θ) outliers, so the noise model order is not too high.

The 40 m/s track is number 13 of 15, and δ'_{G_I} to $\delta'_{G_{VIII}}$ are shown in Figure 5.10, Figure 5.11 and Figure 5.12. Again an 1100m to 1400m section of the 4km track is shown.

Figure 5.10: Time history for part of track 13, subject 2, 2.5m width, U=40 m/s, showing δ'_{G_I}, $\delta'_{G_{II}}$, $\delta'_{G_{III}}$. For PSD magnitude 1dB=1°²/Hz

Figure 5.10 shows that δ'_{G_I} to $\delta'_{G_{III}}$ differ at 40 m/s. This is consistent with the findings of chapter 4 where it was found that $\delta(t)$ was similar for models G_I to G_{III} at low speed, but differed at high speed when (v, ω) became significant. In the sample shown δ'_{G_I} is closer to the driver's steer angle δ than $\delta'_{G_{II}}$ or $\delta'_{G_{III}}$, giving the lowest prediction error of the three models $\Xi(\upsilon) = 10.3°$.

The prediction error $\Xi(\upsilon)$ is significantly different for the three models at this speed which shows up in the differences between the three noise models. The noise models show the frequencies at which the errors differ for the three models. The real driver noise η must be the same for all models, so differences in the noise model arise from differences in the model error $(G - G')$. G_{III} appears to have more error (or noise) than G_I below 0.5 Hz, whereas G_{II} has larger error from 0.5 to 2 Hz.
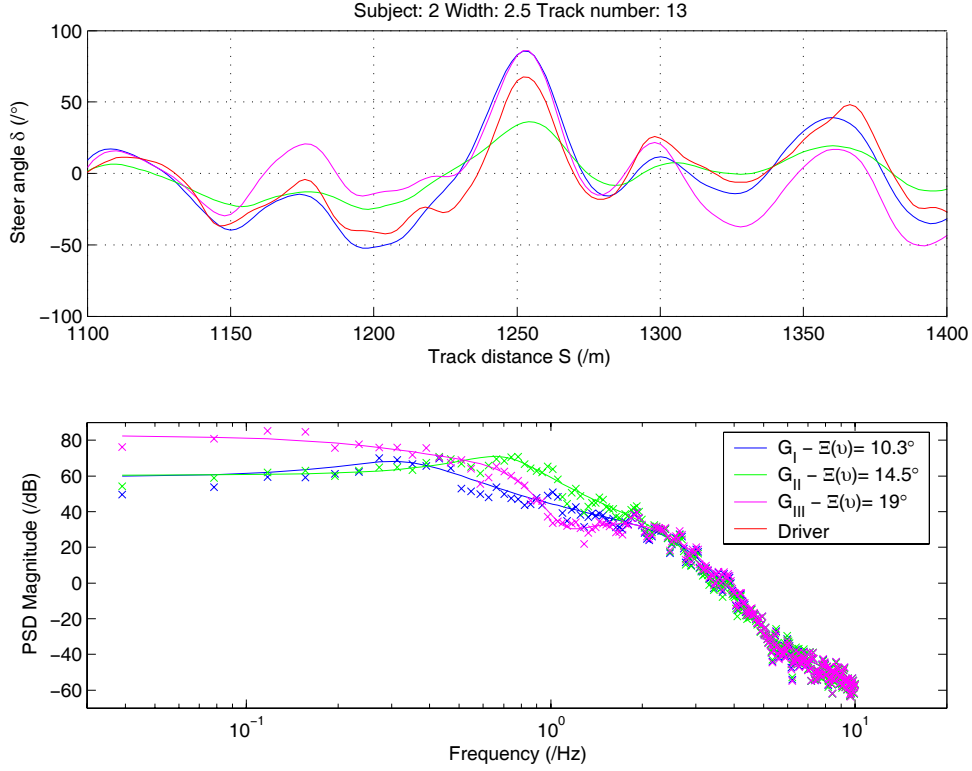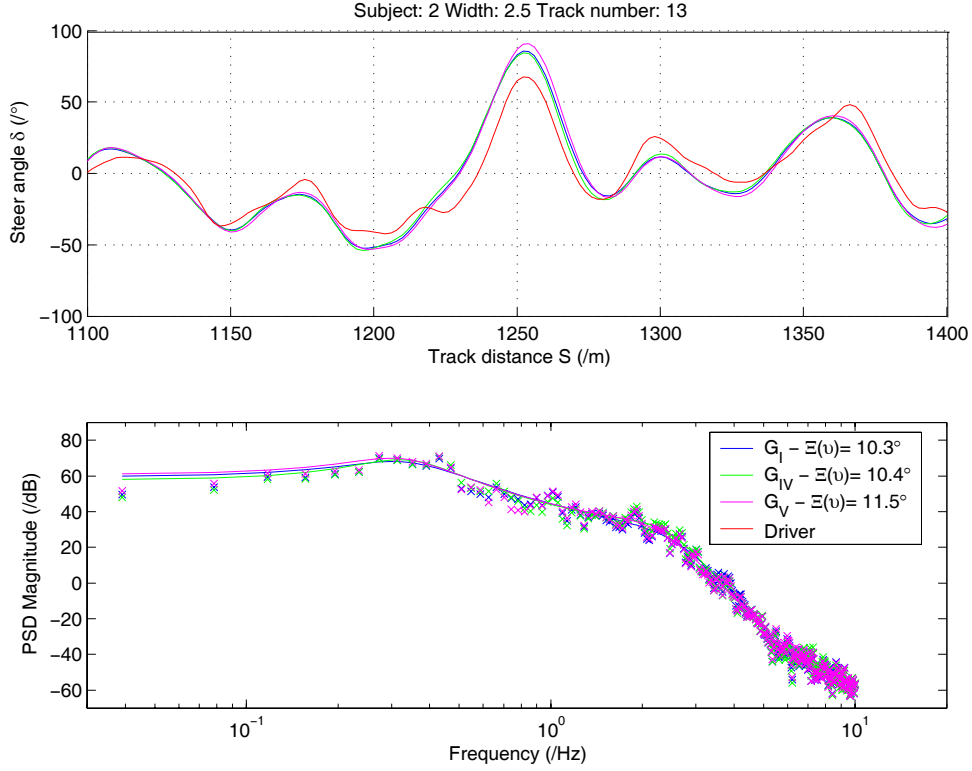
Figure 5.11: Time history for part of track 13, subject 2, 2.5m width, U=40 m/s, showing δ'_{G_I}, $\delta'_{G_{IV}}$, δ'_{G_V}. For PSD Magnitude 1dB=1$°^2$/Hz

Examining models G_I, G_{IV} and G_V in Figure 5.11, it can be seen that $\delta'_{G_{IV}}$ is close to that of δ'_{G_I}, giving similar prediction error $\Xi(\upsilon)$ for both. As seen in chapter 4, the delay states only make slight differences to $\delta'_{G_{IV}}$, even at high speed.

The steer angle δ'_{G_V} does not differ much from δ'_{G_I} in the sample shown. Even at this higher speed, the influence of the NMS is not visible in the steer angle. This may be because the NMS is highly damped, meaning that it only has significant influence above its natural frequency (approximately 2.5 Hz). The parameter values $\{q_y', q_\theta', \omega_n', \xi'\}$ fitted to the models G_I to G_{VIII} are described in section 5.3.3.

All three models have similar noise model shape at $U = 40$ m/s, which is different to that at 20 m/s. At 20 m/s there was a single cut-off frequency at 1 Hz, whereas at 40 m/s there are two cut-offs: one at 0.3Hz, and one at 2Hz. The noise model appears to fit the features sufficiently well, so there is no need to increase the noise model order.
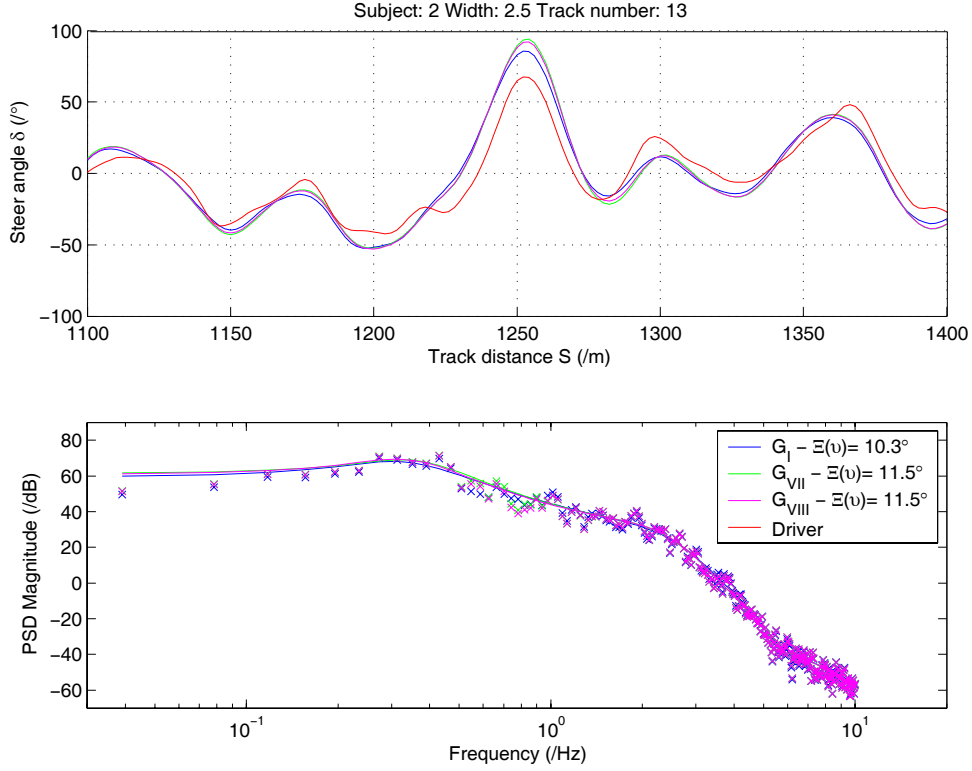
Figure 5.12: Time history for part of track 13, subject 2, 2.5m width, U=40 m/s, showing δ'_{G_I}, $\delta'_{G_{VII}}$, $\delta'_{G_{VIII}}$. For PSD magnitude 1dB=1°²/Hz

Examining models G_I, G_{VII} and G_{VIII} in Figure 5.12, it can be seen that the steer angles δ'_{G_I}, $\delta'_{G_{VII}}$, and $\delta'_{G_{VIII}}$ are very similar at high speed, with only small differences in prediction error $\Xi(\upsilon)$ between them. So, even at high speed, the NMS has little influence on the steer angle of the models. Their noise models are again very similar, with only slight differences apparent in the 0.3 to 0.4 Hz frequency range.

5.3.3 Model parameters

It is useful to compare the parameter estimates (q_y', q_θ') and (ω_n', ξ') for models G_I to G_{VIII} in order to show how their mean and variance differs between models, and where these differences arise, particularly as for later analysis (section 5.4 onwards), only model G_I was used.

Figure 5.13 shows $\mu_{[1:5]}(q_y{}')$ and $\mu_{[1:5]}(q_\theta{}')$ for models G_I, G_{II} and G_{III}. Error bars show the standard deviation of the estimates about this mean i.e. $\sigma_{[1:5]}(q_y{}')$ and $\sigma_{[1:5]}(q_\theta{}')$ where:

$$\sigma_{[1:5]}(q_y{}'_{\{U=30\}}) = \sigma\left(q_y{}'_{[1]\{U=30\}}, q_y{}'_{[2]\{U=30\}}, q_y{}'_{[3]\{U=30\}}, q_y{}'_{[4]\{U=30\}}, q_y{}'_{[5]\{U=30\}}\right) \quad (5.3)$$

Although tests were carried out at $U = [20, 25, 30, 35, 40]\,\text{m/s}$, the points are shown artificially shifted slightly along the speed axis in Figure 5.13, Figure 5.14, and Figure 5.15 to improve the visibility of the error bars.
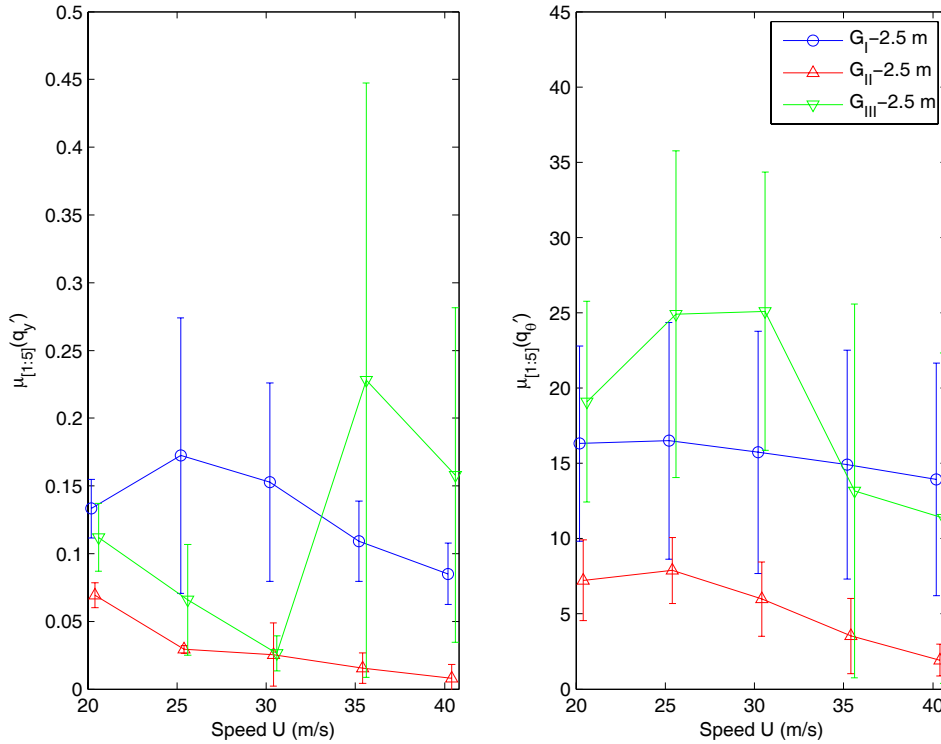
Figure 5.13: $\mathbf{\mu_{[1:5]}(q_y{}')}$ **vs. speed, and** $\mathbf{\mu_{[1:5]}(q_\theta{}')}$ **vs. speed for** $\mathbf{G_I, G_{II}}$ **and** $\mathbf{G_{III}}$**. Mean of subjects 1 to 5. Error bars show one standard deviation each side of mean**

G_I was established in section 5.3.1 as having close to the lowest $\Xi(\upsilon)$ of all the models, so its estimates should be more likely to reflect the mean properties of the test subjects. Figure 5.13 shows that the standard deviation of $q_\theta{}'$ for G_I is up to 50% of the mean parameter value $\mu_{[1:5]}(q_\theta{}')$ throughout the speed range, and for $q_y{}'$ is

between 10% and 50%. Parameter variance can arise from several sources: poor model fit leading to biased estimates; poor consistency of control by the driver i.e. changing their strategy between or during tests at a given speed; or from different subjects using different controllers. This latter source is investigated in section 5.4.3 and is the primary cause of the large variance in q_θ' for G_I.

Differences in q_y' and q_θ' between G_I, G_{II} and G_{III} are to be expected given that each model has quite different steer angle for a given q_y', q_θ' (as shown in chapter 4), and all are trying to fit to the same driver steer angle δ.

G_{II} had lower values of q_y' and q_θ' than the other two models throughout the speed range, and showed a similar trend of reducing q_y' and q_θ' with speed. G_{II} had the smallest parameter variance of the three models, implying that the parameter estimates for each subject were repeatable, and also similar from subject to subject. However, G_{II} also had the largest prediction error $\Xi(\upsilon)$ (see Figure 5.6), so its fit is least likely to reflect the properties of the driver during tests.

G_{III} had a less clear pattern of q_y' and q_θ' with speed, and very large variance for the 35m/s result. High prediction error $\Xi(\upsilon)$ suggested that this model was not suitable for the ensemble of subjects, but it may be suitable for a novice driver.
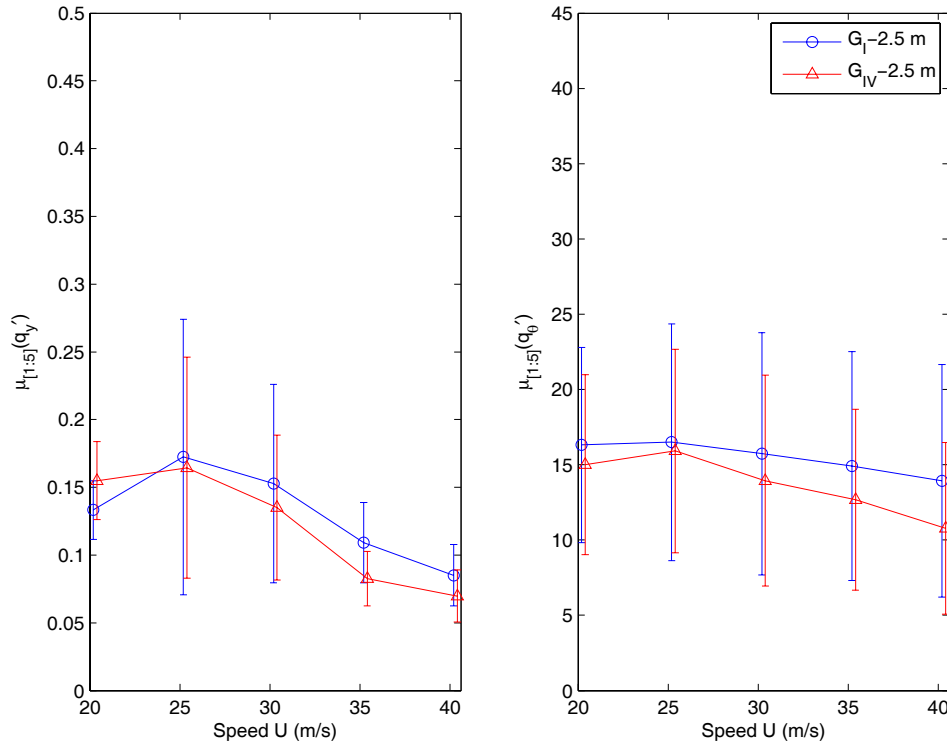
Figure 5.14: $\mu_{[1:5]}(\mathbf{q'_y})$ vs. speed, and $\mu_{[1:5]}(\mathbf{q'_\theta})$ vs. speed for $\mathbf{G_I}$ and $\mathbf{G_{IV}}$. **Mean of subjects 1 to 5. Error bars show one standard deviation each side of mean**

Figure 5.14 shows that G_{IV} had very similar variation of $\mu_{[1:5]}(q_y{'})$ and $\mu_{[1:5]}(q_\theta{'})$ with speed to G_I. However, for G_{IV} both of the parameters $\mu_{[1:5]}(q_y{'})$ and $\mu_{[1:5]}(q_\theta{'})$ are around 10% smaller than for G_I. The standard deviations $\sigma_{[1:5]}(q_y{'})$ and $\sigma_{[1:5]}(q_\theta{'})$ are also very similar for models G_I and G_{IV}. This is consistent with the two models having very similar steer angle for a given (q_y, q_θ) as shown in chapter 3.
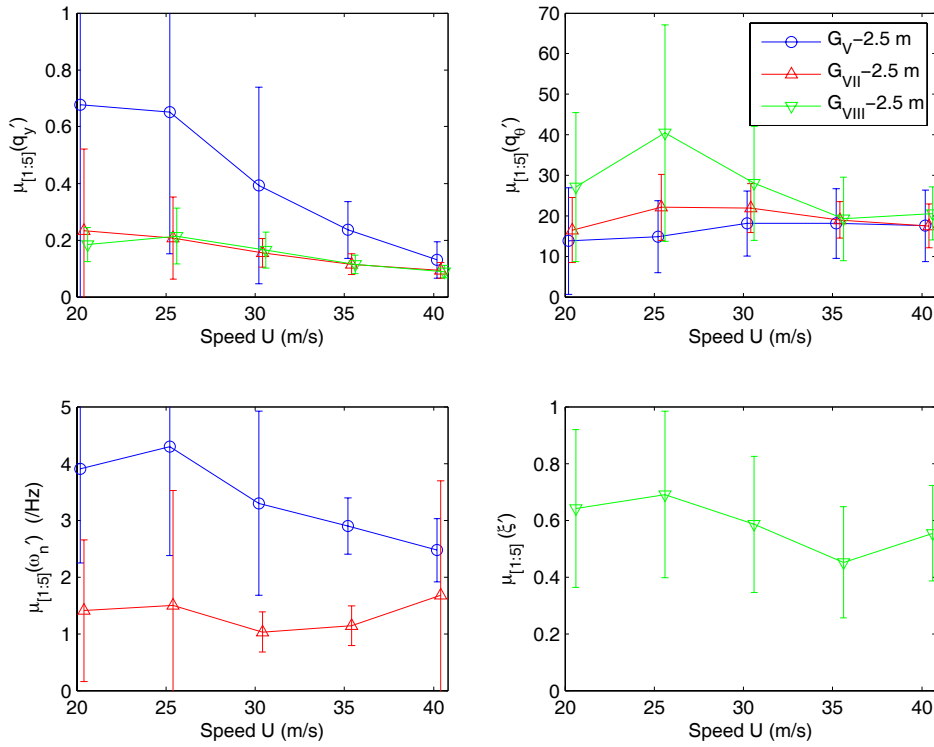
Figure 5.15: $\mu_{[1:5]}(q_y')$ vs. speed, $\mu_{[1:5]}(q_\theta')$ vs. speed, $\mu_{[1:5]}(\omega_n')$ vs. speed, and $\mu_{[1:5]}(\xi')$, for G_V, G_{VII}, and G_{VIII}. **Mean of subjects 1 to 5. Error bars show one standard deviation each side of mean**

Figure 5.15 shows that G_V has much higher $\mu_{[1:5]}(q_y')$ than any other model, but lower $\mu_{[1:5]}(q_\theta')$ which increases with speed, in contrast to other models. The presence of the neuromuscular system filter without corresponding internal states clearly has a marked effect on the resulting $\mu_{[1:5]}(q_y')$ and $\mu_{[1:5]}(q_\theta')$ selected. The q_y estimates at low speed are, however, very variable for G_V.

The mean NMS natural frequency $\mu_{[1:5]}(\omega_n')$ for model G_V is significantly higher than that for model G_{VII}. The fact that a larger phase delay NMS has been found for model G_{VII} is consistent with the idea that the LQR controller in G_{VII} has some phase lead due to its NMS state feedback and the time shifting of its preview gains. This phase lead must be sufficient to overcome the phase delaying effect of a lower natural frequency of NMS for model G_{VII} (around 1.5Hz as opposed to 3.5Hz for G_V). The phase lead must also be sufficient to overcome the extra time delay of $\tau' = 0.2$ s for

204

G_{VII} (whereas G_V uses $\tau' = 0.1\,\text{s}$). Model G_{VII} has lower prediction error $\Xi(\upsilon)$ than G_V, so the natural frequency estimate $\mu_{[1:5]}(\omega_n')$ for G_{VII} is likely to be a more accurate estimate than $\mu_{[1:5]}(\omega_n')$ for G_V. Though an intrinsic natural frequency of 3.7Hz was recorded by Pick [36] for tensed arms, active control of steer angle would not be expected to be possible at this frequency due to delays in the reflex control loop. It seems likely that the high NMS natural frequency of G_V is an artefact of the model's poor fit, rather than a feature of the driver's control.

For G_{VII} and G_{VIII}, the NMS parameters $\mu_{[1:5]}(\omega_n')$ and $\mu_{[1:5]}(\xi')$ are consistent for the range of speeds, implying that NMS parameters are independent of speed for the subjects tested.

The large variance of $\mu_{[1:5]}(q_y')$ for G_{VII} at $U = 20\,\text{m/s}$ is consistent with the large variance of identification seen for this model in the validation of chapter 4. Model G_{VII} does not give the same $\mu_{[1:5]}(q_\theta')$ values as G_{VIII} despite being based on the same model, because the NMS natural frequency ω_n for model G_{VII} does not exactly match the 1 Hz that was assumed for model G_{VIII}. Similarly the NMS damping of model G_{VII} of $\xi = 0.45$ does not exactly match the values found for model G_{VIII}.

Overall, G_I has similar $\mu_{[1:5]}(q_y')$ vs. speed, and $\mu_{[1:5]}(q_\theta')$ vs. speed to the other models with low prediction error $\Xi(\upsilon)$ (G_{IV}, G_{VII} and G_{VIII}). The analysis of the speed, subject and width dependence of these parameters $\mu_{[1:5]}(q_y')$ and $\mu_{[1:5]}(q_\theta')$ will therefore be undertaken using model G_I throughout section 5.4.

5.3.4 Preview controllers

The $\mu_{[1:5]}(q_y')$ and $\mu_{[1:5]}(q_\theta')$ values identified for G_I to G_{VIII} differ from those values investigated in chapter 3. It will therefore be useful to investigate the preview controllers that arise from the parameter values identified in the previous section.

Controllers for each of G_I to G_{VIII} were evaluated for speeds of 20 m/s and 40 m/s. Figure 5.16 shows preview gains for models G_I, G_{II}, G_{III} and G_{IV} with parameter values $[\mu_{[1:5]}(q'_y), \mu_{[1:5]}(q'_\theta)]$ at 20 m/s, for the 2.5m lane width.
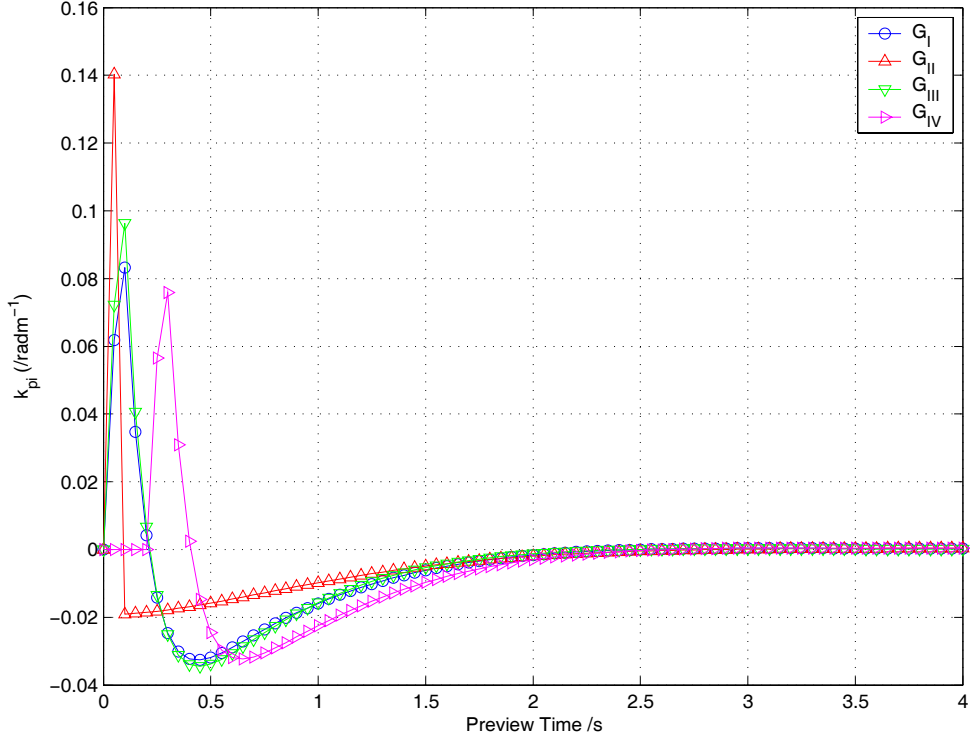
Figure 5.16: Preview gains for $\mathbf{G_I}$, $\mathbf{G_{II}}$, $\mathbf{G_{III}}$ and $\mathbf{G_{IV}}$ at 20 m/s

Preview gains for G_I to G_{IV} are of similar amplitude ranging from +0.1 close to the driver, to -0.03 further from the driver. G_{II} differs but this model fits poorly. For all four, the preview gains drop to zero within 2.5 seconds of preview time, implying that the driver is not using any more than this amount of preview.

The preview gains for model G_{III} have very similar shape to the preview gains for G_I, so it must be the absence of a sideslip state gain in the model G_{III} which explains the higher prediction error $\Xi(\upsilon)$ of model G_{III} demonstrated in Figure 5.6.

The different parameters $\mu_{[1:5]}(q'_y)$ and $\mu_{[1:5]}(q'_\theta)$ identified for each model have resulted in quite similar preview gains. This is in contrast to the controllers shown in chapter 4, where constant (q_y, q_θ) were used, and led to quite different controllers.
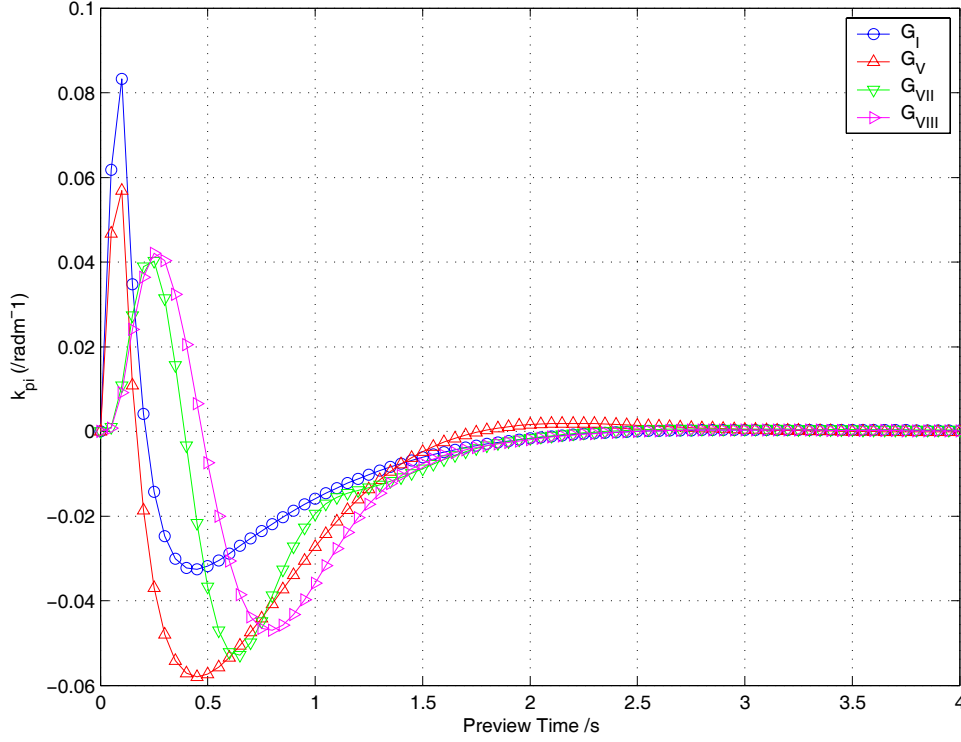
Figure 5.17: Preview gains for G_I, G_V, G_{VII} and G_{VIII} at 20 m/s

Figure 5.17 shows preview gains for models G_I, G_V, G_{VII} and G_{VIII} with parameter values $[\mu_{[1:5]}(q'_y), \mu_{[1:5]}(q'_\theta), \mu_{[1:5]}(\omega'_n), \mu_{[1:5]}(\xi')]$ at 20 m/s for the 2.5m lane width. Again preview time is shorter than 2.5s so the preview of 4s used to derive the LQR controllers was sufficient.

G_V has the same LQR controller as G_I, but different parameters $\mu_{[1:5]}(q'_y)$ and $\mu_{[1:5]}(q'_\theta)$ have caused the preview gains to differ. This is likely to be in order to compensate for presence of a NMS filter.

The controllers of G_{VII} and G_{VIII} give a similar time shift in their preview gains k_{pi} to that of the delay state model G_{IV}. All three of these controllers (G_{IV}, G_{VII} and G_{VIII}) shift the peaks of the preview gains approximately 0.1 seconds further ahead of the

207

vehicle than those of G_I. The similarity between the preview gains of G_{IV}, G_{VII} and G_{VIII} may indicate that the preview gains used by the driver are similar to these controllers. Shifting of the preview gains enables the prediction error $\mu_{[1:5]}(\Xi(\upsilon))$ of these models (G_{IV}, G_{VII} and G_{VIII}) to similar to that of model G_I despite the extra sources of lag present for these models (the delay N_d for G_{IV} and the NMS for G_{VII} and G_{VIII}).

G_{VII} and G_{VIII} have similar preview gains, but the differences in $\mu_{[1:5]}(q'_\theta)$, $\mu_{[1:5]}(\omega'_n)$, and $\mu_{[1:5]}(\xi')$ between the two models cause the gains to differ slightly. G_{VII} has a 'wavelength' for its preview oscillations around 25% shorter than G_{VIII}. This is consistent with the natural frequency of G_{VIII} being 30% lower ($\omega_n\{G_{VIII}\} = 1\,\text{Hz}$, whereas $\omega_n\{G_{VII}\} = 1.3\,\text{Hz}$). G_{VIII} therefore implies earlier steering inputs by the driver than G_{VII}.
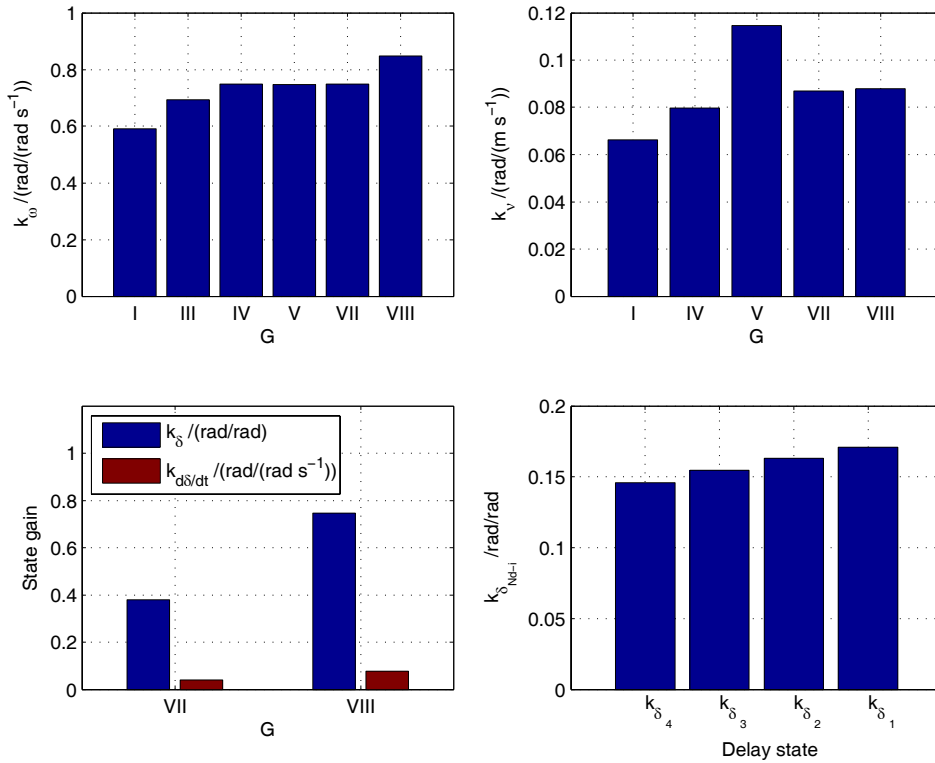
Figure 5.18: State gains for models G_I to G_{VIII} at 20 m/s with
$$[q_y, q_\theta, \omega_n, \xi] = [\mu_{[1:5]}(q'_y), \mu_{[1:5]}(q'_\theta), \mu_{[1:5]}(\omega'_n), \mu_{[1:5]}(\xi')]$$

Figure 5.18 shows state gains for models G_I to G_{VIII} with parameter values $[\mu_{[1:5]}(q'_y), \mu_{[1:5]}(q'_\theta), \mu_{[1:5]}(\omega'_n), \mu_{[1:5]}(\xi')]$ at 20 m/s for the 2.5m lane width. k_ω is similar for all models which use this state gain. All models are within 20% of the mean $\mu(k_\omega)$. k_υ differs by around 20% of the mean $\mu(k_\upsilon)$ between models except for $k_\upsilon\{G_V\}$ which is notably higher. The high $k_\upsilon\{G_V\}$ comes about due to the high q_y value for this model at 20 m/s (see Figure 5.15).

k_δ and $k_{d\delta/dt}$ for G_{VII} and G_{VIII} do differ significantly due to the differences in $\mu_{[1:5]}(q'_\theta)$, $\mu_{[1:5]}(\omega'_n)$ and $\mu_{[1:5]}(\xi')$ between the two models at 20 m/s.

The similarity of state and preview gains between models lends weight to the idea that these gains are similar to the driver's controller gains. However, the model set is restricted to optimal LQR controllers, so this may be a facet of that restriction.

Figure 5.19 shows preview gains for models G_I, G_{II}, G_{III} and G_{IV} with parameter values $[\mu_{[1:5]}(q'_y), \mu_{[1:5]}(q'_\theta)]$ at 40 m/s for the 2.5m lane width.
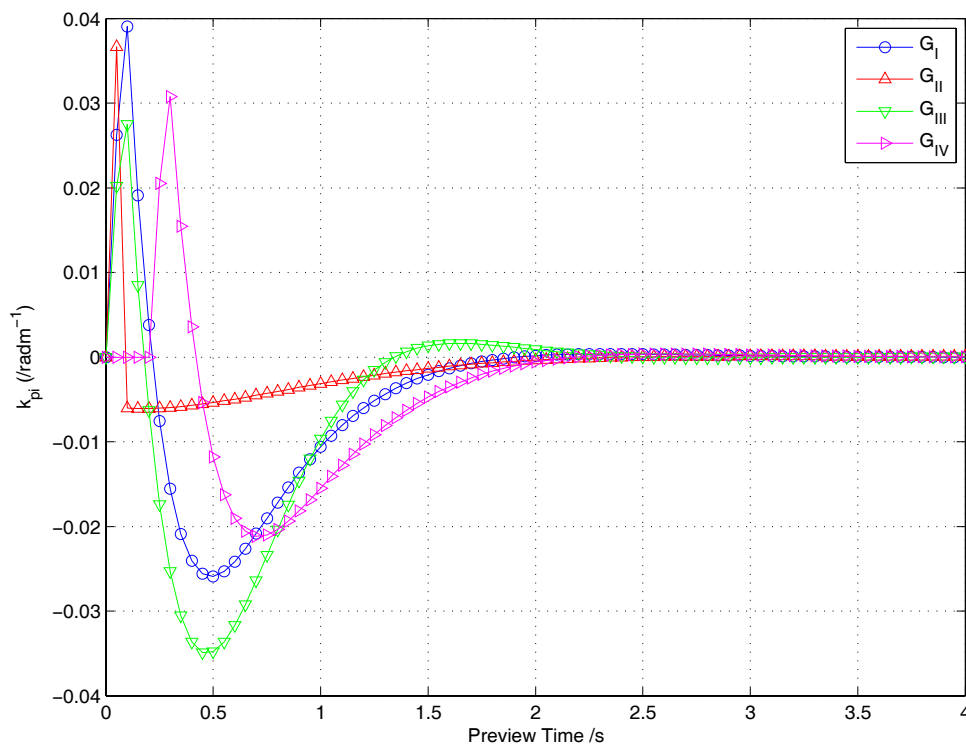
Figure 5.19: Preview gains for $\mathbf{G_I}$, $\mathbf{G_{II}}$, $\mathbf{G_{III}}$ and $\mathbf{G_{IV}}$ at 40 m/s

The preview gains k_{pi} for all controllers have changed from those at 20 m/s. However, the preview gains for all controllers have reached zero a similar time ahead of the vehicle to the controllers at 20m/s. This preview time of around 2 seconds implies a doubling of the preview distance from that at 20 m/s.

G_{III} has changed shape to be less similar to that of G_I. It is at this speed that the prediction error $\Xi(\upsilon)$ is largest for model G_{III}, so this controller is unlikely to closely reflect the drivers' controller.
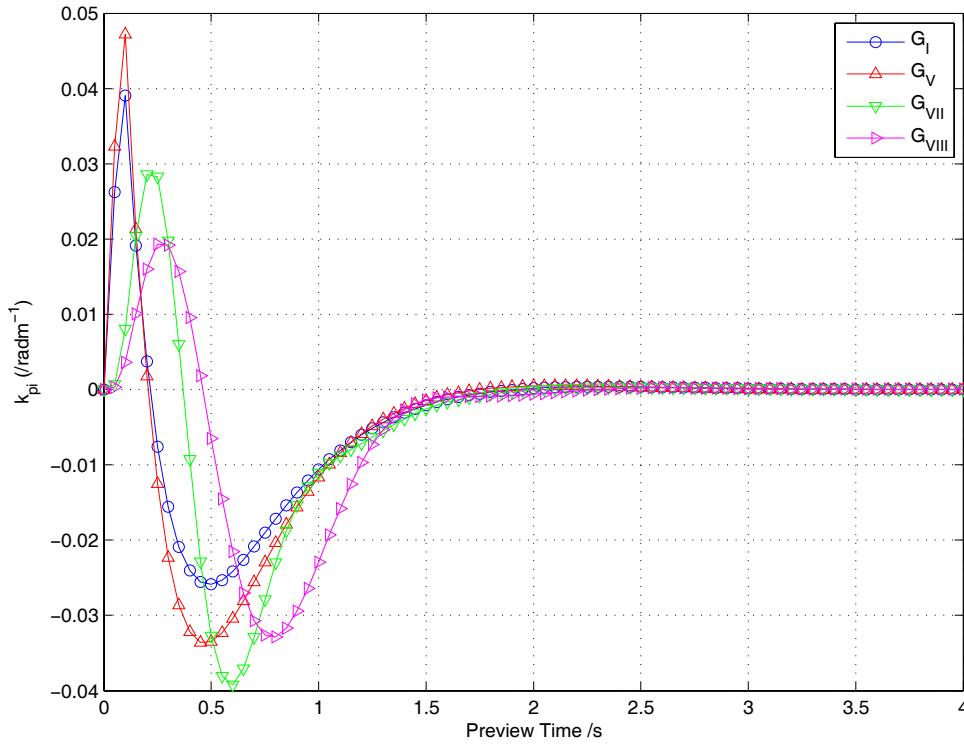
Figure 5.20: Preview gains for $\mathbf{G_I}$, $\mathbf{G_V}$, $\mathbf{G_{VII}}$ and $\mathbf{G_{VIII}}$ at 40 m/s

The preview gains for model G_V are very similar to that of G_I because the two LQR models are the same, and have very similar $[\mu_{[1:5]}(q'_y), \mu_{[1:5]}(q'_\theta)]$ at this speed (see Figure 5.15). Again the difference in preview gain 'wavelength' between G_{VII} and G_{VIII} corresponds to the difference in ω'_n between the two models.
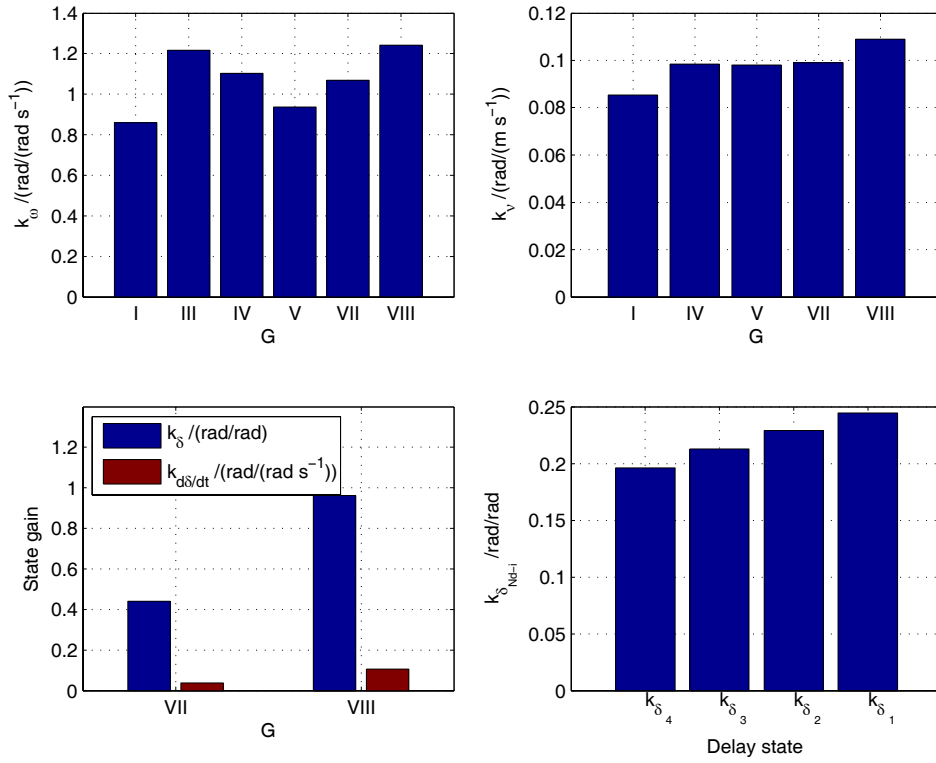
Figure 5.21: State gains for models G_I to G_{VIII} at 40 m/s with $[q_y, q_\theta, \omega_n, \xi] = [\mu_{[1:5]}(q'_y), \mu_{[1:5]}(q'_\theta), \mu_{[1:5]}(\omega'_n), \mu_{[1:5]}(\xi')]$

Figure 5.21 shows that the values of k_ω and k_υ have increased by only around 20% for all models from their values at 20 m/s. This is in contrast to the doubling which was seen in chapter 3 when q_y and q_θ were kept constant for the two speeds (though this comparison was for 20m/s and 50 m/s).

The controllers at 20 m/s and 40 m/s speed seem more similar than would be expected from the results seen in chapter 3 with constant q_y, q_θ. It is possible that the subjects intentionally avoided changing their preview and state gains with speed, and changed their control priorities with speed via q_y and q_θ to achieve this.

5.4 Parameter variation with speed, width and subject

Having established that the models are fitting to the data, model parameters can now be examined to see how they vary with the independent variables of the experiment, namely test subject, vehicle speed, and lane width. G_I was used as the driver model for this analysis due to its combination of goodness of fit, and simplicity requiring only parameters q_y and q_θ.

As previously, to analyse trends caused by one variable, parameters are averaged across the other variables. The effect of speed and width will be dealt with in two parts: their effect on lateral error and heading error in section 5.4.1; then their effect on the parameters (q_y', q_θ') in section 5.4.2. The variation of path error and (q_y', q_θ') as a function of speed should then enable the development of a new speed choice model, which is discussed in section 5.5.

The experiments were designed in order to gather data for the variation of path error with speed for a range of road widths, while at the same time measuring the accompanying changes in driver effort or control strategy shown by q_y and q_θ. Modifications were made to the hypothesis proposed in chapter 2 to account for the inclusion of the controller weights q_y and q_θ.

It was hypothesised that for a given width W_1 at low speed path error would stay constant with increasing speed due to increased driver effort. This should show up in increased q_y and q_θ, as shown by the blue lines in Figure 5.22. As speed continued to increase the driver would run out of control effort, and path error would increase. This is shown in Figure 5.22 where control effort (measured using controller weight q) reaches a maximum q_{max} at speed U_1, above which the lateral error increases to exceed the lane width. Figure 5.22 shows lateral error, but a similar trend was anticipated for the heading error. It is this path error increase that would cause the driver to have to limit their speed to U_1 to stay within the road width.

For wider road this pattern was expected to be repeated, but with larger path error at low speed due to the wider road. This would enable lower controller weights q to be used by the driver to ease the control effort. This is shown as a red line in Figure 5.22. Again for low speeds control effort q would increase with speed to allow path error to stay constant. As control effort was saturated at q_{max} at speed U_2, path error would increase. The driver would therefore choose a higher speed U_2 on the wider road.
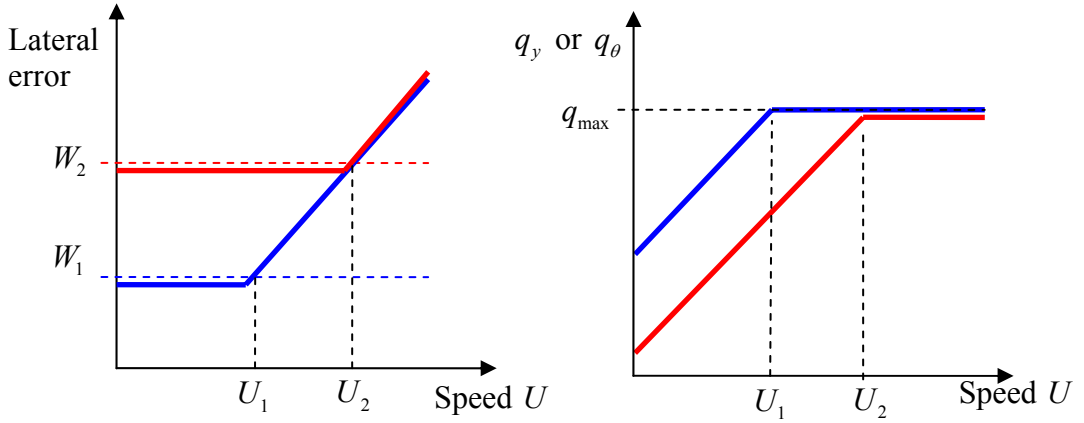
Figure 5.22: Hypothesised variation of path error and controller weights (q) with speed for lane widths W_1 (blue) and W_2 (red)

5.4.1 Path and heading error vs. width and speed

Figure 5.23 shows the steering controller parameters $\mu_{[1:5]}(q_y)$ and $\mu_{[1:5]}(q_\theta)$ and the prediction error $\mu_{[1:5]}(\Xi(\upsilon))$ in the upper three subplots. Figure 5.23 also shows the mean 95th percentile lateral error $\mu_{[1:5]}(\rho_{95}(y_{p0}))$, mean 95th percentile heading error $\mu_{[1:5]}(\rho_{95}(\theta))$ and mean 95th percentile driver steer angle $\mu_{[1:5]}(\rho_{95}(\delta))$ in the lower three subplots. The figures are arranged to show the variables y_{p0}, θ and δ involved in the steering controller cost function (chapter 3 equation (3.9)), as well as the resulting parameters q_y and q_θ. All parameters are shown for 2.5m, and 3.5m lane width. The data from all subjects is averaged as before. As mentioned in section 5.1.2, different speed ranges were used for each width in order to be easy to keep within the road width at low speed, and very hard to keep within road width at the highest speed.
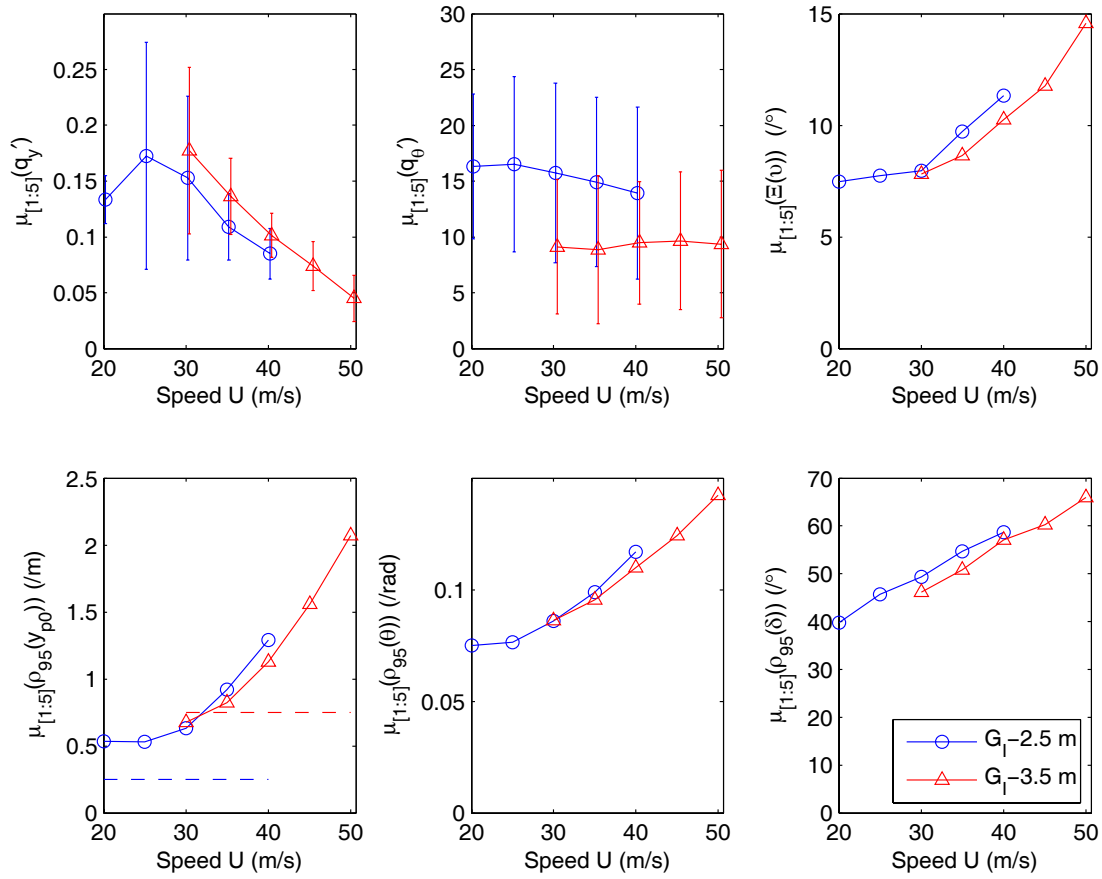
Figure 5.23: Parameters vs. speed for widths 2.5 and 3.5m. G_I fitted to all subjects

For the 2.5m wide road, lateral error ($\mu_{[1:5]}(\rho_{95}(y_{p0}))$) in the lower left plot and heading error ($\mu_{[1:5]}(\rho_{95}(\theta))$) in the lower centre plot were constant for low speeds (20 and 25 m/s). Above 25 m/s they increased, as expected.

For 3.5m lane width this sudden increase of lateral error and heading error with speed is not visible. Also, the lateral error did not increase for the wider road as was expected, and not by the amount that the available road width $(W - W_v)/2$ increased (3 times). It is possible that the speed was not low enough, and that the curve would flatten out for lower speeds giving constant lateral error for low speeds. However, this minimum lateral error would still be much lower relative to the available road width than was the case for the 2.5m road (see the dashed lines in the lower left subfigure showing width of road available).

In fact, contrary to expectation, there is slightly less lateral error on the wider road. From the prediction error $\mu_{[1:5]}(\Xi(\upsilon))$ it seems subjects produce more noise on the narrower road for a given speed. This additional noise would then feed back to give poorer path following (higher $\mu_{[1:5]}(\rho_{95}(y_{p0}))$ and $\mu_{[1:5]}(\rho_{95}(\theta))$). Higher steer angle $\mu_{[1:5]}(\rho_{95}(\delta))$ for a given speed on the narrower road is consistent with this.

This same reasoning could help to explain the sudden increase in $\mu_{[1:5]}(\Xi(\upsilon))$ for the 2.5m road above 30 m/s, which could be caused by the increase in driver noise as their muscle activity increases. It is known from work by Pick [36] that muscle activation noise increases with muscle activity.

5.4.2   Parameters vs. width and speed

The changes of q_y, q_θ with speed have been mentioned throughout this chapter, but not in the context of speed choice.

Figure 5.23 shows that for 2.5m width, q_y increases with speed initially. This is consistent with the idea that the driver initially keeps path error constant by increasing control effort (increasing q_y). This increase in control effort shows up in the increased steer angle $\mu_{[1:5]}(\rho_{95}(\delta))$, with no increase in lateral error $\mu_{[1:5]}(\rho_{95}(y_{p0}))$.

Above 30 m/s q_y decreases for both 2.5m and 3.5m width roads. At these speeds, though the driver's steering angle $\mu_{[1:5]}(\rho_{95}(\delta))$ does increase, the driver is unable to increase input enough to keep their path error constant. The driver does not have sufficient bandwidth to increase the steer angle at the frequency required to keep the path error constant. For this LQR controller G_I, with no output bandwidth limit, this is equivalent to prioritising steer angle minimisation ahead of path error minimisation.

When road width is changed, the most marked parameter difference is in q_θ. For the wider road, q_θ is increased by an average of 41.3% (for 30 to 40 m/s), and q_y is

increased by an average of 20.0%. This change in q_θ could indicate a difference in driver attitude toward heading errors if there is more room to the edge of road.

Additional insight into the variation of q_y and q_θ with speed in Figure 5.23 can usefully be gained by calculating ratios of steer angle to lateral error, and steer angle to heading error.

$$\Pi_y = \frac{\mu_{[1:5]}(\rho_{95}(\delta)}{\mu_{[1:5]}(\rho_{95}(y_{p0}))} \tag{5.4}$$

$$\Pi_\theta = \frac{\mu_{[1:5]}(\rho_{95}(\delta))}{\mu_{[1:5]}(\rho_{95}(\theta))} \tag{5.5}$$

The ratios Π_y and Π_θ for the data from Figure 5.23 are shown in Figure 5.24:
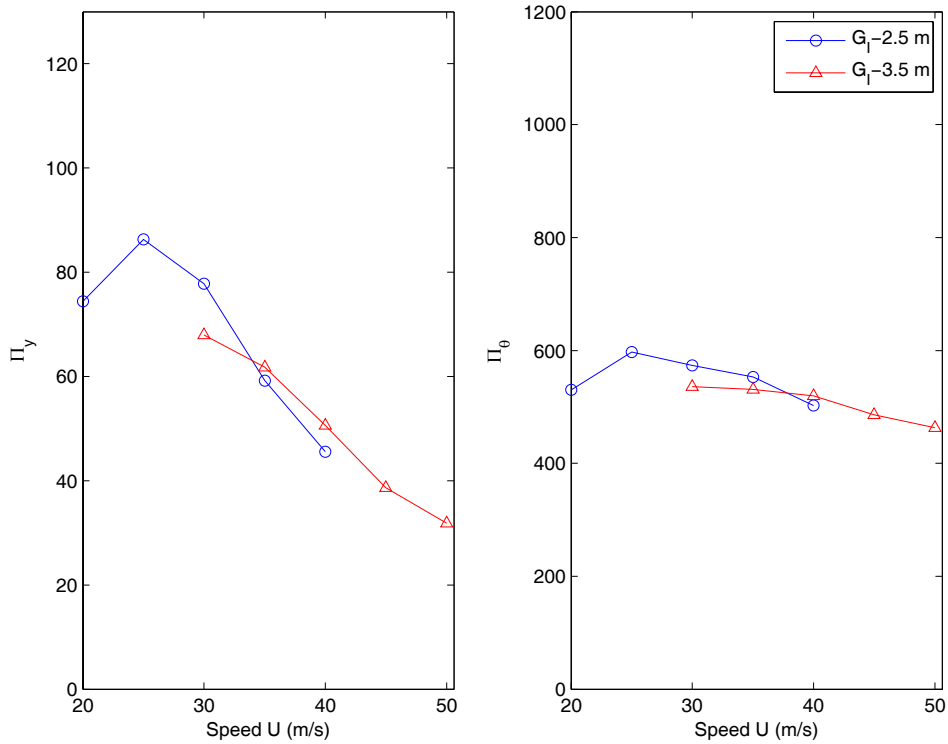
Figure 5.24: Π_y **vs. speed, and** Π_θ **vs. speed for 2.5m, and 3.5m width, mean of results from all subjects**

In many ways these results for Π_y and Π_θ are consistent with the trends in $\mu_{[1:5]}(q_y{}')$, and $\mu_{[1:5]}(q_\theta{}')$ respectively.

For 2.5m width, q_y increases with speed initially, corresponding to gradient of $\mu_{[1:5]}(\rho_{95}(\delta))$ exceeding that of $\mu_{[1:5]}(\rho_{95}(y_{p0}))$. Above 30 m/s the trend for 2.5m and 3.5m looks similar, where q_y decreases, corresponding to the gradient of $\mu_{[1:5]}(\rho_{95}(y_{p0}))$ exceeding that of $\mu_{[1:5]}(\rho_{95}(\delta))$. In this case the driver does not increase steering angle input enough to keep lateral error constant. The driver is therefore prioritising steer angle minimisation ahead of lateral error minimisation.

The ratios Π_y and Π_θ also make it easier to explain why q_θ is nearly independent of speed for both widths, because above 25 m/s, $\mu_{[1:5]}(\rho_{95}(\theta))$ and $\mu_{[1:5]}(\rho_{95}(\delta))$ have similar gradient, corresponding to the nearly constant $\mu_{[1:5]}(q_\theta')$.

What Figure 5.24 does not explain, though, is the difference in q_θ for the two widths. It might be expected that the change in $\mu_{[1:5]}(q_\theta')$ with width would give rise to a change in the ratio Π_θ whereas the ratio is the same for both widths. The decrease in $\mu_{[1:5]}(\rho_{95}(\delta))$ from the 2.5m width to the 3.5m width is largely matched by the decrease in heading error $\mu_{[1:5]}(\rho_{95}(\theta))$. A similar observation applies to the (smaller) change in $\mu_{[1:5]}(q_y')$ with width.

5.4.3 Parameters vs. subject

Comments in the previous sections refer to the 'ensemble of subjects' by using the mean of parameters across all subjects. As was mentioned in the previous section, it is possible that results from one atypical subject might have skewed the mean to be unrepresentative of the ensemble.

In this section the subjects' results are shown individually to examine differences between subjects, and to establish whether the parameter mean is a fair representation of the ensemble. It is also important to establish whether variance is caused by individual subjects being variable, or by differences between subjects. Model G_I is used throughout this section with the results from the 2.5m road width.

Figure 5.25 shows parameters $\mu(q_y')$, $\mu(q_\theta')$, $\mu(\Xi(\upsilon))$, $\mu(\rho_{95}(y_{p0}))$ $\mu(\rho_{95}(\theta))$, and $\mu(\rho_{95}(\delta))$ as a function of speed with one line per subject for subjects 1, 2 and 3. Figure 5.26 shows the same parameters for subjects 4 and 5. Each point is the average of three parameter estimates, and the error bars show one standard deviation each side of the mean.
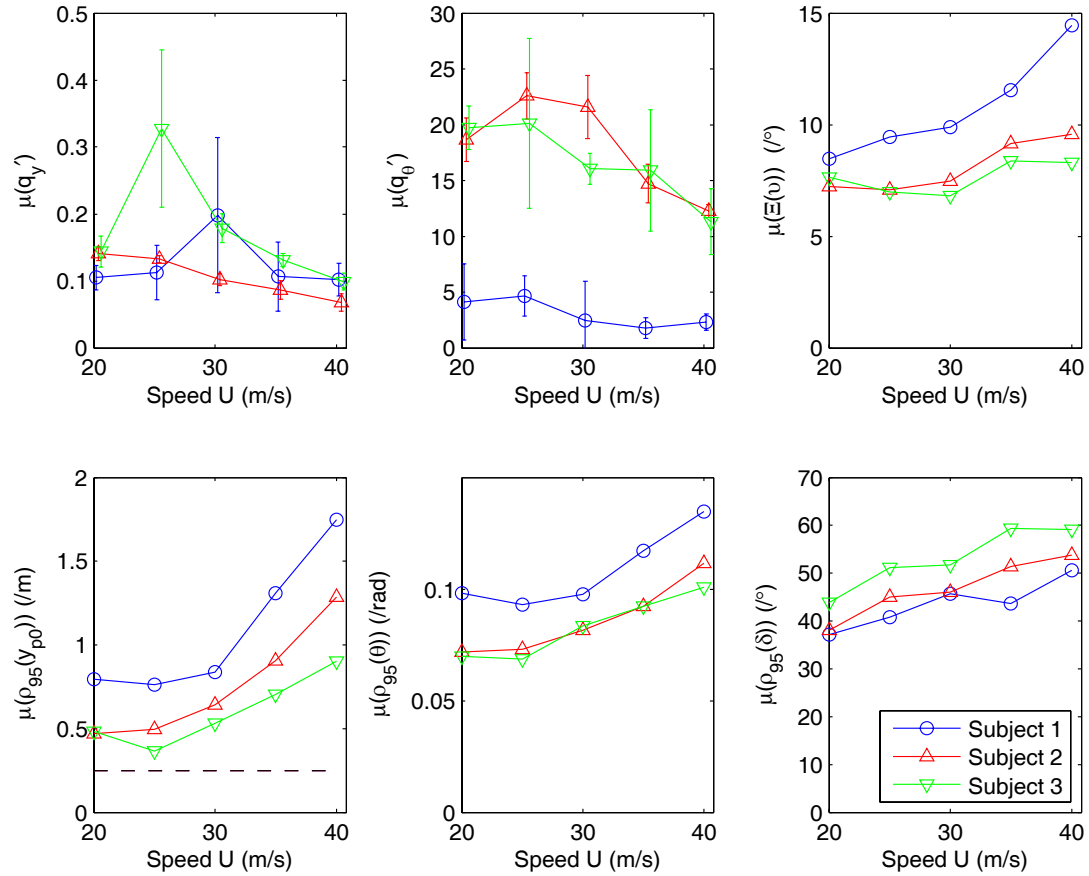
Figure 5.25: Parameters vs. speed for $\mathbf{G_I}$, 2.5m width, fitted to subjects 1, 2 and 3
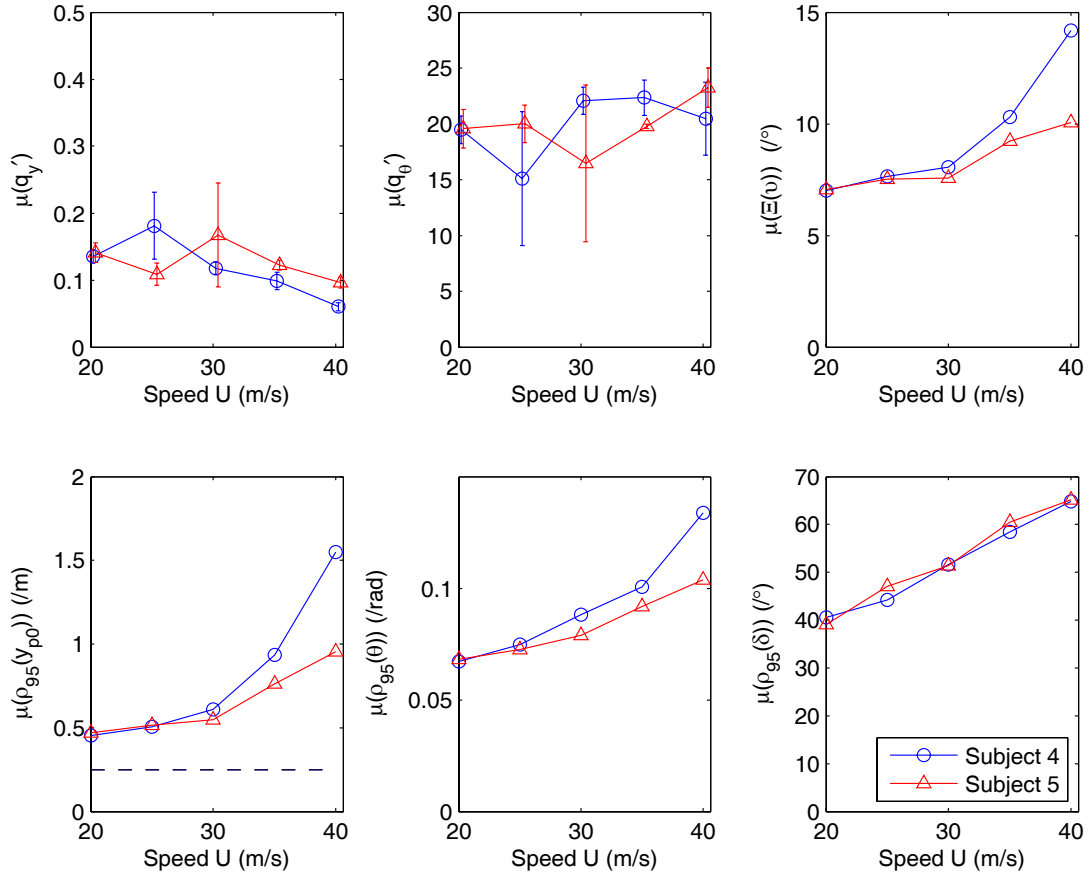
Figure 5.26: Parameters vs. speed for G_I fitted to subjects 4 and 5

The results show that individual subjects have low $\left\{q_y',q_\theta'\right\}$ variance in most cases, but that the means $\mu(q_y')$ and $\mu(q_\theta')$ differ between the subjects. An ensemble average of the parameters from all subjects loses this information, and appears to have large parameter variance.

Subject 3 achieves lower lateral error $\mu(\rho_{95}(y_{p0}))$ than other subjects by using larger steer angle $\mu(\rho_{95}(\delta))$. This shows up as a higher $\mu(q_y')$ than subject 2 for the 25 to 40 m/s range. This variation of $\mu(q_y')$ is consistent with the ratio Π_y in section 5.4.2.

Subject 1 has higher lateral error $\mu(\rho_{95}(y_{p0}))$ than most of the other subjects. Subject 1 also has significantly higher heading error $\mu(\rho_{95}(\theta))$, but lower steer angle $\mu(\rho_{95}(\delta))$. This combination gives rise to much lower $\mu(q_\theta')$, consistent with ratio

Π_θ, but not the expected reduction in q_y which would be consistent with ratio Π_y. It is likely that subject 1's poor fit (large $\mu(\Xi(\upsilon))$) may explain the inconsistency with ratio Π_y in this case.

Subject 1 has chosen a control strategy which weights reduced steer angle more than reduced path error. Subject 1 is a non-driver, and had a visibly different attitude to the driving task to the other subjects (less concerned about leaving the road). Given that subject 1 was a non-driver it is possible that a simpler driver model could fit their behaviour better. Figure 5.27 therefore shows prediction error $\mu(\Xi(\upsilon))$ vs. speed for subjects 1 to 5 for G_{II}, the simplest driver model.
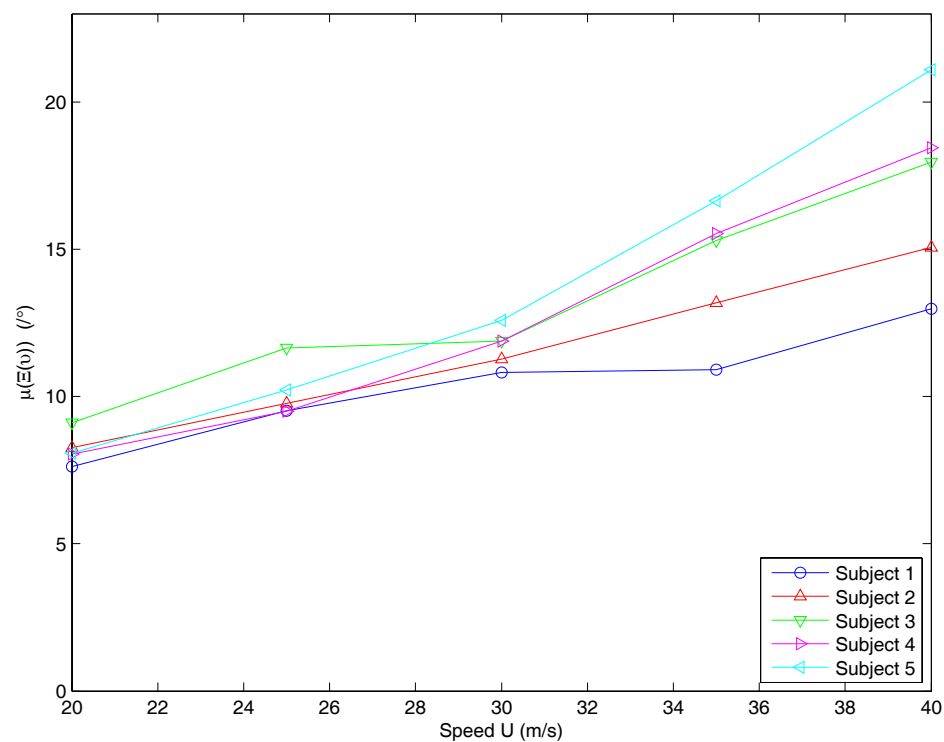
Figure 5.27: $\mu(\Xi(\upsilon))$ vs. speed for subjects 1 to 5. for model $\mathbf{G_{II}}$

It is clear from Figure 5.27 that subject 1 has the lowest prediction error $\mu(\Xi(\upsilon))$, and hence fits better to G_{II} than any other subject. This suggests that this novice subject is better modelled without vehicle state gains. Subject 1 is not as well modelled by G_{III}, suggesting that for this driver, the point mass model of the vehicle on which G_{II} is based reflects their internal model of the vehicle more closely than the more

sophisticated G_{III}. Given the discrepancy between subject 1 and the rest of the group, it is tempting to exclude this subject from the ensemble. If subject 1 were excluded, the mean of the parameter estimates of the remaining subjects could be used as a representation of a 'typical' experienced driver using model G_I. Subject 1 could then represent a novice driver using model G_{II}. The controller weights and prediction error for these two groups are shown for low and high speed in Table 5.4.

	Model	20 m/s			40 m/s		
		q_y	q_θ	$\Xi(\upsilon)$	q_y	q_θ	$\Xi(\upsilon)$
Subject 1 (novice) μ_1	G_{II}	0.0546	8.48	7.63	0.0150	2.33	13.0
Subjects 2-5 (typical) $\mu_{2:5}$	G_I	0.140	19.4	7.24	0.0809	16.8	10.5

Table 5.4: Mean parameter values for novice and typical subject groups, for 2.5m wide road.

Figure 5.25 and Figure 5.26 show that most subjects have similar gradients for prediction error $\mu(\Xi(\upsilon))$, lateral error $\mu(\rho_{95}(y_{p0}))$ and heading error $\mu(\rho_{95}(\theta))$ with speed, except subject 4. Subject 4 has similar values for these three parameters to the other subjects at low speed, but much higher values at high speed. The high prediction error $\mu(\Xi(\upsilon))$ for this subject at high speed contributes to the higher mean prediction error for the ensemble $\mu_{[1:5]}(\Xi(\upsilon))$ for the 2.5m width road seen in Figure 5.23.

In Figure 5.25 and Figure 5.26, the shape of $\mu(q_y')$ and $\mu(q_\theta')$ vs. speed is not consistent between subjects, implying that each subject reacted differently to changes in speed. Subjects 2, 3, 4 and 5 have similar parameter values for both $\mu(q_y')$ and $\mu(q_\theta')$ at low speed. However, whereas subjects 2 and 3 show a marked reduction in $\mu(q_\theta')$ at high speed, subjects 4 and 5 show a slight increase in $\mu(q_\theta')$ at high speed. Both subjects 4 and 5 have larger steer angles $\mu(\rho_{95}(\delta))$ at high speed than subjects 2 or 3, which is consistent with subjects 4 and 5 showing increased values of $\mu(q_y')$ and $\mu(q_\theta')$ for these speeds (given that all four subjects have similar path error $\mu(\rho_{95}(y_{p0}))$ and $\mu(\rho_{95}(\theta))$).

5.5 Implications for speed choice model

The use of these results to verify the speed choice hypothesis was not carried out within the time frame of this work, and could be undertaken as future work as detailed in chapter 6. However, there are some possibilities for a speed choice model which can be identified at this stage from the results shown in section 5.4.1 and 5.4.2.

The lateral error vs. speed vs. width surface used for the speed choice hypothesis in chapter 2 is available from this data. It should therefore be possible to test the original hypothesis against this data. Both q_y and q_θ change with width, so the variation of driver effort with width that was empirically represented in chapter 2 by the lateral error percentile λ vs. width relationship could be replaced by a measure of driver effort through q_y and q_θ.

Other speed choice hypotheses may also be possible given the new data. For example the driver's internal noise He (measurable using the prediction error $\mu(\Xi(\upsilon))$) changes with speed and width. It may be possible to use the variation in internal noise as an alternative to path error as a cue to the driver's speed choice. Such a model might entail the driver using the internal noise as a measure of driving 'comfort', and limiting their speed choice to keep their internal noise below a threshold level.

An alternative hypothesis might be based around the fact that the drivers' preview controller gains, and state gains were found to be fairly consistent with speed (section 5.3.4). It is possible that a driver could choose their speed in order to allow a constant controller to be used. Speed could then be limited by the path width achievable with this constant controller.

5.6 Conclusions

The identification procedure set out in chapter 4 was used to identify driver parameters for data collected in simulator experiments on five subjects at a range of speeds, and two lane widths. Ten iteration loops were found to be sufficient for convergence to estimates q_y' and q_θ'. A [5/5] order noise model was found to be flexible enough to fit well to the real driver data, and be of low enough order not to cause q_y' and q_θ' outliers.

The weighted prediction error minimised during the identification $\Xi(\varepsilon)$ could not be compared between different fits due to different noise models. So the unweighted prediction error $\Xi(\upsilon)$ was used to compare the goodness of fit of the models.

Time delay τ' could not be identified reliably in the validation of chapter 4, so a value of $\tau' = 0.2$ s was used for most models based on values found from previous research [36, 39]. $\tau' = 0.1$ s was used for G_V as it was the only value which gave an NMS natural frequency ω_n' within the domain (0 to 9 Hz). Changing τ' was found to affect only the magnitude of q_y' and q_θ' so any findings relating to the variation of these parameters with speed would still be valid even if τ' later turned out to be incorrect.

Models G_I to G_{VIII} were compared based on their prediction error $\Xi(\upsilon)$. G_I, G_{IV}, G_{VII} and G_{VIII} were found to give similar, low prediction error $\mu_{[1:5]}(\Xi(\upsilon))$ for all speeds, so were all suitable candidates for modelling the ensemble of subjects. G_{II}, G_{III} and G_V gave higher prediction error $\mu_{[1:5]}(\Xi(\upsilon))$ than the other models especially for higher speeds, meaning that they were not suitable to model the majority of subjects. Model G_I gave the best compromise between low prediction error $\Xi(\upsilon)$ and model simplicity so was used for later comparisons.

The parameter estimates $q_y{}'$ and $q_\theta{}'$ were compared between the driver models. Models G_I, G_{IV} , G_{VII} and G_{VIII} gave very similar q_y and q_θ because their steer angles for a given q_y and q_θ were found to be similar in chapter 3. q_y for G_V differed from all other models due to the presence of a neuromuscular filter which does not feature in its LQR controller. Identified NMS parameters were constant for the range of speeds. Model G_{VII} consistently gave $\omega_n \approx 1.4\,\text{Hz}$, and G_{VIII} consistently gave $\xi \approx 0.6$ for all speeds. G_V gave a different ω_n but gave higher prediction error $\mu_{[1:5]}(\Xi(\upsilon))$.

The controller gains of the fitted driver models were compared at $U = 20\,\text{m/s}$, and $U = 40\,\text{m/s}$, as well as the time histories of the predicted steer angle. At $U = 20\,\text{m/s}$ the time histories of steer angle predicted by all models were similar, so their prediction error $\Xi(\upsilon)$ was also similar. Additional model complexity did not therefore help to fit the driver data better at low speed. At 20 m/s all preview controllers also had similar preview length and gain magnitudes. G_{IV}, G_{VII} and G_{VIII} all showed preview shifting by 0.1 seconds. This preview shifting negated the lagging effect of the delay N_d, and the NMS in these models.

At $U = 40\,\text{m/s}$, models G_I, G_{IV}, G_V, G_{VII} and G_{VIII} all gave similar steer angles, confirming the reason for their similar prediction error $\mu_{[1:5]}(\Xi(\upsilon))$. At $U = 40\,\text{m/s}$ models G_{II} and G_{III} gave different steer angles to G_I, and had much higher prediction error $\mu_{[1:5]}(\Xi(\upsilon))$, implying their absence of vehicle state feedback made them worse models of the behaviour of the majority of subjects. At 40 m/s the preview gains for all models were only slightly changed from their counterparts at 20 m/s, giving a doubling of preview distance.

State gains were only 20% different for the two speeds $U = 20\,\text{m/s}$ and $U = 40\,\text{m/s}$, implying that the subjects may not change their vehicle state gains appreciably with speed. Any differences in state gains between models did not appear to be correlated to prediction error $\mu_{[1:5]}(\Xi(\upsilon))$, so the values of q_y and q_θ were not being fitted solely to replicate a particular vehicle state gain used by the test subjects.

The variation of path error with lane width and vehicle speed were compared to the expectation from a modified speed choice hypothesis. For 2.5m width, lateral error $\mu_{[1:5]}(\rho_{95}(y_{p0}))$ was constant at low speeds due to increasing driver steering activity indicated by increased $\mu_{[1:5]}(\rho_{95}(\delta))$. As speed increased, lateral error and heading error increased as the driver's internal noise *He* increased. The increase in *He* could have been caused by increased steering activity. This observation agreed with the expectation of the variation of path error with speed from the modified hypothesis. For 3.5m width, contrary to expectation no sudden change in gradient of path error vs. speed was found for increasing speed. For 3.5m width it was found that $\mu_{[1:5]}(\rho_{95}(y_{p0}))$, $\mu_{[1:5]}(\rho_{95}(\theta))$, $\mu_{[1:5]}(\rho_{95}(\delta))$, and $\mu_{[1:5]}(\Xi(\upsilon))$ all reduced slightly from those of 2.5m. This could have been due to the reduced internal noise caused by the lower steering activity.

The variation of $q_y{}'$ and $q_\theta{}'$ with lane width and vehicle speed were also compared to the expectation from the modified speed choice hypothesis. For the 2.5m wide road at low speeds $\mu_{[1:5]}(q_y{}')$ increased with speed as expected indicating increased driver effort. For higher speeds, $\mu_{[1:5]}(q_y{}')$ reduced with increasing speed as the increase in lateral error exceeded the increase in steer angle, indicating a change in preference toward steer angle minimisation rather than lateral error minimisation. Increased road width gave a dramatic reduction in $\mu_{[1:5]}(q_\theta{}')$, consistent with the idea that the driver would reduce their weighting on heading error if the road edge was further away. Ratios Π_y and Π_θ were found to correlate with the variation of $\mu_{[1:5]}(q_y{}')$ and $\mu_{[1:5]}(q_\theta{}')$ for a given width. They did not correlate well to the changes in $\mu_{[1:5]}(q_y{}')$ and $\mu_{[1:5]}(q_\theta{}')$ between widths.

The path following errors, prediction errors, and steering controller weights were compared between subjects. Most subjects' results were found to fit well to the ensemble means used earlier in the chapter. However, Subject 4 was found to have higher internal noise than other subjects at high speed, leading to higher lateral error $\mu(\rho_{95}(y_{p0}))$ and heading error $\mu(\rho_{95}(\theta))$ at high speed. Subject 1 was found to be

different to the other subjects in his attitude and path following ability. This was thought to be due to the fact that subject 1 was a non-driver, and was found to be better modelled by the simpler model G_{II} than by model G_I.

Controller weights and prediction error were listed in Table 5.4 for two subject groups: subjects 2 to 5 as a representation of typical experienced drivers using model G_I; subject 1 as a representation of a novice driver using model G_{II}. Results were for the 2.5m wide road only as the 3.5m wide road was not analysed separately for each subject.

The possibility of using this data for the development of a revised speed choice model was discussed. Some possible formulations were proposed, including using the controller weights q_y and q_θ to replace the driver effort parameter identified in chapter 2.

Chapter 6: Conclusions and future work

 A programme of work was carried out into the topic of driver speed choice. In this chapter a summary of the work carried out and the main conclusions are given in sections 6.1 and 6.2. The results highlighted some key areas for future work, which are described in section 6.3.

6.1   Summary of work

6.1.1   Review of driver speed choice and steering models (Chapter 1)

In chapter one, speed choice was identified as an important factor in road accidents, and also in driver learning. Improved understanding of speed choice could assist in the design of roads and vehicles to aid more appropriate, and therefore safer, speed choice. Research into the speed choice behaviour of drivers was therefore proposed.

The findings from the literature review and resulting research objectives can be summarised as follows:

Path error based models of speed choice can predict the observed reduction in lateral acceleration of drivers at high speed. However, the link between measured path error and speed choice of drivers has not been examined. To examine this link, simulator experiments to measure driver path error and speed choice as a function of road geometry were proposed.

In order to model driver speed choice accurately, an understanding of the generation of path error as a result of the driver's steering control is required. To aid this understanding, accurate models are required of the driver's preview steering control and how it varies with speed and road width. Models of preview steering control of drivers are well developed, but bias free estimates of the preview model controller weights used by drivers were not found in the literature. The development of experiments and identification algorithms designed to minimise bias during the identification of driver steering control models was therefore proposed.

Any differences between the steering control of experienced and inexperienced drivers may be significant in the generation of different amounts of path error and therefore different speed choice for experienced and inexperienced drivers. Driver internal models with simplified vehicle dynamics have been proposed to represent the less sophisticated preview control of a novice driver. However, these controllers have not been demonstrated to give better fit to data collected from novice drivers than controllers whose internal models have more sophisticated vehicle dynamics. It was therefore proposed to develop models suitable for representing a novice driver, and fit this model to measured driver data.

The effect of the driver's neuromuscular system (NMS) on their steering control bandwidth may be significant in the path error performance that can be achieved by real drivers. It may therefore be important to include the effect of the driver's NMS in the formulation of driver steering models. Neuromuscular system models have been studied and included in driver models, but had not been incorporated into the driver's internal model to represent a driver who modifies their control to take account of knowledge of their own neuromuscular system. It was proposed that driver models be developed to incorporate the effect of the NMS into the driver's internal model. This would allow assessment of the effect of including the driver's knowledge of their own bandwidth limitation on their preview controller. It might also provide a more accurate driver model.

6.1.2 Driver speed choice modelling (Chapter 2)

In chapter two, data from a simulator test of speed choice were used to compare the models of speed choice found in the literature review. From this analysis, none of the models could provide all three requirements of good fit: a mechanistic model whose assumptions were met by the fitted parameters and an ability to predict both the width and radius dependence of speed choice.

A speed choice hypothesis was developed to incorporate the important features of the previous models. This path error prediction hypothesis was assessed using measured data from a simulator test.

During the simulator test, the subject's lateral error was independent of bend curvature, but his speed was not, indicating that his speed was changed in order to keep lateral error constant. The subject's lateral error changed with width, but not by enough to keep the ratio of lateral error to available tolerance constant. This behaviour was identified as either a risk strategy, or a change in steering control strategy (effort) by the driver. A variable percentile of lateral error with width was added to the path error based speed choice model to take account of this behaviour, but it was necessary to assume constant driver effort.

A change of driver effort (or steering strategy) could not be ruled out in real driving situations, so new experiments were proposed to measure changes in driver steering strategy with speed and road width. These experiments were intended to determine if changes in driver steering control strategy influenced driver speed choice. The experiments proposed involved driving random roads at a range of fixed speeds, and a range of road widths. The driver steering strategy was to be determined by fitting preview steering control models to the measured steering control action of the driver.

6.1.3 Models of driver steering control (Chapter 3)

A requirement was identified in chapter two for a driver model which included a steering strategy parameter, so models of the driver were developed based on Sharp's LQR controller structure. The models included cost function weights to allow the driver's strategy to be altered in favour of lateral error minimisation, heading error minimisation, or steer angle minimisation.

In chapter one, the need was identified for models to represent the novice driver, and to incorporate the effect of the NMS into the driver's internal model. A driver model with simplified vehicle dynamics was developed to represent novice drivers, and a range of models including the driver's neuromuscular system was also developed.

The following range of LQR controllers was developed:

- Model G_I: Sharp's controller using a 2DOF bicycle internal model.

- Model G_{II}: a point mass internal vehicle model to represent a novice driver.

- Model G_{III}: a single degree of freedom internal model with no sideslip.

- Model G_{IV}: as G_I with added steer angle delay states.

- Model G_V: internal model as G_I, but with output steer angle filtered through an NMS model

- Models G_{VI}, G_{VII} and G_{VIII}: G_I with added internal NMS states and output steer angle filtered through an NMS model.

The preview and state gains of the controllers were compared for low and high speed. Reasons for the differences in state gains and preview gains were explained based on the differences between the models and changes in system dynamics with speed.

The driver models were simulated driving a vehicle along a random road path at low and high speed, and with and without driver delay. The performance of the models was compared and explained based on the differences found in their preview and state gains. Models G_{IV}, and G_{VI} to G_{VIII} were found to give very similar steer angles to G_I due to good open loop inversion of the system being controlled. This was achieved by preview shifting and additional state gains. Model G_V had degraded closed loop steering performance due to the presence of an NMS filter that was not included in the LQR controller formulation.

6.1.4 *Identification of driver steering models (Chapter 4):*

It was necessary to ensure that models identified from driver data did not suffer from identification bias, so chapter four developed the procedure necessary to ensure bias free estimates from experimental data. An iterative procedure using the direct method was designed for use in identifying driver model parameters.

Bias of identification was demonstrated when a white noise model was used to identify data created using realistically coloured driver noise. A perfect noise model eliminated bias when the driver noise was coloured.

Validation of the identification bias of the LQR controller cost function weights was carried out using model G_I for the following parameters: track PSD amplitude, road spectral density roll-off gradient and track wavenumber cut-off. Suitable values were determined for use in experiments. Vehicle speed was found not to affect identification bias or variance.

A noise model of too low an order led to identification bias, but a noise model of too high an order was prone to identification outliers. The order of the noise model had therefore to be just sufficient to express the driver noise present.

Driver time delay was nearly perfectly identified when a perfect noise model was used. However, with an identified (i.e. imperfect) noise model, time delay could not be identified reliably for a realistic driver noise level.

Identification of each of the driver models G_I to G_{VIII} was validated at a low and a high speed with an identified noise model, but with correct time delay. Small bias was found for model estimates G_I' to G_V'. G_{VI}' had very large variance of the identified LQR controller weights, so was too unreliable for use in driver identification in chapter five. G_{VII}' and G_{VIII}' were more successful than G_{VI}' at identifying NMS parameters and cost function weights so were used for the identification of NMS parameters in chapter five.

6.1.5 Driver model identification results (Chapter 5)

A requirement to determine the changes in control strategy of drivers with speed and road width was identified in chapter two, so chapter five describes work aimed at fulfilling this requirement.

Experiments were carried out on subjects using a fixed base simulator. Five subjects drove roads at a set of fixed speeds, on two road widths. The identification procedure set out in chapter four was used to identify driver parameters for data collected in the simulator experiments. Sufficient iteration loops and noise model order were used to reliably identify the data.

As demonstrated in chapter four, time delay could not be reliably identified, so a fixed value was used. Changing the delay was found to affect the magnitude of the controller cost function weights, but not their dependence on speed, so any findings relating to the variation of these parameters with speed would still be valid even if the chosen delay later turned out to be incorrect.

Models G_I to G_{VIII} were compared based on their unweighted prediction error, controller cost function weights, controller gains, and time histories of their predicted steer angle. Models without vehicle state feedback gave poor fit to the behaviour of the majority of subjects. Preview controllers and state gains for all models were found to be similar for low and high speeds. Consistent NMS parameters were identified for all speeds with model G_{VII}. Model G_I was used for later comparisons as it gave very close to the lowest prediction error and was simpler than model G_{IV}.

The path following errors, prediction errors, and steering controller weights were compared between subjects. Most subjects' results were found to fit well to the ensemble means used earlier in the chapter. However, the subject with no driving experience differed from the other subjects and was found to be better modelled by the driver model with a simplified internal vehicle model (G_{II}) than by model G_I.

The variation of path error with lane width and vehicle speed were compared to the expectation from a speed choice hypothesis modified to include steering controller weights. For the narrower road width, the results agreed with the modified hypothesis. For the wider road, contrary to expectation, no sudden change in gradient of path error vs. speed was found for increasing speed. Path error and steering angle were found to reduce as road width increased, possibly due to reduced internal noise caused by the lower steering activity.

The variation of the cost function weights with lane width and vehicle speed was also compared to the expectation from the modified speed choice hypothesis. The variation of controller weights was not well predicted by the hypothesis, however, the variation in lateral error weight with speed did indicate a change in preference toward steer angle minimisation rather than lateral error minimisation as speed increased. Also, as predicted, increasing road width gave a reduction in the heading error cost function weight.

The possibility of using this data for the development of a revised speed choice model was discussed. Some possible formulations were proposed, including using the LQR controller cost function weights as the driver effort parameter identified in chapter two.

6.2 Conclusions

Driver speed choice modelling (Chapter 2):

- Driver steering control effort needs to be quantified for a successful path error based speed choice model.

Models of driver steering control (Chapter 3):

- Models with added delay states and neuromuscular system states gave similar steer angles to Sharp's model when driven in closed loop with a vehicle. This was due to good open loop inversion of the system dynamics by preview shifting and their additional state gains.

Identification of driver steering models (Chapter 4):

- The elimination of identification bias was demonstrated using an iterative algorithm based on Ljung's direct method.
    - Parameters were found for a random road excitation to give successful identification of artificially created driver data.
    - Time delay could not be identified with an identified noise model.
    - Too low noise model order was found to give bias, and too high order gave outliers.
- The algorithm was proven to give correct identification with each of the driver models derived in chapter 3 at 20m/s and 50 m/s.
    - All models except the 6 state NMS model could be identified with a bias of the steering controller weightings of less than 6.2%, and variance of less than 36.7%.
    - The bias and variance of the lateral error weighting q_y was around 1/3 of those of the heading error weighting q_θ.
    - For the 6 state NMS model, bias and variance were too high if both NMS parameters were identified at the same time, so was not used for identification.

234

o Identifying the NMS parameters with separate models gave improved bias of less than 15.4% for the controller weights, but up to 31.5% for the NMS damping. Variance was as high as 66.5% for the heading error weight, and 136% for the NMS damping.

Driver model identification results (Chapter 5)

- The algorithm validated in chapter 4 was used to fit seven models to data from five drivers on two road widths at a range of speeds. Unbiased controller weightings and prediction error were derived, allowing comparison of subjects and models as a function of road width and vehicle speed.

- The assumed driver delay was found to affect the values of the controller weights, but not their trends with speed, so a delay of 0.2s was assumed.

- Differences between the fitted models were found when comparing their prediction error and derived model parameters for data from the narrow road.

   o Similar state and preview gains were seen for most models, suggesting that these gains may be similar to those of the real drivers.

   o All fitted models gave similar steer angles to Sharp's model at low speed, hence similar prediction error, but those with simplified internal models gave poor fit at high speed.

   o Including an NMS did not improve model fit, but inclusion of delay states gave a slight improvement in the unweighted prediction error.

   o Consistent NMS parameters were identified for a range of speeds with a mean natural frequency of 1.35 Hz and damping coefficient of 0.59.

- Differences in behaviour between subjects were found on the narrow road which could be interpreted as differences between novice and experienced drivers.

   o The point mass driver model was found to be the most suitable model for the novice subject, whereas Sharp's model was the most suitable model for the experienced subjects.

- Changes in driver control strategy were found as a function of speed and road width using the fitted results from Sharp's model for the ensemble of subjects.

   o Contrary to expectation, path error reduced for increased road width, possibly due to reduced driver noise.

- Increased road width from 2.5m to 3.5m gave a 41.3% reduction in heading error weight, but an unexpected 20.0% increase in lateral error weight.
- A modified speed choice hypothesis correctly predicted the variation of path error and steer angle with speed for the narrow road, but not for the wider road.
- Similar state and preview gains were seen for all speeds suggesting drivers may keep a constant controller for a range of speeds.

6.3   Recommendations for future work

The results and conclusions of this work highlighted some key areas for future work.

6.3.1   Analysis of full interactions

A detailed analysis of all of the data should be undertaken to determine the interactions between parameters now that the important first order effects have been shown.

The analysis of parameter changes with speed, width and subject was carried out using only driver model G_I. This same analysis should be carried out at least on models G_{VII} and G_{IV}. The former because it includes a neuromuscular system, and the latter because it gave lower prediction error than G_I, and may therefore be a better model of the driver.

Also, the parameter variations with each subject were only compared for the narrower road. A similar comparison should also be carried out for the wider road, to give insight into the reasons for ensemble parameter changes on the wider road.

6.3.2   Derived model validation

The direct method fitting procedure was validated in chapter five, but the models fitted in chapter five have not been validated. The next step is to simulate these controllers in closed loop with a vehicle to check that they reflect the behaviour of a real driver.

Also, a method should be found to identify, rather than presume a driver delay. The dependence of driver delay on subject, width, and speed could then be determined, and model fit may be improved.

6.3.3 Larger model set

The model set is currently restricted to LQR preview models, but model predictive control (MPC) might usefully represent the driver's reaction to the constraints provided by the road edges. Alternatively, the cost function used for the LQR model could be modified to include other driver effort measures beyond simply steer angle. Finally, a more sophisticated neuromuscular model could be developed, as the NMS used in this work did not significantly improve the fit of the model.

6.3.4 Hypothesis for path error vs. speed

Use should be made of the free speed choice data gathered during the experiments described in chapter five. The speed choice models proposed in chapter five incorporating the measured preview model cost function weights could be validated using these data.

6.3.5 Further testing

With the increasing availability of accurate vehicle positioning systems an assessment of path error and speed choice of drivers in real vehicles could be undertaken to further validate a path error based speed choice model. This would allow the influence of realistic non-linear vehicle dynamics, and more realistic driver risk stimuli to be assessed. As an intermediate step, tests on a moving base simulator, and the inclusion of more realistic steering torque feedback would give useful insight.

6.3.6 Driver learning

The interconnection between speed choice and driver learning of the steering control task was outlined in the introduction to this dissertation. If a validated model of driver steering control (such as that described in this dissertation) could be linked to a path error based speed choice model, a closed loop driver steering and speed choice model could be constructed. This model could be used to explore the effect on speed choice

of the driver's learning of their own steering competence by interpolation and extrapolation of their path error vs. speed vs. curvature surface. This would be particularly important for a non-linear vehicle model, where the more complex dependence of vehicle dynamics on vehicle states might lead to the driver making poor predictions of their path error, and hence poor speed choices. This would in turn affect the driver's learning of the non-linear vehicle dynamics.

Appendix A: Vehicle model parameters

The parameters used for the vehicle model for the 180° curve tests in chapter 2 are shown in Table A.6.1. The parameters used for the vehicle model for chapters 3, 4 and 5 are shown in Table A.6.2.

Variable	Value	Units	
C_f	152386	N/rad	Front axle tyre stiffness
C_r	152386	N/rad	Rear axle tyre stiffness
a	1.31	m	Front axle to CG distance
b	1.31	m	Rear axle to CG distance
L	2.62	m	Wheelbase of vehicle
M	1673	Kg	Mass of vehicle
I	2550	Kg m^2	Yaw moment of inertia of vehicle
W_v	2.0	m	Vehicle width
K_{sw}	16	-	Steer angle to wheel angle gain

Table A.6.1: Parameters used for vehicle model for 180º curve tests of (chapter 2)

Variable	Value	Units	
C_f	152386	N/rad	Front axle tyre stiffness
C_r	152386	N/rad	Rear axle tyre stiffness
a	1.2	m	Front axle to CG distance
b	1.4	m	Rear axle to CG distance
L	2.6	m	Wheelbase of vehicle
M	1673	Kg	Mass of vehicle
I	2811	Kg m^2	Yaw moment of inertia of vehicle
K_{sw}	16	-	Steer angle to wheel angle gain
W_v	2.0	m	Vehicle width
K_{col}	0.08	N m/deg	Spring return on column angle stiffness
λ_{col}	0.004	Nms/deg	Damping on column velocity

Table A.6.2: Parameters used for vehicle testing for random roads (chapters 3 to 5)

Appendix B: Simulator vehicle longitudinal dynamics model
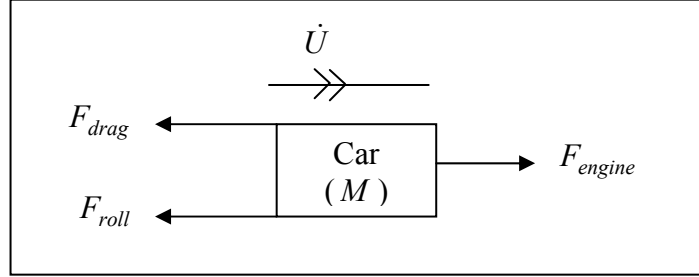
Figure B.1: Free body diagram of longitudinal vehicle model

$$F_{engine} - F_{drag} - F_{roll} = \frac{P_{max}.\phi_{thr}}{U} - U^2 A.C_d - F_{roll} = M.\dot{U} \qquad (B.1)$$

where:

F_{engine} = Engine thrust F_{roll} = Rolling resistance

F_{drag} = Aerodynamic drag force

P_{max} = Max engine power (1000 kW)

ϕ_{th} = Throttle proportion (from −1 to 1)

U = Forward speed

$A_1 C_d$ = Frontal Area (4 m^2) x Aero drag coefficient

M = Vehicle mass

F_{engine} is a forward force from the engine, whose power output is proportional to throttle proportion. F_{drag} is a simplified aerodynamic drag force term, while F_{roll} is a frictional rolling resistance. A saturator ensures that longitudinal force cannot exceed that necessary to produce an acceleration of 1g as a model of the traction limit of the tyres. The values of these parameters are not chosen to reflect any specific car's performance (e.g. 1000 kW engine used is very large) though they are qualitatively realistic, but are chosen to allow the driver to change speed easily with little requirement to plan ahead their speed changes.

Appendix C: Lateral error calculation for 180º curves

Lateral error estimation for 180º curves depends on which part of the curve is being traversed, the straight, transition, or constant curvature part. For the straight error equals the lateral offset position y. For the constant curvature part error is the difference between the curve radius and the distance of the car from the centre point of the arc. For the transition in Figure C.1, an iterative routine is used to find the point on the path (P) whose perpendicular passes through the vehicle's position (A). The distance (y_{p0}) between this point and the vehicle's position is then evaluated.
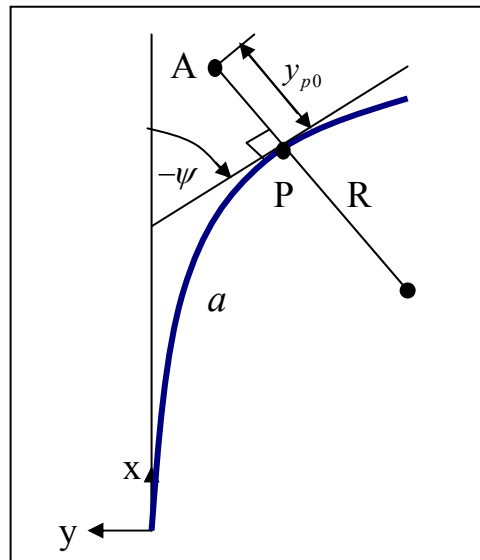

Figure C.1: Lateral error calculation for transition section

Appendix D: Lateral error evaluation using intrinsic co-ordinates

An algorithm for 'on the fly' calculation of lateral error normal to the intended path of the vehicle was derived from first principles. Input is an intrinsic road profile, with sufficient resolution to approximate a continuous profile. The resolution necessary will depend on the wavelength content of the profile, however, 0.1m resolution was found to be adequate. The vehicle trajectory is determined from the vehicle states (v, θ) and the forward speed U.
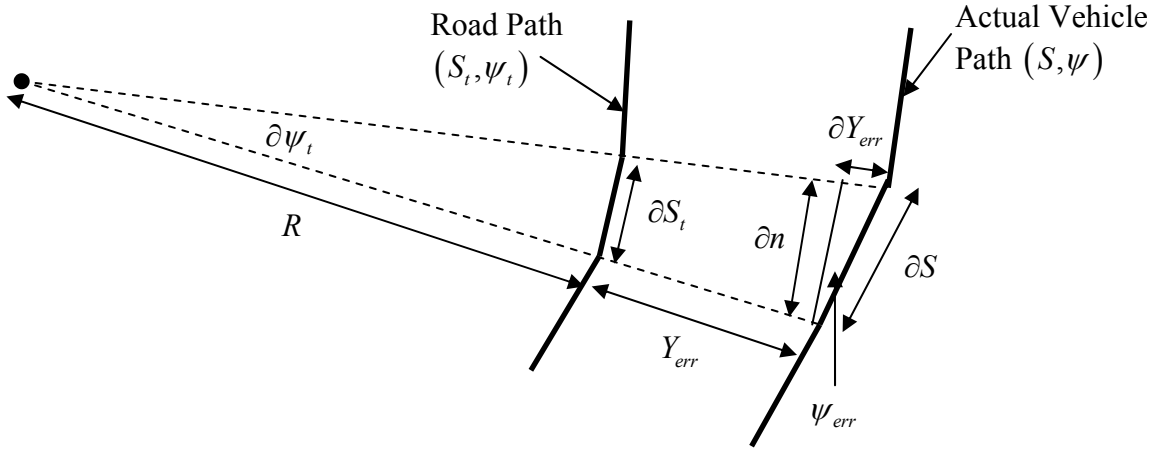

Figure D.1: Geometric definitions for derivation of intrinsic lateral error estimation

From Figure D.1:

$$\partial S_t = R \partial \psi_t \qquad (\text{D.1})$$

$$\partial n = (R + Y_{err}) \partial \psi = \partial S_t + Y_{err} \partial \psi_t \qquad (\text{D.2})$$

$$\partial S \cos(\psi_{err}) = \partial n = \partial S_t + Y_{err} \partial \psi_t \qquad (\text{D.3})$$

$$\partial S = \frac{\partial x_t + Y_{err} \dfrac{\partial \psi_t}{\partial S_t} \partial S_t}{\cos(\psi_{err})} \qquad (\text{D.4})$$

So as $\partial S \Rightarrow 0$:

$$\frac{dS_t}{dS} = \frac{\cos(\psi_{err})}{1 + Y_{err} \dfrac{d\psi_t}{dS_t}} \tag{D.5}$$

Note that:

$$dS = \sqrt{v^2 + U^2}\, dt \tag{D.6}$$

$$\psi_{err} = \psi - \psi_t \tag{D.7}$$

$$\psi = \frac{v}{U} + \theta \tag{D.8}$$

So as a function of time equation (D.5) becomes (using equation(D.6)):

$$\frac{dS_t}{dt} = \frac{\cos(\psi - \psi_t)\sqrt{v^2 + U^2}}{1 + Y_{err} \dfrac{d\psi_t}{dS_t}} \tag{D.9}$$

Similar equations can be derived for lateral displacement from the path (lateral error):

$$\partial Y_{err} = \partial S \sin(\psi_{err}) \tag{D.10}$$

So as $\partial s \Rightarrow 0$, and incorporating equation (D.6) and (D.7):

$$\frac{dY_{err}}{dt} = \sin(\psi - \psi_t)\sqrt{v^2 + U^2} \tag{D.11}$$

In implementing an algorithm for evaluation of S_t and Y_{err} from equations (D.9) and (D.11) the correct values of ψ_t and $\dfrac{d\psi_t}{dS_t}$ must be determined at the present point in the track. This is defined by the present value of S_t, and requires lookup tables of these variables to be used. Figure D.2 shows a flow diagram of the above algorithm used in MATLAB Simulink during simulator tests.
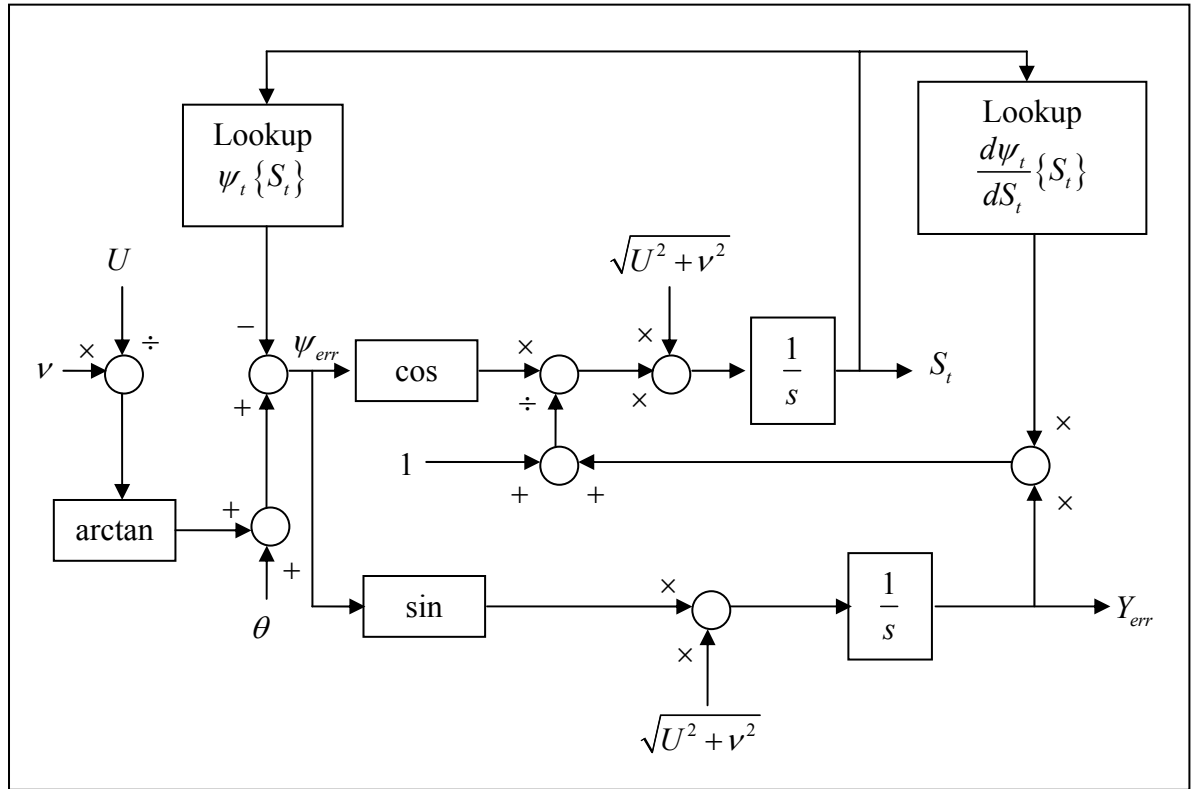
Figure D.2: Flow diagram for intrinsic lateral error estimation using MATLAB Simulink

Appendix E: White noise curvature case in random road profiles

A value of $\gamma = -2$ is significant because it corresponds to a white noise track curvature spectrum as shown in equations (E.1) to (E.4). Firstly, for white curvature input, spectral density of curvature $\left(\Phi_{\frac{d\psi_t}{dS}}(\chi) \right)$ must be white:

$$\Phi_{\frac{d\psi_t}{dS}}(\chi) = \mathrm{K} \tag{E.1}$$

Curvature spectral density corresponds to angle spectral density according to:

$$\Phi_{\frac{d\psi_t}{dS}}(\chi) = \chi^{-2}\Phi_{\psi_t}(\chi) \tag{E.2}$$

Equations (E.1) and (E.2) lead to the following angle spectral density profile for a white curvature spectrum:

$$\Phi_{\psi_t}(\chi) = \mathrm{K}\chi^2 \tag{E.3}$$

Which implies the following parameters for a road profile:

$$\begin{aligned} \gamma &= -2 \\ \kappa &= K \end{aligned} \tag{E.4}$$

References

[1]   Sabey, B. *How fast is fast enough?* in *Scottish Road Safety Campaign Seminar, Killing speed saving lives*. 1993.

[2]   Carsten, O.M.J., et al., *Urban Accidents: Why do they happen?* 1989, AA Foundation for Road Safety Research, Basingstoke.

[3]   Maycock, G., Brocklebank, P.J., and Hall, *Road layout design standards and driver behaviour*. 1998, Transport Research Laboratory TRL, Crowthorne. Report no. 332.

[4]   Quimby, A., et al., *The factors that influence a drivers choice of speed a questionnaire study*. 1999, Transport Research Laboratory TRL, Crowthorne. Report no. 325.

[5]   Quimby, A., et al., *Drivers speed choice an in-depth study*. 1999, Transport Research Laboratory TRL, Crowthorne, Report no. 326.

[6]   Taylor, M., Lynam, D., and Baruya, A., *The effects of drivers speed on the frequency of road accidents*. 2000, Transport Research Laboratory TRL, Crowthorne.

[7]   Winkler, C.B., et al., *Rollover of commercial vehicles*. SAE, 2000.

[8]   Winkler, C.B., et al., *Evaluation of Innovative Converter Dollies*. 1993, University of Michigan Transportation Research Institute, Ann Arbour, MI, USA.

[9]   Kusters, J.J., *Increasing Roll-Over Safety of Commercial Vehicles by Application of Electronic Systems*, in *Smart Vehicles*, J.P. Pauwelussen and Pacejka, H.B., Editors. 1995. p. 326-377.

[10]   Levison, W.H., *Interactive Highway Safety Design Model: Issues Related to Driver Modeling*. Transportation Research Record, 1998. **1631**: p. 20-27.

[11]   Russell, S. and Norvig, P., *Artificial Intelligence*. 3rd ed. 1995: Prentice-Hall, New Jersey.

[12]   Ritchie, M.L., McCoy, W.K., and Welde, W.L., *A Study of the Relation Between Forward Velocity and Lateral Acceleration in Curves During Normal Driving*. Human Factors, 1968. **10**(3): p. 255-258.

[13]   Drury, C.G., *Movements with Lateral Constraint*. Ergonomics, 1971. **14**(2): p. 293-305.

[14]   Glennon, J.A. and Weaver, G.D., *The Relationship of Vehicle Paths to Highway Curve Design*. 1971, Texas Transportation Institute report. p. 134-135.

[15]   Herrin, G.D. and Neuhardt, J.B., *An Empirical Model for Automobile Driver Horizontal Curve Negotiation*. Human Factors, 1974. **16**(2): p. 129-133.

[16]   McLean, J.R., *Driver Behaviour on Curves - A Review*. ARRB Proceedings, 1974. **7**(5): p. 129-147.

[17]   Taragin, A., *Driver performance on horizontal curves*. Proc. Highway Research Board., 1954. **33**.

[18]   Emmerson, J., *Speed of cars and sharp horizontal curves*. Traffic Engineering and Control, 1969: p. 135-137.

[19]   Felipe, E. and Navin, F., *Automobiles on Horizontal Curves, Experiments and Observations*. Transportation Research Record, 1998. **1628**: p. 50-56.

[20] Bottoms, D.J., *The interaction of driving speed, steering difficulty and lateral tolerance with particular reference to agriculture.* Ergonomics, 1983. **26**(2): p. 123- 139.

[21] DeFazio, K., Wittman, D., and Drury, C.G., *Effective Vehicle Width in Self-Paced Tracking.* Applied Ergonomics, 1992. **23**(6): p. 382-386.

[22] Cole, D.J., *Influence of Vehicle Response on the Driver's Preview Control of Speed.* EPSRC Research Proposal, 2002, CUED.

[23] Reymond, G., et al., *Role of Lateral Acceleration in Curve Driving: Driver Model and Experiments on a Real Vehicle and a Driving Simulator.* Human Factors, 2001. **43**(3): p. 483-495.

[24] Van Winsum, W. and Godthelp, H., *Speed Choice and Steering Behaviour in Curve Driving.* Human Factors, 1996. **38**(3): p. 434-441.

[25] Savkoor, A.R. and Ausejo, S., *Analysis of driver's steering and speed control strategies in curve negotiation.* Vehicle System Dynamics, 2000. **v 33**(n Suppl): p. p 94-109.

[26] Wade, A.R., Rosenthal, T.J., and Hogue, J.R., *Modeling and simulation of driver/vehicle interaction.* SAE Special Publications, 1996(n 1141): p. p 27.

[27] Sharp, R.S., Casanova, D., and Symonds, P., *A mathematical model for driver steering control, with design, tuning and performance results.* Vehicle System Dynamics, 2000. **33**(5): p. 289-326.

[28] Prokop, G., *Modeling Human Vehicle Driving by Model Predictive Online Optimisation.* VSD, 2001. **35**(1): p. 19-53.

[29] Denton, G.G., *A Subjective Scale of Speed when Driving a Motor Vehicle.* Ergonomics, 1966. **9**(3): p. 203-210.

[30] Denton, G.G., *The Influence of Adaptation on Subjective Velocity for an Observer in Simulated Rectilinear Motion.* Ergonomics, 1976. **19**(4): p. 409- 430.

[31] Fineberg, M.L., *The Effects of Previous learning on the Visual Perception of Velocity.* Human Factors, 1977. **19**(2): p. 157-162.

[32] Matthews, M.L. and Cousins, L.R., *The Role of Vehicle Characteristics in Drivers' Perception of Automobile Velocity.* Proceedings of the Human Factors Society, 1978. **22**: p. 110-114.

[33] Salvatore, S., *The Estimation of Vehicular Velocity as a Function of Visual Stimulation.* Human Factors, 1968. **10**(1): p. 27-32.

[34] Gawron, V.J. and Ranney, T.A., *Curve Negotiation Performance in a Driving Simulator as a Function of Curve Geometry.* Applied Ergonomics, 1990. **21**(1): p. 22-38.

[35] Guo, K. and Guan, H., *Modelling of Driver/Vehicle Directional Control System.* VSD, 1993. **22**: p. 141-184.

[36] Pick, A.J., *Neuromuscular Dynamics and the Steering Task*, PhD Thesis, Engineering Department, Cambridge University.

[37] Rutherford, S., *Driver Speed Choice and Vehicle Handling*, MEng Thesis, Engineering Department, Cambridge University.

[38] McRuer, D.T. and Krendel, E.S., *The Human Operator as a Servo System Element Part II.* Journal of the Franklin Institute, 1959. **267**: p. 511-536.

[39] McRuer, D.T. and Krendel, E.S., *The Man-Machine System Concept.* Proceedings of the IRE, 1962: p. 1117-1123.

[40] Weir, D.H. and McRuer, D.T., *Dynamics of Driver Vehicle Steering Control.* Automatica, 1970. **6**: p. 87-98.

[41] MacAdam, C.C., *Application of an Optimal Preview Control for Simulation of Closed-Loop Automobile Driving*. IEEE Trans, 1981. **SMC-11**(6): p. 393-399.

[42] Peng, H., *Evaluation of driver assistance systems - a human centred approach*. Proceedings AVEC, 2002.

[43] Sharp, R.S. and Valtetsiotis, V., *Optimal Preview Car Steering Control*. VSD, 2001. **Supp 35**: p. 101-117.

[44] Maciejowski, J.M., *Predictive Control with Constraints*. 2002: Prentice Hall.

[45] Magdaleno, R.E. and McRuer, D.T., *Experimental Validation and Analytical Elaboration For Models of the Pilot's Neuromuscular Subsystem in Tracking Tasks*. Contractor report, 1971, NASA.

[46] MacAdam, C., *Development of a driver model for near/at-limit vehicle handling*. 2001, University of Michigan.

[47] Ljung, L., *System Identification Theory for the User*. 2nd ed, ed. T. Kailath. 1999: Prentice Hall.

[48] Rix, J., *Identification of the closed-loop steering behaviour of a driver*, PhD Thesis, Engineering Department, Cambridge University.

[49] McRuer, D.T. and Jex, H.R., *Review of quasi-linear pilot models*. IEEE Transactions on Human Factors in Electronics, 1967. **v HFE-8**(n 3): p. 231-249.

[50] Peng, H., *An Adaptive Lateral Preview Driver Model*. Vehicle System Dynamics, 2005. **v 43**(n 4): p. 245-259.

[51] Johansson, M. and Nordin, *A Survey of Driving Simulators and their Suitability for Testing Volvo Cars*, Masters Thesis, Chalmers University.

[52] Furukawa, Y., et al., *A Review of Four-Wheel Steering Studies from the Viewpoint of Vehicle Dynamics and Control*. VSD, 1989. **18**: p. 151-186.

[53] Senger, K.H. and Schwartz, W., *The Influence of a Four Wheel Steering System on the Stability Behaviour of a Vehicle-Driver System*. VSD, 1987. **supp**: p. 388-402.

[54] Sharp, R.S. and Crolla, D.A., *Controlled Rear Steering for Cars- a Review*. Proc. IMechE Int. Conf. on Advanced Suspensions, 1988.

[55] Cole, D.J., Pick, A.J., and Odhams, A.M.C., *Predictive and Linear Quadratic Methods for Potential Application to Modelling Driver Steering Control*. Vehicle System Dynamics, 2006. **v 44**(n 3): p. p 259-284.

[56] Sharp, R.S., *CUED Control seminar on LQR preview control for motorbikes*, 2005.

[57] Picardo, L., *Lateral Characteristics of Roads*, MEng Thesis, Engineering Department, Cambridge University.